# Near-field scattering solutions using mixed bases with application to electromagnetic and thermographic ispection of technical materials

Anastassios Skarlatos

## To cite this version:

Anastassios Skarlatos. Near-field scattering solutions using mixed bases with application to electromagnetic and thermographic ispection of technical materials. Engineering Sciences [physics]. Université Paris-Saclay, 2023. tel-04052729

**HAL Id: tel-04052729**

**https://hal.science/tel-04052729**

Submitted on 30 Mar 2023

Habilitation à diriger des recherches

# Near-Field Scattering Solutions using Mixed Bases with Application to Electromagnetic and Thermographic Inspection of Technical Materials

**Habilitation à diriger des recherches**
**de l'Université Paris-Saclay**

**présentée et soutenue à Gif-sur-Yvette, le 31/01/2023, par**

## Anastassios SKARLATOS

### Composition du jury

| | |
|---|---|
| **Herbert DE GERSEM**<br>Professeur des Universités, Technische Universität Darmstadt | Rapporteur |
| **André NICOLET**<br>Professeur des universités, Aix-Marseille Université, Institut Fresnel (UMR CNRS 6133) | Rapporteur |
| **Antonello TAMBURRINO**<br>Professeur des universités, Università degli studi di Cassino e del Lazio Meridionale | Rapporteur |
| **Laurent DANIEL**<br>Professeur des universités, Université Paris-Saclay, CentraleSupélec | Examinateur |
| **Theodoros THEODOULIDIS**<br>Professeur des universités, University of Western Mecedonia | Examinateur |
| **Ruth VAZQUEZ SABARIEGO**<br>Professeur des universités, Katholieke Universiteit Leuven | Examinatrice |

université
PARIS-SACLAY

**Titre :** Solution du problème de diffraction en champ proche à partir des développements sur bases mixtes, avec application aux contrôles non-destructifs électromagnétiques et thermiques.

**Mots clés :** diffraction en champ proche, méthodes spectrales, contrôle non-destructif

**Résumé :** L'inspection par courants de Foucault et la thermographie sont des méthodes bien établies pour le contrôle non destructif et l'évaluation de matériaux utilisés dans un grand nombre d'applications industrielles.

Ces deux méthodes reposent sur des régimes physiques similaires (équation de diffusion), ce qui leur fait partager un certain nombre de caractéristiques communes, la plus importante d'entre elles étant le caractère local de la région de détection. Pour cette raison, les méthodes d'inspection par courants de Foucault (CF) et thermiques peuvent être condidérées comme des méthodes de « diffusion en champ proche ».

Du point de vue de la modélisation, on peut tirer parti du caractère localisé de la solution, du fait que les détails compliqués de la géométrie loin de la sonde peuvent être négligés et on peut se concentrer sur les caractéristiques géométriques essentielles au voisinage de la source.

Sur cette base, le travail présenté ici procède à une construction systématique de solutions rapides pour les problèmes de CF et de propagation de la chaleur appliqués à un certain nombre de configurations avec une importance pratique.

La ligne directrice de tous ces développements est l'exploitation optimale des symétries de la pièce au voisinage de la sonde et le choix de la représentation la mieux adaptée à la configuration donnée. Les méthodes dites spectrales jouent ici un rôle central; la solution est développée à partir de la base propre associée à la géométrie considéré, cette base pouvant être complétée par des représentations mixtes spectrales/spatiales dans les cas les plus complexes.

A la fin de ce document, un aperçu des tendances actuelles et des sujets qui, du point de vue de l’auteur, peuvent faire l’objet de futures recherches, est donné.

**Title :** Near-Field Scattering Solutions using Mixed Bases with Application to Electromagnetic and Thermographic Inspection of Technical Materials

**Keywords :** near-field scattering, spectral methods, non-destructive testing

**Abstract:** Eddy-current and thermographic inspection are well-established tools for the non-destructive testing and evaluation of technical materials involved in a great number of applications.

Both methods are governed by similar physics (diffusion equation), which makes them share a number of common features, the most important one being the local character of the sensing region. For this reason, both eddy-current and thermal inspection methods can be grouped together under the common term: ”near-field scattering” methods.

From the modelling point of view, one can take advantage of the localised character of the solution, since complicated details of the geometry located far from the sensing probe can be safely ignored, and one can concentrate on the essential geometrical features in the vicinity of the source.

Based upon this feature, this work proceeds to a systematic construction of fast solutions for the eddy-current and heat propagation problems, applied to a number of configurations with practical importance. The guiding line in all these developments is the optimal exploitation of the workpiece symmetries in the vicinity of the probe and the adoption of the best suited representation for the given configuration. A central role in this programe is played by the so-callled spectral methods, where the solution is developed in the proper eigenbase of the geometry at hand, complemented by mixed spectral/spatial representations for the more complicated cases.

The work concludes with an overview of the present trends and an outlook of the topics, which, to the author’s point of view, can be the focus for future research.

**Université Paris-Saclay**
Espace Technologique / Immeuble Discovery
Route de l'Orme aux Merisiers RD 128 / 91190 Saint-Aubin, France

# Acknowledgements

The herein presented research work has been accomplished thanks to the implication and the support of several persons.

Prof. T. Theodoulidis is the person who introduced me to the world of semi-analytical approaches for the treatment of electromagnetic non-destructive evaluation problems, and many of the presented results are a direct outcome of the extremely fruitful conversations with him. He has offered me a valuable vision of the domain, which consists in an equilibrated fusion of theory, precise experimental validation and practical reason.

I had the privilege of attending Prof. G. Dasios' lectures on applied mathematics. Prof. Dasios is an outstanding teacher, and his lectures have been a subject of reference and inspiration for me ever since. I do also feel deeply honoured by his kindness to read this text and provide me his valuable comments.

The fertile work environment is a prerequisite for a successful creative work, and for this I am indebted to all my colleagues of the *Laboratoire de Simulation et Modélisation Electromagnétique* of *CEA LIST* and especially to Dr. C. Reboud, who has been the head of the laboratory for the last 10 years. I would also like to thank Dr. D. Lesselier for accompanying me all these years, in the beginning as my post-doctoral advisor and further as co-advisor in a number of jointly supervised Ph.D. works.

I would also like to address my honest gratitude to all the jury members who kindly accepted the task of evaluating these works, and whose excellent remarks contributed to a clear improvement of the final text.

To my parents, Dimitris and Eleni, I owe my most sincere acknowledgement for their lifelong dedication and support. Their love and guidance from the very first steps of my education have been determinant for my studies and my later work as a researcher.

The final word goes to my family, my wife Athena and our children Adrian and Stephane, to whom I wish to dedicate this work. Their support and patience, but most importantly their love, is the most valuable provision and source of courage I have for overcoming all obstacles and facing life with optimism.

**Université Paris-Saclay**
Espace Technologique / Immeuble Discovery
Route de l’Orme aux Merisiers RD 128 / 91190 Saint-Aubin, France

# Contents

# Chapter 1

# Preface

This text summarises the research work carried out at the Department of Imaging and Simulation in Control (Département imagerie et simulation pour le contrôle, DISC) of the French Atomic Energy Commission (Commissariat à l'énergie atomique et aux énergies alternatives, CEA), part of the Paris-Saclay University during my activity as permanent researcher.

This work comprises the development of several theoretical solutions and simulation codes dedicated to the modelling and simulation of nondestructive testing techniques (NDT) using electromagnetic (electromagnetic testing, ET) and thermographic (infrared IR) methods[1]. Under the term NDT is understood the measurement of certain characteristic physical variables (magnetic field, magnetic flux density, temperature) on the surface or above an interrogated specimen, and the thereupon related processing and analysis of the acquired data. The purpose of the measurement is the detection of anomalies with respect to the expected specimen response indicating the existence of defects of the material or the deduction of characteristic parameters of the piece, such as its thickness, its electrical conductivity its magnetic permeability etc. In the former case we are speaking of *classical NDT procedures*, whereas the latter category is usually met in the literature or in the industrial praxis under the term *material characterisation.* It is easily understood that the applied method depends each time from the properties of the material at hand. Eddy-current techniques are restricted to electrically conducting materials (in particular metals), magnetostatic methods are specialised to ferromagnetic specimens (in the vast majority of applications steels), whereas carbon fiber materials are inspected using thermal methods. Other NDT methods such as ultrasonic testing (UT) or radiographic testing/imaging using X-rays (RT) may be better adapted for a specific specimen yet only the aforementioned ET/IR techniques will interest us here.

The common point of the (low-frequency) electromagnetic and thermal methods is that they share very similar physics, i.e. both are described by a diffusion

---

[1] The adopted acronyms of the NDT methods follow the standards of the americal society for nondestructive testing (ASNDT): `www.asndt.org`.

equation. This similarity permits the usage of nearly the same tools for the modelling.

The guiding line for the organisation of the material was the problem geometry. **Chapter 2** provides as a brief introduction of the basic governing equations for the two physical domains of interest in this work, namely the low-frequency electromagnetic and the heat propagation problem, which is meant to serve exclusively the text self-containedness. In the same chapter, the potential formulations for the electromagnetic problem and a couple of important principles, which will extensively utilized in the further chapters, will be presented.

In **chapter 3**, we consider homogeneous pieces with non-crossing boundaries. Special effort is given in order to shed light to the common features of the spectral solutions that can be developed with the aid of the second order vector potential (SOVP) and the truncated region eigenfunction expansion (TREE), the two main tools that will be used throughout this work. The development of the spectral solutions is understood as projections of boundary potential distributions to bases of eigenfunctions spanning the geometrical space of the boundaries. Useful tools towards the construction of an abstract formulation will be the introduction of the Darboux frame and the Dirac ket-bra notation. In the context provided by this abstract language, concrete solutions to specific problems of common interest in NDT applications will be derived.

The restriction of piecewise homogeneous domains will be relaxed in **chapter 4**, where the considered pieces are allowed to dispose a number of internal layers. For the sake of classification, this type of domains will be referred to as pieces with crossing boundaries. The approach developed in chapter 3 will be extended to tackle these geometries. It will be shown that the proposed solution approach (which is essentially the mode-matching method) can be viewed as a special type of homogenisation.

Local material variations (defects) as well as gradients of material properties will be addressed in **chapter 5**, where two different approaches will be considered: the volume integral equation approach (best suited for small defects) and the 3D spectral method, or equivalently the use of global functions (which is more efficient for extended inhomogeneous zones). The calculation of a defect signature as response to external excitation is the central problem in NDT techniques, thus special attention will be given providing detailed comparisons with experimental signals.

Time domain (TD) solutions are of interesting for broad-spectrum (pulsed excited) eddy-current techniques as well as for thermographic methods. Both problems are considered in **chapter 6**. Two different approaches exist here, namely the solution of the problem in the Laplace domain and direct integration in time using time-stepping techniques. The optimal choice depends on the problem, in particular whether we are interested in short/medium or long-time response. The combination of the spectral method with time-stepping is shown to be mathematically isomorphic with the scattering problem containing volumetric (extended) sources, and hence the tools developed for this class of problems are directly applicable here.

In **chapter 7**, the combination of a mesh-based method, namely the finite integration technique, introduced by T. Weiland in the late seventies and been further developed in the two following decades, with spectral methods, is examined. The purpose here is to extend the domain of applicability of the latter, without the need to resort to the numerical complexity of the 3D spatial discretisation.

The solution of the non-linear electromagnetic induction problem is the topic of **chapter 8**. The calculation of the electromagnetic field in materials with non-linear and hysteretic material law is the keystone for the development of simulation codes for material characterisation applications. When the fixed-point approach is used for the problem linearisarion, the problem is translated to the solution of Helmholtz equation with unknown equivalent volumetric sources. As a consequence, the tools developed for the treatment of inhomogeneous pieces are directly applicable. This is particularly interesting since the spectral approach can be also used here, with obvious benefits for the computational speed.

The text is ending with **chapter 9**, which gives an overview of the perspectives of the developments presented in the main part of the text, which are positioned with respect to the state-of-the-art.

Since we are mainly dealing with problems of engineering interest the use of the S.I. system of units has been judged as the most suitable choice, and hence it will be consistently used throughout this text.

# Chapter 2

# Governing equations

In this first chapter we shall proceed to a brief presentation of the underlying physical equations for the two classes of diffusion problems that will be considered throughout this work: the eddy-current induction problem, with magnetostatics being treated as an asymptotic case valid for vanishing frequency, and the heat transfer problem.

Two important theorems that will be repeatedly used in the following chapters, namely the equivalence principle and the reciprocity theorem will be presented for the electromagnetic problem. The former provides a very convenient way of forming classes of equivalent problems that are more easy to treat, and serves as basis for building hybrid approaches. The latter will arm us with a very elegant and efficient way of calculating the inductor response upon its interaction with the surrounding medium, a physical variable of major interest since it stands for the main experimental observable in electromagnetic inspection applications.

## 2.1 Maxwell equations

Starting point for the analysis of the electromagnetic problem is the Maxwell equations which in their full form read[1] [1–4]

$$\nabla \times \mathbf{E} = -\frac{\partial \mathbf{B}}{\partial t} \tag{2.1}$$

$$\nabla \times \mathbf{H} = \frac{\partial \mathbf{D}}{\partial t} + \mathbf{J} \tag{2.2}$$

$$\nabla \cdot \mathbf{D} = \rho \tag{2.3}$$

$$\nabla \cdot \mathbf{B} = 0. \tag{2.4}$$

where **E**, **H** are the electric and magnetic field strength, **D**, **B** the electric and magnetic flux density, **J** stand for the total current density (eddy-currents and

---

[1] The SI unit system will be adopted throughout this text, and consequently the Maxwell equations and all electromagnetic quantities will be expressed in this system.

sources), and $\rho$ is the free electric charge density.

From the conjugate field variables used in the Maxwell equations to express the electric and magnetic field effect, only $\mathbf{E}$ and $\mathbf{B}$ are experimentally observable, with $\mathbf{D}$ and $\mathbf{H}$ being auxiliary mathematical quantities introduced to account for the field interaction with the material. They are related with the former via the constitutive laws of the medium, which in their most general form read

$$\mathbf{D} = \varepsilon_0\mathbf{E} - \mathbf{P}(\mathbf{E}) \tag{2.5}$$

$$\mathbf{B} = \mu_0\mathbf{H} + \mathbf{I}(\mathbf{H}) \tag{2.6}$$

where $\varepsilon_0$, $\mu_0$ are the electric permittivity and magnetic permeability of the free space[2] and $\mathbf{P}, \mathbf{I}$ the electric and magnetic polarisation, respectively. The latter stand for the volume density of elementary electric and magnetic dipoles in the medium, and are defined via the relations

$$\mathbf{P} \coloneqq \frac{1}{V}\sum_i \mathbf{p}_i \tag{2.7}$$

and

$$\mathbf{I} \coloneqq \frac{\mu_0}{V}\sum_i \mathbf{m}_i. \tag{2.8}$$

Note that in the majority of the textbooks the preferred variable is the the magnetisation $\mathbf{M}$ rather than the magnetic polarisation, the two variables differing by the magnetic permeability constant[3], i.e.

$$\mathbf{I} = \mu_0\mathbf{M}. \tag{2.9}$$

The electric polarisation and magnetisation are functions of the electric and magnetic field. The derivative of the electric polarisation and the magnetisation with respect to the respective field is known as electric and magnetic susceptibility, giving the degree that the medium is susceptible to polarisation under the action of the respective field. In the case of linear anisotropic materials without hysteresis these are field-independent second rank tensors, and they are given by the relations

$$\mathbf{P} = \varepsilon_0\overline{\chi}_e \cdot \mathbf{E} \tag{2.10}$$

and

$$\mathbf{I} = \mu_0\overline{\chi}_m \cdot \mathbf{H} \tag{2.11}$$

---

[2] In the SI system, the electric permittivity and magnetic permeability values are $\varepsilon_0 = 8.8541878128(13) \times 10^{-12}$ F m$^{-1}$ and $4\pi \times 10^{-7}$ H m$^{-1}$, respectively.

[3] The distinction is relevant for the SI units. In other unit systems like the cgs or the Heaviside-Lorentz system, for example, both variables are identical. The reason for introducing the magnetic constitutive relation using $\mathbf{I}$ is purely aesthetic since with this variable the two constitutive laws are more symmetric. In the rest of the text, both $\mathbf{I}$ and $\mathbf{M}$ will be used interchangeably, the particular choice being dictated each time by the notational convenience.

which implies for the corresponding flux densities

$$\mathbf{D}(\mathbf{E}) = \varepsilon_0 \left(\bar{\mathbf{I}} - \overline{\chi}_e\right) \cdot \mathbf{E} \tag{2.12}$$

$$\mathbf{B}(\mathbf{H}) = \mu_0 \left(\bar{\mathbf{I}} + \overline{\chi}_m\right) \cdot \mathbf{H}. \tag{2.13}$$

The terms in parenthesis are called the relative electric permittivity and magnetic permeability of the medium $\overline{\varepsilon}_r$ and $\overline{\mu}_r$ defined as

$$\overline{\varepsilon}_r = \bar{\mathbf{I}} - \overline{\chi}_e \tag{2.14}$$

$$\overline{\mu}_r = \bar{\mathbf{I}} + \overline{\chi}_m \tag{2.15}$$

Things are more complicated in case of non-linear materials, where there are different ways of defining the susceptibilities. For the magnetic field in particular, we distinguish between the usual proportionality relation, the differential and the incremental susceptibility/permeability [5]. More details on this topic will be given when considering the non-linear problem in chapter 8.

The last constitutive relation is concerned with the induced currents. The current density term $\mathbf{J}$ in the Maxwell equations comprises three contributions: the excitation (or source) current density $\mathbf{J}_s$, the conductivity current density $\mathbf{J}_c$, which is due to the conductivity of the medium, and the free-charges current $\mathbf{J}_f$ density

$$\mathbf{J} = \mathbf{J}_s + \mathbf{J}_c + \mathbf{J}_f. \tag{2.16}$$

The conductivity current is produced in conductive media as the result of the interaction of the charge carriers in the medium (free electrons in the case of metals, electron and holes in the case of semiconductors) with the electric field, which is determined by another constitutive relation. For the materials and the field intensities we are here considering, it is a linear constitutive relation, known as Ohm's law. In the most general case of an anisotropic medium it is expressed by the relation

$$\mathbf{J}_c = \overline{\sigma} \cdot \mathbf{E} \tag{2.17}$$

where $\overline{\sigma}$ stands for the tensor electric conductivity. In the special case that $\mathbf{J}_c$ is caused by electromagnetic induction, we refer to it as eddy current. Note, however, that the eddy currents are not the only electric currents that can exist in the conductive medium. Any potential drop imposed by an external source (e.g. a battery) will result in a current flow in the medium, which is not an eddy current in the strict sense. Nevertheless, since this kind of currents will not be of our concern in this text, all currents governed by Ohm's law will be considered to be eddy currents without distinction.

The last term of (2.16), namely the free-charge current $\mathbf{J}_f$ is of interest in plasma physics problems, where the free-charge densities are non-negligible, and it will not be considered any further in this text.

Although the above set of seven equations (the four Maxwell equations together with the three constitutive relations) account for all macroscopic electromagnetic phenomena, in many particular situations, only a subset of them needs to be addressed in many cases depending on the excitation frequency and the material. Five different regimes can be distinguished by considering the different possible combinations of the above two factors: electrostatics, magnetostatics, quasi-electrostatics, quasi-magnetostatics and full wave regime. In the following, we shall consider only the magnetostatic and quasi-magnetostatic formulations, since these formulations are useful for the most electromagnetic inspection applications, which are the target of the herein developed modelling techniques (acknowledging though the potential interest of electrostatic methods in some special cases).

## 2.2 Boundary and interface conditions

The differential form of the Maxwell equations presented above is applicable in all regions, where physical properties vary continuously. When material discontinuities (or surface sources) are involved, the solution will be also discontinuous across those interfaces.

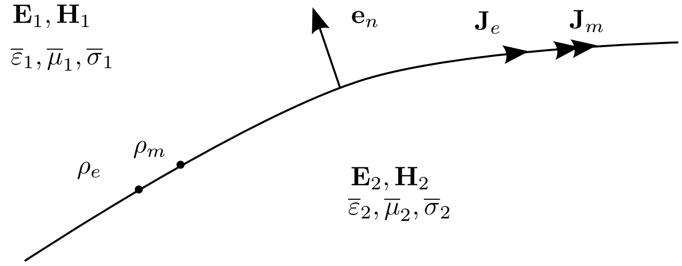

Figure 2.1: Field and flux density discontinuity across boundaries with electric/magnetic current and charge distributions. $\mathbf{e}_n$ stands for the unit normal vector.

Let an interface separating two adjacent domains as shown in Fig. 2.1. The relations that the electromagnetic field must satisfy at that surface read

$$\mathbf{e}_n \times (\mathbf{H}_2 - \mathbf{H}_1) = \mathbf{J}_e \tag{2.18}$$

$$\mathbf{e}_n \cdot (\mathbf{D}_2 - \mathbf{D}_1) = \rho_e \tag{2.19}$$

where $\mathbf{H}_1, \mathbf{D}_1$ are the magnetic field and the electric flux density in the first domain and $\mathbf{H}_2, \mathbf{D}_2$ the corresponding quantities in the second. $\mathbf{J}_e, \rho_e$ stand for the surface current density and the surface electric charge density at the boundary as shown in Fig. 2.1. The proof of (2.18)-(2.21) can be found in any classical electrodynamics text book such as [1–4], just to mention some, and will not be reproduced here.

Invoking the symmetry of the Maxwell equations, we can also write an analogous pair of conditions for the electric field and the magnetic flux density, namely

$$\mathbf{e}_n \times (\mathbf{E}_2 - \mathbf{E}_1) = \mathbf{J}_m \tag{2.20}$$

$$\mathbf{e}_n \cdot (\mathbf{B}_2 - \mathbf{B}_1) = \rho_m \tag{2.21}$$

where here $\mathbf{E}_1, \mathbf{B}_1$ are the electric field and the magnetic flux density in the first domain and $\mathbf{E}_2, \mathbf{B}_2$ in the second. The corresponding sources $\mathbf{J}_m, \rho_m$ express surface magnetic current and surface magnetic charge densities. To be compatible with the Maxwell equations, these must be complemented in the following way

$$\nabla \times \mathbf{E} = -\frac{\partial \mathbf{B}}{\partial t} - \mathbf{J}_m \tag{2.22}$$

$$\nabla \cdot \mathbf{B} = \rho_m. \tag{2.23}$$

These sources are non-physical quantities that are normally zero at any **physical interface** (which implies that the tangential electric field and the normal magnetic induction components should be continuous across those interfaces). As purely mathematical auxiliary quantities, $\mathbf{J}_m$ and $\rho_m$ prove, however, to be very useful in defining classes of equivalent problems by introducing **fictitious interfaces** to the problem. It can be easily shown that this notion of fictitious currents and charges is equivalent to the Huygens principle. This concept will be rigorously introduced in the following section, where is discussed the equivalence principle, and excessively exploited in the following chapters.

## 2.3 Surface equivalence theorem and Huygens principle

In the treatment of electromagnetic problems, it is often very convenient to replace the actual sources by equivalent ones, which have the same effect to the solution. This replacement is allowed thanks to the surface equivalence theorem, which is nothing more than a mathematical description of the Huygens principle. The term *surface* is used here to distinguish from the volume equivalence theorem, which will be derived in chapter 5 where the electromagnetic problem is studied for inhomogeneous materials.

The principle of the surface equivalent theorem is explained in Fig. 2.2. Let as assume a closed boundary $S$ dividing the computational domain into two subdomains, $V_1$ and $V_2$. The surface $S$ can be a real interface or a fictitious boundary. We additionally assume an arbitrary electric and magnetic electric current distribution, which is entirely contained in domain $V_1$, as it is shown in Fig. 2.2a. The problem is equivalent with the configuration described by Fig. 2.2b, where the actual field source $\mathbf{J}_e, \mathbf{J}_m$ has been replaced by an equivalent surface distribution $\mathbf{J}_e^{eq}, \mathbf{J}_m^{eq}$ on $S$ defined as

$$\mathbf{J}_e^{eq} = \mathbf{n} \times (\mathbf{H} - \mathbf{H}') \tag{2.24}$$

$$\mathbf{J}_m^{eq} = -\mathbf{n} \times (\mathbf{E} - \mathbf{E}') \tag{2.25}$$

where $\mathbf{E}, \mathbf{H}$ stands for the solution of the original problem, $\mathbf{E}', \mathbf{H}'$ is the solution in $V_1$ in the equivalent formulation and $\mathbf{n}$ is the unit normal on the boundary $S$. We are free to choose the value of $\mathbf{E}', \mathbf{H}'$, as long as we are not interested in the solution in that part of the geometry. A useful option is to set both fields to zero, i.e. $\mathbf{E}' = \mathbf{H}' = \mathbf{0}$. In this case, we eliminate the effects of the geometry in $V_1$, since a zero field does not interact with it, and hence replace the actual geometry with a material of choice (free-space, perfect electric conductor (PEC), perfect magnetic conductor (PMC), etc.), which results in a significant simplification of the problem. The main difficulty here is that the equivalent current is not known a priori but depends on the solution. For that reason the equivalent problem is treated using an integral equation approach or iteratively [6, 7].

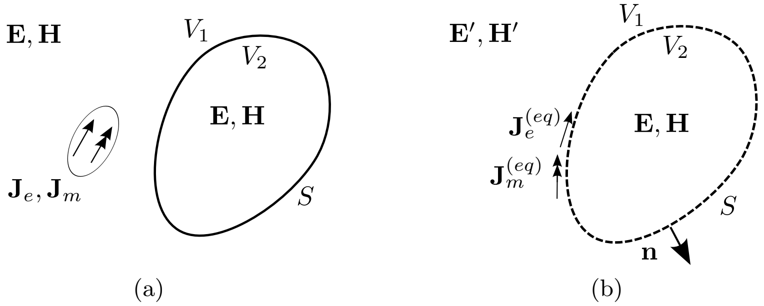

Figure 2.2: (a) Actual and (b) equivalent problem for a given pair of electric and magnetic sources.

A second interesting option in case that $V_1$ is free of any material is to decompose the field in that subdomain into a primary and scattered field contribution provided. The infinite space solution is defined here as primary (source) field $\mathbf{E}^{(p)}, \mathbf{H}^{(p)}$, whereas the scattered field term $\mathbf{E}^{(s)}, \mathbf{H}^{(s)}$ is reserved for the perturbation due to the geometry in $V_2$. The decomposition and the formulation of the equivalent problem in this case is sketched in Fig. 2.3. The equivalent sources defined for this decomposition read

$$\mathbf{J}_e^{eq} = -\mathbf{n} \times \mathbf{H}^{(p)} \tag{2.26}$$

$$\mathbf{J}_m^{eq} = \mathbf{n} \times \mathbf{E}^{(p)} \tag{2.27}$$

The latter formulation of the equivalence principle is mentioned in [3] as the *induction theorem.* Its basic advantage with respect to the first formulation is that the equivalent sources are given explicitly by Biot-Savart's law (or an equivalent calculation) and there is no need for iteration. This latter form of the equivalence theorem will be used in several occasions in the remaining of this work.

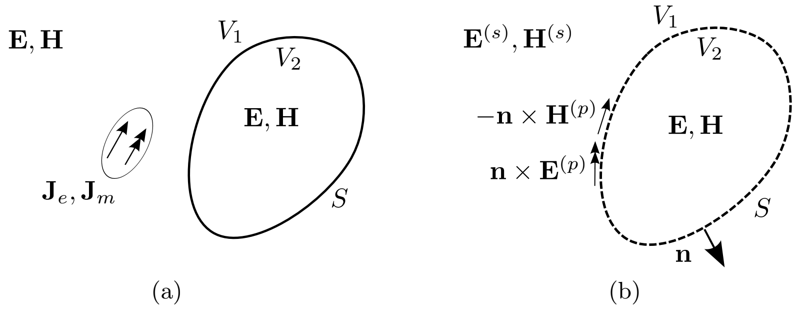

Figure 2.3: (a) Actual and (b) equivalent problem for a given pair of electric and magnetic sources.

## 2.4 Potential formulations: scalar decomposition of the field problem

### 2.4.1 Magnetostatics: the scalar magnetic potential formulation

Setting $d/dt = 0$, the Maxwell equations split into two uncoupled sets of equations, one for the electric and one for the magnetic field. The two subsets stand for the electrostatic and the magnetostatic formulation respectively. For the particular case of a static magnetic field, the resulting state equations read

$$\nabla \times \mathbf{H} = \mathbf{J}_e \tag{2.28}$$

$$\nabla \cdot \mathbf{B} = 0 \tag{2.29}$$

with $\mathbf{J}_e$ being an arbitrary, time invariant, solenoid current ($\nabla \cdot \mathbf{J}_e = 0$). The zero-curl condition of the macroscopic currents is necessary in order to be consistent with Ampère's equation (2.28). We shall also assume that the considered domain is piecewise homogeneous and that each current source is entirely contained in one of the homogeneous subdomains (no internal boundaries are allowed).

The total magnetic field can be decomposed into two terms, i.e. $\mathbf{H} = \mathbf{H}_s + \mathbf{H}_d$, where $\mathbf{H}_s$ is an arbitrary solution to (2.28) and $\mathbf{H}_d$ a compensation curl-free field

$$\nabla \times \mathbf{H}_d = 0 \tag{2.30}$$

which enforces Gauss' law (2.29).

Since we have the liberty of choice for the particular solution, we let $\mathbf{H}_s$ be the magnetic field induced by source in the infinite medium; in other words we choose for $\mathbf{H}_s$ the field given by the Biot-Savart law (recall that by hypothesis the subdomain containing the considered source is homogeneous). $\mathbf{H}_d$ will be result of the source field $\mathbf{H}_s$ interaction with the domain boundaries. By virtue of (2.30), we can express $\mathbf{H}_d$ as the gradient of a scalar potential, exactly in direct analogy with the electrostatic potential [1]

$$\mathbf{H}_d = -\nabla\Phi \tag{2.31}$$

where the minus sign is added solely to maintain the similarity with the electrostatics. Using the magnetic constitutive relation (2.6) and substituting in Gauss' law (2.29), we obtain

$$\nabla \cdot (\overline{\mu} \cdot \nabla\Phi) = -\nabla \cdot (\overline{\mu} \cdot \mathbf{H}_s] \tag{2.32}$$

where we have taken into account the solenoid character of the Biot-Savart field $\nabla \cdot \mathbf{H}_s = 0$.

Our main concern for the class of applications considered in this work is the calculation of the magnetic field inside and in the vicinity of conducting and/or magnetic pieces. Since all independent current sources are located in the air and at a certain distance (lift-off) from the pieces, we shall restrict our analysis in source-free case, i.e. $\mathbf{J} = 0$ in the region of interest. Following the standard approach, the problem can be reformulated in these regions using a scalar magnetic potential

$$\mathbf{B} = -\nabla\Phi \tag{2.33}$$

which satisfies the Laplace equation

$$\nabla^2\Phi = 0. \tag{2.34}$$

The boundary conditions introduced in section 2.2 for the tangential magnetic field and the normal magnetic induction reduce in magnetostatics to continuity relations for the potential and its normal derivative (for the source-free case) across the domain boundaries, namely

$$\Phi_i = \Phi_{i+1} \tag{2.35}$$

and

$$\mu_i \partial_n \Phi_i = \mu_{i+1} \partial_n \Phi_{i+1}. \tag{2.36}$$

### 2.4.2 Eddy-current diffusion problem: the vector magnetic potential $(\mathbf{A}, \Phi)$ formulation

We wish to address now the case where the sources are no longer static but are varying with the time. A basic assumption made throughout this text will be that the time variation of the source is slow enough for the displacement currents to be negligible. This is the so-called quasi-static approximation, and it is valid for the applications considered in the context of non-destructive testing (NDT) and materials evaluation.

Since in most of this work we shall be interested in harmonic excitations, we shall restrict ourselves in harmonic currents for the development of the general formulation, in this and the subsequent chapters. All physical variables admit therefore a time variation of the form $e^{i\omega t}$ with $\omega$ being the angular frequency and $i$ standing for the imaginary unit $i = \sqrt{-1}$. The transient case will be considered in detail in chapter 6.

Using the above simplifications and assuming both electric and magnetic currents (2.1)-(2.4) are written

$$\nabla \times \mathbf{E} = -i\omega\mathbf{B} - \mathbf{J}_m \tag{2.37}$$

$$\nabla \times \mathbf{H} = \sigma\mathbf{E} + \mathbf{J}_e \tag{2.38}$$

$$\nabla \cdot \mathbf{D} = 0 \tag{2.39}$$

$$\nabla \cdot \mathbf{B} = \rho_m. \tag{2.40}$$

where we have integrated Ohm's law to separate the eddy-current terms $\sigma\mathbf{E}$ from the independent current sources.

The usual practice in quasi-static problems it to reformulate the initial vector formulation in terms of the magnetic vector potential $\mathbf{A}$, which in absence of magnetic sources $(\mathbf{J}_m, \rho_m)$ is defined via the relation

$$\mathbf{B} = \nabla \times \mathbf{A} \tag{2.41}$$

which results for the electric field

$$\mathbf{E} = -i\omega\mathbf{A} - \nabla\Phi. \tag{2.42}$$

$\Phi$ is a scalar potential whose role it to account for the curl-free part of the electric field according to the Helmholtz decomposition. Since the divergence of $\mathbf{A}$ has not been fixed yet, we are free to choose any convenient value for it. The standard choice in the low-frequency case (where no wave propagation is present) is to set it equal to zero

$$\nabla \cdot \mathbf{A} = 0. \tag{2.43}$$

This is the so-called Coulomb gauge. With the application of the Coulomb gauge and in absence of free charges, (2.42) simply becomes

$$\mathbf{E} = -i\omega\mathbf{A}. \tag{2.44}$$

Substitution of (2.41) and (2.44) to Ampère's equation yields the so-called curl-curl equation for the vector magnetic potential

$$\nabla \times \left(\mu^{-1}\nabla \times \mathbf{A}\right) + i\omega\sigma\mathbf{A} = \mathbf{J} \tag{2.45}$$

We are particularly interested in solutions for piecewise homogeneous media[4], which implies that the permeability can be drawn out of the curl operator inside each subdomain. In conjunction with the Coulomb gauge this results in the inhomogeneous Helmholtz equation for the vector magnetic potential

$$\left(\nabla^2 - k^2\right)\mathbf{A} = -\mu\mathbf{J} \tag{2.46}$$

---

[4] This restriction will be relaxed in chapter 7 where hybrid numerical-modal schemes will be developed.

with the separation constant

$$k^2 = i\omega\mu\sigma. \tag{2.47}$$

The $(\mathbf{A}, \Phi)$ formulation is not amenable to a scalar equation except for the 2D TM case, which involves 3-component solutions with the magnetic field lying in the normal to the symmetry axis plane. Practically, this case is met in the following cases

- Pieces with translational symmetry excited by an infinitely long current filament (or current strip or rod) parallel to the symmetry axis, i.e. $\mathbf{J} = J\mathbf{e}_c$ with $\mathbf{e}_c$ being a unit vector parallel to the symmetry axis. In this case, $\mathbf{A}$ can be written as one component vector in the direction of the current $\mathbf{A} = A\mathbf{e}_c$ .

- Pieces with rotational symmetry, with a circular filament (or coil) concentric with the symmetry axis, i.e. $\mathbf{J} = J\mathbf{e}_\phi$ with $\mathbf{e}_\phi$ being the azimuthal unit vector in the cylindrical coordinate system defined by the symmetry. For this class of problems, the $\mathbf{A} = A\mathbf{e}_\phi$ ansatz is applied.

The scalarisation of (2.46) in the first case is straight forward. For the rotational symmetry, however, the Laplacian of the $\mathbf{e}_\phi$ gives rise to an additional term resulting to the scalar equation

$$\left(\nabla^2 - \frac{1}{\rho^2} - k^2\right) A = -\mu J \tag{2.48}$$

where $\rho$ is the radial direction.

### 2.4.3 Second order potential $(W_a, W_b)$ formulation

As analysed in the previous paragraph, the $(\mathbf{A}, \Phi)$ formulation allows us to reduce the original vector field problem to a scalar one if the entire configuration (piece and sources) is translationally or rotationally symmetric. For 3D problems, however, the scalarisation is not possible anymore with this approach.

This difficulty can be overcome either by introducing a dual to $\mathbf{A}$ vector potential, i.e. $\mathbf{F}$, and proceeding in a one-component ansatz for both $\mathbf{A}, \mathbf{F}$ (see for example [3]) or by introducing a higher-order potential. The potentials of the second approach, which proves to be equivalent with the former one, are known in the literature under different names, such as Hertz and Debye potentials or second order vector potential (SOVP). A thorough overview of the different definitions can be found in Tab. 1.2 of [8], which is reproduced in Tab. 2.1 of this text for convenience. There is a great number of research papers using those potentials', hence the list does not claim completeness. The focus remains (beside some very classical references) on the literature devoted to the eddy-current problem.

| **Potential name** | **Symbols** | **Source** |
|---|---|---|
| Hertz | $\Gamma, \Pi$ | Jackson [1], Weaver [9], Burke [10] |
| Hertz | $\Pi^*, \Pi$ | Stratton [2] |
| Hertz | $\Pi_m^*, \Pi_e^*$ | Wait |
| Debye | $\pi_e, \pi_m$ | Chew [4], Wait and others |
| Debye | $\Pi_1, \Pi_2$ | Bouwkamp and Casimir [11], Debye [12] |
| Hertzian | $\psi', \psi$ | Bowler [13] |
| Second order | $W_a, W_b$ | Smythe [14], Theodoulidis [8] |
| Higher order | $W_1, W_2$ | Weigelt [15], Bowler [16] |
| Higher order | $P_1, P_2$ | Hannakam [17, 18] |
| Higher order | $P_{\mathrm{TE}}, P_{\mathrm{TM}}$ | Nethe [19] |

Table 2.1: Symbols and names of the vector potential used in the scalarisation of the vector field. Classification following Theodoulidis and Kriezis [8] (updated and complemented with further references).

For consistency with recent work on the semi-analytical formulation, in particular with the work of Theodoulidis, Bowler et al., where the potential of choice is SOVP ($W_a, W_b$), and given the fact that this formulation has been used in the published work this text is based upon, the SOVP potential conventions will be adopted henceforth.

Recalling that the **A** is divergence-free (a property imposed by Coulomb's gauge), one can express **A** in terms of another vector potential **W**

$$\mathbf{A} = \nabla \times \mathbf{W}. \tag{2.49}$$

The magnetic induction is written in terms of the SOVP as follows

$$\mathbf{B} = \nabla \times \nabla \times \mathbf{W} \tag{2.50}$$

which justifies the term *second order*. From (2.49) one easily obtains for the electric field

$$\mathbf{E} = -i\omega \nabla \times \mathbf{W}. \tag{2.51}$$

Let us now express **W** in terms of two scalar potentials $W_a$ and $W_b$ as follows

$$\mathbf{W} = W_a \mathbf{c} + \nabla W_b \times \mathbf{c} \tag{2.52}$$

where **c** is a pivoting vector. The definition of the pivoting vector and the resulting scalarisation for these coordinates systems amenable to the separation of the Helmholtz equation is summarised in Tab. 2.2.

| **Coordinate system** | **Pivoting vector** |
|---|---|
| Cartesian | $\mathbf{e}_x, \mathbf{e}_y, \mathbf{e}_z$ |
| Cylindrical | $\mathbf{e}_z$ |
| Elliptical | $\mathbf{e}_z$ |
| Parabolic | $\mathbf{e}_z$ |
| Spherical | $\mathbf{r}$ |
| Conic | $\mathbf{r}$ |

Table 2.2: SOVP scalarisation for the coordinate systems admitting separation of the Helmholtz equation. By virtue of the cartesian system isotropy, the pivoting vector can be aligned with any of the $x, y, z$ directions. For all the other systems this symmetry does not exist and the choice of $\mathbf{c}$ is unique. Table reproduced from Tab. 1.2 in [8].

From (2.52) it is clear that the $W_a, W_b$ potentials correspond to the TE$_c$ and TM$_c$ mode respectively. Written in matrix form (2.52) becomes

$$\mathbf{W} = (\mathbf{c} \quad \nabla \times \mathbf{c}) \cdot \begin{pmatrix} W_a \\ W_b \end{pmatrix} \tag{2.53}$$

whence

$$\mathbf{B} = \nabla \times \nabla \times (\mathbf{c} \quad \nabla \times \mathbf{c}) \cdot \begin{pmatrix} W_a \\ W_b \end{pmatrix} \tag{2.54}$$

and

$$\mathbf{E} = -i\omega \nabla \times (\mathbf{c} \quad \nabla \times \mathbf{c}) \cdot \begin{pmatrix} W_a \\ W_b \end{pmatrix} \tag{2.55}$$

The above equations for the electric and the magnetic field can be brought together in a common matrix form as follows

$$\begin{pmatrix} \mathbf{B} \\ \mathbf{E} \end{pmatrix} = \begin{pmatrix} \nabla \times \nabla \times \mathbf{c} & \nabla \times \nabla \times \nabla \times \mathbf{c} \\ -i\omega \nabla \times \mathbf{c} & -i\omega \nabla \times \nabla \times \mathbf{c} \end{pmatrix} \cdot \begin{pmatrix} W_a \\ W_b \end{pmatrix} \tag{2.56}$$

Equation (2.56) is important because it establishes the link between the state variables (the potentials $W_a$ and $W_b$) with the physical observables, namely the magnetic induction $\mathbf{B}$ and the electric field $\mathbf{E}$. It can be seen as the analogue of the corresponding magnetostatic expression (2.33), where the role of the scalar magnetostatic potential is taken over from the potential doublet $(W_a \quad W_b)^T$. We can assert thus that the latter is the state vector of the eddy-current problem. A simpler form can be obtained by applying the vector identity

$$\nabla \times \nabla \times = \nabla \nabla \cdot - \nabla^2 \tag{2.57}$$

whence

$$\begin{pmatrix} \mathbf{B} \\ -\mathbf{E}/i\omega \end{pmatrix} = \begin{pmatrix} c\nabla \partial_c - \nabla^2 \mathbf{c} & -\nabla^2 (\nabla \times \mathbf{c}) \\ \nabla \times \mathbf{c} & c\nabla \partial_c - \nabla^2 \mathbf{c} \end{pmatrix} \cdot \begin{pmatrix} W_a \\ W_b \end{pmatrix} \tag{2.58}$$

and taking into account that both $W_{a,b}$ satisfy the Helmholtz operator as well as that the Laplacian operator commutes with the pivoting vector[5], the transition operator can be simplified further

$$\left( \begin{array}{c} \mathbf{B} \\ -\mathbf{E}/i\omega \end{array} \right) = \left( \begin{array}{cc} c\nabla\partial_c - k^2\mathbf{c} & k^2\mathbf{c}\times\nabla \\ -\mathbf{c}\times\nabla & c\nabla\partial_c - k^2\mathbf{c} \end{array} \right) \cdot \left( \begin{array}{c} W_a \\ W_b \end{array} \right). \tag{2.59}$$

We now seek to establish the equation of state for the $W_a, W_b$ potentials. The procedure is similar with that followed for **A**, that is, we substitute (2.49) and (2.50) in Ampère's equation, yielding

$$\nabla\times\nabla\times\nabla\times\mathbf{W} + k^2\nabla\times\mathbf{W} = \mu\mathbf{J} \tag{2.60}$$

with $k^2$ being given by (2.47).

Taking the curl of both sides and upon application of the vector identity (2.57) we obtain

$$\nabla\times\nabla\times\left(\nabla^2 - k^2\right)\mathbf{W} = -\mu\nabla\times\mathbf{J} \tag{2.61}$$

where we have tacitly assumed that the medium is piecewise homogeneous. In a source-free medium ($\mathbf{J} = 0$) the above relation implies

$$\left(\nabla^2 - k^2\right) W_{a,b} = 0. \tag{2.62}$$

In other words, in a source-free, homogeneous medium, the state equation for the SOVP potential reduces to two independent scalar Helmholtz equations. It must however be underlined that the two resulting scalar problems (for $W_a$ and $W_b$) are not, in general, independent of each other, since there might be a coupling via the boundaries. In order for the $W_a$ and $W_b$ solutions to be independent, i.e. for a complete problem scalarisation there is another condition that must be fulfilled, which imposes that the pivot vector is normal to the geometry interfaces [4]. This condition is verified in stratified planar and spherical media and cylindrical geometries with stratification along the $z$ axis.

## 2.5 Reciprocity theorem

The impedance variation of the sensing coil is a basic observable in eddy-current testing (ECT) applications. Therefore, its precise calculation is of central importance. An accurate and elegant way of calculating this quantity is through the application of the reciprocity theorem, which in its quintessence is based upon the exchange of "source" and "measurement". In the case of field calculations, the latter term is understood as the field value at a certain reference (measurement) position. The analogy with the equivalence principle is obvious, since in both cases, the problem is transformed into an equivalent one by introducing virtual sources.

---

[5] For the cartesian and the cylindrical system this is obvious. For the spherical one, it can be shown that $\nabla^2\mathbf{r} = 0$.

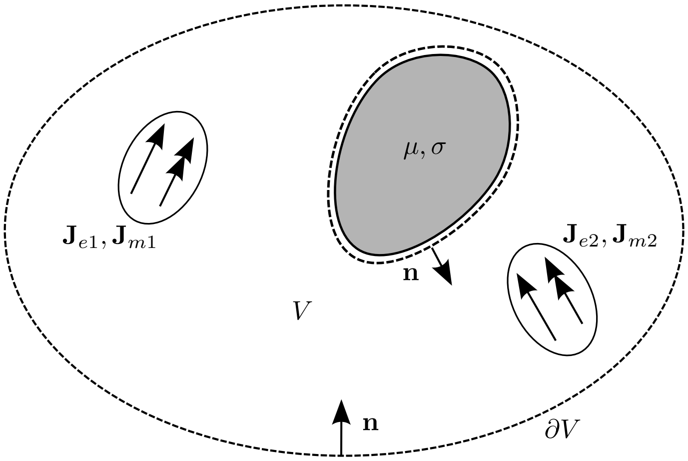

Figure 2.4: Application of the reciprocity theorem in a domain enclosing a pair of electric and magnetic sources $\mathbf{J}_{e1}, \mathbf{J}_{m1}$ and $\mathbf{J}_{e1}, \mathbf{J}_{m1}$.

Let $\mathbf{E}_1$, $\mathbf{H}_1$ and $\mathbf{E}_2$, $\mathbf{H}_2$ be any two solutions to Maxwell's equations that correspond to two pairs of electric and magnetic sources $\mathbf{J}_{e1}, \mathbf{J}_{m1}$ and $\mathbf{J}_{e2}, \mathbf{J}_{m2}$, respectively. The examined configuration is illustrated in Fig. 2.4. We assume also that all sources have a harmonic time dependence (the time-domain version of the reciprocity theorem will be examined in the dedicated chapter).

In any homogeneous domain $V_f$, it can be proven that the two solutions satisfy the following formula, known as the Lorentz reciprocity theorem [3]:

$$-\nabla \cdot (\mathbf{E}_1 \times \mathbf{H}_2 - \mathbf{E}_2 \times \mathbf{H}_1) = \mathbf{E}_1 \cdot \mathbf{J}_{e2} + \mathbf{H}_2 \cdot \mathbf{J}_{m1} - \mathbf{E}_2 \cdot \mathbf{J}_{e1} - \mathbf{H}_1 \cdot \mathbf{J}_{m2} \tag{2.63}$$

Integrating in $V$ and applying the Gauss' theorem leads to the following equivalent form of the reciprocity theorem

$$\begin{aligned} &\int\limits_V (\mathbf{E}_1 \cdot \mathbf{J}_{e2} + \mathbf{H}_2 \cdot \mathbf{J}_{m1} - \mathbf{E}_2 \cdot \mathbf{J}_{e1} - \mathbf{H}_1 \cdot \mathbf{J}_{m2})\,\mathrm{d}V \\ &= \oint\limits_{\partial V} (\mathbf{E}_1 \times \mathbf{H}_2 - \mathbf{E}_2 \times \mathbf{H}_1) \cdot \mathbf{n}\mathrm{d}S \end{aligned} \tag{2.64}$$

with $\partial V$ standing for the domain boundary and $\mathbf{n}$ the inward pointing unit vector.

In case that the exciting sources are induction coils, $\mathbf{J}_{m1} = \mathbf{J}_{m2} = \mathbf{0}$ and the volume integral in (2.64) becomes

$$\int\limits_V (\mathbf{E}_1 \cdot \mathbf{J}_{e2} - \mathbf{E}_2 \cdot \mathbf{J}_{e1})\,\mathrm{d}V = I_1 I_2 (Z_{21} - Z_{12}) \tag{2.65}$$

where $I_1 Z_{12}$ is the voltage induced to the second coil (which is functioning in pick-up mode) when the first coil (source) is fed with current $I_1$, and $Z_{12}$ stands for their mutual impedance. In the same fashion, $I_2 Z_{21}$ yields the voltage in the first coil due to the excitation current $I_2$ in the second one. If we further assume that $\mathbf{E}_1$, $\mathbf{H}_1$ is the solution in the free space (i.e. $\sigma = 0, \mu_r = 1$), whereas $\mathbf{E}_2$, $\mathbf{H}_2$ stand for the field solution in the presence of the medium, we can write for the mutual impedances

$$Z_{12} = Z_0 + \Delta Z_{12} \tag{2.66}$$

$$Z_{21} = Z_0 \tag{2.67}$$

where $Z_0$ is the mutual impedance in the air (it is the same for both coils due to symmetry), and $\Delta Z_{11}$ is the impedance change due to the presence of the material. Substitution in (2.65), taking into account (2.64) yields after some trivial manipulations

$$\Delta Z_{12} = \frac{1}{I_1 I_2} \oint\limits_{\partial V} (\mathbf{E}_1 \times \Delta\mathbf{H}_2 - \Delta\mathbf{E}_2 \times \mathbf{H}_1) \cdot \mathbf{n} \mathrm{d}S \tag{2.68}$$

where $\Delta\mathbf{E}_2$, $\Delta\mathbf{H}_2$ is the corresponding variation in the field solution due to the presence of the conductor. Equation (2.68) has been first proposed by Auld [20–22]. It provides a very convenient and accurate way of calculating the impedance change since it is given directly in variational form and that the integration is carried out on the boundary and not along the coil turns.

Another useful form of the reciprocity theorem is obtained by letting the $\partial V$ boundary extend to infinity, enclosing in this way the interrogated piece in the integration domain. In this case the surface integral of (2.64) vanishes, whereas the volume integral takes care of the piece contribution via the equivalent electric and magnetic current sources that the latter introduces

$$\Delta Z_{12} = -\frac{1}{I_1 I_2} \int\limits_{V} (\mathbf{E}_1 \cdot \mathbf{J}_{e2} - \mathbf{H}_1 \cdot \mathbf{J}_{m2}) \, \mathrm{d}V \tag{2.69}$$

This form of reciprocity theorem is particularly adapted for the calculation of anomalies in the inspected piece and will be studied in detail in a dedicated chapter later in this text, where the equivalent volumetric sources $\mathbf{J}_{e2}, \mathbf{J}_{m2}$ will be defined.

## 2.6 Heat equation

Heat propagation is also a diffusion problem, like the eddy-current induction problem, with the main difference with the latter being its scalar nature. The similar physics allows us to employ the same computational tools with those used for the eddy-current problem. In this paragraph, we shall proceed to a brief overview of the governing equations for the heat propagation problem in the absence of conduction terms, identify the variables of interest, and we shall provide the appropriate boundary conditions that allow to pose the problem, in order to prepare the discussion on the construction of solutions in the next chapters.

The temperature distribution $T(\mathbf{r})$ in a domain where the thermal equilibrium has not been established, is described by two equations, namely the energy conservation and Fourier's law. The energy conservation law in an arbitrary medium reads

$$\nabla \cdot \mathbf{J} = -\rho c_p \frac{\partial T}{\partial t} + \dot{q} \tag{2.70}$$

where $\rho$ is the mass density of the medium, $c_p$ its specific heat capacity under constant pressure[6], $\dot{q}$ stands for the heat production or absorption rate by external sources, and $\mathbf{J}$ gives the density of the thermal current, which expresses the heat transfer across the medium.

Fourier's law is a conduction relation connecting the thermal current density with the temperature gradient, in analogy with Ohm's law for the electric currents and Fick's law for particle diffusion. In the general case of an anisotropic medium, Fourier's law takes the form of a tensor relation

$$\mathbf{J} = -\overline{\kappa} \cdot \nabla T \tag{2.71}$$

where $\overline{\kappa}$ is the thermal conductivity tensor of the medium.

Combining (2.70) with (2.71) we obtain the heat equation

$$\nabla \cdot (\overline{\kappa} \cdot \nabla T) - \rho c_p \frac{\partial T}{\partial t} = -\dot{q}. \tag{2.72}$$

In the case of isotropic and homogeneous media, the thermal conductivity becomes a scalar coefficient and (2.72) reduces to the more compact (and familiar) form involving the Laplace operator

$$\nabla^2 T - \alpha^{-1} \frac{\partial T}{\partial t} = -\kappa^{-1} \dot{q}. \tag{2.73}$$

where $\alpha$ is the diffusivity of the medium defined as $\alpha = \kappa/\rho c_p$. In heat propagation problems, the mass density and the specific heat terms always appear as a product, hence there is no need to consider them separately. Hence, it is more convenient to use the volumetric heat capacity $\mathscr{C}_p$ instead, defined as

$$\mathscr{C}_p = \frac{C_p}{V} = \rho c_p \tag{2.74}$$

where $C_p$ is the heat capacity and $V$ the volume of the piece. Using this definition, the diffusivity becomes $\alpha = \kappa \mathscr{C}_p^{-1}$.

Let us now assume a piecewise homogeneous medium consisting of a number of subdomains. The thermal coefficients $\kappa$, $c_p$ and $\rho$ are constant throughout the medium, yet their value may differ from domain to domain. We consider

---

[6] Since we are almost always under a constant (atmospheric) pressure experimental condition, we use the isobaric $c_p$ instead of the isochoric $c_v$ variant of the specific heat capacity, the latter being measured at constant volume.

the boundary between the $i$th and the $(i+1)$th domain. The temperature and the normal to the surface heat flux should be continuous across the boundary, that is

$$T_i = T_{i+1} \tag{2.75}$$

and

$$\kappa_i \partial_n T_i = \kappa_{i+1} \partial_n T_{i+1} \tag{2.76}$$

where $n$ stands for the normal to the boundary direction.

No mention has been made so far about the temperature scale. The fact that $T$ appears in (2.73) preceded by differentiation operators (in both spatial and time domains) implies that the heat equation is symmetric to any gauge transformation. This in its turn means that we can work either using the K or the °C scale interchangeably. Since the latter is more spread in the technical world, we shall assume henceforth that all temperature variables are expressed in the °C scale.

The state equation (2.73) together with the continuity relations expressed by (2.75) and (2.76) consist the full statement of the heat propagation problem.

# Chapter 3

# Geometries with non-intersecting interfaces

In this chapter, we shall focus on geometries consisting of a number of non-intersecting interfaces, which separate homogeneous domains. We shall assume that all interfaces satisfy symmetry relations along their two principal axes. It can be shown that in this case the problem solution can be expressed in suitable spectral (Fourier) bases, and we shall try to introduce a general formalism in order to treat the problems mixing interfaces of different symmetries in a unified manner.

## 3.1 Description of the problem

Let us consider a geometry comprising a number of objects, whose interfaces do not intersect each other. A sketch of such a geometry is shown in Fig. 3.1, which depicts a layered medium embedding a number of voids. The material inside each consisting object is assumed to be homogeneous and isotropic. The entire structure is illuminated by an arbitrary closed current source represented by the current loop in the same figure.

Now consider a solution domain composed by $N$ homogeneous subregions, separated by $N-1$ non-crossing interfaces. For reasons that will become clear in the following paragraphs, we will distinguish between two indexing systems for the boundaries of the solution domain: one counting the boundaries as geometrical entities of the structure, i.e. $\alpha = 1, \dots, (N-1)$, and one scanning through all oriented side of the surfaces, that is $i = 1, \dots, 2(N-1)$. For avoiding confusion between the two indexing systems, we shall use greek letters for the first and latin letters for the second. The indexing of the subdomains themselves presents no ambiguities so no special care will be taken to adopt notation conventions for it.

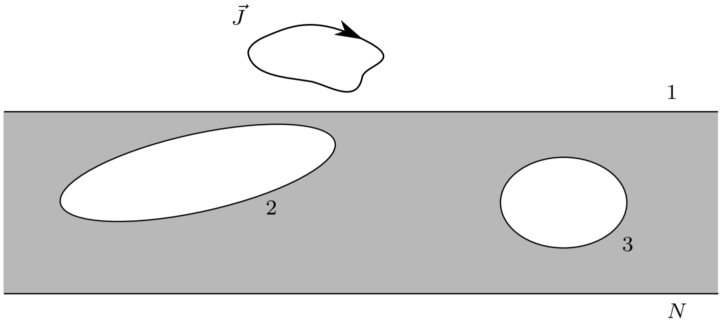

Figure 3.1: Cross-section of a layered medium containing a number of voids with non-intersecting interfaces, excited by an arbitrary current source.

## 3.2 Continuity relations: the trace operator

Before proceeding to the development of the method itself, the continuity relations for the three diffusion problems, i.e. the magnetostatic, eddy-current and the heat conduction problem, introduced in chapter 2, will be reformulated using a more compact notation based on matrix operators. This more abstract way of posing the continuity of the state variables will prove useful for the construction of common generic expressions applicable for all different considered problem classes.

Since the continuity relations are associated with the interfaces of the medium, a usefull tool will be the Darboux reference frame that will be briefly introduced. This generic frame will allow us to express the continuity relations in an independent from the specific coordinate system form.

### 3.2.1 The Darboux reference frame and the principal curvatures

Let $S$ be an oriented surface in the three-dimensional Euclidean space $\mathbb{R}^3$, and let a therein embedded curve parametrised by arc length $\gamma(s) \in S$. At each point of the curve $\mathbf{p}$, one may attach a unique unit normal vector $\mathbf{n}(\mathbf{p})$, whose orientation is determined by the orientation of the surface. The Darboux frame is defined at $\mathbf{p}$ via the following relations

$$\mathbf{e}_t(s) = \gamma'(s) \tag{3.1}$$

$$\mathbf{e}_n(s) = \mathbf{e}_n(s) \tag{3.2}$$

$$\mathbf{e}_g(s) = \mathbf{e}_n(s) \times \mathbf{e}_t(s)\,. \tag{3.3}$$

The triplet $(\mathbf{e}_g, \mathbf{e}_t, \mathbf{e}_n)$ defines a positively oriented orthonormal basis attached to each point of the curve.

The Darboux frame is closely related with the Frenet-Serret frame, whose normal vectors are defined by the relations

$$\mathbf{e}_T(s) = \gamma'(s) \tag{3.4}$$

$$\mathbf{e}_N(s) = \frac{\mathbf{e}'_T(s)}{|\mathbf{e}'_T(s)|} \tag{3.5}$$

$$\mathbf{e}_B(s) = \mathbf{e}_T(s) \times \mathbf{e}_N(s)\,. \tag{3.6}$$

Since the tangent vectors are the same in both cases, there is a unique angle $\alpha$ such that a rotation in the plane of $N$ and $B$ produces the pair $g$ and $n$:

$$\begin{pmatrix} \mathbf{e}_t \\ \mathbf{e}_g \\ \mathbf{e}_n \end{pmatrix} = \begin{pmatrix} 1 & 0 & 0 \\ 0 & \cos\alpha & \sin\alpha \\ 0 & -\sin\alpha & \cos\alpha \end{pmatrix} \begin{pmatrix} \mathbf{e}_T \\ \mathbf{e}_N \\ \mathbf{e}_B \end{pmatrix}. \tag{3.7}$$

The previous definition of the Darboux frame is quite general since it has not been specified how $\gamma(s)$ is chosen. A common choice for $\gamma(s)$ and the thereupon derived Darboux trihedron $\mathbf{e}_t, \mathbf{e}_g, \mathbf{e}_n$ is based at the principal planes of the surface.

As normal plane at $\mathbf{p}$ is defined one that contains the normal vector $\mathbf{n}$, and will therefore also contain a unique direction tangent to the surface. Its intersection with the surface $S$ is a plane curve, called normal section. It is known from differential geometry that this curve will have in general different curvatures for different normal planes at $\mathbf{p}$. The principal curvatures at $\mathbf{p}$, denoted $k_1$ and $k_2$, are the maximum and minimum values of this curvature [23,24]. If the two principal curvatures share the same value, then the principal directions are undefined. It can be shown [24] that when defined, the principal directions are always orthogonal to each other and normal to $\mathbf{n}$. Setting thus $\gamma(s)$ as the curve defined by the section of one of the principal normal planes with the surface $S$, the principal directions coincide with $\mathbf{e}_g$ and $\mathbf{e}_t$ forming together with $\mathbf{n}$ the Darboux trihedron. The directions of the three unit vectors are illustrated in Fig. 3.2.

In order to be able to use the Darboux frame without ambiguities, we need to adopt a number of conventions concerning the association of the Darboux trihedron to the principal directions.

The basic hypothesis of this work is recalled here, i.e. all the considered geometries dispose a symmetry axis (the excitation being excluded from any symmetry assumptions). We discern the following cases:

- **The principal directions are defined**. We choose the bi-normal vector
- $\mathbf{e}_g$ along the symmetry direction.
- **The principal directions are undefined**. This statement is equivalent with saying that there is an infinity of equal curvatures, i.e. the geometry possesses a second axis of symmetry. This is the case for planar and spherical geometries, disposing a translational and rotational symmetry in two mutually perpendicular axes, respectively. In this case, we arbitrarily

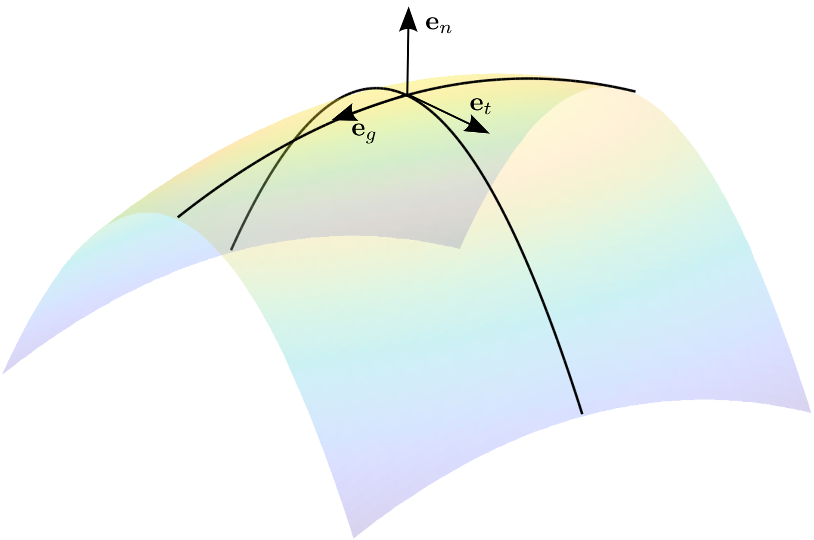

Figure 3.2: The Darboux reference frame defined with respect to the surface principal directions.

> choose $\mathbf{e}_g = \mathbf{e}_y$ for the planar and ($\mathbf{e}_g = \mathbf{e}_\phi$) for the spherical case. The particular choice has been made in order to conform $(t, g, n)$ with the $(x, y, z)$ and $(r, \theta, \phi)$ permutations of the native to the geometry cartesian and spherical coordinate systems, respectively.

An overview of these conventions and the correspondence to the respective native coordinate system for the most common workpiece geometries, is summarised in Tab. 3.1.

| Geometry | Coordinate System | Symmetry axis | Associated Darboux frame $(t, g, n)$ |
|---|---|---|---|
| Plate | Rectangular | $y$ | $(x, y, z)$ |
| Plate | Cylindrical | $\phi$ | $(\rho, \phi, z)$ |
| Tube/rod (coaxial) | Cylindrical | $\phi$ | $(z, \phi, -\rho)$ |
| Tube/rod (eccentric) | Cylindrical | $z$ | $(\phi, z, \rho)$ |
| Sphere | Spherical | $\phi$ | $(\theta, \phi, \rho)$ |

Table 3.1: Assignment of the Darboux axes in some particular piece geometries with practical interest.

The same conventions can be applied to other coordinate systems like the elliptical and the spheroidal (either prolate or oblate). Yet these systems are not further considered in this work.

### 3.2.2 Trace operator for the magnetostatic problem

Armed with the definition of the Darboux reference frame, we return to our initial problem of the boundary conditions and examine how this definition applies at an arbitrary interface separating the $i$th and the $i+1$th domains. For simplicity, we shall consider that the interface does not contain surface sources (either physical or equivalent). The generalisation to interfaces with sources is straightforward.

Introducing the continuity (trace) operator $\hat{\boldsymbol{C}}$

$$\hat{\boldsymbol{C}} = \begin{pmatrix} \hat{\mathbf{1}} \\ \partial_n \end{pmatrix} \tag{3.8}$$

and the material operator in the $i$th subdomain $\hat{\boldsymbol{\mu}}_i$

$$\hat{\boldsymbol{\mu}}_i = \begin{pmatrix} 1 & 0 \\ 0 & \mu_i \end{pmatrix} \tag{3.9}$$

(2.35) and (2.36) can be merged in a single expression involving matrix operators

$$\hat{\boldsymbol{\mu}}_i \hat{\boldsymbol{C}} \Phi_i = \hat{\boldsymbol{\mu}}_{i+1} \hat{\boldsymbol{C}} \Phi_{i+1} \tag{3.10}$$

with $\Phi_i$ and $\Phi_{i+1}$ being the potential solution in the two adjacent subdomains.

### 3.2.3 Trace operator for the heat conduction problem

Following the same considerations, the continuity relations for the heat conduction problem (2.75) and (2.76) can be transformed in matrix form resulting in

$$\hat{\boldsymbol{\kappa}}_i \hat{\boldsymbol{C}} T_i = \hat{\boldsymbol{\kappa}}_{i+1} \hat{\boldsymbol{C}} T_{i+1} \tag{3.11}$$

where $T_i$ and $T_{i+1}$ is the temperature in the two domains, $\hat{\boldsymbol{C}}$ is the same with and the material operator $\hat{\boldsymbol{\kappa}}_i$ defined as

$$\hat{\boldsymbol{\kappa}}_i = \begin{pmatrix} 1 & 0 \\ 0 & \kappa_i \end{pmatrix}. \tag{3.12}$$

### 3.2.4 Trace operator for the eddy-current problem

According to section 2.4.3, the state variable for the eddy-current problem is not scalar anymore but the doublet of the scalar potentials $W_a$ and $W_b$[1]. Furthermore, as already stated in the respective section, we distinguish between two kinds of interfaces: (a) between air and conducting piece and (b) between two conductors.

---

[1] We shall consider only the $(W_a, W_b)$ representation here, the $(\mathbf{A}, \Phi)$ being reserved for the 2D problem, for which it reduces to a scalar formulation. The $(\mathbf{A}, \Phi)$ representation will be the subject of a later part of this work where mixed spatial/spectral bases will be used for the treatment of pieces with arbitrary cross-sectional geometry.

Let us consider the case of an air-conductor interface, separating the $i$ and $i+1$ subdomains, and let us assign $i$ to the non-conducting one. The state variable in the air region is the corresponding magnetostatic potential, resulting the following Darboux representation for the magnetic field components on the considered interface

$$\begin{pmatrix} B_t \\ B_b \\ B_n \end{pmatrix}_i = -\begin{pmatrix} \mathbf{e}_t \cdot \nabla \\ \mathbf{e}_g \cdot \nabla \\ \mathbf{e}_n \cdot \nabla \end{pmatrix} \Phi_i. \tag{3.13}$$

In the conductor region, the magnetic induction is expressed in terms of the state vector $\mathbf{W} = (W_a, W_b)^T$ according to (2.59)

$$\begin{pmatrix} B_t \\ B_b \\ B_n \end{pmatrix}_{i+1} = \begin{pmatrix} \mathbf{e}_t \cdot \nabla \partial_c - k^2 (\mathbf{e}_t \cdot \mathbf{c}) & -k^2 (\mathbf{e}_t \times \mathbf{c}) \cdot \nabla \\ \mathbf{e}_g \cdot \nabla \partial_c - k^2 (\mathbf{e}_g \cdot \mathbf{c}) & -k^2 (\mathbf{e}_b \times \mathbf{c}) \cdot \nabla \\ \mathbf{e}_n \cdot \nabla \partial_c - k^2 (\mathbf{e}_n \cdot \mathbf{c}) & -k^2 (\mathbf{e}_n \times \mathbf{c}) \cdot \nabla \end{pmatrix} \cdot \begin{pmatrix} W_a \\ W_b \end{pmatrix}_{i+1} \tag{3.14}$$

Introducing (3.13),(3.14) to the boundary conditions (2.18),(2.21) we obtain

$$\hat{\boldsymbol{\nu}}_i \hat{\boldsymbol{C}}_i \Phi_i = \hat{\boldsymbol{\nu}}_{i+1} \hat{\boldsymbol{C}}_{i+1} \mathbf{W}_{i+1} \tag{3.15}$$

with the trace operators

$$\hat{\boldsymbol{C}}_i = -\begin{pmatrix} \nabla_t \\ \nabla_g \\ \nabla_n \end{pmatrix} \tag{3.16}$$

$$\hat{\boldsymbol{C}}_{i+1} = \begin{pmatrix} \nabla_t \partial_c - k^2 (\mathbf{e}_t \cdot \mathbf{c}) & -k^2 (\mathbf{e}_t \times \mathbf{c}) \cdot \nabla \\ \nabla_g \partial_c - k^2 (\mathbf{e}_g \cdot \mathbf{c}) & -k^2 (\mathbf{e}_b \times \mathbf{c}) \cdot \nabla \\ \nabla_n \partial_c - k^2 (\mathbf{e}_n \cdot \mathbf{c}) & -k^2 (\mathbf{e}_n \times \mathbf{c}) \cdot \nabla \end{pmatrix} \tag{3.17}$$

and the material operator

$$\hat{\boldsymbol{\nu}}_i = \begin{pmatrix} \nu_i & 0 & 0 \\ 0 & \nu_i & 0 \\ 0 & 0 & 1 \end{pmatrix}. \tag{3.18}$$

where we have set $\nabla_a = \mathbf{e}_a \cdot \nabla, \ (a = t, g, n)$ for brevity.

The corresponding formalism for the conductor-conductor interface is obtained in the same fashion, recalling that the boundary condition has to ensure the continuity of the tangential components for both the magnetic and electric field, delivering the relation

$$\hat{\boldsymbol{\nu}}_i \hat{\boldsymbol{C}}_i \mathbf{W}_i = \hat{\boldsymbol{\nu}}_{i+1} \hat{\boldsymbol{C}}_{i+1} \mathbf{W}_{i+1} \tag{3.19}$$

where

$$\hat{\boldsymbol{C}}_i = \begin{pmatrix} \nabla_t \partial_c - k^2 (\mathbf{e}_t \cdot \mathbf{c}) & -k^2 (\mathbf{e}_t \times \mathbf{c}) \cdot \nabla \\ \nabla_g \partial_c - k^2 (\mathbf{e}_g \cdot \mathbf{c}) & -k^2 (\mathbf{e}_b \times \mathbf{c}) \cdot \nabla \\ (\mathbf{e}_t \times \mathbf{c}) \cdot \nabla & \nabla_t \partial_c - k^2 (\mathbf{e}_t \cdot \mathbf{c}) \\ (\mathbf{e}_g \times \mathbf{c}) \cdot \nabla & \nabla_g \partial_c - k^2 (\mathbf{e}_g \cdot \mathbf{c}) \end{pmatrix} \tag{3.20}$$

and

$$\hat{\boldsymbol{\nu}}_i = \begin{pmatrix} \nu_i & 0 & 0 & 0 \\ 0 & \nu_i & 0 & 0 \\ 0 & 0 & 1 & 0 \\ 0 & 0 & 0 & 1 \end{pmatrix}. \tag{3.21}$$

with the corresponding definitions for the $\hat{\boldsymbol{C}}_{i+1}$ and $\hat{\boldsymbol{\nu}}_{i+1}$ following analogously.

Instead of using the magnetostatic potential in the air regions, we can address the problem using the $W_a$ potential by recalling that in air

$$\mathbf{B} = c\nabla\partial_c W_a \tag{3.22}$$

where $\mathbf{c}$ is the pivoting vector, which means that the two potentials are related via

$$\Phi = c\partial_c W_a. \tag{3.23}$$

Using $W_a$ instead of $\Phi$ can interesting since it leads to more uniform expressions involving a single type of potential. The drawback is the higher derivative which makes the expressions less elegant. Both formulations are equivalent and will be used interchangeably throughout the text.

The explicit relations for the trace operators of the scalar and the vector (eddy-current) problem for the Darboux surfaces summarised in Tab. 3.1 are given in the appendix.

## 3.3 Solution description by means of analytic propagators

In chapter 2, it has been demonstrated that the eddy-current problem can be scalarised using either a single component magnetic potential $A\mathbf{c}$ or using the SOVP duplet $(W_a, W_b)$. In both cases, $A, W_a$ and $W_b$ satisfy independently the Helmholtz equation. Magnetostatics can be formally considered as the zero-frequency limit ($\omega \to 0$) and/or zero-conductivity ($\sigma \to 0$) limit of the eddy-current problem, and it can be described by means of a scalar potential which is linked with the $W_a$.

We may therefore pursue the analysis by considering a generic scalar potential (which can be $\Phi, A, W_a$ or $W_b$), to which we shall assign the generic symbol $\Psi$, and which satisfies the Helmholtz equation (2.62), rewritten here in operator form

$$\left(\hat{\boldsymbol{L}} - k^2\right)\Psi = 0 \tag{3.24}$$

where $\hat{\boldsymbol{L}} \coloneqq \nabla^2$ is the Laplace operator and $k$ the separation constant defined in (2.47). As mentioned above, the magnetostatic problem is the limiting case with $k = 0$.

Let us now consider a bounded homogeneous domain $V$, and assume that the potential $\Psi$ is known along the domain boundary $\partial V$ (cf. Fig. 3.3).

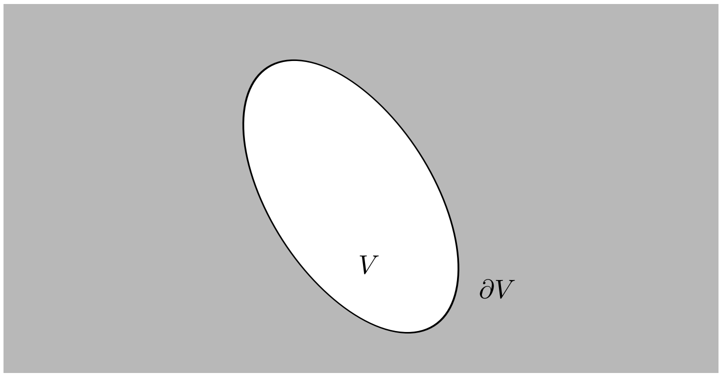

Figure 3.3: Bounded homogeneous domain. We assume the potential distribution at the boundary $\partial V$ being known

We know from the uniqueness theorem, that if the potential is given on the boundary $\partial V$, then it is uniquely defined throughout the entire domain $V$. We shall seek to formally express the solution at any interior point in $V$ through the potential value on the boundary. This mapping from the domain boundary to its interior is achieved making use of Green's second identity

$$\begin{aligned}\Phi(\mathbf{x}) &= \oint\limits_{\partial V} \left[\Phi(\mathbf{x}')\, \nabla' g(\mathbf{x},\mathbf{x}') - g(\mathbf{x},\mathbf{x}')\, \nabla'\Phi(\mathbf{x}')\right] \cdot \mathrm{d}\mathbf{S}' \\ &= \oint\limits_{\partial V} \left[\partial_n' g(\mathbf{x},\mathbf{x}') - g(\mathbf{x},\mathbf{x}')\, \partial_n'\right] \Phi(\mathbf{x}')\, \mathrm{d}S', \;\; \mathbf{x} \in V \end{aligned} \tag{3.25}$$

where $g(\mathbf{x},\mathbf{x}')$ stands for Green's function of free space, defined via

$$\left(\nabla^2 - k^2\right) g(\mathbf{x},\mathbf{x}') = \delta(\mathbf{x}-\mathbf{x}') \tag{3.26}$$

with $\delta(\bullet)$ the Dirac delta function, and $\mathbf{n}$ the outward pointing unit normal vector. $\partial_n'$ denotes the directional derivative along the normal direction acting on the primed coordinates.

The scalar Green's function expression in the free space is known in closed form, and is given by

$$g(\mathbf{x},\mathbf{x}') = \frac{e^{ik|\mathbf{x}-\mathbf{x}'|}}{4\pi\,|\mathbf{x}-\mathbf{x}'|}. \tag{3.27}$$

We define a Darboux frame associated with the $\partial V$ boundary surface according to the conventions of 3.2.1, and we assume that the Helmholtz operator is separable in the coordinate system associated with this frame (this is always possible if the surface is a characteristic surface in one of the 11 separable coordinate systems [25]). Then, there exists a complete orthogonal basis of $\hat{\boldsymbol{L}}_T$ eigenfunctions (with the subscript $T$ standing for the "tangential", which spans the $(t,g)$ subspace

$$\hat{\boldsymbol{L}}_T f_\alpha(x_t,x_g) = \lambda_\alpha(x_n)\, f_\alpha(x_t,x_g) \tag{3.28}$$

with the associated inner product

$$\langle f_\alpha, f_\beta \rangle = \oint\limits_{\partial V} f_\alpha(\mathbf{x})^\dagger \, f_\beta(\mathbf{x}) \, dS = \delta_{\alpha\beta}, \ \mathbf{x} \in \partial V \tag{3.29}$$

$\delta_{\alpha\beta}$ being the Kronecker delta[2]. Notice that the eigenvalue $\lambda_\alpha$ is in the general case a function of the normal coordinate (take for example the case of the cylindrical of spherical coordinate system). Since the basis is complete, $f_\alpha(\mathbf{x})$ will also satisfy the completeness relation

$$\sum_\alpha f_\alpha(\mathbf{x})^\dagger \, f_\alpha(\mathbf{x}') = \delta(\mathbf{x} - \mathbf{x}') \, , \ \mathbf{x} \in T. \tag{3.30}$$

$\Psi$ can be expanded in the vicinity of $\partial V$ in terms of the eigenfunction basis as follows

$$\Psi(\mathbf{x}) = \sum_\alpha c_\alpha f_\alpha(x_t, x_g) \tag{3.31}$$

The development coefficients $c_\alpha$ are determined by the potential value on the boundary $\partial V$

$$c_\alpha = \oint\limits_{\partial V} f_\alpha(\mathbf{x})^\dagger \, \Psi(\mathbf{x}) \, dS. \tag{3.32}$$

In the same fashion, we can develop the normal derivative of the potential at $\partial V$ in an eigenfunction series

$$\partial_n \Psi(\mathbf{x}) = \sum_\alpha d_\alpha f_\alpha(x_t, x_g) \tag{3.33}$$

with

$$d_\alpha = \oint\limits_{\partial V} f_\alpha(\mathbf{x})^\dagger \, \partial_n \Psi(\mathbf{x}) \, dS \tag{3.34}$$

accordingly. Notice that $c_n$ and $d_n$ are not independent since the potential and its normal derivative must satisfy the Helmholtz equation. Besides, the independence of the potential and its derivative would contradict the uniqueness theorem. Assume that they are related via a linear relation

$$d_\alpha = R_\alpha c_\alpha. \tag{3.35}$$

The coefficient $R_\alpha$ will be determined below, when the herein abstract formulation will be specialised for the most common coordinate systems. For the moment, we may underline the formal resemblance with Ohm's law. Indeed, this relation describes a Robin's type condition, which is nothing less than an impedance-like link between the two state variables.

---

[2] All bases will be henceforth tacitly implied being normalised unless otherwise stated.

Introducing (3.31) and (3.33) into (3.25), we obtain

$$\begin{aligned}\Psi(\mathbf{x}) &= \sum_{\alpha} \left[c_\alpha \langle \partial'_n g, f_\alpha\rangle + d_\alpha \langle g, f_\alpha\rangle\right] \\ &= \sum_{\alpha} c_\alpha \langle \partial'_n g + R_\alpha g, f_\alpha\rangle \end{aligned} \tag{3.36}$$

which can be written as

$$\Phi(\mathbf{x}) = \sum_{\alpha} c_\alpha \hat{\boldsymbol{P}}_\alpha f_\alpha(x'_t, x'_g) \tag{3.37}$$

where $\hat{\boldsymbol{P}}_\alpha$ is a "propagation" operator defined as

$$\hat{\boldsymbol{P}}_\alpha f_\alpha(x'_t, x'_g) \coloneqq \langle \partial'_n \left(g e^{R_\alpha x'_n}\right), f_\alpha\rangle e^{-R_\alpha x'_n}. \tag{3.38}$$

The explicit expression of $\hat{\boldsymbol{P}}_n$ for a given projection basis is obtained by substituting $g(\mathbf{x}, \mathbf{x}')$ from (3.27) and carrying out the integration. In the following, we shall perform this evaluation for the three most common coordinate systems, namely the rectangular, the cylindrical and the spherical ones in order to derive the respective explicit expressions for the propagator in these systems.

### 3.3.1 Cartesian coordinates

We start the analysis with the rectangular system. For convenience, we shall work directly in the cartesian coordinates system assuming that $\mathbf{e}_n = \mathbf{e}_z$ converting the final result to the Darboux frame afterwards.

Let us consider the integration plane at $z' = \text{const.}$ and let us assume that the observation point lies at $z \geq z'$. Although it is possible to work directly with the continuous eigenvalues spectrum of the infinite plate, it is preferable for reasons of notational simplicity and consistence with the rest of the text to discretise the spectrum by truncating the computational domain. Indeed, solutions to the diffusion (or static) problem are characterised by a rapid decrease as we are moving apart from the region of interest (following roughly an inverse square law), hence we can assume that they practically vanish at a sufficient distance. As a consequence, we may truncate the computational domain at that distance using a convenient termination condition (Dirichlet, Neumann or periodic), without significant impact to the solution. This is the major assumption of the truncated region eigenfunctions expansion (TREE method, which allows the conversion of a continuous to a discrete eigenvalues spectrum. It is the same assumption made when solving the problem using a mesh-based method, like the finite elements method (FEM) of the finite integration technique (FIT), where a finite computational domain is achieved by applying an artificial truncation using one of the above-mentioned conditions. Things are different when wave propagation is the major mechanism, in which case a specially designed absorbing truncation condition like the perfectly matched layer is necessary to exclude numerical reflections back into the domain.

We apply a periodic boundary condition at $x = \pm L/2$ and $y = \pm L/2$, which results in the following eigenfunction basis

$$f_{m,n}(x, y) = \frac{1}{L} e^{i\kappa_m x + i\lambda_n y} \tag{3.39}$$

with the eigenvalues

$$\kappa_m = \frac{2\pi m}{L} \tag{3.40}$$

and similarly for $\lambda_n$.

To continue with the calculation of the inner products, we seek to express the Green's function into a more convenient form. This can be achieved by recalling the Weyl identity [4]

$$\frac{e^{-kr}}{r} = -\frac{1}{2\pi} \int\limits_{-\infty}^{\infty} \int\limits_{-\infty}^{\infty} \frac{e^{ik_x x + ik_y y - k_z |z|}}{k_z} d\kappa_x d\kappa_y \tag{3.41}$$

where

$$r = \sqrt{(x - x')^2 + (y - y')^2 + (z - z')^2} \tag{3.42}$$

and $v$ is the root of the dispersion relation

$$k^2 = k_x^2 + k_y^2 - k_z^2 \tag{3.43}$$

which for the truncated medium considered herein results in the following expression for the Green's function

$$g(\mathbf{x}, \mathbf{x}') = -\frac{1}{2L^2} \sum_{m=-\infty}^{\infty} \sum_{n=-\infty}^{\infty} \frac{e^{i\kappa_m (x-x') + i\lambda_n (y-y') - v_{mn}|z-z'|}}{v_{mn}} \tag{3.44}$$

with $v_{mn} = \sqrt{k^2 + \kappa_m^2 + \lambda_m^2}$. For the derivation of the last relation we have taken into account the orthogonality of the exponential functions

$$\int\limits_{-L/2}^{L/2} e^{i(\kappa_m - \kappa_l)x} dx = L\delta_{m,l}. \tag{3.45}$$

with $\delta_{ml}$ the Kronecker delta. Substituting (3.44) in (3.36) and taking (3.39) into account, we obtain

$$\Psi(\mathbf{x}) = \frac{1}{2L} \sum_{m=-\infty}^{\infty} \sum_{n=-\infty}^{\infty} \left( c_{mn} + \frac{d_{mn}}{v_{mn}} \right) e^{i\kappa_m x + i\lambda_n y} e^{-v_{mn}(z-z')} \tag{3.46}$$

and projecting onto $f_{mn}$ at $z = z'$

$$c_{mn} = \langle f_{m,n}, \Psi \rangle = \frac{1}{2} \left( c_{mn} + \frac{d_{mn}}{v_{mn}} \right) \tag{3.47}$$

To determine $d_n$ we differentiate (3.44) with respect to $z$ and obtain

$$\partial_n \Psi(\mathbf{x}) = \frac{1}{2L} \sum_{m=-\infty}^{\infty} \sum_{n=-\infty}^{\infty} \left(-v_{mn} c_{mn} + d_{mn}\right) e^{i\kappa_m x + i\lambda_n y} e^{-v_{mn}(z-z')} \tag{3.48}$$

whence we conclude

$$d_n = \langle f_{m,n}, \partial_n \Psi \rangle = \frac{1}{2} \left(-v_{mn} c_{mn} + d_{mn}\right) \tag{3.49}$$

The coefficients $c_{mn}$ and $d_{mn}$ must thus verify the system

$$\begin{pmatrix} 1 & 1/v_{mn} \\ v_{mn} & 1 \end{pmatrix} \begin{pmatrix} c_{mn} \\ d_{mn} \end{pmatrix} = \begin{pmatrix} 0 \\ 0 \end{pmatrix} \tag{3.50}$$

which has a zero determinant. We thus verify that $c_{mn}$ and $d_{mn}$ are linearly dependent with the Robin's coefficient as defined in (3.35) equal to $R_{mn} = v_{mn}$.

We have arrived thus at the point where we can determine the propagator as

$$\hat{\boldsymbol{P}}_{mn|z' \to z} = e^{-v_{mn}(z-z')}. \tag{3.51}$$

### 3.3.2 Cylindrical coordinates: propagation in $z$

Due to its anisotropy, the development basis and the propagation along the normal direction are different for propagation in the $\rho$, $\phi$ and $z$ axis. We shall be interested for the first and the last case, since these are the usual situations that will be encountered in the problems we wish to treat.

We shall first consider the case where the integration surface is a constant $z$ plane. We shall assume that the computational domain is bounded at $\rho = \rho_L$ using a Dirichlet type condition for the considered potential. In this case, the development basis will be

$$f_{m,n}(x, y) = \frac{1}{\sqrt{\pi} \rho_L J_{m+1}(\kappa_{mn} \rho_L)} e^{im\phi} J_m(\kappa_{mn} \rho) \tag{3.52}$$

where the eigenvalues $\kappa_{mn}$ are determined by the zeros of the Bessel functions

$$J_m(\kappa_{mn} \rho_L) = 0. \tag{3.53}$$

The Green's function in a cylindrical pot bounded at $\rho_L$ can be shown having the form [3]

$$g(\mathbf{x}, \mathbf{x}') = \sum_{m=-\infty}^{\infty} \sum_{n=0}^{\infty} \frac{1}{2\pi \rho_L^2 J_{m+1}^2(\kappa_{mn} \rho)\, v_{mn}} J_m(\kappa \rho)\, J_m(\kappa \rho')\, e^{im(\phi - \phi')} e^{-v|z-z'|}. \tag{3.54}$$

With substitution in the Green's identity (3.36) and assuming $z > z'$ we obtain the potential expression

$$\Psi(\mathbf{x}) = \frac{1}{4\pi} \sum_{m=-\infty}^{\infty} e^{im\phi} \sum_{n=0}^{\infty} \left( c_{mn} + \frac{d_{mn}}{v_{mn}} \right) J_m(\kappa_{mn}\rho)\, e^{-v_{mn} z}. \tag{3.55}$$

The rest of the proof is identical with the cartesian geometry, yielding the same expression for the propagator

$$\hat{\boldsymbol{P}}_{mn|z'\to z} = e^{-v_{mn}(z-z')}. \tag{3.56}$$

### 3.3.3 Cylindrical coordinates: propagation in $\rho$

We move now to the cylindrical coordinate system by considering an integration surface of constant radius $\rho'$ with $\mathbf{e}_n = \mathbf{e}_\rho$, and we develop solutions in the half-space $\rho \geq \rho'$ (outward evanescent fields). In order to work with a discrete spectrum, we shall truncate the domain at $z = \pm L/2$, as we did for the cartesian coordinate system. Note that the spectrum in the azimuthal direction is already discrete since it must fulfill the periodicity condition at $\phi = 2\pi$.

The eigenfunctions associated with the integration surface are given by the relation

$$f_{m,n}(x, y) = \frac{1}{\sqrt{2\pi L}} e^{im\phi + i\kappa_n z} \tag{3.57}$$

with the eigenvalues

$$\kappa_n = \frac{2\pi n}{L} \tag{3.58}$$

The identity corresponding to the Sommerfeld integral for propagation along $z$ we shall use in this case (derived by the former) reads [4]

$$\frac{e^{-kr}}{r} = \frac{1}{\pi} \sum_{m=-\infty}^{m} e^{im\phi} \int_{-\infty}^{\infty} I_m(k_\rho \rho')\, K_m(k_\rho \rho)\, e^{ik_z z} d\kappa \tag{3.59}$$

where $I_m$ and $K_m$ are the modified Bessel functions of the first and second kind, respectively [26], and the spectral variables $k_\rho$ and $k_z$ satisfy the dispersion relation

$$k^2 = k_\rho^2 - k_z^2 \tag{3.60}$$

Adapting (3.59) to the spectrum of the truncated domain, we obtain the Green's function

$$g(\mathbf{x}, \mathbf{x}') = \frac{1}{2\pi L} \sum_{m=-\infty}^{m} e^{im(\phi-\phi')} \sum_{n=-\infty}^{\infty} I_m(v_n \rho')\, K_m(v_n \rho)\, e^{i\kappa_n (z-z')} \tag{3.61}$$

with $v_n = \sqrt{k^2 + \kappa_n^2}$. Substitution to (3.36) yields for the potential solution

$$\Psi(\mathbf{x}) = \frac{\rho'}{\sqrt{2\pi L}} \sum_{m=-\infty}^{\infty} e^{im\phi} \sum_{n=-\infty}^{\infty} [c_{mn} v_n I_m'(v_n \rho') - d_{mn} I_m(v_n \rho')]\, K_m(v_n \rho)\, e^{i\kappa_n z} \tag{3.62}$$

and projecting to the eigenfunction space we arrive at the relation for the series coefficients (recall that we are observing at $\rho = \rho'$)

$$c_{mn} = \rho' \left[c_{mn} v_n I'_m(v_n\rho') - d_{mn} I_m(v_n\rho')\right] K_m(v_n\rho') \tag{3.63}$$

The corresponding calculation for the normal potential derivative yields for $d_{mn}$

$$d_{mn} = v_n\rho' \left[c_{mn} v_n I'_m(v_n\rho') - d_{mn} I_m(v_n\rho')\right] K'_m(v_n\rho') \tag{3.64}$$

resulting in the linear system

$$\begin{pmatrix} 1 - v_n\rho' I'_m(v_n\rho')\, K_m(v_n\rho') & \rho' I_m(v_n\rho')\, K_m(v_n\rho') \\ -v_n^2\rho' I'_m(v_n\rho')\, K'_m(v_n\rho') & 1 + v_n\rho' I_m(v_n\rho')\, K'_m(v_n\rho') \end{pmatrix} \begin{pmatrix} c_{mn} \\ d_{mn} \end{pmatrix} = \begin{pmatrix} 0 \\ 0 \end{pmatrix} \tag{3.65}$$

The system determinant reads

$$D = 1 - v_n\rho' \left[I'_m(v_n\rho')\, K_m(v_n\rho') - I_m(v_n\rho')\, K'_m(v_n\rho')\right]. \tag{3.66}$$

The bracketed expression is recognised as the Wronskian of the Bessel function, whose value is $1/v_n\rho'$, whence we conclude that the system's determinant is zero, verifying again the linear dependence of the $c_{mn}$ and $d_{mn}$ coefficients. The Robin's coefficient is easily determined as

$$R_{mn} = -\frac{1 - v_n\rho' I'_m(v_n\rho')\, K_m(v_n\rho')}{\rho' I_m(v_n\rho')\, K_m(v_n\rho')} \tag{3.67}$$

resulting the following expression for the propagator

$$\hat{\boldsymbol{P}}_{mn|\rho'\to\rho} = \frac{K_m(v_{mn}\rho)}{K_m(v_{mn}\rho')}. \tag{3.68}$$

### 3.3.4 Spherical coordinates

The normalised eigenfunctions in the spherical system are the spherical harmonics

$$Y_{mn}(\theta, \phi) = \sqrt{\frac{(n-m)!}{(n+m)!}\frac{2n+1}{4\pi}} P_n^m(\cos\theta)\, e^{im\phi} \tag{3.69}$$

with $n = 0, \ldots, \infty$, $m = -n, \ldots, n$.

The Green's function can be expanded in the spherical system by recognising the fact that the relation $e^{ikr}/r$ is proportional to the zero order spherical Bessel function $\mathrm{i}_0(kr)$ and applying the addition theorem for the spherical Bessel functions [4, 26], which results in the identity

$$\frac{e^{ik|\mathbf{x}-\mathbf{x}'|}}{4\pi|\mathbf{x}-\mathbf{x}'|} = \frac{2k}{\pi} \sum_{n=0}^{\infty} \sum_{m=-n}^{n} \mathrm{i}_n(kr_>)\, \mathrm{k}_n(kr_<)\, Y_{mn}(\theta, \phi)\, Y^*_{mn}(\theta, \phi) \tag{3.70}$$

where $r = |\mathbf{x}|$, and $r_{\lessgtr}$ indicates the smaller/larger of the source/observation point distance respectively. We shall assume observation points in the outer region ($r' > r$) as we did for the cylindrical system.

The analysis is similar as for the previous cases. We substitute (3.70) into (3.36) and we perform the integrations, taking account the orthogonality of the spherical harmonics

$$\Psi(\mathbf{x}) = \frac{2kr'^2}{\pi} \sum_{n=0}^{\infty} \sum_{m=-n}^{n} \left[c_{mn} k \mathrm{i}'_n(kr') - d_{mn} \mathrm{i}_n(kr')\right] \mathrm{k}_n(kr)\, Y_{mn}(\theta, \phi) \tag{3.71}$$

which results for the $c_{mn}$ coefficients in

$$c_{mn} = \frac{2kr'^2}{\pi} \left[c_{mn} k \mathrm{i}'_n(kr') - d_{mn} \mathrm{i}_n(kr')\right] \mathrm{k}_n(kr) \tag{3.72}$$

Derivating (3.71), we obtain the analogous relation for the $d_{mn}$ coefficients

$$d_{mn} = \frac{2kr'^2}{\pi} k \left[c_{mn} k \mathrm{i}'_n(kr') - d_{mn} \mathrm{i}_n(kr')\right] \mathrm{k}'_n(kr) \tag{3.73}$$

Equations (3.72),(3.73) form the system of equations

$$\begin{pmatrix} 1 - 2(kr')^2 \pi^{-1} \mathrm{i}'_n(kr')\, \mathrm{k}_n(kr') & 2kr'^2 \pi^{-1} \mathrm{i}_n(kr')\, \mathrm{k}_n(kr') \\ -2k(kr')^2 \pi^{-1} \mathrm{i}'_n(kr')\, \mathrm{k}'_n(kr') & 1 + 2(kr')^2 \pi^{-1} \mathrm{i}_n(kr')\, \mathrm{k}'_n(kr') \end{pmatrix}$$
$$\times \begin{pmatrix} c_{mn} \\ d_{mn} \end{pmatrix} = \begin{pmatrix} 0 \\ 0 \end{pmatrix} \tag{3.74}$$

with determinant

$$D = 1 + \frac{2(kr')^2}{\pi} \left[\mathrm{i}'_n(kr')\, K_n(kr') - \mathrm{i}_n(kr')\, K'_n(kr')\right]. \tag{3.75}$$

The bracketed expression is the Wronskian of the spherical Bessel functions, which equals $-\pi/2(kr')^2$, hence the derivative is zero.

Solution of (3.73) by replacement of the Wronskian yields for $d_{mn}$

$$d_{mn} = k \frac{K'_n(kr')}{K_n(kr')} c_{mn} \tag{3.76}$$

which results in the expression for the propagator

$$\hat{\boldsymbol{P}}_{mn|r' \to r} = \frac{\mathrm{k}_m(kr)}{\mathrm{k}_m(kr')}. \tag{3.77}$$

The corresponding expression for $r < r'$ (inwards evanascent solution) reads

$$\hat{\boldsymbol{P}}_{mn|r' \to r} = \frac{\mathrm{i}_m(kr)}{\mathrm{i}_m(kr')}. \tag{3.78}$$

A special case of interest is when $k \to 0$, which is met when treating solutions in air. The form of the propagator can be obtained either by starting from the Green's function expression for the magnetostatic and repeating the above procedure, or by using (3.77),(3.78) and applying the asymptotic form for the spherical Bessel functions for small arguments, namely [26]

$$\mathrm{i}_n(z) \sim z^n/(2n+1)!! \tag{3.79}$$

$$\mathrm{k}_n(z) \sim (2n+1)!!/z^{n+1} \tag{3.80}$$

The double factorial denotes the product of all the integers from 1 up to $n$ that have the same parity (odd or even) as $n$. Taking (3.79),(3.80) into account, we obtain for the outwards evanescent solutions

$$\hat{\boldsymbol{P}}_{mn|r'\to r} = \left(\frac{r}{r'}\right)^{-(n+1)} \tag{3.81}$$

and for the inwards evanescent solutions

$$\hat{\boldsymbol{P}}_{mn|r'\to r} = \left(\frac{r}{r'}\right)^{n}. \tag{3.82}$$

### 3.3.5 Concluding remarks

The uniqueness theorem assures that the knowledge of the state variable (one of the above introduced potentials in our case) at the boundary of the domain $\partial V$ determines the solution at any point in the interior of the domain $\mathbf{x} \in V$. Choosing thus a representation basis on this boundary we can map the surface distribution to any other point of the domain, and this mapping is carried out with the action of a propagation operator upon the representation bases (3.37).

If the basis is a Helmholtz eigenbasis in the Darboux frame of the boundary, it can be shown that it is also an eigenbasis of the propagator, and hence the mapping takes a particularly simple form, which in the cartesian and the cylindrical system is given by (3.51) and (3.51) respectively.

### 3.3.6 Generalisation

If the domain's boundary is non-simply connected, the Green's theorem is still valid. In fact, we can always choose a set of cuts for connecting the individual surfaces of the boundary, as shown in Fig. 3.4.

Via the introduction of cuts, the boundary integral of (3.25) can be written as the sum of surface integrals each one accounting for the scattering of one of the contributing surfaces

$$\oint\limits_{S_o \cup S_1 \cup S_2 \ldots \cup S_N} \ldots \mathbf{n}\mathrm{d}S = \int\limits_{S_o} \ldots \mathbf{n}_o \mathrm{d}S + \sum_{i=1}^{N} \int\limits_{S_i} \ldots \mathbf{n}_i \mathrm{d}S \tag{3.83}$$

where the $S_o$ contribution is the source term.

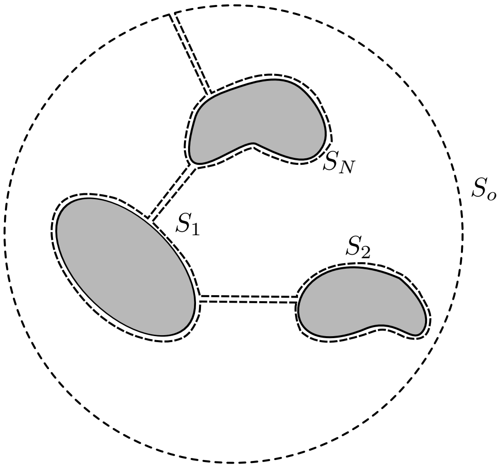

Figure 3.4: Separation of a non-simply-connected boundary into individual simply-connected-surfaces through the introduction of cuts.

Assigning one Darboux frame at each of the $S_i$ surfaces, we can express the total field at any point of the domain as the superposition of the individual surface distributions propagated at the observation point, i.e.

$$\Psi(\mathbf{x}) = \Psi_s(\mathbf{x}) + \sum_{i=1}^{N} \sum_{\alpha} c_{\alpha}^{(i)} \hat{\boldsymbol{P}}_{\alpha|S_i \to \mathbf{x}} f_{\alpha}^{(i)} \tag{3.84}$$

where $\Psi_s$ stands for the source term.

## 3.4 The Dirac ket-bra notation

### 3.4.1 Brief overview of the notational framework and conventions

At this point, it is be useful to adopt a more abstract description, and the vehicle to this attempt will be the Dirac notation originally introduced for the description of quantum-mechanical states. The benefits from this abstraction will be notational simplicity, and in particular, a very compact and elegant way for expressing transitions between different representation bases. On a more conceptual basis, the Dirac notation provides also a way of considering physical states of the system without paying attention to the details of the specific representation at hand.

An arbitrary state of the problem is represented via the ket vector $|\phi\rangle$. The ket vector is an arbitrary way of representing the given state of the problem, and it cannot be expressed explicitly in any coordinate system but only via its projection to the elements of a given basis. To the ket vector we associate the adjoint bra vector defined via

$$\langle\phi| \coloneqq (|\phi\rangle)^{\dagger}\,. \tag{3.85}$$

Based on the above definitions, the inner product of two state vectors $|\phi\rangle$ and $|\psi\rangle$ can be written as follows

$$\langle\psi,\phi\rangle \coloneqq \langle\psi|\phi\rangle\,. \tag{3.86}$$

Let $|n\rangle$ stand for an orthonormal and complete basis. Following the standard quantum-mechanical convention for the representation of the basis elements, we shall refer each element by giving its index inside the ket/bra symbol. The development of $|\phi\rangle$ in this basis reads

$$|\phi\rangle = \sum_n c_n\,|n\rangle \tag{3.87}$$

with $c_n$ being the development coefficients, which in the general case are complex scalars, that is $c_n \in \mathbb{C}$. The $m$th coefficient is obtained by projecting the $|\phi\rangle$ vector to the $m$th element of the basis, namely

$$\langle m|\phi\rangle = \sum_n c_n\,\langle m|n\rangle = c_m \sum_n c_n\delta_{mn} = c_m \tag{3.88}$$

where $\delta_{mn}$ stands for the Kronecker's delta. In the last relation the basis' orthonormality was used.

Let us now examine the action of an operator $\hat{\boldsymbol{A}}$ on $|\phi\rangle$. The result of the operation $\hat{\boldsymbol{A}}\,|\phi\rangle$ is fully determined in a given representation basis by projecting the result of the operator to every element of the basis, i.e.

$$\langle m|\,\hat{\boldsymbol{A}}\,|\phi\rangle = \sum_{n=0}^{\infty} c_n\,\langle m|\,\hat{\boldsymbol{A}}\,|n\rangle = \sum_{n=0}^{\infty} A_{mn}c_n. \tag{3.89}$$

The quantity $A_{mn}$ is a matrix, which represents the action of the operator in the given basis.

Interesting relations can be obtained by using the following identity

$$\hat{\boldsymbol{I}} = \sum_n |n\rangle\,\langle n| \tag{3.90}$$

where $\hat{\boldsymbol{I}}$ stands for the identity operator. The meaning of (3.90) is that $|n\rangle$ forms a complete basis and hence the application of (3.90) to any arbitrary vector will leave the latter intact. Indeed, from the definition of the unit operator we obtain

$$|\phi\rangle \equiv \hat{\boldsymbol{I}}\,|\phi\rangle = \sum_n |n\rangle\,\langle n|\phi\rangle = \sum_n c_n\,|n\rangle\,. \tag{3.91}$$

Identity (3.90) proves very useful for changing the representation basis. Take for example the inner product of two state vectors $|\phi\rangle$ and $|\psi\rangle$ and let $|n\rangle$ stand for the basis vectors of a given basis. Inserting (3.90) in the inner product $\langle\psi|\phi\rangle$, we obtain

$$\langle\psi|\phi\rangle = \langle\psi| \left(\sum_n |n\rangle\langle n|\right)|\phi\rangle = \sum_n \langle\psi|n\rangle\langle n|\phi\rangle = \sum_n d_n^* c_n \tag{3.92}$$

where $c_n = \langle n|\phi\rangle$ and $d_n = \langle n|\psi\rangle$ are the projections of the two vectors to the elements of the basis. Equation (3.92) is the so-called Parseval's theorem. Now let $|n'\rangle$ a new basis. Repeating the same operation for the inner products of $|\phi\rangle$, we obtain

$$\begin{aligned}\langle\psi|\phi\rangle &= \sum_n \langle\psi|n\rangle\langle n|\phi\rangle = \sum_n \langle\psi|n\rangle\langle n| \left(\sum_{n'} |n'\rangle\langle n'|\right)|\phi\rangle \\ &= \sum_n \langle\psi|n\rangle \left(\sum_{n'} \langle n|n'\rangle\langle n'|\phi\rangle\right) = \sum_n d_n^* \left(\sum_{n'} R_{nn'} c_{n'}\right)\end{aligned} \tag{3.93}$$

and so on. In the last relation $R_{nn'}$ is the transformation matrix from one basis to the other.

Since a change of basis is of central importance this work, it would be meaningful to adopt the Einstein convention **for spectral sums** in an effort to simplify the notation. According to this notation, the sum symbol is dropped and the summation is implied for all repeated indices (also known as dummy indices) spanning the value range that those indices admit. As a demonstration, let us see how this rule works in the case of the basis change performed in the last relation

$$\langle\psi|\phi\rangle = \langle\psi|n\rangle\langle n|\phi\rangle = \langle\psi|n\rangle\langle n|n'\rangle\langle n'|\phi\rangle = d_n^* R_{nn'} c_{n'}. \tag{3.94}$$

It should be noted here that the Einstein convention is mostly used in the field of tensor algebra and its application with spectral bases may be seen a little unusual. Yet, its introduction can simplify the notation making the procedure more transparent, bringing the main ideas of the analysis in the foreground.

The above concepts will become clearer if we shall apply them to a specific example. Let $|\mathbf{x}\rangle$ be the common cartesian coordinates basis, which, as is always the case for the Dirac notation, is defined via its projection to the state vector, namely

$$\phi(\mathbf{x}) \coloneqq \langle\mathbf{x}|\phi\rangle\,. \tag{3.95}$$

The meaning of the above expression is that the projection of the state vector onto the $|\mathbf{x}\rangle$ basis is identical to its functional expression in the cartessian coordinates system $\phi(\mathbf{x})$, which is called in quantum-mechanics as position representation.

We consider now two state vectors $\phi$ and $\psi$, and we form their inner product $\langle\psi|\phi\rangle$. Using the above presented framework, we can write

$$\langle\psi|\phi\rangle = \langle\psi|\mathbf{x}\rangle\langle\mathbf{x}|\phi\rangle\,. \tag{3.96}$$

Taking (3.95) into account and recalling the Einstein convention, where this time the "index" $\mathbf{x}$ runs through $\mathbb{R}^3$, the last product yields in the cartesian coordinates system

$$\langle\psi|\mathbf{x}\rangle\,\langle\mathbf{x}|\phi\rangle = \int\limits_{\mathbf{x}} \psi^*(\mathbf{x})\,\phi(\mathbf{x})\,d\mathbf{x}. \tag{3.97}$$

We introduce now a second basis $|\mathbf{n}\rangle$. The inner product in this basis is given by (3.92). Now, let us specify the basis and explicitly compute the projection coefficients $c_{\mathbf{n}}$ and $d_{\mathbf{n}}$ (in contrast with (3.92) the indices here are vector quantities since the basis spans the three dimensions of the space).

$$c_{\mathbf{n}} = \langle\mathbf{n}|\phi\rangle = \langle\mathbf{n}|\mathbf{x}\rangle\,\langle\mathbf{x}|\phi\rangle = \langle\mathbf{x}|\mathbf{n}\rangle^*\,\langle\mathbf{x}|\phi\rangle \tag{3.98}$$

which yields in the spatial representation

$$c_{\mathbf{n}} = \int\limits_{\mathbf{x}} \mathbf{n}^*(\mathbf{x})\,\phi(\mathbf{x})\,d\mathbf{x}. \tag{3.99}$$

### 3.4.2 Application to the scattering problem

Let us return now to (3.84), which will try to rewrite following the Dirac notation and the above introduced conventions. We introduce the state vector $|\psi\rangle$ for the potential solution and $|m\rangle_i$ stand for the eigensolution base associated to the Darboux frame of the surface $i$, according to the previous discussion. The potential solution as superposition of the surface-associated states is written as follows

$$|\psi\rangle = |\psi_s\rangle + \sum_{i=1}^{N} c_m^{(i)}\,\hat{\boldsymbol{P}}_i\,|m\rangle\,. \tag{3.100}$$

In order to obtain the solution value at a specific point, we need to observe (project) the above representation to this point.

$$\langle\mathbf{x}|\psi\rangle = \langle\mathbf{x}|\psi_s\rangle + \sum_{i=1}^{N} c_m^{(i)}\,\langle\mathbf{x}|\,\hat{\boldsymbol{P}}_i\,|m\rangle \tag{3.101}$$

which is a different way of writing (3.84).

The solution must satisfy the continuity relations at all the boundaries of the domain, and a compact way of expressing these relations is via the trace operator defined in section 3.2. The continuity relations in the new notation read

$$\hat{\boldsymbol{\nu}}_{j^+}\hat{\boldsymbol{C}}_{j^+}\,\left|\psi_{j^+}\right\rangle - \hat{\boldsymbol{\nu}}_{j^-}\hat{\boldsymbol{C}}_{j^-}\,\left|\psi_{j^-}\right\rangle = \mathbf{0}, \quad \forall j. \tag{3.102}$$

Here, $j$ runs over all the physical interfaces of the geometry and the sign stands for the positive or negative side of the interface according to the $\mathbf{n}$ orientation. Substituting (3.100), we obtain

$$\sum_{i=1}^{2N} c_{m_i}\left(\hat{\boldsymbol{\nu}}_{j^+}\hat{\boldsymbol{C}}_{j^+}\hat{\boldsymbol{P}}_{i\to j^+} - \hat{\boldsymbol{\nu}}_{j^-}\hat{\boldsymbol{C}}_{j^-}\hat{\boldsymbol{P}}_{i\to j^-}\right)|m_i\rangle = \mathbf{0}, \quad \forall j. \tag{3.103}$$

In the last relation, the $i$ index runs over the **oriented and not the physical** surfaces, i.e. we assume a different development for each side of the surface. This point must be explained a little further. We match the solutions valid in each separate subdomain of the configuration (which can be a physical piece or fictitious domain), which implies that the solution must be considered for each side of every boundary surface independently (recall that the uniqueness theorem applies to a closed domain). However, not all the combinations of $i$ and $j\pm$ correspond to a physical solution; they must belong to the same domain. Technically, this requirement can be embedded in the propagation operator, which vanishes for every non-physical combination. With that said, one of the $\hat{\boldsymbol{P}}_{i\to j^+}$, $\hat{\boldsymbol{P}}_{i\to j^-}$ must vanish depending on which side of $j$ lies $i$.

To complete the formulation and construct a system of equations, which will allow the calculation of the series coefficients, (3.103) is weighted at each interface, with one of the series bases that correspond to that interface (for example the basis at the positive side). Since we are considering pieces with non-intersecting boundaries $|m_{j+}\rangle = |m_{j-}\rangle = |m_j\rangle$, i.e. the two bases are equal and hence this is not relevant. Things will be different, however, in the next chapter, where surface discontinuities will be tackled. Equation (3.103) then yields

$$\sum_{i=1}^{2N} \Big[ \langle m_j | \, \hat{\boldsymbol{\nu}}_{j^+} \hat{\boldsymbol{C}}_{j^+} \hat{\boldsymbol{P}}_{i\to j^+} - \hat{\boldsymbol{\nu}}_{j^-} \hat{\boldsymbol{C}}_{j^-} \hat{\boldsymbol{P}}_{i\to j^-} \, |m_i\rangle \Big] c_{m_i} = \boldsymbol{0}, \qquad \forall j \tag{3.104}$$

The calculation of the matrices can be carried our in a systematic way by successive application of the identity (3.90). Inserting thus the identity operator between $\hat{\boldsymbol{\nu}}$, $\hat{\boldsymbol{C}}$ and $\hat{\boldsymbol{P}}$, (3.104) becomes

$$\begin{aligned} \sum_{i=1}^{2N} \Big[ & \langle m_j | \, \hat{\boldsymbol{\nu}}_{j^+} \, |n_j\rangle \, \langle n_j | \, \hat{\boldsymbol{C}}_{j^+} \, |\ell_j\rangle \, \langle \ell_j | \, \hat{\boldsymbol{P}}_{i\to j^+} \, |m_i\rangle \\ & - \langle m_j | \, \hat{\boldsymbol{\nu}}_{j^-} \, |n_j\rangle \, \langle n_j | \, \hat{\boldsymbol{C}}_{j^-} \, |\ell_j\rangle \, \langle \ell_j | \, \hat{\boldsymbol{P}}_{i\to j^-} \, |m_i\rangle \Big] c_{m_i} = \boldsymbol{0}, \qquad \forall j. \end{aligned} \tag{3.105}$$

The material operator $\hat{\boldsymbol{\nu}}$ as well as the continuity operator $\hat{\boldsymbol{C}}$ are observed in the native frame of the boundary, and hence their projections will be given by the relations of section 3.2. As long as the geometry interfaces have the same Darboux frame, $\langle m_j | \, \hat{\boldsymbol{P}}_i \, |m_i\rangle$ will be diagonal as shown above. The operator diagonalisation is lost, when the piece comprises surfaces of different geometry. In that case $|m_i\rangle$ and $|m_j\rangle$ does not belong to the same coordinate system anymore and the matrix $\langle m_j | \, \hat{\boldsymbol{P}}_i \, |m_i\rangle$ involves mode mixing.

The essence of the introduced formalism is to provide a systematic way to produce these matrices and to compile the final system. This procedure will become more clear by working with specific examples.

## 3.5 Problem dimensionality: Domain and spectrum truncation

The development bases associated with the principal directions of the interfaces are infinite. Depending on the reference frame at hand they can be continuous (e.g. cartesian system) or discrete (e.g. azimuthal direction in the cylindrical or spherical coordinate system)[3]. In order to be able to solve numerically the system of equations of (3.104), we need to reduce the bases' dimensions to a finite number.

In the case of the parabolic problems considered here the continuous spectra can be always reduced to discrete ones by taking advantage of the rapid decrease of the solution as we are moving apart from the source (magnetostatics is an elliptic problem but its solutions share the same behaviour with the diffusive ones). The fact that the field becomes negligible at a relatively small distance from the source allows us to truncate the domain there using a simple boundary condition such as Dirichlet or Neumann, since the condition will not interact with the (practically zero) field there. The specific choice of the boundary condition has no consequence to the solution itself and is dictated by best mathematical convenience (symmetry conditions are however different in the sense that the field is non-negligible, and hence their choice has a direct impact to the final field distribution).

This technique is known in the literature as *domain truncation* and has enabled the treatment of a large number of problems using spectral techniques. A practical question that arises here is the minimum distance of the truncation boundary that can be safely used in order not to alter the results. Unfortunately, there are no strict mathematical rules (recall that the same question arises when defining the computational box for a calculation using the finite element method, FEM). Rule-of-thumbs can be, however, used, which are based on geometrical criteria [27–29]. Thus, truncation distances of 10 times the longest coil dimension is generally considered safe. Of course, one must also take the coil orientation and the material into account. A final judge is numerical experimentation and comparison with reference data.

Once the spectrum has been discretised, one needs to truncate it in order to reduce its (infinite) dimension to a numerically tractable finite number. Again, no general rule exists for the optimum number of terms (modes) that need to be taken into account. Experience suggests that a number of modes between 100 and 200 is sufficient for the majority of the problems treated with this technique. It should be underlined that the discussion on the definition of the computational spectrum is the analogous to the definition of the adequate grid resolution in spatial methods like the FEM.

---

[3] A rigorous response to this question can be given in the context of the group theory by considering the symmetries of the frame.

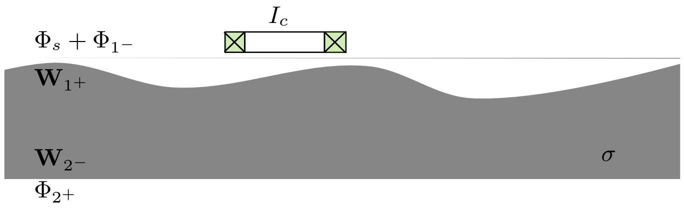

Figure 3.5: Piece with two interfaces and potentials associated to the interfaces.

## 3.6 Application to pieces with two interfaces

Having provided the general framework, we shall examine how this formalism applies for the solution of a concrete problem: the calculation of the eddy-current flow in a conducting piece with two interfaces. The shape of the interfaces is intentionally left unspecified to keep the analysis general enough. The thereupon constructed system of equations will be later specialised afterwards for two specific geometries: an infinite tube with eccentric walls and a conducting half-space containing a spherical inclusion.

For simplicity, we assume that the piece is not magnetic, which allows us to ignore the reluctivity matrix. The field is excited by a coil source located in the air region enclosed by the first interface. The bases associated with the two surfaces will be names $|m\rangle$ and $|n\rangle$ respectively. The source term will be expanded in its own reference frame (which will be specialised for each problem) using the base $|s\rangle$

The potentials associated with the geometry surfaces are named after the usual convention, which is also shown in Fig. 3.5 for convenience. More precisely, the expansions for the source term and the reflection from the first interface are given in terms of the scalar potentials

$$|\Phi_s\rangle = c_a^{(s)}\,|a\rangle \tag{3.106}$$

$$|\Phi_{1^-}\rangle = c_m^{(1^-)}\,|m\rangle\,. \tag{3.107}$$

Inside the piece we have the SOVP terms associated with the two internal interfaces

$$|\mathbf{W}_{1^+}\rangle = c_m^{(1^+)}\,|m\rangle \tag{3.108}$$

$$|\mathbf{W}_{2^-}\rangle = c_n^{(2^-)}\,|n\rangle\,. \tag{3.109}$$

Finally, the solution in the third (external) region reads

$$|\Phi_{2^+}\rangle = c_n^{(2^+)}\,|n\rangle \tag{3.110}$$

Application of the general expression (3.103) results in the following equations system

$$\begin{bmatrix} -\langle m|\,\hat{\boldsymbol{C}}_{1^-}\hat{\boldsymbol{P}}_{1^-1^-}\,|m'\rangle & \langle m|\,\hat{\boldsymbol{C}}_{1^+}\hat{\boldsymbol{P}}_{1^+1^+}\,|m'\rangle & \langle m|\,\hat{\boldsymbol{C}}_{1^+}\hat{\boldsymbol{P}}_{2^-1^+}\,|n'\rangle & \mathbf{0} \\ \mathbf{0} & \langle n|\,\hat{\boldsymbol{C}}_{2^-}\hat{\boldsymbol{P}}_{1^+2^-}\,|m'\rangle & \langle n|\,\hat{\boldsymbol{C}}_{2^-}\hat{\boldsymbol{P}}_{2^-2^-}\,|n'\rangle & -\langle n|\,\hat{\boldsymbol{C}}_{2^+}\hat{\boldsymbol{P}}_{2^+2^+}\,|n'\rangle \end{bmatrix}$$

$$\times \begin{bmatrix} c_m^{(1)} \\ c_m^{(2)} \\ c_n^{(3)} \\ c_n^{(4)} \end{bmatrix} = \begin{bmatrix} \langle m|\,\hat{\boldsymbol{C}}_{1^-}\hat{\boldsymbol{P}}_{a1^-}\,|a\rangle\, c_a^{(s)} \\ \mathbf{0} \\ \mathbf{0} \\ \mathbf{0} \end{bmatrix} \tag{3.111}$$

In the last relation, we have abbreviated the propagator notation $\hat{\boldsymbol{P}}_{i\to j}$ to $\hat{\boldsymbol{P}}_{ij}$ for brevity. It is recalled that the mode indices $m$, $n$ and $a$ run through all set of eigenvalues per direction according to our convention (extended Einstein's convention). All $\langle m|\ldots|n\rangle$ are hence expected to represent matrices. The source coefficients $c_a^{(s)}$ are considered known, and they are obtained by direct integration of the coil current (Biot-Savart law).

### 3.6.1 Eccentric tube

We shall apply now the above generic scheme to the specific problem of a coil interacting with an infinite tube with eccentric walls. The exact geometry is depicted in Fig. 3.6. The coil is air-cored and is free to move along the interior of the tube. Although the approach is applicable for an arbitrary coil geometry, position and orientation, we shall restrict the analysis to the case of a bobbin coil, that is a cylindrical coil with its axis parallel to the tube axis. The centre of the coil can be shifted with respect to the tube axis in order to take the wobble effect as shown in Fig. 3.7. The domain is truncated at $z = 0$ and $z = L$ using a PEC and a PMC condition respectively. As it will be mentioned in this text several times, this particular combination of BCs is convenient since it removes the zero-order term.

The two interfaces of the structure are the cylindrical interfaces of the tube with radii $\rho_1$ and $\rho_2$ respectively. The axes of the two cylindrical systems are shifted by a distance $d$. To each of the two surfaces we assign a Darboux frame with $(t, g, n) = (z, \phi, -\rho)$ (cf. conventions in Tab. 3.1). The development series will be thus given in the spatial representation by

$$\begin{aligned} \langle \mathbf{x}|m\rangle = \langle \mathbf{x}|n\rangle &= \frac{1}{\sqrt{\pi L}} e^{im_1\phi}\cos(\kappa_{m_2} z) \\ m_1 = n_1 &= -N_1, \ldots N_1, \\ m_2 = n_2 &= 1, \ldots N_2 \end{aligned} \tag{3.112}$$

with $\kappa_{m_2} = (m_2 - 1/2)\pi/L$. The abbreviated mode indices $m$ and $n$ span the duplet sets $(m_1, m_2)$, $(n_1, n_2)$, respectively.

The submatrices in (3.111) are projected separately to the series bases on the left and the right according to (3.105). It is thus

$$\langle m|\,\hat{\boldsymbol{C}}_{1^-}\hat{\boldsymbol{P}}_{1^-1^-}\,|m'\rangle = \langle m|\,\hat{\boldsymbol{C}}_{1^-}\,|\ell\rangle\,\langle \ell|\,\hat{\boldsymbol{P}}_{1^-1^-}\,|m'\rangle \tag{3.113}$$

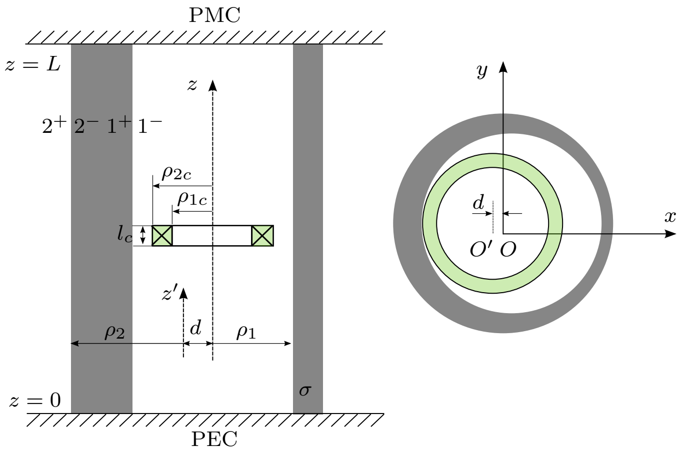

Figure 3.6: Tube with eccentric interfaces excited by a bobbin coil.

etc.

Taking (3.13),(3.14) into account, the projected continuity operators read

$$\langle m| \hat{\boldsymbol{C}}_{1^-} |\ell\rangle = \begin{pmatrix} -\kappa_{m_2}^2 \\ im_1\kappa_{m_2}\rho_1^{-1} \\ -\kappa_{m_2}^2 \end{pmatrix} \boldsymbol{\delta}_{m\ell}, \tag{3.114}$$

$$\langle m| \hat{\boldsymbol{C}}_{1^+} |\ell\rangle = \begin{pmatrix} -\kappa_{m_2}v_{m_2} & im_1\rho_1^{-1} \\ im_1\kappa_{m_2}\rho_1^{-1} & -v_{m_2} \\ \kappa_{m_2}^2 & \mathbf{0} \end{pmatrix} \boldsymbol{\delta}_{n\ell} \tag{3.115}$$

and

$$\langle n| \hat{\boldsymbol{C}}_{2^-} |\ell\rangle = \begin{pmatrix} -\kappa_{n_2}v_{n_2} & in_1\rho_2^{-1} \\ im_1\kappa_{n_2}\rho_2^{-1} & -v_{n_2} \\ \kappa_{n_2}^2 & \mathbf{0} \end{pmatrix} \boldsymbol{\delta}_{n\ell}, \tag{3.116}$$

$$\langle n| \hat{\boldsymbol{C}}_{2^+} |\ell\rangle = \begin{pmatrix} \kappa_{n_2}^2 \\ in_1\kappa_{n_2}\rho_2^{-1} \\ \kappa_{n_2}^2 \end{pmatrix} \boldsymbol{\delta}_{n\ell}. \tag{3.117}$$

Note that each operator is calculated in its proper reference frame, whence the diagonal form of the projected operators indicated by the Kronecker symbols $\delta_{m\ell}$ and $\delta_{n\ell}$.

The $\langle\ell| \hat{\boldsymbol{P}}_{1^-1^-} |m'\rangle$, $\langle\ell| \hat{\boldsymbol{P}}_{1^+1^+} |m'\rangle$, $\langle\ell| \hat{\boldsymbol{P}}_{2^-2^-} |n'\rangle$ and $\langle\ell| \hat{\boldsymbol{P}}_{2^+2^+} |n'\rangle$ operators propagate the surface field solution to itself, therefore

$$\langle\ell| \hat{\boldsymbol{P}}_{1^-1^-} |m'\rangle = \langle\ell| \hat{\boldsymbol{P}}_{1^+1^+} |m'\rangle = \langle\ell| \hat{\boldsymbol{P}}_{2^-2^-} |n'\rangle = \langle\ell| \hat{\boldsymbol{P}}_{2^+2^+} |n'\rangle = \mathbf{I} \tag{3.118}$$

where $\mathbf{I}$ is the unit matrix.

It remains to determine $\langle\ell| \hat{\boldsymbol{P}}_{1^+2^-} |m'\rangle$ as well as $\langle\ell| \hat{\boldsymbol{P}}_{2^-1^+} |n'\rangle$ which yield the propagation of the solution between the internal to the tube wall side of the structure interfaces. These matrices are responsible for the coupling between the two bases. Their explicit form can be derived using the Graf's addition theorem for the Bessel functions passing from the spatial representation, i.e.[4]

$$\langle \ell | \hat{\boldsymbol{P}}_{1+2-} | m' \rangle = \langle \ell | \mathbf{x} \rangle \langle \mathbf{x} | \hat{\boldsymbol{P}}_{1+2-} | \mathbf{x}' \rangle \langle \mathbf{x}' | m' \rangle \tag{3.119}$$

where

$$\langle \mathbf{x} | \hat{\boldsymbol{P}}_{1+2-} | \mathbf{x}' \rangle \langle \mathbf{x}' | m' \rangle = \cos(\kappa_{l_2} z') \sum_{m_1'=-N_1}^{N_1} (-1)^{\left(m_1'-l_1\right)} I_{m_1'-l_1}\big(v_{m_2'} d\big)\, e^{i m_1' \phi'} \tag{3.120}$$

which yields the final relation for the operator matrix

$$\langle \ell | \hat{\boldsymbol{P}}_{1+2-} | m' \rangle = (-1)^{\left(m_1'-\ell_1\right)} I_{m_1'-\ell_1}\big(v_{m_2'} d\big) \tag{3.121}$$

Note that the propagator has been normalised with $I_{m_1'}\big(v_{m_2'}\rho_1\big)$ as proposed in 3.3.3 in order to keep the expressions short and to avoid overflows due to the Bessel function's exponential behaviour for increasing argument.

In the same fashion we obtain for the $\langle \mathbf{x} | \hat{\boldsymbol{P}}_{2-1+} | \mathbf{x}' \rangle \langle \mathbf{x}' | n' \rangle$ matrix

$$\langle \mathbf{x} | \hat{\boldsymbol{P}}_{2-1+} | \mathbf{x}' \rangle \langle \mathbf{x}' | n' \rangle = \cos(\kappa_{l_2} z') \sum_{n_1'=-N_1}^{N_1} I_{n_1'-l_1}\big(v_{n_2'} d\big)\, e^{i n_1' \phi'}. \tag{3.122}$$

whence

$$\langle \ell | \hat{\boldsymbol{P}}_{-1+} | n' \rangle = I_{n_1'-\ell_1}\big(v_{n_2'} d\big)\,. \tag{3.123}$$

Here the normalisation factor is $K_{n_1'}\big(v_{n_2'}\rho_2\big)$.

The source term $\langle m' | \hat{\boldsymbol{P}}_{a1-} | a \rangle$ can be obtained in a similar way by calculating the coil field on the inner tube surface in the spatial domain and projecting onto the test function space. For the specific case of the bobbin coil with wobble, we follow the same recipe, namely we calculate the field in the coil proper frame and use the addition theorem of the Bessel functions to translate the calculation to the reference frame of the inner wall. We give directly the final result. The details on the calculation are given in [30] as well as [31]

$$\langle m | \hat{\boldsymbol{C}}_{1-} \hat{\boldsymbol{P}}_{a1-} | a \rangle\, c_a^{(s)} = D_c(\kappa_{m_2})\, I_{m_1}(\kappa_{m_2}\rho_0)\, K_{m_1}(\kappa_{m_2}\rho_1)\, e^{-i m_1 \phi_0}. \tag{3.124}$$

where again $\kappa_{a_2} = (a_2 - 1/2)\pi/L$. $(\rho_0, \phi_0)$ are the coordinates of the coil centre with respect to the centre of the inner tube surface (cf. Fig. 3.7). The coefficients

---

[4] In deployed form $\langle n | \hat{\boldsymbol{A}} | m \rangle = \int_x \int_{x'} \langle n | x \rangle \langle x | \hat{\boldsymbol{A}} | x' \rangle \langle x' | m \rangle \, dx dx'$, whence $\langle n | \hat{\boldsymbol{A}} | m \rangle = \int_x \phi_n(x)\, dx \int_{x'} A(x, x')\, \phi_m(x')\, dx'$. The inner integral gives the propagated basis function $\phi_m(x')$ on the observation surface of the test function $\phi_n(x)$.

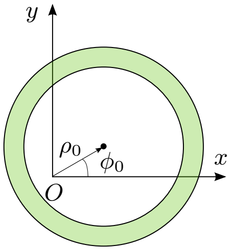

Figure 3.7: Coil shift with respect to the inner surface reference frame.

$D_c(\kappa)$ stand for the series coefficients of the coil field in the air and they admit a closed-form expression [8, 31]

$$D_c(\kappa) = \frac{\mu_0}{\pi} \frac{N_c I_c}{(\rho_{2c} - \rho_{1c})\, l_c} \frac{1}{\kappa^3} \sin\left(\frac{\kappa l_c}{2}\right) \int\limits_{\kappa\rho_{1c}}^{\kappa\rho_{2c}} x I_1(x)\, dx \tag{3.125}$$

where $\rho_{1c}, \rho_{2c}$ the inner and outer coil radius, $l_c$ the coil length, $N_c$ the number of turns and $I_c$ the feed current.

The field solution obtained via the inversion of (3.111) can be used to calculate the coil impedance variation by applying the reciprocity theorem presented in section 2.5. Application of (2.68) with $I_1 = I_2 = I_c$ taking into account the potential definition relation (2.33) yields

$$\Delta Z = -\frac{i\omega}{\mu_0 I_c^2} \int\limits_0^L \int\limits_{-\pi}^{\pi} \left( \Phi_{1^-} \frac{\partial \Phi_s}{\partial \rho} - \frac{\partial \Phi_{1^-}}{\partial \rho} \Phi_s \right)_{\rho=\rho_1} \rho_1 d\varphi dz. \tag{3.126}$$

Substitution of the potential expressions and use of the orthogonality results in the expression

$$\Delta Z = -\frac{i\omega 4\pi^2}{\mu_0 I_c^2} \sum_{m_1=-N_1}^{N_1} \sum_{m_2=1}^{N_2} c^{(s)}_{m_1,m_2} c^{(1^-)}_{-m_1,m_2}. \tag{3.127}$$

The mode index $m = (m_1, m_2)$ in the last relation has been deployed since $m_1$ and $m_2$ apply with different sign.

Some representative results have been produced for the case of a tube with inner and outer radii of 10 mm and 12 mm, respectively, and varying eccentricity. The considered tube is made of 304-type austenitic stainless steel (non-magnetic) having a nominal conductivity of $\sigma$=1.45 MS/m. The coil inner and outer radius are equal to $\rho_{c1}$=7 mm and $\rho_{c2}$=8 mm, its length is $l_c$=2 mm and its number of turns $N_c$=200. The coil inductance in the air can be calculated from the relation

$$Z_0 = \frac{i2\pi\omega\mu_0 N^2}{(r_{c2} - r_{c1})^2\, l_c^2} \int\limits_0^\infty \frac{1}{\kappa^6} \left[ \int\limits_{k_z b_1}^{k_z b_2} x J_1(x)\, dx \right]^2 \left( l_c \kappa + e^{-\kappa l} - 1 \right) d\kappa \tag{3.128}$$

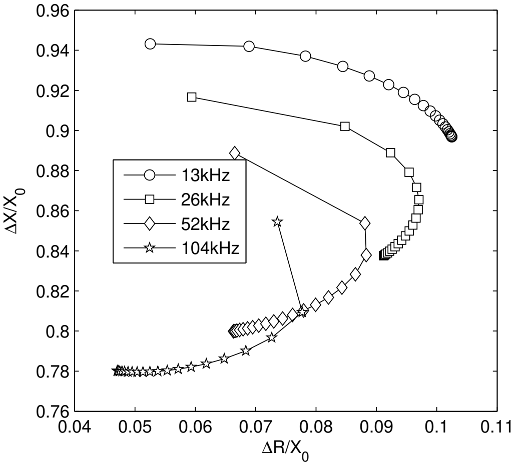

Figure 3.8: Normalized coil impedance variation for increasing eccentricity at four frequencies for zero coil offset. The zero eccentricity case corresponds to the smallest value of normalized reactance in each of the curves. The solid curves represent the solution obtained using the spectral approach, whereas the markers show the reference numerical results obtained using FEM.

which upon replacement of the coil characteristics gives the value 943.6 $\mu H$.

The theoretical results obtained by the model of this section have been compared with reference numerical results obtained using the FEM package COMSOL Multiphysics ® [32]. In Fig. 3.8 is shown the variation of the normalised $\Delta Z$ as function of the tube eccentricity for four different frequencies. The impedance variation is plotted in the complex plane, which is the standard way of representation for the NDT results. The coil is without offset.

The effect of the coil offset is visualised in Fig. 3.9, where the normalised impedance variation is plotted as a function of the coil eccentricity for four different coil offsets. The arrow shows the variation produced by the coil offset in a concentric tube, an increase in the resistance and decrease in the total reactance of the coil when it moves towards the inner tube wall and agrees with a previous observation [31]. Finally, if we connected corresponding data points at different coil position azimuthal angles we would get the impedance variation produced by the azimuthal movement of the coil in an eccentric tube.

### 3.6.2 Planar half-space with a spherical inclusion

The problem we deal with here is the calculation of the eddy-current signature of a close-to-the-surface hollow sphere embedded in a conducting half-space. The problem configuration is illustrated in Fig. 3.10. We define a global cylindrical coordinate system, whose $z$ axis is normal to the half-space interface and passes from the centre of the sphere. The coordinate system origin is set to the

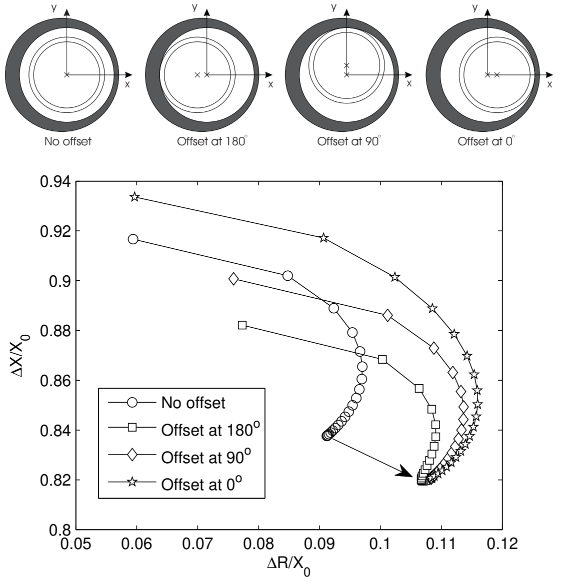

Figure 3.9: Normalized coil impedance variation for increasing eccentricity at 26 kHz and a coil offset of 2 mm at three coil position azimuthal angles. For comparison, the normalized coil impedance for zero coil offset is also appended. The inner and outer radii of the tube are 10 mm and 12 mm respectively. The solid curves represent the solution obtained using the spectral approach, whereas the markers show the reference numerical results obtained using FEM.

intersection point of the $z$ axis with the half-space interface. The computational domain is truncated by a cylindrical PMC boundary at $\rho = \rho_L$.

The Darboux frame associated to the planar surface of the half-space coincides with the global cylindrical system with $(t, g, n) = (\rho, \phi, z)$. The development basis is defined in (3.52) and rewritten here using the conventions of this section

$$\begin{aligned} \langle \mathbf{x} | m \rangle &= \frac{1}{\sqrt{\pi L}} e^{i m_1 \phi} J_{m_1}(\kappa_{m_1, m_2} \rho) \,, \\ m_1 &= -N_1, \ldots N_1, \\ m_2 &= 1, \ldots N_2. \end{aligned} \tag{3.129}$$

the $\kappa$ eigenvalues being determined by the roots of the Bessel functions

$$J_{m_1}(\kappa_{m_1, m_2} \rho_L) = 0. \tag{3.130}$$

To the spherical interface we assign a local spherical coordinate system, which is related to the respective Darboux frame with $(t, g, n) = (\theta, \phi, -r)$. To

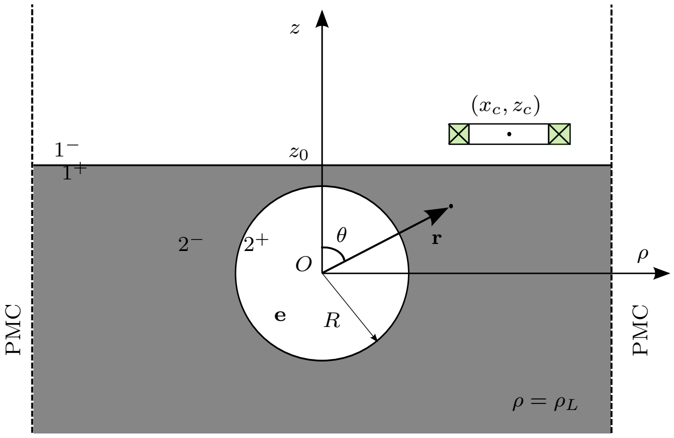

Figure 3.10: Planar half-space with spherical inclusion.

the spherical interface we associate a basis of spherical harmonics (3.69)

$$\begin{aligned} \langle \mathbf{x}|n\rangle &= P_{n_2}^{n_1}(\cos\theta)\, e^{in_1\phi}, \\ n_1 &= -N_1, \dots N_1, \\ n_2 &= m_1, \dots N_2 \end{aligned} \tag{3.131}$$

where $P_{n_2}^{n_1}(\cos\theta)$ are the associated Legendre functions of the first kind. The abbreviated modes indices $m$ and $n$ span the duplets sets $(m_1, m_2)$, $(n_1, n_2)$ as in the previous example.

We consider first the terms which emanate from the half-space interface and are observed at the same boundary, i.e. the terms $\langle m|\, \hat{\boldsymbol{C}}_{1^-} \hat{\boldsymbol{P}}_{1^-1^-} \,|m'\rangle$ and $\langle m|\, \hat{\boldsymbol{C}}_{1^+} \hat{\boldsymbol{P}}_{1^+1^+} \,|m'\rangle$. An extra complexity with respect to the previous problem is that the trace operator at the planar interface mixes the Bessel functions with their derivatives, when we are calculating the projections. A simple trick can be applied here recalling the Bessel functions property

$$\pm x J_m'(x) = x J_{m\mp 1}(x) - m J_m(x) \tag{3.132}$$

We introduce thus a new mixing operator

$$\hat{\boldsymbol{M}}_c = \begin{pmatrix} 1 & i & 0 \\ -i & 1 & 0 \\ 0 & 0 & 1 \end{pmatrix} \tag{3.133}$$

and we multiply the first row in (3.111) from the left with $\hat{\boldsymbol{M}}_c$. The final relation for the projected trace operator will thus be

$$\langle m|\,\hat{\boldsymbol{M}}_c\hat{\boldsymbol{C}}_{1^-}\,|\ell\rangle = \begin{pmatrix} \kappa_m \\ \kappa_m \\ -\kappa_m \end{pmatrix} \boldsymbol{\delta}_{m\ell}, \tag{3.134}$$

$$\langle m|\,\hat{\boldsymbol{M}}_c\hat{\boldsymbol{C}}_{1^+}\,|\ell\rangle = \begin{pmatrix} \kappa_{m_1,m_2}v_{m_1,m_2} & -i\kappa_{m_1,m_2} \\ \kappa_{m_1,m_2}v_{m_1,m_2} & i\kappa_{m_1,m_2} \\ \kappa^2_{m_1,m_2} & \mathbf{0} \end{pmatrix} \boldsymbol{\delta}_{n\ell}. \tag{3.135}$$

The similar trick will be used also for the continuity relations at the spherical boundary since again the trace operators involve the derivatives of the associated Legendre functions. The orthogonality relation involving derivatives of the associated Legendre functions is derived by writing the associated Legendre equation in the Sturm-Liouville form

$$\frac{d}{dx}(1-x^2)\frac{df}{dx} + \left[n(n+1) - \frac{m^2}{1-x^2}\right] f = 0 \tag{3.136}$$

which weighted with the test function yields

$$\langle g, \frac{d}{dx}(1-x^2)\frac{df}{dx}\rangle + n(n+1)\langle g, f\rangle - m^2\langle g, \frac{1}{1-x^2}f\rangle = 0. \tag{3.137}$$

Using the hermiticity of the derivative operator and rearranging the terms, the last relation can be also written as follows

$$\langle \frac{dg}{dx}, (1-x^2)\frac{df}{dx}\rangle - m^2\langle g, \frac{1}{1-x^2}f\rangle = -n(n+1)\langle g, f\rangle. \tag{3.138}$$

With $f, g$ being the associated Legendre functions, the right-hand side of the relation is non-zero only for $f = g$ and hence the same holds of the left-hand side. Using spherical coordinates the sought relation becomes [2,33]

$$\begin{aligned} &\int\limits_0^\pi \left[\frac{dP_\ell^m(\cos\theta)}{d\theta}\frac{dP_n^m(\cos\theta)}{d\theta} + \frac{m^2}{\sin^2\theta}P_\ell^m(\cos\theta)\,P_n^m(\cos\theta)\sin\theta d\theta\right] \\ &= \frac{2\ell(\ell+1)}{2\ell+1}\frac{(\ell+m)!}{(\ell-m)!}\delta_{\ell n}. \end{aligned} \tag{3.139}$$

Having this form in mind and regarding the form of the continuity operators in the spherical system (cf. appendix A), it turns out that the second row in (3.111) must be multiplied by left with an operator that mixes the $\theta$ and $\phi$ continuity relations [34]

$$\hat{\boldsymbol{M}}_s = \begin{pmatrix} 1 & 0 & 0 \\ 0 & \sin\theta\partial_\theta\frac{1}{\sin\theta} & \frac{im}{\sin\theta} \\ 0 & \frac{im}{\sin\theta} & \sin\theta\partial_\theta\frac{1}{\sin\theta} \end{pmatrix} \tag{3.140}$$

resulting in the following expressions for the projected continuity operator

$$\langle n|\,\hat{\boldsymbol{M}}_s\hat{\boldsymbol{C}}_{2^-}\,|\ell\rangle = \frac{1}{kR}\begin{pmatrix} n_2(n_2+1)\hat{K}_{n_2}(kR) & \mathbf{0} \\ \hat{K}'_{n_2}(kR) & \mathbf{0} \\ \mathbf{0} & \hat{K}_{n_2}(kR) \end{pmatrix}\boldsymbol{\delta}_{n\ell}, \tag{3.141}$$

$$\langle n|\,\hat{\boldsymbol{M}}_s\hat{\boldsymbol{C}}_{2^+}\,|\ell\rangle = \frac{1}{kR}\begin{pmatrix} n_2\mathbf{1} \\ \mathbf{1} \\ \mathbf{0} \end{pmatrix}\boldsymbol{\delta}_{n\ell}. \tag{3.142}$$

$\hat{I}_\ell(.)$ and $\hat{K}_\ell(.)$ stand for Schelkunoff's Bessel functions of the first and second kind, respectively. These are linked to the modified spherical Bessel function via the relations $\hat{I}_\ell(x) = xI_\ell(x)$ and $\hat{K}_\ell(x) = xK_\ell(x)$.

The propagators for the considered terms project the solutions to themselves and are hence unit matrices, in a strict analogy with the eccentric tube problem

$$\langle\ell|\,\hat{\boldsymbol{P}}_{1^-1^-}\,|m'\rangle = \langle\ell|\,\hat{\boldsymbol{P}}_{1^+1^+}\,|m'\rangle = \langle\ell|\,\hat{\boldsymbol{P}}_{2^-2^-}\,|n'\rangle = \langle\ell|\,\hat{\boldsymbol{P}}_{2^+2^+}\,|n'\rangle = \mathbf{I}. \tag{3.143}$$

We now move to the transverse terms, which couple the two boundaries. The extra complexity here comparing with the previous case of the eccentric cylinder is that the pivoting vector for the potentials associated with the two surfaces is not the same. The propagation operators are no longer scalar. A simple way to bypass this difficulty is to resort to the conversion relations between the vector wave functions in the cylindrical ($\mathbf{N}_m^{(i)}$, $\mathbf{M}_m^{(i)}$) and spherical system ($\mathbf{n}_{m\ell}^{(o)}$, $\mathbf{m}_{m\ell}^{(o)}$) as proposed in [34].

Both wave functions are derived by the corresponding potential terms. Thus for the cylindrical wave functions we obtain

$$\mathbf{N} = k^{-1}\nabla\times\nabla\times(\mathbf{e}_z W_{a1^+}) \tag{3.144}$$

$$\mathbf{M} = \nabla\times(\mathbf{e}_z W_{b1^+}). \tag{3.145}$$

The corresponding definition for the spherical wave functions reads

$$\mathbf{n} = k^{-1}\nabla\times\nabla\times(\mathbf{r} W_{a2^-}) \tag{3.146}$$

$$\mathbf{m} = \nabla\times(\mathbf{r} W_{b2^-}). \tag{3.147}$$

Note that the cylindrical wave functions are denoted using uppercase, whereas lowercase is used for the names of the spherical wave functions for better readability.

The outwards propagating $\mathbf{n}_{m\ell}^{(o)}$ and $\mathbf{m}_{m\ell}^{(o)}$ spherical wave functions can be expanded in terms of upwards evanescent cylindrical wave functions $\mathbf{N}_m^{(i)}$ and $\mathbf{M}_m^{(i)}$ using the following expression [34, 35]

$$\mathbf{n}_{m\ell}^{(o)}(\mathbf{r}) = \int_0^\infty \Big[a_{m\ell}(\kappa)\,\mathbf{N}_m^{(i)}(\mathbf{x},\kappa) - b_{m\ell}(\kappa)\,\mathbf{M}_m^{(i)}(\mathbf{x},\kappa)\Big]\,d\kappa. \tag{3.148}$$

and

$$\mathbf{m}^{(o)}_{m\ell}(\mathbf{r}) = \int_0^\infty \Big[ a_{m\ell}(\kappa)\, \mathbf{M}^{(i)}_m(\mathbf{x},\kappa) + b_{m\ell}(\kappa)\, \mathbf{N}^{(i)}_m(\mathbf{x},\kappa) \Big]\, d\kappa. \tag{3.149}$$

The series coefficients $a_{m\ell}$ and $b_{m\ell}$ admit closed form relations

$$a_{m\ell}(\kappa) = (-i)^m [\mathrm{sgn}(z)]^{n-m+1} \frac{\pi}{2} \frac{\kappa}{k^2 v} \frac{dP^\ell_m(\cos\alpha)}{d(\cos\alpha)} \tag{3.150}$$

$$b_{m\ell}(\kappa) = -(-i)^m [\mathrm{sgn}(z)]^{n-m} \frac{\pi}{2} \frac{im}{\kappa v} P^\ell_m(\cos\alpha) \tag{3.151}$$

where $\alpha$ is the spectral angle $\cos\alpha = v/k$.

Equations (3.148),(3.149) can be grouped together in a matrix expression as follows

$$\Big[ \mathbf{n}^{(o)}_{m\ell}(\mathbf{x})\; \mathbf{m}^{(o)}_{m\ell}(\mathbf{x}) \Big] = \int_0^\infty \Big[ \mathbf{N}^{(i)}_m(\mathbf{x},\kappa)\; \mathbf{M}^{(i)}_m(\mathbf{x},\kappa) \Big] \cdot \begin{bmatrix} a_{m\ell}(\kappa) & -b_{m\ell}(\kappa) \\ b_{m\ell}(\kappa) & a_{m\ell}(\kappa) \end{bmatrix} d\kappa. \tag{3.152}$$

Assuming a spherical wave expansion with coefficients $(c^{(a2^-)}_{n\ell}, c^{(b2^-)}_{n\ell})$, we can write for the truncated at $\rho = \rho_L$ medium

$$\begin{aligned} &\sum_{n_1=-N_1}^{N_1} \sum_{n_2=1}^{N_2} \Big[ \mathbf{n}^{(o)}_{n_1,n_2}(\mathbf{x})\; \mathbf{m}^{(o)}_{n_1,n_2}(\mathbf{x}) \Big] \cdot \begin{bmatrix} c^{(a2^-)}_{n_1,n_2} \\ c^{(b2^-)}_{n_1,n_2} \end{bmatrix} \\ &= \sum_{n_1=-N_1}^{N_1} \sum_{n_2=1}^{N_2} \sum_{\ell=0}^{N_2} \Big[ \mathbf{N}^{(i)}_{n_1,\ell}(\mathbf{x})\; \mathbf{M}^{(i)}_{n_1,\ell}(\mathbf{x}) \Big] \cdot \begin{bmatrix} a_{n_1,n_2,\ell} & -b_{n_1,n_2,\ell} \\ b_{n_1,n_2,\ell} & a_{n_1,n_2,\ell} \end{bmatrix} \cdot \begin{bmatrix} c^{(a2^-)}_{n_1,n_2} \\ c^{(b2^-)}_{n_1,n_2} \end{bmatrix}. \end{aligned} \tag{3.153}$$

The expressions for the discrete conversion operators can be easily obtained from (3.150),(3.151) by imposing the truncation condition, which results for $a_{m\ell n}$

$$a_{m\ell n} = \frac{2\kappa_n a_{m\ell}(\kappa_n)}{[\kappa_n \rho_L J_{m+1}(\kappa_n \rho_L)]^2}, \tag{3.154}$$

with a similar relation being obtained for $b_{m\ell n}$.

The left hand side of (3.153) is the magnetic field, which evaluated at the $z = 0$ interface performs the continuity operator task. Projection of (3.153) onto the cylindrical function duplet $\Big[\mathbf{N}^{(i)}_{n_1,\ell}(\mathbf{x}), \mathbf{M}^{(i)}_{n_1,\ell}(\mathbf{x})\Big]$ provides us the sought expression for the projected propagator-continuity matrix, which couples the series coefficients at the two surfaces

$$\begin{bmatrix} c^{(a2^-)}_{n_1,n_2} \\ c^{(b2^-)}_{n_1,n_2} \end{bmatrix} = \sum_{\ell=0}^{N_2} \begin{bmatrix} a_{n_1,n_2,\ell} & -b_{n_1,n_2,\ell} \\ b_{n_1,n_2,\ell} & a_{n_1,n_2,\ell} \end{bmatrix} \cdot \begin{bmatrix} c^{(a2^-)}_{n_1,n_2} \\ c^{(b2^-)}_{n_1,n_2} \end{bmatrix}. \tag{3.155}$$

The final relation for the projected continuity condition reads [34]

$$\begin{aligned}&\langle m|\,\hat{\boldsymbol{M}}_c\hat{\boldsymbol{C}}_{1^-}\hat{\boldsymbol{P}}_{2^-1^+}\,|\ell\rangle\\ &=\frac{\kappa_{m_1,m_2}}{k}e^{-v_{m_1,m_2}z_0}\begin{pmatrix} v_{m_1,m_2}a_{m_1\ell m_2} & v_{m_1,m_2}b_{m_1\ell m_2} & -ikb_{m_1\ell m_2} & ika_{m_1\ell m_2}\\ v_{m_1,m_2}a_{m_1\ell m_2} & v_{m_1,m_2}b_{m_1\ell m_2} & ikb_{m_1\ell m_2} & -ika_{m_1\ell m_2}\\ -v_{m_1,m_2}a_{m_1\ell m_2} & -v_{m_1,m_2}b_{m_1\ell m_2} & 0 & 0\end{pmatrix}\end{aligned} \tag{3.156}$$

The cross terms for the spherical boundary, $\langle\ell|\,\hat{\boldsymbol{P}}_{1^+2^-}\,|m'\rangle$ and $\langle\ell|\,\hat{\boldsymbol{P}}_{2^-1^+}\,|n'\rangle$, will be determined using the same approach. This time however we need the conversion relations from downwards evanecent cylindrical wave functions to inwards propagating spherical wave functions. The relations are given in [35] and adapted in [34]

$$\mathbf{N}_m^{(o)}(\mathbf{r},\kappa)=\sum_{\ell=m}^{\infty}\left[A_{m\ell}(\kappa)\,\mathbf{n}_{m\ell}^{(i)}(\mathbf{x})-B_{m\ell}(\kappa)\,\mathbf{m}_{m\ell}^{(i)}(\mathbf{x})\right], \tag{3.157}$$

and

$$\mathbf{M}_m^{(o)}(\mathbf{r},\kappa)=\sum_{\ell=m}^{\infty}\left[A_{m\ell}(\kappa)\,\mathbf{m}_{m\ell}^{(i)}(\mathbf{x})+B_{m\ell}(\kappa)\,\mathbf{n}_{m\ell}^{(i)}(\mathbf{x})\right] \tag{3.158}$$

which in matrix form reads

$$\left[\mathbf{N}_m^{(o)}(\mathbf{x},\kappa)\,\mathbf{M}_m^{(o)}(\mathbf{x},\kappa)\right]=\sum_{\ell=m}^{\infty}\left[\mathbf{n}_{m\ell}^{(i)}(\mathbf{x})\,\mathbf{m}_{m\ell}^{(i)}(\mathbf{x})\right]\cdot\begin{bmatrix}A_{m\ell}(\kappa) & B_{m\ell}(\kappa)\\ -B_{m\ell}(\kappa) & A_{m\ell}(\kappa)\end{bmatrix} \tag{3.159}$$

The expansion coefficients $A_{m\ell}$ and $B_{m\ell}$ are given by the relations

$$A_{m\ell}(\lambda)=-(-1)^n i^m\frac{(2\ell+1)(\ell-m)!}{\ell(\ell+1)(\ell+m)!}k\sin^2\alpha\frac{dP_\ell^m(\cos\alpha)}{d(\cos\alpha)} \tag{3.160}$$

$$B_{m\ell}(\lambda)=(-1)^n i^m\frac{(2\ell+1)(\ell-m)!}{\ell(\ell+1)(\ell+m)!}imkP_\ell^m(\cos\alpha) \tag{3.161}$$

where the spectral angle $\alpha$ has been defined above. Multiplication with $(c_{m\ell}^{(a1^+)}, c_{m\ell}^{(b1^+)})$ from the right and projection to the spherical surface basis yields the coupling expression between the development coefficients

$$\begin{bmatrix}c_{n_1,n_2}^{(a1^+)}\\ c_{n_1,n_2}^{(b1^+)}\end{bmatrix}=\sum_{\ell=0}^{N_2}\begin{bmatrix}A_{m_1,m_2,\ell} & B_{m_1,m_2,\ell}\\ -B_{m_1,m_2,\ell} & A_{m_1,m_2,\ell}\end{bmatrix}\cdot\begin{bmatrix}c_{n_1,n_2}^{(a1^+)}\\ c_{n_1,n_2}^{(b1^+)}\end{bmatrix} \tag{3.162}$$

which finally yields the projected trace-propagation operator at the spherical interface

$$\begin{aligned}&\langle n|\,\hat{\boldsymbol{M}}_s\hat{\boldsymbol{C}}_{2^+}\hat{\boldsymbol{P}}_{1^+2^-}\,|\ell\rangle\\ &=\frac{1}{kR}\begin{pmatrix}\hat{K}_\ell(kR) & 0 & \hat{I}_\ell(kR)\,A_{n_1,n_2,\ell} & \hat{I}_\ell(kR)\,B_{n_1,n_2,\ell}\\ \hat{K}'_\ell(kR) & 0 & \hat{I}'_\ell(kR)\,A_{n_1,n_2,\ell} & \hat{I}'_\ell(kR)\,B_{n_1,n_2,\ell}\\ 0 & \hat{K}'_\ell(kR) & \hat{I}'_\ell(kR)\,A_{n_1,n_2,\ell} & -\hat{I}'_\ell(kR)\,B_{n_1,n_2,\ell}\end{pmatrix}.\end{aligned} \tag{3.163}$$

The presented model has been applied to the inspection situation depicted in Fig. 3.10, where a spherical inclusion with different radii and a highly conducting half-space are considered. The half-space conductivity is $\sigma$=35.4 MS/m. The coil inner and outer radius is 2 mm and 4 mm respectively, its length is 1 mm and it is wound with 200 turns. The coil is moved at a constant lift-off equal to 0.2 mm from the half-space interface.

The results are compared against numerical simulations obtained using the three-dimensional FEM package COMSOL Multiphysics ® in Fig. 3.11 for two frequencies: 1 kHz and 5 kHz. The first inclusion has 5 mm radius and its ligament from the half-space free surface is 0.5 mm. The second one is smaller with 1 mm radius and a ligament of 0.1 mm.

As a figure of merit, the truncation zone for the TREE solution can be taken equal to about 10 times the radial extend of the coil (provided that the inclusion volume is entirely contained in the domain defined by this limit). Truncation radii greater than the previous one have an almost negligible impact to the accuracy of the results. From the computational point of view, larger $\rho_L$ values impose larger number of radial modes to be taken into account, which leads to a cubic increase (due to the full system matrix) of the computational time.

It is interesting to proceed at this point to a comparison between the computational times required for the two solutions. The calculation of a complete scan comprising 60 points using the spectral approach with the above mentioned truncation limit was at most 5 s for both inclusions and both frequencies. The respective FEM calculation time instead is estimated to 1.5 min per scan point, both times being measured using a standard workstation.

These computational times are justified by the rapid convergence of the solution series, which allowed us to consider only a few modes resulting a system with a limited number of degrees of freedom. More precisely, the number of the cylindrical modes did not exceed 25 for $m_1$ and 80 for $m_Z$ in all cases, whereas the maximum number of spherical modes was at most 15. This is a non-surprising remark, since the cylindrical and spherical functions bases used for the solution expansion are partial solutions of the given geometry, and thus they are already very close to the final solution.

## 3.7 Publications related with the chapter content

The herein developed theory is a formalisation effort of results published in a number of journal articles and communicated in international conferences.

More precisely, the calculation of the coil interaction with a conducting tube having eccentric walls is given in [30]. The problem of a conducting half-space with a parallel to its interface hole is treated in [36]. The calculation of the coil impedance for arbitrarily oriented coils in the exterior of tubes is given in [37]. ECT signatures from spherical inclusions in a half-space are calculated in [34]. The similar problem of the magnetostatic field response from an air void in a

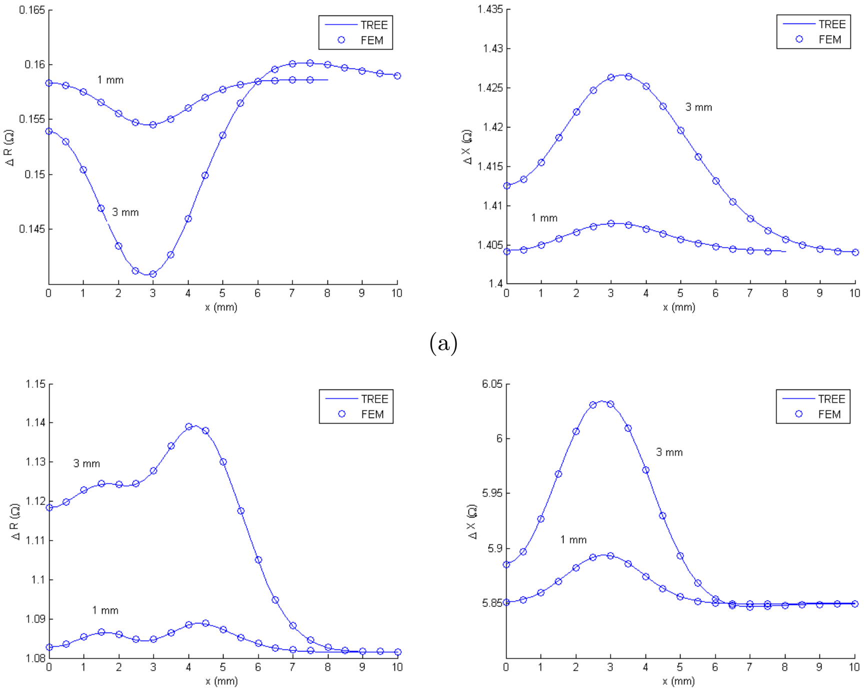

(a)

(b)

Figure 3.11: Semi-analytical (TREE) vs. FEM simulation results for spheres of different radii at: (a) 1 kHz, and (b) 5 kHz. $\Delta R$ stands for the real (ohmic) part of the coil impedance due to the presence of the conductor (the ohmic resistance of the coil windings being ignored), whereas $X$ is the coil reactance. The solid line stand for semi-analytical results whereas the marker points for FEM.

ferromagnetic medium is studied in [38].

# Chapter 4

# Geometries with intersecting boundaries

The next step towards a generalisation of the spectral approach developed in chapter 3 consists in allowing the internal stratification of the subdomains defined by simple non-intersecting surfaces, and which have been assumed so-far homogeneous. In other words, we introduce a second layer of interfaces that affect each domain separately. To distinguish this class of problems with respect to the ones treated in chapter 3, we shall name this type of geometries as **geometries with intersecting boundaries**.

The method that will be used to address these problems is not new: the following developments are variations of the well-established mode-matching technique [4]. The objective of this chapter is to reframe the method in the context of low-frequency problems, where the domain truncation is the basic tool, and try to integrate it in a systematic hierarchical framework, within which the problems of chapter 3 form a special case.

From the point of view of practical applications, the hereafter developed solutions will allow the treatment of important problems like the end-effect in planar and cylindrical structures, the inspection of boreholes, and the NDT of tubular configurations involving discontinuities such as support plates. The interest of the spectral methods is not only justified from numerical performance considerations. As we will see in the following, they provide a mean to construct integral kernels (Green's dyads), which combined with dedicated formalisms based on the integral equation approach allow the efficient treatment of arbitrarily shaped flaws, a problem of central importance for NDT applications.

## 4.1 Problem geometry and conventions

The general structure of the problem is described in Fig. 4.1. We consider $N$ infinite interfaces which divide the computational domain in $N+1$ layers. This set of interfaces will be referred to as *primary interfaces* or *primary layering.*

In contrast to the previous chapters where we had a relative freedom in terms of the interface geometry, the primary layers considered here will be only of rectangular or cylindrical shape. This restriction is not a strict limitation of the method, but rather a focus to a specific subclass of problems of particular interest from the application point of view.

We assume then that the thus defined subdomains (or a subset of them) are further divided via another set of coordinate surfaces, normal to one of the two subdomain interfaces. To each subdomain a different material is associated.

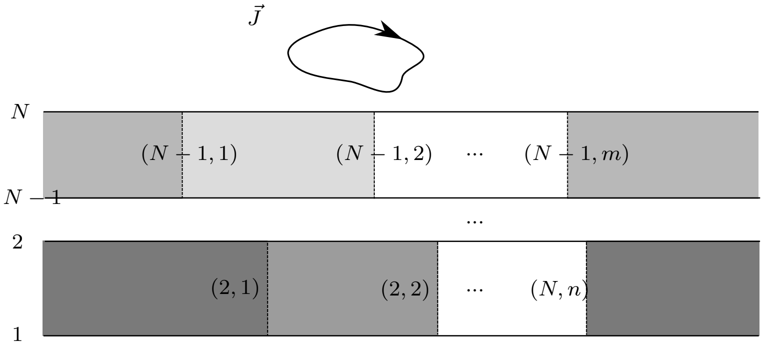

Figure 4.1: Multilayer structure with internal interfaces in the layers. To each layer subdivision a different material is associated. The medium is assumed to be infinite in the normal to the drawing direction.

We use a double index system to label the interfaces. The primary interfaces are associated to an integer index starting from the one with the lowest coordinate in the normal direction and advancing in the positive direction. The internal interfaces are numbered (independently from each other) using a second index following again the positive direction of the respective coordinate of their normal.

Each layer is labelled using a pair of indices corresponding to the primary and internal bounding interfaces. E.g. the layer labelled $(2,3)$ is upper bounded by the 2nd primary and the 3rd internal interface. Practically, this rigorous definition, indispensable for posing the problem in an unambiguous way for a general medium with more internal stratifications, will not be really used in the remaining of the chapter, where the study will be concentrated to couple of characteristic problems comprising a single set of internal layers. Thus, no risc of confusion exists.

## 4.2 Eigenvalues calculation for a planar multilayer medium

Let us consider a planar multilayer medium, whose interfaces are normal to the $z$ axis of a local cartesian coordinate system as shown in Fig. 4.2. The medium has a finite lateral dimension extending between $x_1$ and $x_2$. Each layer $i$ is assigned to a material with electrical conductivity $\sigma_i$ and a magnetic permeability $\mu_i$. The domain is bounded at $z = 0$ using a PEC condition and at $z = L$ with a PMC condition. This particular combination of BCs eliminates the zero-order term and thus establishes a usual choice for this kind of problems [34, 39, 40]. Different combinations can be of interest when dealing with solutions of specific parities [39]. It must though be underlined that the choice of one or another BC combination has no impact to the method itself; it solely influences the eigenvalues and the form of the eigenfunctions.

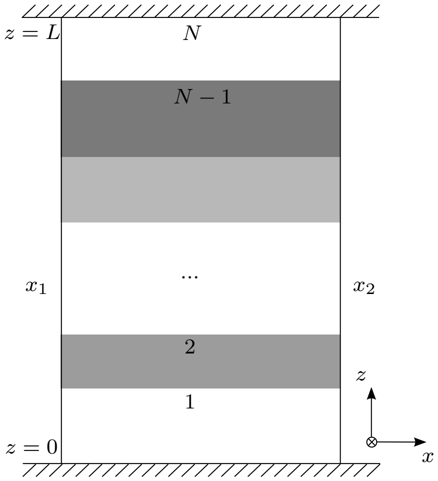

Figure 4.2: Planar multilayer medium of finite thickness.

We are seeking solutions for the $W_a$ and $W_b$ potentials that satisfy the Helmholtz equation in the stratified medium, and which will be used to construct a development eigenbasis. There are two ways of addressing this problem: either by considering it a separate multilayer problem consisting of homogeneous media employing the methods of chapter 3, or by considering it as an inhomogeneous 1D problem and treating it numerically.

### 4.2.1 Treating each layer separately: the transcendental equation approach

Following the methodology developed in the previous chapter, we assign a Darboux frame at each of the $x$ interfaces, i.e. we set $(t, g, n) = (z, y, -x)$ and solving the problem by propagating the potential solution of sub-plane $([0, z_1], [z_1, z_2], \ldots)$ at those interfaces along the $x$ direction (direction of the propagator). In the rest of this section we shall work directly in the cartesian coordinate system since it is more convenient.

It can be proven (cf. [4]) that when the pivot vector is normal to the interface the TE and TM modes are independent of each other. For the SOVP approach, this means that we can work out the $W_a$ and $W_b$ potentials separately.

We postulate that **the propagator is the same in each layer**. Despite the liberty we have in our disposal when proposing sub-solution combinations, this postulate may be seem at a first glance as arbitrary. Its choice will be better understood at a later point, when the eigenvalue equation for an arbitrary multilayer problem will be derived. The general formulation for the $W_a$ potential reads

$$W_a(x,y,z) = \sum_{m=1}^{N_m}\sum_{n=1}^{N_n} c_{mn} e^{-v_{mn}(x-x_1)} \sin(\lambda_n y)\, f^{(i)}\Big[q_m^{(i)} z\Big] \tag{4.1}$$

with the $z$ function given by

$$f\Big[p_m^{(i)} z\Big] = \begin{cases} a_1 \sin\Big[q_m^{(1)} z\Big], & z_1 \leq z \leq z_2, \quad i = 1 \\ a_i \sin\Big[q_m^{(i)} z\Big] + b_i \cos\Big[q_m^{(i)} z\Big], & z_i \leq z \leq z_{i+1}, i = 2, \ldots, N-1 \\ b_N \cos\Big[q_m^{(N)} (L - z)\Big], & z \geq z_N, \qquad i = N. \end{cases} \tag{4.2}$$

The eigenvalues $p_m^{(i)}$ are related with $\lambda_n$ and $v_{mn}$ via the dispersion relation

$$\Big[q_m^{(i)}\Big]^2 = v_{mn}^2 - \lambda_n^2 - k_i^2. \tag{4.3}$$

The $p_m^{(i)}$ values are determined by imposing $f\Big[p_m^{(i)} z\Big]$ to satisfy the continuity of the tangential magnetic field and the normal magnetic flux density across the boundaries. This is translated to continuity relations for the potential value and its normal derivative. Application of the continuity relations to the ensemble of the internal interfaces delivers the system of equations

$$\begin{bmatrix} \mathbf{A}\ \mathbf{B} \\ \mathbf{C}\ \mathbf{D} \end{bmatrix} \cdot \begin{bmatrix} a_1 \\ \vdots \\ a_{N-1} \\ b_2 \\ \vdots \\ b_N \end{bmatrix} = \mathbf{0} \tag{4.4}$$

with

$$\mathbf{A} = \begin{bmatrix} \sin\Big[q_m^{(1)} z_2\Big] & \sin\Big[q_m^{(2)} z_2\Big] & \ldots & 0 \\ & & \vdots & \\ 0 & 0 & \ldots & \sin\Big[q_m^{(N)} (L - z_N)\Big] \end{bmatrix} \tag{4.5}$$

$$\mathbf{B} = \begin{bmatrix} \cos\Big[q_m^{(2)} z_2\Big] & 0 \ldots & 0 \\ & \vdots & \\ 0 & 0 \ldots & \cos\Big[q_m^{(N)} (L - z_N)\Big] \end{bmatrix} \tag{4.6}$$

$$\mathbf{C} = \begin{bmatrix} \nu_1 q_m^{(1)} \cos\Big[q_m^{(1)} z_2\Big] & \nu_2 q_m^{(2)} \cos\Big[q_m^{(2)} z_2\Big] & \dots & 0 \\ & & \vdots & \\ 0 & 0 & \dots & \nu_{N-1} q_m^{(N)} \cos\Big[q_m^{(N-1)}(L - z_N)\Big] \end{bmatrix} \tag{4.7}$$

and

$$\mathbf{D} = \begin{bmatrix} -\nu_2 q_m^{(2)} \sin\Big[q_m^{(2)} z_2\Big] & 0 \dots & 0 \\ & \vdots & \\ 0 & 0 \dots & \nu_N q_m^{(N)} \sin\Big[q_m^{(N)}(L - z_N)\Big] \end{bmatrix} \tag{4.8}$$

Equation (4.4) has a non-trivial solution when

$$\det\left(\begin{bmatrix} \mathbf{A} & \mathbf{B} \\ \mathbf{C} & \mathbf{D} \end{bmatrix}\right) = 0 \tag{4.9}$$

Recalling that $q_m^{(i)}$ are all related with $v_{mn}$ via the dispersion relation (4.3), (4.9) provides a non-linear relation for $v_{mn}$ whose roots will provide the sought values.

As a representative example we consider the case of a two-layer medium (half-space). The system becomes in this case

$$\begin{bmatrix} \sin\Big[q_m^{(1)} z_2\Big] & \cos\Big[q_m^{(N)}(L - z_2)\Big] \\ \nu_1 q_m^{(1)} \cos\Big[q_m^{(1)} z_2\Big] & \nu_N q_m^{(N)} \sin\Big[q_m^{(N)}(L - z_2)\Big] \end{bmatrix} \cdot \begin{bmatrix} a_1 \\ b_2 \end{bmatrix} = \begin{bmatrix} 0 \\ 0 \end{bmatrix} \tag{4.10}$$

which results

$$\nu_N q_m^{(N)} \tan\Big[q_m^{(1)} z_2\Big] - \nu_1 q_m^{(1)} \cot\Big[q_m^{(N)}(L - z_2)\Big] = 0 \tag{4.11}$$

Equation (4.11) is the transcendental equation for the two-layer medium, which has been already studied in the literature for the solution of different problems [29,39,41].

### 4.2.2 Complex root finding

The numerical calculation of the complex roots of the transcendental equation is a challenging task for a number of reasons. The equation is highly non-linear which makes many standard numerical tools developed for polynomials root-finding, inappropriate. Furthermore, the algorithm must be able to distinguish roots that lie very close to each other. This proximity is particularly severe when highly magnetic media are involved.

An obvious choice is the application of the Newton-Raphson (NR) method. The drawback of this approach is that it suffers from stability issues, hence relaxation might be needed. The NR efficiency can be significantly improved and the convergence issues can be remediated to a great extend by providing an initial guess that is close to the root.

A robust method for locating initial estimates of the roots is one based on a procedure given by Delves and Lyness [42, 43]. The key step uses Cauchy's theorem to test whether a pole or several poles of a given function lie in a prescribed region of the complex plane. By finding the poles of a function, one implicitly locates the zeros of its reciprocal.

Let $f(z)$ be a complex function of $z$, analytic inside and on a closed contour $C$ in the complex plane, and which does not pass through a zero of $f(z)$. One can show using Cauchy's theorem that

$$s_n = \frac{1}{2\pi i} \oint_C z^n \frac{f'(z)}{f(z)} dz = \sum_{i=1}^{N} \xi_i^n, \qquad n = 1, 2, \ldots, \infty \tag{4.12}$$

where the summation is over the enclosed poles. $\xi_i$ are the zeros of $f(z)$. The path integral, evaluated for $n = 0$ equals the number of zeros of $f(z)$ enclosed by contour $C$

$$s_0 = \frac{1}{2\pi i} \oint_C \frac{f'(z)}{f(z)} dz = \sum_{i=1}^{N} \xi_i^0 = N. \tag{4.13}$$

The application of (4.12) for different values of $n > 1$ yields a non-linear system of equations with respect to the enclosed poles.

The computational algorithm works as follows. Setting a number of poles $N_{\max}$ to be traced by iteration, we start exploring the complex plane by dividing the domain of interest in a number of areas (e.g. rectangular) and evaluating (4.13). If $s_0 = 0$, which means that the current area does not contain any pole, we move to the following domain. If instead $s_0 > N_{\max}$, we subdivide the area to two subdomains, and we repeat the procedure until $s_0 \leq N_{\max}$. Should that be the case, we proceed to the evaluation of $s_1, \ldots, s_{N\max}$ and we solve the related system of equations to determine the $f(z)$ zeros.

The $N_{\max}$ value is a trade-off between number of iterations and computational complexity (number of integrations per area and order of the non-linear system of equations). Usually $N_{\max}$ should not exceed 3 for optimal performance.

With the combination of the Lyness-Delves method (initial prediction) with the Newton-Raphson method (refinement), a very satisfactory accuracy of the eigenvalues calculation can be achieved even in the presence of ferromagnetic media.

### 4.2.3 Eigenvalue equation for a vertically layered medium

The curl-curl equation for the electric field reads

$$\nabla \times \nu \nabla \times \mathbf{E} + i\omega\sigma\mathbf{E} = \mathbf{0}. \tag{4.14}$$

Projecting (4.14) to the $z$ axis and taking into account that the conductivity is function only of the $z$ coordinate, namely $\sigma = \sigma(z)$, we obtain

$$\frac{\partial}{\partial z}\left(\frac{\partial E_x}{\partial x} + \frac{\partial E_y}{\partial y}\right) - \frac{\partial^2 E_z}{\partial x^2} - \frac{\partial^2 E_z}{\partial y^2} + i\omega\mu\sigma E_z = 0 \tag{4.15}$$

Using the continuity equation[1]

$$\nabla \cdot \sigma \mathbf{E} = 0 \tag{4.16}$$

the first term can be written as follows

$$\frac{\partial E_x}{\partial x} + \frac{\partial E_y}{\partial y} = -\sigma^{-1}\frac{\partial}{\partial z}\sigma E_z \tag{4.17}$$

which upon substitution into (4.15) yields

$$\frac{\partial^2 E_z}{\partial x^2} + \frac{\partial^2 E_z}{\partial y^2} + \frac{\partial}{\partial z}\sigma^{-1}\frac{\partial}{\partial x}\sigma E_z - i\omega\mu\sigma E_z = 0. \tag{4.18}$$

Using the spatial expressions along the $x$ and $y$ direction, we arrive at the eigenvalue equation for the TM term

$$\frac{\partial}{\partial z}\sigma^{-1}\frac{\partial}{\partial x}\sigma E_z - \left(k_x^2 + k_y^2 + k^2\right) E_z = 0. \tag{4.19}$$

The $E_z$ component is expressed in terms of the $W_b$ potential as follows (2.55)

$$E_z = -(\partial^2 - k^2)W_b = (k_x^2 + k_y^2)W_b \tag{4.20}$$

whence conclude that (4.19) is also the eigenvalue equation for $W_b$

$$\left(\frac{\partial}{\partial z}\sigma^{-1}\frac{\partial}{\partial z}\sigma - k^2\right) W_b = -p^2 W_b. \tag{4.21}$$

with $p^2 = -k_x^2 - k_y^2$. It is recalled that the $W_b$ potential can be considered a priori equal to zero in regions with zero conductivity. The reason is that in these regions the quasi-static formulation reduces to the magnetostatic one, and hence only one degree of freedom is needed to describe the solution ($W_a$). It is therefore more practical instead of calculating the eigenvalues for the entire domain to split the problem to a number of independent equations, one for each subdomain bounded by air.

In a similar way, starting from the curl-curl equation for the magnetic field

$$\nabla \times \sigma^{-1}\nabla \times \mathbf{H} + i\omega\mu\mathbf{H} = 0 \tag{4.22}$$

---

[1] In order to avoid divisions by zero in domains with air, we consider for consistency reasons the effective conductivity complemented by the displacement currents: $\sigma + i\omega\varepsilon$. This elaboration proves useful for the derivation of the eigenvalue equation, in practice, however, we overcome the problem a priori by imposing a zero solution in the air regions.

and following the same procedure as before, we can derive the corresponding equation for the $W_a$ potential

$$\left(\frac{\partial}{\partial z}\mu^{-1}\frac{\partial}{\partial z}\mu - k^2\right)W_a = -p^2 W_a. \tag{4.23}$$

An important special case are nonmagnetic materials. In these cases, $\mu(z) = \mu_0$ and (4.23) reduces to the simple Helmholtz equation

$$\left(\frac{\partial^2}{\partial z^2} - k^2\right)W_a = -p^2 W_a. \tag{4.24}$$

Since the medium is invariant along the $y$ direction, a standard spectral development can be applied there, with the corresponding $k_y$ spectral variable admitting a discrete number of values $k_y = \lambda_n, n = 1, 2, \ldots, \infty$. From the dispersion equation it yields then

$$p_{mn}^2 = -\lambda_n^2 + v_{mn}^2 \tag{4.25}$$

where we have set $k_x^2 = -v_{mn}^2$ for consistency with the notation conventions of the previous chapter. Equation (4.25) can be interpreted as the dispersion equation in an equivalent homogeneous medium with complex eigenvalues along $x$ ($t$ in the Darboux frame). In other words, the mode matching approach can be interpreted as a kind of homogenisation procedure. The propagator function in this medium will be $e^{\pm v_{mn}x}$, i.e. common for all layers, in accordance with our postulate when we treated each layer separately.

### 4.2.4 Eigenvalue computation using the Galerkin approach

The numerical computation of the eigenvalues for (4.21) and (4.23) is straightforward using the Galerkin approach. Indeed, let us consider a development basis $f_i(z)\,, i = 1, \ldots, \infty$. The potential function can be approximated by its projection onto this basis, namely

$$W_{a,b} \approx \sum_{i=0}^{N} c_i f_i(z)\,. \tag{4.26}$$

Different choices of basis functions are possible provided that the basis elements are continuously differentiable functions ($f_i(z) \in C^1$). An obvious choice is to use the same basis of trigonometrical (global) functions; which has been used for pieces with no internal interfaces in the previous chapters. Assuming a PEC BC at $z = 0$ the basis elements are sine functions with spatial frequencies determined by the termination condition at $z = L$. For example, for a PEC/PMC combination the basis functions admit the form

$$f_i(z) = \sin(\kappa_i z) \tag{4.27}$$

with $\kappa_i = (n - 1/2)\pi/L$. For a different BC combination the basis elements and the $\kappa_i$ must be adapted accordingly.

Another usual choice of basis functions are triangular pulses (local functions), which offer an enhanced versatility for treating media with very inhomogeneous layering (or continuous media with strong gradients). Here, we divide the $z$ domain in a number of intervals $[z_0, z_1], [z_1, z_2], \ldots, [z_{N-1}, z_N]$ (the sampling points do not need to be equidistant). The basis functions take the form

$$f_i(z) = \begin{cases} \frac{z - z_{i-1}}{z_i - z_{i-1}}, \, z_{i-1} \leq z \leq z_i \\ \frac{z_{i+1} - z}{z_{i+1} - z_i}, \, z_i \leq z \leq z_{i+1} \end{cases} \tag{4.28}$$

with the boundary elements

$$f_0(z) = \frac{z - z_0}{z_1 - z_0}, \qquad z_0 \leq z \leq z_i \tag{4.29}$$

and

$$f_N(z) = \frac{z_N - z}{z_N - z_{N-1}}, \qquad z_{N-1} \leq z \leq z_N. \tag{4.30}$$

Substituting (4.26) in (4.23) and weighting with the same set taking into account the hermiticity of the operator, we obtain the system of equations

$$\sum_{i=0}^{N} \left[ \langle f_j', \mu^{-1} f_i' \mu \rangle - \langle f_j, k^2 f_i \rangle \right] c_i = q^2 \sum_{i=0}^{N} \langle f_j, f_i \rangle c_i. \tag{4.31}$$

The sought eigenvalues $q_n^2, n = 1, \ldots, N$ are equal to the eigenvalues of the system matrix $\langle f_j', \mu^{-1} f_i' \mu \rangle - \langle f_j, k^2 f_i \rangle$, which are computed using standard linear algebra tools. The same calculation applies also for the $W_b$ eigenvalues.

## 4.3 Case study: planar medium with an infinite slot

The previous theory will become more clear via a concrete example. The problem configuration is depicted in Fig. 4.3. An infinite half-space affected by an infinitely long and deep slot is inspected by means of a long rectangular coil. The depth of the slot is much larger than the skin depth, which allows us to ignore the effect of its bottom and approximate it as infinitely deep. Similarly, the coil is long enough to consider is as equivalent with two parallel wires. The problem can be therefore considered with good accuracy as 2D. The computational domain is truncated in $x = L$.

Note that since the axis of interest is $x$ in this case, we set $\mathbf{e}_x$ as pivot vector for the $W_a$ potential and apply the above developed methodology by interchanging the $z$-axis with $x$. The slotted specimen is considered as an equivalent homogenised piece with complex $x$-eigenvalues, which are calculated using the Galerkin approach with a basis of sinusoidal functions. Since the geometry is invariant along $y$, no development will be performed in this direction.

Fig. 4.4 shows the first 20 computed eigenvalues in the complex plane for a wedge configuration with $c_1 = L/2$, $c_2 = L = 100$ mm and $\sigma = 35.4$ MS/m for

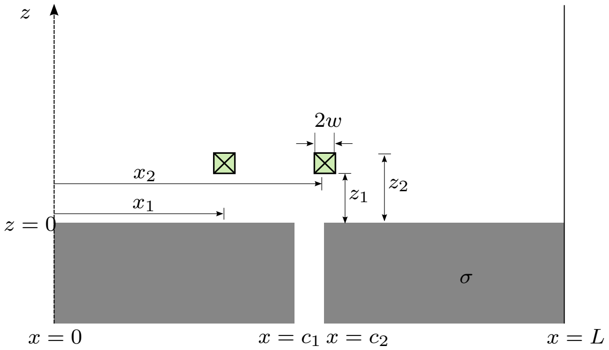

Figure 4.3: Multilayer structure with internal interfaces in the layers. A different material is associated to each layer subdivision.

two frequencies. This particular case simulates the plate end-effect. It is interesting to note that for higher frequencies (smaller skin depths) the eigenvalues tend to separate in two sets, the upper and the lower. It is also notable that the number of eigenvalues in each of these sets depends on the ratio $c_1/L$. This is easily observed in Fig. 4.5 where the two eigenvalue sets are depicted for the same $L$ and $\sigma$ but for different $c_1/L$ ratios.

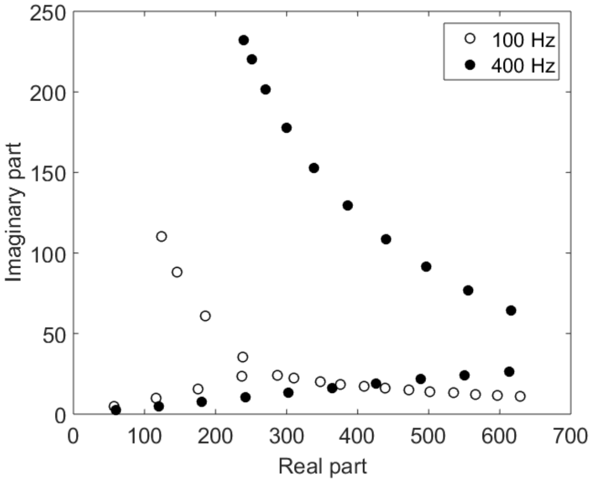

Figure 4.4: Complex eigenvalue sets for a conductive wedge at two frequencies.

There are two limiting cases for the region $z \leq 0$: when it is just air, that is $c_1 = 0$ and $c_2 = L$, and when it is a conductive half-space with constant conductivity, that is $c_1 = c_2$. In the first case, only the lower set of eigenvalues

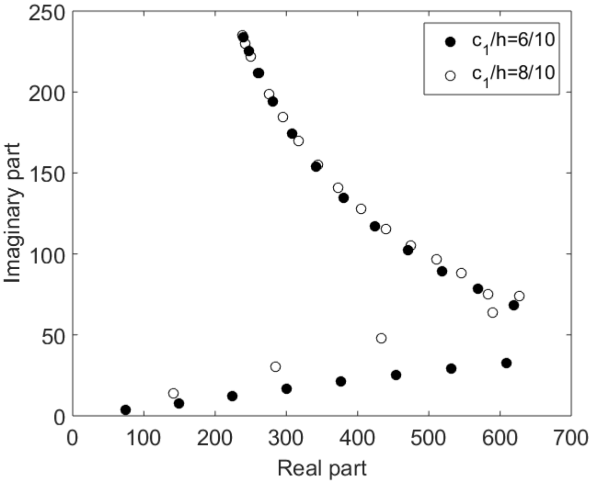

Figure 4.5: Complex eigenvalue sets for a conductive wedge with different $c_1/L$ ratios at a frequency of 1 kHz.

survives, which are equal to the eigenvalues in a homogeneous piece

$$q_n = n\pi/L. \tag{4.32}$$

In the second case, only the upper set of eigenvalues survives and these can be computed from the expression

$$q_{mn} = \sqrt{(n\pi/L) - k^2} \tag{4.33}$$

which describe a hyperbola locus in the complex plane.

We consider now a centered slot of opening $c_2 - c_1 = 10$ mm with $L = 200$ mm. The piece conductivity $\sigma = 18.5$ MS/m and the inspection frequency $f = 1$ kHz. Fig. 4.6 shows the first 20 computed eigenvalues in the complex plane. It is clear that as the opening is decreased the number of eigenvalues in the lower set also decreases with a simultaneous increase in the upper set. For very small openings, only the upper set survives.

These computed eigenvalues and eigenvectors are used to calculate the impedance change of the coil as this is moved above the slot. Fig. 4.7 shows numerical results for the normalized impedance change as the 2D coil is moved above the slot. The number of terms is set to $N_S = 100$. A further increase of this number is not necessary as convergence is achieved. The normalization factor is the inductive reactance of the coil in air $X_0 = \omega L_0$, with the inductance calculated after [8] to 9.633 mH. The coil dimensions are: $x_2 - x_1 = 10.2$ mm, $w = 4.1$ mm, $z_1 = 1.3$ mm, $z_2 = 10.8$ mm and the number of windings $N = 158$. Two peaks are observed in both the real and imaginary parts of the impedance change. These peaks correspond to the two coil branches as the coil passes over

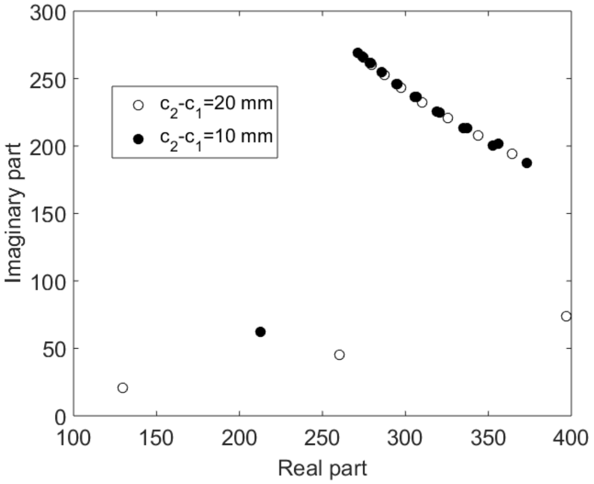

Figure 4.6: Complex eigenvalue sets for a conductive half-space with a slot.

the opening and the branches interact in turn with it, through the induced eddy currents.

## 4.4 Eigenvalues calculation for an axially layered cylindrical medium

We shift now to the cylindrical geometry, and we consider an axially layered cylindrical shell with inner and outer radii $\rho_1$ and $\rho_2$, in analogy with the planar slab depicted in Fig. 4.2.

Developing (4.23) in the cylindrical coordinates we arrive at

$$\left(\nabla^2_{\rho z} + \frac{\partial}{\partial z}\mu^{-1}\frac{\partial}{\partial z}\mu - k^2\right) W_a = 0. \tag{4.34}$$

Using the following ansatz for the potential expression

$$W_a(\rho,\phi,z) = \sum_{m=1}^{N_m}\sum_{n=1}^{N_n} c_{mn} \left\{ \begin{array}{c} I_m(p_{mn}\rho) \\ K_m(p_{mn}\rho) \end{array} \right\} e^{im\phi} f(q_m z) \tag{4.35}$$

(4.34) becomes

$$\left(\frac{\partial}{\partial z}\mu^{-1}\frac{\partial}{\partial z}\mu - k^2\right) W_a = -p^2_{mn} W_a. \tag{4.36}$$

which is identical with (4.23) for the cartesian case. This is not an unexpected result, since the topology of the medium seen in the $z$-axis is the same for both systems. In the same fashion, we can show that the corresponding eigenvalue equation for $W_b$ is (4.21).

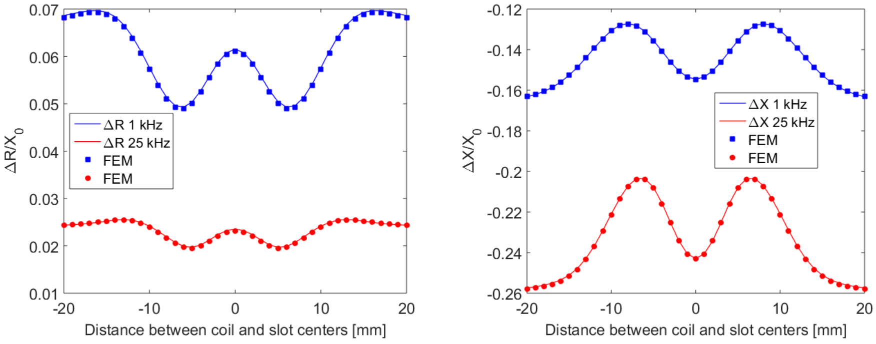

(a) (b)

Figure 4.7: Impedance due to a conductive halfspace with a slot (a) real and (b) imaginary part.

A different situation occurs when the layering takes place along the radial direction. In this case, and given that the pivot vector in the cylindrical system is always in the $z$ direction (recall that this is the only possibility to obtain a separable form of the Helmholtz equation), the TE and TM solution cannot be treated separately. Thus, the basic working assumption, namely that the eigenvalues can be divided into two distinct sets, does not hold anymore. The above workflow can be still applied for the 2D case, where the TM solution is identically zero, yet this case is of limited interest (coil-ferrite configurations being one of the potential geometries then can be tackled using an eigensolution development in the radial direction).

With the previous discussion in mind, we conclude that the general strategy one must follow when layering is involved in both axial and radial directions consists in considering the medium as a compilation of cylindrical shells, each one being treated as an equivalent homogenised medium, wherein the (4.35) ansatz is applied with the spectrum determined by (4.23),(4.21).

## 4.5 Modelling of the sources

In chapter 3 the coil sources have been treated indirectly by the boundary conditions in the embedding layers. For geometries involving layering in two directions, the coil field may be shared by multiple domains which makes its treatment more complicated. The situation can be better explained via an example. Consider the case of a borehole inspection using a coil scanning the piece parallel to its upper interface, as illustrated in Fig. 4.8. Since the primary layering is always carried out along the radial direction for the reasons explained above, there are scan positions where the coil will be intersected by the domains boundaries, in particular the cylindrical surface defined by the hole.

A possible way out would be to split the coil into two pieces, with each part

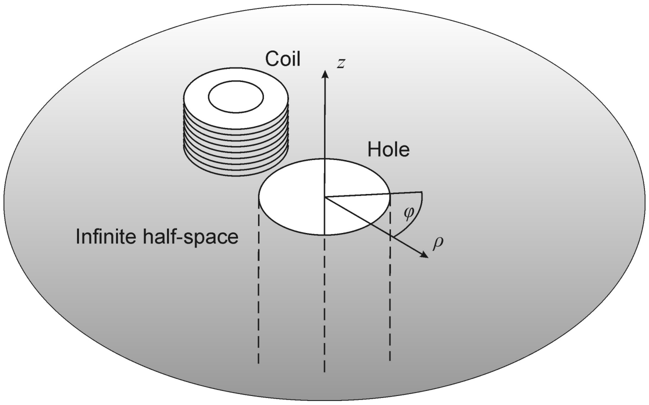

Figure 4.8: Borehole inspection using a cylindrical probe coil. The coil is located above the half-space interface and is moving parallel to it.

being located in a single domain. This approach is, however, theoretically less elegant and computationally cumbersome, especially when a complete scan has to be calculated, which is translated to a number of different splits.

A much more elegant solution consists in tackling the problem in a two-level approach as proposed in [29,39,44]. We first calculate the coil field in the entire air region that is physically bounded by the piece: that is, the air-column inside and above the hole and the air domain above the rest of the piece. Once this field has been evaluated we treat the multilayer problem for each subdomain of the principal layering **ignoring any interaction between domains.**

The decomposition scheme is schematically depicted in Fig. 4.9. $W_a^{(s)}$ stands for the potential associated with the source field, $W_a^{(r)}$, $W_a^{(t)}$, $W_b^{(t)}$ are the terms arising from the interaction of the source with the horizontal boundary at $z = c$, and $W_a^{(0)}$, $W_a^{(1)}$, $W_b^{(1)}$ are the terms produced by the interaction of the sub-solutions in the two cylindrical domains of the primary layering with the vertical interface at $\rho_a$. Note that the domain is truncated twice, at $\rho = \rho_L$ (for the treatment of the horizontal layering) and at $z = L$ (for the solution associated with the vertical layering).

The formal solution obtained with this approach for the source field and the reflection and transmission terms $\rho \geq \rho_a$ reads

$$W_a^{(s)}(\rho, \phi, z) = \sum_{m=-\infty}^{\infty} e^{im\phi} \sum_{n=1}^{\infty} c_{mn}^{(s)} J_m(\kappa_{mn}\rho)\, e^{\kappa_{mn}(z-c)}, \tag{4.37}$$

$$W_a^{(r)}(\rho, \phi, z) = \sum_{m=-\infty}^{\infty} e^{im\phi} \sum_{n=1}^{\infty} c_{mn}^{(r)} J_m(\kappa_{mn}\rho)\, e^{-\kappa_{mn}(z-c)}. \tag{4.38}$$

and

$$W_a^{(t)}(\rho, \phi, z) = \sum_{m=-\infty}^{\infty} e^{im\phi} \sum_{n=1}^{\infty} c_{mn}^{(t)} J_m(\kappa_{mn}\rho)\, e^{v_{mn}(z-c)}, \tag{4.39}$$

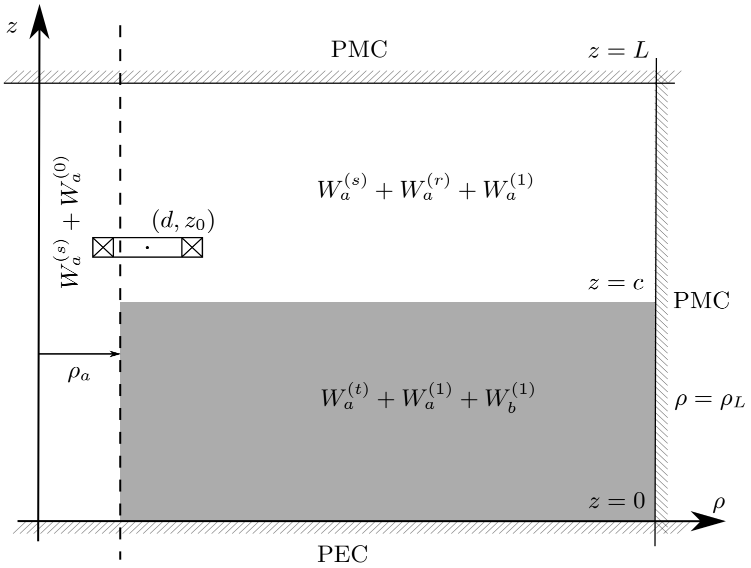

Figure 4.9: Solution decomposition for the treatment of the borehole inspection problem with a scanning probe.

with $v_{mn}^2 = \kappa_{mn}^2 + k^2$. The $W_b$ term is zero for the air-column region [8]. The $\kappa_{mn}$ eigenvalues are determined by imposing zero tangential field on the $\rho = \rho_L$ boundary, which yields

$$J_m(\kappa_{mn}\rho_L) = 0. \tag{4.40}$$

The modal expansions for the potentials terms associated to the perturbation from the hole are given by the expressions

$$W_a^{(0)}(\rho,\phi,z) = \sum_{m=-\infty}^{\infty} e^{im\varphi} \sum_{n=1}^{\infty} c_{mn}^{(0)} I_m(u_m\rho)\cos(u_m z)\,, \tag{4.41}$$

$$W_a^{(1)}(\rho,\phi,z) = \sum_{m=-\infty}^{\infty} e^{im\varphi} \sum_{n=1}^{\infty} c_{mn}^{(a1)} K_m(p_n\rho)\, f_n(z) \tag{4.42}$$

and

$$W_b^{(1)}(\rho,\phi,z) = \sum_{m=-\infty}^{\infty} e^{im\varphi} \sum_{n=1}^{\infty} c_{mn}^{(b1)} K_m(s_n\rho)\cos(r_n z) \tag{4.43}$$

where $f_n(z)$ and $\cos(r_n z)$ are the solutions of (4.23) and (4.21) with respective eigenvalues $a_n$ and $r_n$, with the corresponding spectral variables $p_n^2 = q_n^2 + k^2$ and $s_n^2 = r_n^2 + k^2$.

The $u_n$ eigenvalues are directly determined by the PMC condition at the $z = h$ plane since the air column in the hole region does not dispose any internal interface

$$\cos(u_n h) = 0, \tag{4.44}$$

which implies $u_n = (n - 1/2)\,\pi/h, n = 1, 2, \ldots, \infty$. The $r_n$ values also admit a closed-form expression since $W_b$ is confined in the $z \leq c$ domain (plate), and (4.21) reduces to the simple Helmholtz equation with constant $k^2$. Hence, demanding a zero normal component of the eddy-current flow on the $z = c$ boundary we obtain for $r_n$

$$\cos(r_n c) = 0 \tag{4.45}$$

which results $r_n = (n - 1/2)\,\pi/c, n = 1, 2, \ldots, \infty$. The remaining eigenvalues $q_n$ will be determined numerically following the approach of 4.2.3.

The partial solution represented by the $W_a^{(s)}$, $W_a^{(r)}$ and $W_a^{(t)}$ terms is discontinuous at the $\rho = \rho_a$. The thus introduced discontinuity is resolved by the $W_a^{(0)}$, $W_a^{(1)}$ and $W_a^{(1)}$ during the treatment of the radial layering. An alternative interpretation of the adopted decomposition can be given in terms of the equivalence theorem, namely the the discontinuity introduced by the $W_a^{(s)}$, $W_a^{(r)}$ and $W_a^{(t)}$ solution is equivalent with a surface electric current and magnetic charge distribution on the $\rho = \rho_a$ interface. The explicit form of the latter can be obtained using the spectral expressions (4.37)-(4.39), which yields

$$\begin{aligned}\sigma_m(z) =&H(c-z)\sum_{m=1}^{\infty} e^{im\phi}\sum_{n=1}^{\infty}\kappa_{mn}v_{mn}c_{mn}^{(t)}J'_m(\kappa_{mn}\rho_a)\,e^{v_{mn}(z-c)}\\ &-H(c-z)\sum_{m=1}^{\infty} e^{im\phi}\sum_{n=1}^{\infty}\kappa_{mn}^2 c_{mn}^{(s)}J'_m(\kappa_{mn}\rho_a)\,e^{\kappa_{mn}(z-c)}\\ &+H(z-c)\sum_{m=1}^{\infty} e^{im\phi}\sum_{n=1}^{\infty}\kappa_{mn}^2 c_{mn}^{(r)}J'_m(\kappa_{mn}\rho_a)\,e^{\kappa_{mn}(c-z)}\end{aligned} \tag{4.46}$$

$$\begin{aligned}J_\varphi(z) = &-H(c-z)\sum_{m=1}^{\infty} e^{im\phi}\sum_{n=1}^{\infty}\kappa_{mn}^2 c_{mn}^{(t)}J_m(\kappa_{mn}\rho_a)\,e^{v_{mn}(z-c)}\\ &+H(c-z)\sum_{m=1}^{\infty} e^{im\phi}\sum_{n=1}^{\infty}\kappa_{mn}^2 c_{mn}^{(s)}J_m(\kappa_{mn}\rho_a)\,e^{\kappa_{mn}(z-c)}\\ &+H(z-c)\sum_{m=1}^{\infty} e^{im\phi}\sum_{n=1}^{\infty}\kappa_{mn}^2 c_{mn}^{(r)}J_m(\kappa_{mn}\rho_a)\,e^{\kappa_{mn}(c-z)}\end{aligned} \tag{4.47}$$

and

$$\begin{aligned}J_z(z) =&H(c-z)\sum_{m=1}^{\infty}\frac{im}{\rho_a}e^{im\phi}\sum_{n=1}^{\infty}v_{mn}c_{mn}^{(t)}J_m(\kappa_n\rho_a)\,e^{v_{mn}(z-c)}\\ &-H(c-z)\sum_{m=1}^{\infty}\frac{im}{\rho_a}e^{im\phi}\sum_{n=1}^{\infty}\kappa_{mn}c_{mn}^{(s)}J_m(\kappa_n\rho_a)\,e^{\kappa_{mn}(z-c)}\\ &+H(z-c)\sum_{m=1}^{\infty}\frac{im}{\rho_a}e^{im\phi}\sum_{n=1}^{\infty}\kappa_{mn}c_{mn}^{(r)}J_m(\kappa_n\rho_a)\,e^{\kappa_{mn}(c-z)}.\end{aligned} \tag{4.48}$$

$H(z)$ stands for the Heaviside step function.

## 4.6 Impedance variation

The application of the reciprocity theorem for the calculation of the coil impedance (or the mutual impedance in case of driver-pick-up configurations) is subjected to the same complications as the source field when the source crosses one of the interfaces of the primary layering. The analysis of the impedance calculation in these cases will be presented by considering the specific case of the borehole inspection, as we did for the calculation of the source field.

The general form of the reciprocity theorem for the calculation of the impedance variation owing to the conducting piece reads

$$\Delta Z = \frac{1}{\mu_0 I_0^2} \oint_S (\mathbf{E}_s \times \mathbf{B}_{ec} - \mathbf{E}_{ec} \times \mathbf{B}_s) \cdot d\mathbf{S}, \tag{4.49}$$

where $\mathbf{E}_s, \mathbf{B}_s$ are the electric and magnetic field in the absence of the conductor, and $\mathbf{E}_{ec}, \mathbf{B}_{ec}$ the corresponding fields in the presence of the conductor. $I_0$ stands for the excitation current. The integration surface encloses the surface with its normal pointing outwards. We choose as integration surface the closed boundary determined by the $z = c$ plane and the truncation boundaries. Since the magnetic field is assumed to be zero on the latter, the only contribution to the closed integral that survives is the one of the $z = c$ plane. Using the SOVP approach (4.49) becomes

$$\Delta Z = -\frac{i\omega}{\mu_0 I_0^2} \int_0^{\rho_L} \int_0^{2\pi} \left[ W_a^{(ec)} \frac{\partial W_a^{(s)}}{\partial z} - \frac{\partial W_a^{(ec)}}{\partial z} W_a^{(s)} \right] \rho d\rho d\phi, \tag{4.50}$$

where $W_a(s)$ is the potential for the solution in air given by (4.37), whereas $W_a^{(ec)}$ stands for the solution in the presence of the conductor. With the application of the decomposition adopted in section 4.5, (4.50) can be written as follows

$$\Delta Z = -\frac{i\omega 2\pi}{\mu_0 I_0^2} \left\{ \sum_{m=-\infty}^{\infty} \left[ \Delta Z_m^1 + \Delta Z_m^2 + \Delta Z_m^3 \right] + \Delta Z^g \right\}. \tag{4.51}$$

Instead of one integral, which was the case for pieces without internal layering, $\Delta Z$ involves three terms, the first stemming from the partial solution for the horizontally layered medium and the remaining two from the contributions of the vertical layers crossed by the integration surface. The fourth term $\Delta Z^g$ is added to ensure the potential continuity across the integration surface, and will be explained in more detail below.

Since the bases used for the development of the three terms are not mutually orthogonal, the resulting formulae for $\Delta Z_m^1$, $\Delta Z_m^2$ and $\Delta Z_m^3$ will involve double sums per azimuthal mode (orthogonality is preserved along the $\phi$ direction).

Indeed, substituting (4.37),(4.38) and (4.41),(4.42) and using the orthogonality of the $e^{im\varphi}$ functions, the first integral yields after some manipulations

$$\Delta Z_1 = \sum_{\ell=1}^{\infty}\sum_{n=1}^{\infty} c_{m\ell}^{(r)} c_{mn}^{(s)} W\Big[e^{\kappa_{mn}(z-c)}, e^{\kappa_{mn}(c-z)}\Big] \int_0^{\rho_a} \rho J_m(\kappa_\ell \rho)\, J_m(\kappa_n \rho)\, d\rho \quad (4.52)$$

where we have used the property $c_{-mn}^{(s)} = (-1)^m c_{mn}^{(s)}$ as well as the symmetry of the Bessel functions $J_{-m}(.) = (-1)^m J_m(.)$. $W(f,g)$ is the Wronskian of the functions $f$ and $g$, where it is understood that the evaluation takes place at $z = c$.

In the same fashion, we obtain for the second integral

$$\Delta Z_2 = \sum_{\ell=1}^{\infty}\sum_{n=1}^{\infty} c_{m\ell}^{(a0)} c_{mn}^{(s)} W\Big[\sin(r_n z)\,, e^{\kappa_{mn}(c-z)}\Big] \int_0^{\rho_a} \rho I_m(u_\ell \rho)\, J_m(\kappa_n \rho)\, d\rho \quad (4.53)$$

and for the third one

$$\Delta Z_3 = \sum_{\ell=1}^{\infty}\sum_{n=1}^{\infty} c_{m\ell}^{(a1)} c_{mn}^{(s)} W\Big[f_n(z)\,, e^{\kappa_{mn}(c-z)}\Big] \int_{\rho_a}^{\rho_L} \rho K_m(p_\ell \rho)\, J_m(\kappa_n \rho)\, d\rho. \quad (4.54)$$

The integrals involving Bessel functions in (4.53),(4.54) have closed form expressions [45], namely

$$\begin{aligned} &\int \rho I_m(u_\ell \rho)\, J_m(\kappa_n \rho)\, d\rho \\ &= \frac{\rho}{\kappa_{mn}^2 + u_\ell^2}\left[u_\ell I_{m+1}(u_\ell \rho)\, J_m(\kappa_n \rho) + \kappa_{mn} I_m(u_\ell \rho)\, J_{m+1}(\kappa_n \rho)\right], \end{aligned} \quad (4.55)$$

for the first one, and the analogous expression for the second (with opposite sign).

We now arrive to the last term of (4.51), $\Delta Z^g$. It is recalled that the scalar potential in air is defined up to an arbitrary constant term, whose precise value does not have any impact to the field solution itself. Nonetheless, care should be taken with the application of the reciprocity theorem (4.50) since not only the potential gradient but also the potential values themselves are employed in the integral. Given the fact that the potential in each subdomain is defined separately, ambiguities may arise, which will alter in their turn the value of the integral. To remove this ambiguity, one has to re-gauge the potentials in order to impose the same value on the common interface points. This is achieved by choosing a reference point on the common interface of the subdomains and adding a constant gauge term $V_g$ in the potential expression for $\rho \geq \rho_a$ in order to assure the same value between this term and the one calculated by the corresponding expression for $\rho \leq \rho_a$ at the same point. Let us choose $(\rho_a, c)$ as reference point. The continuity of the potential yields thus for the gauge term

$$\Delta Z^g = \sum_{n=1}^{\infty} \Big[ c_{0n}^{(a1)} K_0(p_n\rho_a) \sin\left[p_n(h-c)\right] + c_{0n}^{(r)} J_0(\kappa_{mn}\rho_a) \\ - c_{0n}^{(a0)} I_0(u_n\rho_a)\cos(q_n c)\Big] \tag{4.56}$$

and the corresponding correction term to the impedance calculation becomes (after substituting in (4.51) and carrying out the respective integration)

$$\Delta Z_g = -\frac{j\omega 2\pi}{\mu_0 I_0^2}\rho_a V_g \sum_{n=1}^{\infty} c_{0n}^{(s)} J_1(\kappa_n\rho_a)\,. \tag{4.57}$$

Notice that only the $m = 0$ mode contributes to (4.57) since $V_g$ is constant. The choice of the reference point is arbitrary (except for the fact that it must lie on the $\rho = \rho_a$ interface), something which is verified by the invariance of the impedance results for different point locations.

## 4.7 Results for borehole in a finite-thickness plate

The previous theory has been applied for the solution of the eddy-current problem in a finite-thickness plate comprising a cylindrical through-hole [39]. This type of configurations are met in the inspection of riveted structures, a problem of paramount interest for aerospatial applications, where rivet joints are very common in different parts of the fuselage.

Two independent experimental data sets have been used for the validation of the model. The measurements are obtaiend from independent benchmark campaigns carried out in at CEA, LIST and the University of Western Macedonia, Greece, using different mock-ups and probes.

The first configuration consists of a rectangular plate of 2017A (AU4G) aluminium alloy with (measured) conductivity 19.511 MS/m containing a number of cylindrical holes (all sufficiently remote from each other and from the plate edges to ensure no interaction). The plate width and the diameter of the inspected hole are 3.65 ± 0.1 mm and 6.25 ± 0.1 mm, respectively. The coil inner and outer diameters are 2 mm and 5.3 mm, its length is 10 mm, and it is wound with 336 turns (manufacturer values). The specimen was scanned along a straight line crossing the hole centre and at a constant lift-off equal to 0.0934 mm (fitted value following [46]). Details on the measurement procedure, carried out in CEA, LIST, can be found in [44].

Fig. 4.10 compares the theoretical results for the impedance change along a probe scan at 10 kHz with the corresponding measured data as well as with FEM simulation results. The latter have been obtained using the three dimensional FEM package COMSOL Multiphysics ® [32]. The impedance change loci in the complex plane, are plotted in Fig. 4.11 for three frequencies: 1, 10 and 100 kHz. The skin-depth-to-plate-width ratio at these frequencies is approximately 1, 1/2 and 1/10, i.e. the considered cases represent different penetration regimes: full,

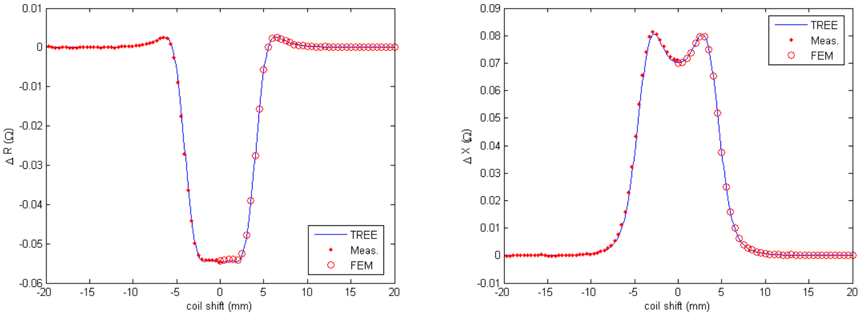

Figure 4.10: Comparison of the model results (solid line) along a coil scan with FEM numerical data (wide circles) and measurements (dots) at 10 kHz. $\Delta R$ and $\Delta X$ stand for real and imaginary part of the coil impedance variation due to the presence of the hole (with respect to the impedance value over an infinite plate).

intermediate penetration and thin-skin regime, respectively. Excellent agreement is observed in all cases. Note that the signals in Fig. 4.11 are normalised with respect to their maximum amplitude, in order to be able to compare them in the same plot. Such plots of the impedance locus as a function of a parameter (the frequency in this case) is the common way of presenting results in ECT.

The second test configuration is taken from the 2013 benchmark problem of the World Federation for NDE Centers (WFNDEC) [47]. The specimen is a 2 mm thick aluminium plate with an electrical conductivity equal to 17.34 MS/m. A vertical borehole of 10 mm radius is located in the centre of the plate. The probe coil used for the inspection has inner and outer radii of 7 mm and 12 mm, respectively, 4 mm length and 1650 turns. The lift-off was fitted to 1.082 mm. As in the previous case, the coil impedance was measured during a number of linear scans, passing through hole axis.

The real and imaginary parts of the impedance change at 1 kHz are shown in Fig. 4.12. The impedance loci at 1 and 5 kHz are shown in Fig. 4.13. We observe the same tendencies as in the previous case, i.e. the signals are symmetric with respect to the hole axis, and the curves peaks are obtained when the coil is located over the hole edges. Again, the agreement with the reference results is excellent for both frequencies.

## 4.8 General formalism using the Dirac notation

The central idea explored in this chapter was that a medium comprising a two-axis-layering (cf. Fig. 4.14a) can be replaced by a medium with a simple layering, where the consisting pieces are obtained by a homogenisation procedure based on the calculation of the 1D eigenfunctions along the direction of the internal layering (cf. Fig. 4.14b). In a further generalisation, this approach can be

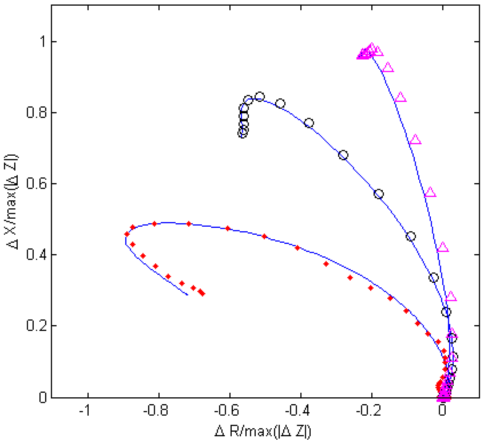

Figure 4.11: Normalised impedance variation along a line scan in the complex plane. The solid lines represent the model results, whereas the markers stand for the measured data. The three curves correspond to the three considered frequencies: 1 kHz (dots), 10 kHz (circles) and 100 kHz (triangles).

applied to layered media with 1D gradients, which can be seen as the continuum limit of an internal layering. Sources that cross the interfaces of the principal layering can be treated in an elegant way by means of equivalent distributions at the layers interfaces as was shown in section 4.5.

With that said, the problem becomes formally equivalent with the situation encountered in chapter 3. It would be thus attractive to adapt the therein developed formalism in order to make it applicable also to this class of problems.

The general expression for the continuity relations at the $j$th (observation) surface in a domain with non-intersecting interfaces is given in (3.26)

$$\sum_{i=1}^{2N} \left( \hat{\boldsymbol{\nu}}_{j^+} \hat{\boldsymbol{C}}_{j^+} \hat{\boldsymbol{P}}_{i\to j^+} - \hat{\boldsymbol{\nu}}_{j^-} \hat{\boldsymbol{C}}_{j^-} \hat{\boldsymbol{P}}_{i\to j^-} \right) |m_i\rangle \, \mathbf{c}_{m_i} = \mathbf{0}, \qquad \forall j \tag{3.103}$$

with the sum running over all the interfaces of the geometry. $|m_i\rangle$ are the basis elements at the $i$th surface, $\hat{\boldsymbol{P}}_{i\to j\pm}$ the propagator from the $i$th to the positive/negative side of the observation surface, and $\hat{\boldsymbol{C}}_{j\pm}$ stands for the continuity operator at this side of the observation surface. Finally $\hat{\boldsymbol{\nu}}_{j\pm}$ is the material operator, which corresponds to the medium lying at the considered side of the observation surface. It is recalled that in case of the eddy-current problem, the series coefficients $\mathbf{c}_{m_i}$ are duplets with each element corresponding to the coefficient for the $W_a/W_b$ potential.

The problem that arises if we try to apply (3.103) to the set of the primary interfaces is that $W_a$ and $W_b$ cannot be described by the same basis, as it was the case in the previous chapter, since they must verify different eigenvalue

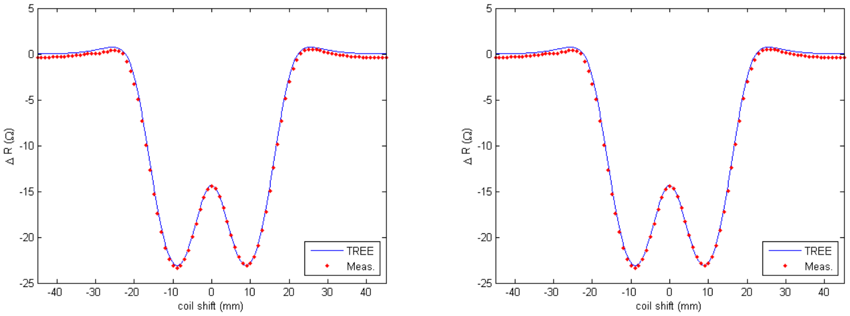

Figure 4.12: Comparison of the model results (solid line) along a coil scan with measurements (dots) at 1 kHz (benchmark problem). $\Delta R$ and $\Delta X$ stand for real and imaginary part of the coil impedance variation due to the presence of the hole (with respect to the impedance value over an infinite plate).

equations, namely (4.23) and (4.21). As a consequence, $|m_i\rangle$ is different for the $W_a$ and $W_b$ elements of the duplet.

The simplest way out is to introduce the selection operator $\hat{\boldsymbol{s}}_{TE/TM}$ which can be defined in terms of the Pauli matrix $\boldsymbol{\sigma}_3$, that is

$$\hat{\boldsymbol{s}}_{TE/TM} \coloneqq \frac{1}{2}\left(\boldsymbol{\sigma}_3 \pm \boldsymbol{\sigma}_3\right) \tag{4.58}$$

with

$$\boldsymbol{\sigma}_3 = \begin{pmatrix} 1 & 0 \\ 0 & -1 \end{pmatrix} \tag{4.59}$$

Using the above definition, (3.103) becomes

$$\sum_{i=1}^{2N} \left(\hat{\boldsymbol{\nu}}_{j^+}\hat{\boldsymbol{C}}_{j^+}\hat{\boldsymbol{P}}_{i\to j^+} - \hat{\boldsymbol{\nu}}_{j^-}\hat{\boldsymbol{C}}_{j^-}\hat{\boldsymbol{P}}_{i\to j^-}\right)|m_i\rangle\, \hat{\boldsymbol{s}}_{m_i}\mathbf{c}_{m_i} = \mathbf{0}, \qquad \forall j \tag{4.60}$$

where now the set of the basis elements is understood as a juxtaposition of the elements for each $TE/TM$ solution separately, namely

$$|m_i\rangle = \left(|1_i\rangle^{TE}, |2_i\rangle^{TE}, \ldots, |N_i\rangle^{TE}, |1_i\rangle^{TM}, |2_i\rangle^{TM}, \ldots, |M_i\rangle^{TM}\right) \tag{4.61}$$

whence it turns out for the selection operators

$$\hat{\boldsymbol{s}}_{m_i} = \frac{1}{2}\begin{cases} \boldsymbol{\sigma}_3 + \boldsymbol{\sigma}_3 & \text{for } 1 \le m_i \le N \\ \boldsymbol{\sigma}_3 - \boldsymbol{\sigma}_3 & \text{for } N+1 \le m_i \le M \end{cases} \tag{4.62}$$

with $N$ and $M$ being the sizes of the TE/TM bases.

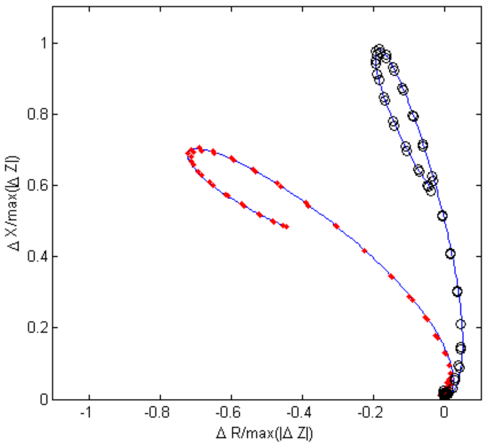

Figure 4.13: Normalised impedance variation along a line scan in the complex plane (benchmark problem). The theoretical results are drawn using solid lines, and the measurements are represented by the markers. The two curves correspond to the two frequencies of the benchmark: 1 kHz (dots) and 5 kHz (circles).

## 4.9 Publications related with the chapter content

The major results of this chapter are the outcome of the research work published in several articles and conference communications.

In particular, the solution of the borehole inspection problem has been presented in [29, 39, 44]. This work has also served as the base for the development of the corresponding integral equation formalism used for the calculation of the flaws response in the proximity of the borehole. The latter developments were carried out in the context of the doctoral research work of Dr. K. Pipis. The applied methodology and the obtained results of that work will be presented in detail in the next chapter.

The eigenvalue calculation in the slotted planar specimen using the Galerkin approach, and the associated evaluation of the ECT signal was presented in [48].

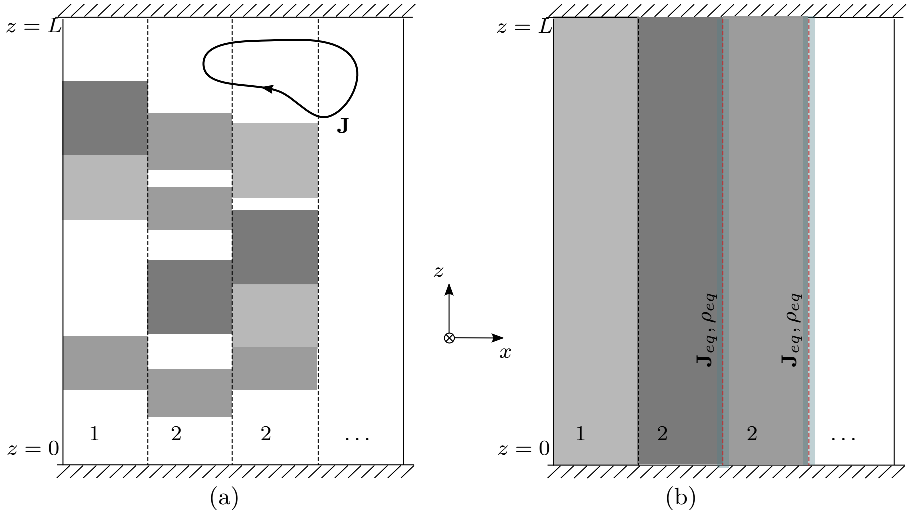

Figure 4.14: Two-level treatment of layered medium by homogenisation of the vertical layers. Sources spanning multiple domains are replaced by equivalent formulations at the primary boundaries.

# Chapter 5

# Inhomogeneous materials

All the pieces examined up to now were homogeneous, which allowed us to focus the analysis on the interaction of the driving field with their interfaces. Nonetheless, the presence of inhomogeneities, real or fictitious, inside a given piece gives rise to diffraction terms emerging from the interaction with the entire piece volume and require a different treatment.

Volume scattering can be triggered by a number of different mechanisms. Some of the most relevant causes of volume scattering in NDT are:

- Presence of material defects.
- Presence of gradients in the material properties. There can be for example variations of the material conductivity or permeability as function of the depth linked to a specific metallurgical treatment (mechanical of thermal) of the piece and the consequent altering of its microstructure.
- Non-linearity. This is the case when ferromagnetic materials are involved under the action of intermediate or strong driving fields. The non-linear magnetic constitutive law in this case is translated to a field-dependent effective permeability. More precisely, the local value of the effective (linearised) permeability depends on the operation point in the $\mathbf{B}(\mathbf{H})$ loop.
- Presence of residual stresses. In case of ferromagnetic materials, an uneven distribution of mechanical stresses can lead to inhomogeneous magnetic properties via the magneto-mechanical coupling effect.

The focus of this chapter will be the development of modelling tools in order to calculate the piece response when one or more of the above-mentioned mechanisms are present. The accent will be given to the mathematical tools themselves, limiting the physical analysis to a minimum.

We shall consider two different approaches for addressing the two aforementioned classes of problems, namely the defect and the material response, mainly as a consequence of the different geometrical features of each. Since material defects, such as corrosion or cracking are small with respect to the host piece, it is more efficient to consider the problem as a perturbation problem and to work using representations involving local bases. Such bases, defined in the spatial domain will be introduced to solve the resulting integral equation problem using the method of moments (MoM). As far as the second category is concerned, i.e. the treatment of material gradients, the use of global (spectral) bases proves to be a more judicious choice, since they provide a more efficient mean of resolving extended inhomogeneities.

## 5.1 Linear media with defect

We consider a linear conducting and/or magnetic medium affected by a local perturbation of its properties as shown in Fig. 5.1. The eddy-currents in the piece are excited by a closed current source, which in the majority of the cases is an induction coil, although different types of sources such as linear current layers or electrodes can be considered (applied in specialised techniques like the alternating current field measurement, ACFM, for instance). The problem described by Fig. 5.1 is a case of great practical importance since it lies in the kernel of the NDT application domain: the detection and characterisation of structural defects. We begin the analysis by presenting the volume equivalence theorem, which forms the basis of the integral equation approach used for the calculation of the defect response.

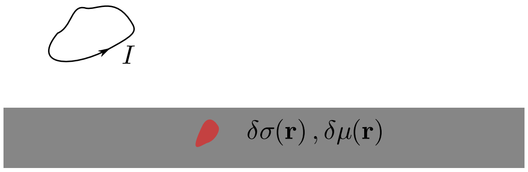

Figure 5.1: Inspection of a defected specimen using a current source.

## 5.2 The volume equivalence theorem

Let us consider the Maxwell equations in a homogeneous, isotropic and linear reference medium, characterised by the material constants $\mu_b, \sigma_b$, the index “b” standing for “base material”. For the reference problem, the first two Maxwell equations read

$$\nabla \times \mathbf{E}_p = -i\omega\mu_b\mathbf{H}_p \tag{5.1}$$

$$\nabla \times \mathbf{H}_p = \sigma_b\mathbf{E}_p + \mathbf{J}. \tag{5.2}$$

The electric and magnetic field in the flawless medium, $\mathbf{E}_p$ and $\mathbf{H}_p$, are referred to as primary electric and magnetic field following the usual naming convention.

We consider now the electromagnetic problem involving the same set of sources in a second medium, whose material distribution can be expressed as a variation of the ones for the reference medium, namely

$$\mu = \mu_b + \delta\mu \tag{5.3}$$

$$\sigma = \sigma_b + \delta\sigma. \tag{5.4}$$

Let us denote **E** and **H** the electric and magnetic field solution in the second medium. Writing the Maxwell equations for the second problem and subtracting from the first set (5.1),(5.2) taking the relations (5.3),(5.4) into account, we can write

$$\nabla \times (\mathbf{E} - \mathbf{E}_p) = -i\omega\mu_b (\mathbf{H} - \mathbf{H}_p) - i\omega\delta\mu\mathbf{H} \tag{5.5}$$

$$\nabla \times (\mathbf{H} - \mathbf{H}_p) = \sigma_b (\mathbf{E} - \mathbf{E}_p) + \delta\sigma\mathbf{E} \tag{5.6}$$

which are formally equivalent with the Maxwell equations for the perturbation (scattering) fields $\delta\mathbf{E} = \mathbf{E} - \mathbf{E}_p$ and $\delta\mathbf{H} = \mathbf{H} - \mathbf{H}_p$ under the action of the equivalent sources

$$\mathbf{J}_e = \delta\sigma\mathbf{E} \tag{5.7}$$

$$\mathbf{J}_m = i\omega\delta\mu\mathbf{H}. \tag{5.8}$$

This problem separation into a primary field in the unperturbed medium and a perturbation term (scattered field) owing to the interaction with the material inhomogeneities is schematically depicted in Fig. 5.2

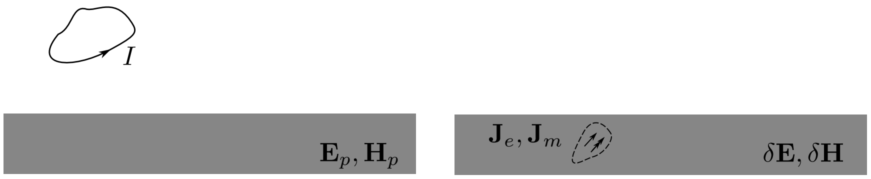

Figure 5.2: Separation of the volume scattering problem into a primary field and a perturbation (scattered) field solution.

Notice that in the above analysis we have ignored the last two Maxwell equations for the flux densities. It is straight-forward to see that the corresponding flux densities variation satisfy the homogeneous Gauss equations, namely

$$\nabla \cdot \delta\mathbf{D} = \mathbf{0} \tag{5.9}$$

$$\nabla \cdot \delta\mathbf{B} = \mathbf{0}. \tag{5.10}$$

Equations (5.5)-(5.6) form the essence of the so-called **volume equivalence theorem** [3]. The importance of the volume equivalence theorem is that it shifts the effect of the material inhomogeneity from the constitutive relations to the sources. Its name indicates the volumetric nature of the equivalent sources, in distinction with the surface equivalent theorem. Based upon this particular position of the scattering problem, we can now devise methods that solve **for the unknown source terms** in piecewise-homogeneous media, in which the Maxwell equations admit a simpler treatment.

## 5.3 The volume integral equation method for volumetric defects

Having expressed the material inhomogeneities in terms of volumetric equivalent sources $\mathbf{J}_e$ and $\mathbf{J}_m$ embedded in the reference flawless medium, we can calculate their effect to the total field by resorting again to the Green's theorem. However, in contrast with the previous sections, where the state variables were scalar quantities (potentials), it is more convenient to work here directly with fields. We will therefore make use of the vector form of the Green's second identity.

Considering an infinite domain, it can be shown that the surface integral term vanishes (the electromagnetic field is zero at infinite distance), and the only remaining terms are the volume integrals related to the equivalent currents [49]. Applying thus the vector Green's theorem twice, with Green's functions associated to an electric $\left(\overline{\mathbf{G}}^{ee}, \overline{\mathbf{G}}^{me}\right)$ and a magnetic source $\left(\overline{\mathbf{G}}^{em}, \overline{\mathbf{G}}^{mm}\right)$ respectively, we arrive at the following set of integral equations (the proof is given in the appendix for completeness).

$$\begin{aligned}\mathbf{E}(\mathbf{r}) = \mathbf{E}_p(\mathbf{x}) &+ \int\limits_{V_f} \overline{\mathbf{G}}^{ee}(\mathbf{x}, \mathbf{x}') \cdot \delta\sigma(\mathbf{x}')\, \mathbf{E}(\mathbf{x})\, dV' \\ &- i\omega \int\limits_{V_f} \overline{\mathbf{G}}^{me}(\mathbf{x}, \mathbf{x}') \cdot \delta\mu(\mathbf{x}')\, \mathbf{H}(\mathbf{x}')\, dV' \end{aligned} \tag{5.11}$$

$$\begin{aligned}\mathbf{H}(\mathbf{x}) = \mathbf{H}_p(\mathbf{x}) &+ \int\limits_{V_f} \overline{\mathbf{G}}^{em}(\mathbf{x}, \mathbf{x}') \cdot \delta\sigma(\mathbf{x}')\, \mathbf{E}(\mathbf{x}')\, dV' \\ &- i\omega \int\limits_{V_f} \overline{\mathbf{G}}^{mm}(\mathbf{x}, \mathbf{x}') \cdot \delta\mu_b(\mathbf{x}')\, \mathbf{H}(\mathbf{x}')\, dV'. \end{aligned} \tag{5.12}$$

Since the involved Green's functions express a vector-to-vector mapping, the corresponding integral kernels (the Green's functions) admit tensor forms (dyads).

Equations (5.11),(5.12) are Fredholm integral equations of the second kind, which means that the unknown function (in this case the electric and magnetic field) appears in the same time both inside and outside the integral operator. The interest of this approach stems from the fact that the integration is carried out over the flaw support $V_f$, which in NDT simulations is a small fraction of the piece at hand.

The $\overline{\mathbf{G}}^{ee}$ and $\overline{\mathbf{G}}^{me}$ dyads are defined as the electric and magnetic field response with a **unit Dirac electric current** source satisfying the Helmholtz equation [4, 49]

$$\nabla \times \nabla \times \overline{\mathbf{G}}^{ee}(\mathbf{x}, \mathbf{x}') + k^2 \overline{\mathbf{G}}^{ee}(\mathbf{x}, \mathbf{x}') = -i\omega\mu_b \overline{\mathbf{I}}\delta(\mathbf{x} - \mathbf{x}') \tag{5.13}$$

$$\nabla \times \nabla \times \overline{\mathbf{G}}^{me}(\mathbf{x}, \mathbf{x}') + k^2 \overline{\mathbf{G}}^{me}(\mathbf{x}, \mathbf{x}') = \nabla \times \left[\overline{\mathbf{I}}\delta(\mathbf{x} - \mathbf{x}')\right] \tag{5.14}$$

where $\delta(\mathbf{x} - \mathbf{x}')$ is the delta function, and $\overline{\mathbf{I}}$ stands for the unit tensor. $k^2 = i\omega\mu\sigma$ is the separation constant defined above. From the previous relations it is evident that $\overline{\mathbf{G}}^{me}$ is the curl of $\overline{\mathbf{G}}^{ee}$

$$\overline{\mathbf{G}}^{me}(\mathbf{x}, \mathbf{x}') = \nabla \times \overline{\mathbf{G}}^{ee}(\mathbf{x}, \mathbf{x}') \,. \tag{5.15}$$

$\overline{\mathbf{G}}^{mm}$ and $\overline{\mathbf{G}}^{em}$ are defined in a similar way, namely as the corresponding magnetic and electric field response under **magnetic current** excitation. It can be easily shown that they satisfy the same equations as their electric counterparts (5.13) and (5.14).

Note that the two pairs are interrelated via the duality principle, i.e. they can be interchanged in (5.13) and (5.14) using the following rule $\overline{\mathbf{G}}^{ee} \leftrightarrow \overline{\mathbf{G}}^{mm}$ and $\overline{\mathbf{G}}^{me} \leftrightarrow \overline{\mathbf{G}}^{em}$, which together with the substitutions $\mathbf{E} \leftrightarrow \mathbf{H}$, $\sigma \leftrightarrow -i\omega\mu$ produce the same set of equations. The duality transformation is hence a symmetry of (5.13) and (5.14). The detailed derivation of the Green's dyads in the planar and cylindrical mediums will be given in a later section.

### 5.3.1 Conductive, non-magnetic medium with volumetric flaws

Equations (5.11),(5.12) address the most general case of a flaw inside a conducting and magnetic medium. However, in practical applications, this general case concerns ferritic steels since steel is the magnetic material used in the vast majority of structures with industrial interest. All other workpieces with technical interest present a negligible magnetic behaviour, i.e. we can consider $\delta\mu = 0$, and (5.11),(5.11) specialise to the following relation for the state equation

$$\mathbf{E}(\mathbf{x}) = \mathbf{E}_p(\mathbf{x}) + \int\limits_{V_f} \overline{\mathbf{G}}^{ee}(\mathbf{x}, \mathbf{x}') \cdot \delta\sigma(\mathbf{x}') \, \mathbf{E}(\mathbf{x}') \, dV'. \tag{5.16}$$

### 5.3.2 Magnetic medium with volumetric flaws

This case concerns magnetic pieces with a local variation of the permeability the same time that its conductivity remains constant (i.e. $\delta\sigma = 0, \delta\mu \neq 0$. The first integral of (5.12) thus vanishes reducing the problem to a single integral equation with solely magnetic contributions

$$\mathbf{H}(\mathbf{x}) = \mathbf{H}_p(\mathbf{x}) - i\omega \int\limits_{V_f} \overline{\mathbf{G}}^{mm}(\mathbf{x}, \mathbf{x}') \cdot \delta\mu_b(\mathbf{x}') \, \mathbf{H}(\mathbf{x}') \, dV'. \tag{5.17}$$

Since the magnetic permeability in low field depends on the material history, every magnetic material without bias magnetic field is characterised by local permeability variations, which means that a magnetic signature may exist even in the absence of defects. It is however extremely difficult to determine this variation experimentally and hence this scenario presents only theoretical interest.

A case with much more practical interest is the calculation of the magnetic flux concentration in inductors with ferrite cores. Nonetheless, since $\sigma_b$ is very low in ferrites the integral term in (5.12) vanishes. Indeed, this equation is derived by Ampère's law and hence is not the adequate approach for the problem. The integral formulation in this case should be derived by the magnetostatic formulation as shown in [50].

An alternative approach for addressing the core problem over a given speciment will be proposed in chapter 7, where a hybrid numerical-semi-analytical formulation will be proposed.

## 5.4 The surface integral equation method for thin cracks

In conductive, non-magnetic media, a further simplification is also possible when the thickness of the defect is negligible with respect to the other dimensions and with respect to the skin depth in the material. This is the case for thin cracks, which is a very common category of material defects comprising the stress-corrosion cracking (SCC) and the fatigue crack (FG) mechanisms. The formalism has been introduced by Bowler et al. [13, 51–54] for the modelling of cracks in infinite media and has been extended in the recent literature by Theodoulidis and Miorelli [55–57]. Further developments have adressed the cases of finite media accounting for the end-effect such as plate edges from Theodoulidis and Bowler [58], boreholes from Pipis, Skarlatos and Theodoulidis [39, 40] and tube edges [59].

Let us consider the case of a crack whose thickness $\Delta$ is very small with respect to its two remaining dimensions and to the skin depth, as shown in Fig. 5.3. A crack fulfilling these properties will be called **thin crack**. If in addition this crack acts as a perfect current barrier (which is the case if the filling material is an insulator, usually air, and no galvanic contact takes place between its two sides), it will be referred to also **ideal crack**.

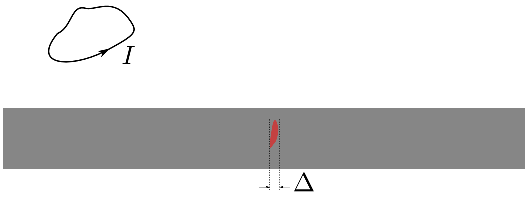

Figure 5.3: Inspection of a defected specimen using a current source.

Using the fact that the normal current component at the surface of an ideal crack must vanish, which in its turn is translated to vanishing normal electric field, (5.16) reduces to

$$\mathbf{n}\cdot\mathbf{E}^{p}(\mathbf{x}) = \lim_{\Delta\to 0}\int\limits_{S_f} \mathbf{n}\cdot\overline{\mathbf{G}}^{ee}(\mathbf{x},\mathbf{x}')\cdot\mathbf{n}\,p(\mathbf{x}')\,dS' \tag{5.18}$$

where $\Delta$ stands for the crack opening, $S_f$ its surface and $p$ expresses the electric dipole distribution over $S_f$, defined as

$$p(\mathbf{x}) = \lim_{\Delta \to 0} \delta\sigma(\mathbf{x})\, \mathbf{n} \cdot \mathbf{E}(\mathbf{x})\, \Delta \tag{5.19}$$

$\mathbf{n}$ being the unit normal to the crack surface vector.

Notice the simplification achieved when moving from (5.16), which is a vector Fredholm integral equation of the second kind, with (5.18), a first order scalar Fredholm equation.

The question that arises here is to which extent the aforementioned assumptions hold for realistic cracks. The answer depends on the crack generation mechanism. Hence, for fatigue cracks the galvanic separation between the crack sides is well satisfied. This is not the case, however for SCC where due to the crack creation mechanism and its very weak thickness there might be a non-negligible normal current component. In this case the above presented formalism needs to be generalised by introducing conducting bonds between the opposing surfaces of the crack, this generalisation is however out of the scope of the present text.

## 5.5 Solution of the integral equation system using the method of moments

In order to solve the system of integral equations (5.11),(5.12) in case of VIM formulation, or the equation (5.18) in case of the SIM formulation for thin cracks, a dedicated formulation of Galerking type known as the method of moments (MoM) is applied [3, 4]. According to this method, the unknown field distribution inside the defect is approximated via a set of functions with local support (rectangular pulses, triangular pulses, etc.) which form a representation basis in the spatial domain, and they are therefore referred to as basis functions[1]

$$\mathbf{E}(\mathbf{x}) = \sum_{i=1}^{N} E_i \mathbf{w}_i(\mathbf{x}) \tag{5.20}$$

$$\mathbf{H}(\mathbf{x}) = \sum_{i=1}^{N} H_i \mathbf{w}_i(\mathbf{x}) \tag{5.21}$$

where $\mathbf{w}_i(\mathbf{x})$ stand for the basis functions. The basis functions considered in the context of this work are three dimensional pulses of equal width. In cartesian coordinates, the latter are expressed in terms of tensor products of 1D pulses, namely

$$\mathbf{w}_i(\mathbf{x}) = \Pi_x(x - x_i)\, \Pi_y(y - y_i)\, \Pi_z(z - z_i)\, \mathbf{e}_i \tag{5.22}$$

---

[1] It must be underlined that the local support is not a prerequisite for the basis functions. Indeed global basis functions can be also utilised, exceeding the support of the unknown field (that is the integration domain). Since, however, local functions are more versatile for describing domains of complex shape they are usually prefered. This text will not be an exception at this point.

with the pulse functions

$$P_x(x - x_i) = H(x - x_i + \Delta x/2) - H(-x + x_i + \Delta x/2) \tag{5.23}$$

where $x_i$ is the centre of the pulse, $\Delta x$ its width and $H(x)$ stands for the Heaviside step function. The definitions for $P_y$ and $P_z$ are similar. $\mathbf{e}_i$ is the unit vector running through all possible orientations $\mathbf{e}_x, \mathbf{e}_y$ and $\mathbf{e}_z$. It is obvious that for a reduced-dimension space (like the crack surface in SIM formulation), the expansion applies only on the corresponding surface.

In cylindrical coordinates, attention must be paid for the $\rho$ coordinate in order to satisfy flux conservation resulting in the following choice for the basis functions in the radial direction [50]

$$\mathbf{w}_i(\mathbf{x}) = \rho \Pi_\rho(\rho - \rho_i)\, \Pi_\phi(\phi - \phi_i)\, \Pi_z(z - z_i)\, \mathbf{e}_\rho \tag{5.24}$$

for all $i$ corresponding to the radially oriented basis functions. The definition for the remaining two directions follows the one for the cartesian system.

Introducing the expansion (5.20),(5.21) in (5.11),(5.12) and weighting with the same set $\mathbf{m}_i$ (the so-called test functions in the MoM jargon), according to Galerkin approach, we obtain the linear system of algebraic equations

$$\begin{bmatrix} \mathbf{T}_\sigma - \hat{\mathbf{G}}_{ee} & i\omega\hat{\mathbf{G}}_{me} \\ -\hat{\mathbf{G}}_{em} & \mathbf{T}_\mu + i\omega\hat{\mathbf{G}}_{mm} \end{bmatrix} \cdot \begin{bmatrix} \hat{\mathbf{J}}_e \\ \hat{\mathbf{J}}_m \end{bmatrix} = \begin{bmatrix} \hat{\mathbf{E}}_p \\ \hat{\mathbf{H}}_p \end{bmatrix} \tag{5.25}$$

where $\hat{\mathbf{G}}_{xy}$ are the weighted Green's dyads

$$\left[\hat{G}_{ee}\right]_{ji} = \int\limits_{V_f} \int\limits_{V_f} \mathbf{w}_j(\mathbf{x}) \cdot \overline{\mathbf{G}}_{xy}(\mathbf{x}, \mathbf{x}') \cdot \mathbf{w}_j(\mathbf{x}')\, dV' dV \tag{5.26}$$

with $xy = ee, em, me$ and $mm$, $\mathbf{T}_\sigma, \mathbf{T}_\mu$ are diagonal matrices occurring from the weighted current terms within (5.11),(5.12)

$$T_{\sigma;ji} = \int\limits_{V_f} \frac{1}{\delta\sigma(\mathbf{x})} \mathbf{w}_j(\mathbf{x}) \cdot \mathbf{w}_i(\mathbf{x})\, dV \tag{5.27}$$

$$T_{\mu;ji} = \int\limits_{V_f} \frac{1}{\delta\mu(\mathbf{x})} \mathbf{w}_j(\mathbf{x}) \cdot \mathbf{w}_i(\mathbf{x})\, dV \tag{5.28}$$

and finally $\hat{\mathbf{E}}_p, \hat{\mathbf{H}}_p$ are the weighted primary fields

$$E_{p;i} = \int\limits_{V_f} \mathbf{w}_j(\mathbf{x}) \cdot \mathbf{E}(\mathbf{x})\, dV \tag{5.29}$$

$$H_{p;i} = \int\limits_{V_f} \mathbf{w}_j(\mathbf{x}) \cdot \mathbf{H}(\mathbf{x})\, dV. \tag{5.30}$$

The system matrix can be given a symmetric form as it can be easily shown using the properties of the Green dyads

$$\begin{bmatrix} \mathbf{T}_\sigma - \hat{\mathbf{G}}_{ee} & \hat{\mathbf{G}}_{me} \\ \hat{\mathbf{G}}_{em} & -\mathbf{T}_\mu/i\omega - \hat{\mathbf{G}}_{mm} \end{bmatrix} \cdot \begin{bmatrix} \hat{\mathbf{J}}_e \\ i\omega\hat{\mathbf{J}}_m \end{bmatrix} = \begin{bmatrix} \hat{\mathbf{E}}_p \\ -\hat{\mathbf{H}}_p \end{bmatrix}. \tag{5.31}$$

The symmetry of the system is a direct consequence of the Galerkin approach, as it is well known; it will not occur if the collocation method is applied (use of Dirac delta functions as test functions).

The numerical treatment of SIM is much simpler since it only involves the electric field instead of electric and magnetic fields and thanks to its mathematical structure (it is Fredholm integral equation of the first kind with the unknown appearing only inside the integral as already mentioned). The final system is given here for completeness

$$\hat{\mathbf{G}}_{ee} \cdot \hat{\mathbf{p}} = \hat{\mathbf{E}}_p. \tag{5.32}$$

It turns out that the collocation approach is sufficient for the SIM equation, which presents some interest also from the implementation point of view since it leads to simpler expressions [55–57].

## 5.6 Construction of the dyadic Green's functions

The definition of the Green's dyads has been given in (5.13),(5.14). To be able to calculate the integrals of the volume integral equation (5.11),(5.12) and the surface integral equation (5.18) formalism, however, we need to dispose of explicit expressions for all dyads. Thanks to duality, only the calculation of one of the two pairs, e.g. the first one ($\overline{\mathbf{G}}^{ee}, \overline{\mathbf{G}}^{me}$) is required the second being obtained by interchanging $\sigma$ with $-i\omega\mu$.

By construction, the Green's dyads domain span the entire computational domain, which for the class of problems we are interested in is a multilayer medium. This means that they consist of two parts corresponding to different diffusion mechanisms that take place in a multilayer medium: direct diffusion and scattering from the medium interfaces. We may comment that the inclusion of the second mechanism in the Green's dyad expression is the price one has to pay for applying the Green's theorem in the entire domain and consequently getting rid of the surface integrals. An alternative approach would be to apply the theorem layer-wise, which in that case would imply that surface integrals terms are needed to accommodate the boundary conditions. This approach leads to the well-known boundary element method (BEM). In this second approach, the dyadic expressions are the ones of the free space (known in closed form) but the addition of the surface integrals results in a computationally heavier scheme. Summarising, one has two choices for tackling the boundary conditions: either including them in the construction of the Green's function or by treating them numerically with the Green's function of the free space.

For the following developments we shall adopt the following notation for the Green's dyads: $\overline{\mathbf{G}}^{ee}_{mn}, \overline{\mathbf{G}}^{ee}_{mn}$ where the subscripts $m, n$ indicate the subdomain/layer index for the observation point $\mathbf{x}$ and the source $\mathbf{x}'$, respectively[2].

As mentioned above we can split the Green's dyads into a direct and a scattered part as follows

$$\overline{\mathbf{G}}^{ee}_{mn}(\mathbf{x}, \mathbf{x}') = \overline{\mathbf{G}}^{ee}_{0}(\mathbf{x}, \mathbf{x}')\, \delta_{mn} + \widetilde{\overline{\mathbf{G}}}^{ee}_{mn}(\mathbf{x}, \mathbf{x}') \tag{5.33}$$

$$\overline{\mathbf{G}}^{me}_{mn}(\mathbf{x}, \mathbf{x}') = \overline{\mathbf{G}}^{me}_{0}(\mathbf{x}, \mathbf{x}')\, \delta_{mn} + \widetilde{\overline{\mathbf{G}}}^{me}_{mn}(\mathbf{x}, \mathbf{x}') \tag{5.34}$$

where $\overline{\mathbf{G}}^{ee}_{0}, \overline{\mathbf{G}}^{me}_{0}$ are the free-space dyads, $\widetilde{\overline{\mathbf{G}}}^{ee}_{mn}, \widetilde{\overline{\mathbf{G}}}^{me}_{mn}$ correspond to the scattering terms and $\delta_{mn}$ is Kronecker's delta. Its presence indicates that there is no direct contribution between points in different layers but only transmission terms.

The dyadic Green's functions for the free-space are derived by the corresponding scalar Green's function according to the relations [4]

$$\overline{\mathbf{G}}^{ee}_{0}(\mathbf{x}, \mathbf{x}') = -i\omega\mu_b \left[\overline{\mathbf{I}} + \frac{\nabla\nabla}{k^2}\right] g(\mathbf{x}, \mathbf{x}') \tag{5.35}$$

$$\overline{\mathbf{G}}^{me}_{0}(\mathbf{x}, \mathbf{x}') = \nabla \times \left[\overline{\mathbf{I}} g(\mathbf{x}, \mathbf{x}')\right] \tag{5.36}$$

with $g(\mathbf{x}, \mathbf{x}')$ given by (3.26) and repeated here for convenience

$$\left(\nabla^2 - k^2\right) g(\mathbf{x}, \mathbf{x}') = \delta(\mathbf{x} - \mathbf{x}')\,. \tag{3.26}$$

Notice that both $\overline{\mathbf{G}}^{ee}_{0}$ and $\overline{\mathbf{G}}^{me}_{0}$ remain invariant upon the duality transformation $\sigma \leftrightarrow -i\omega\mu$, which means that $\overline{\mathbf{G}}^{ee}_{0} = \overline{\mathbf{G}}^{mm}_{0}$ and $\overline{\mathbf{G}}^{me}_{0} = \overline{\mathbf{G}}^{em}_{0}$. This is a plausible result since its reflects the fact that the electric field produced by an electric dipole in free-space is the same as for the magnetic field produced by a magnetic dipole and the electric field produced by a magnetic dipole equals the magnetic field produced by an electric dipole (assuming correct scaling relations between the currents).

$\overline{\mathbf{G}}^{ee}_{mn}(\mathbf{x}, \mathbf{x}')\,, \overline{\mathbf{G}}^{me}_{mn}(\mathbf{x}, \mathbf{x}')$ will be calculated in the spectral domain using all the tools presented in chapters 3 and 4. For this calculation, however, we need first to project the field of the point source onto the appropriate spectral basis associated with some surface. In the following, we will provide this calculation for the cartesian and the cylindrical coordinate system.

Assuming a multilayer medium and a point source embedded in one of the layers, the development (Huygens) surfaces for the source field are shown in Fig. 5.4 for the two systems. The presence of the source gives rise to an upwards and a downwards diffused field front in the first case, whereas in the

---

[2] In (5.11),(5.12), (5.18) it has been tacitly assumed that the defect is contained in a single layer, hence $m = n$ and can be dropped for simplicity. In general case though a defect can cross several layers, in which case all $m$ and $n$ combinations of the affected layers must be taken into account. We shall provide here the guidelines for the construction of the Green's dyads for different layers but only single layers defects will be considered.

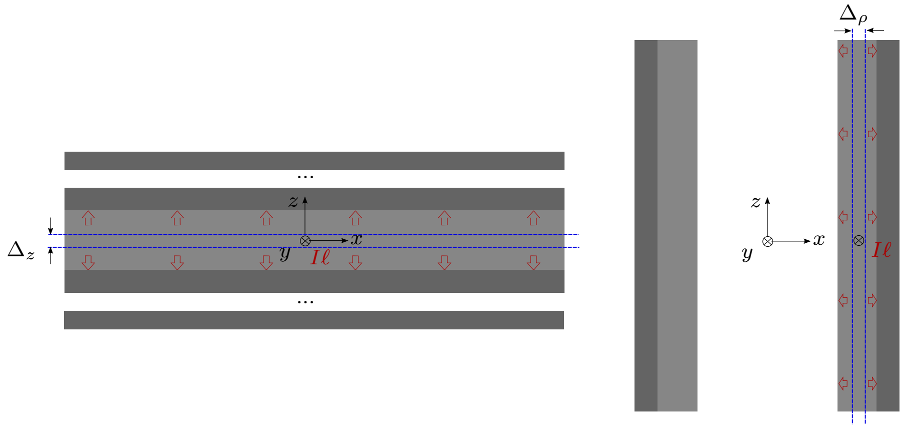

(a) (b)

Figure 5.4: Definition of the equivalent surface sources for the point-source field in the (a) cartesian, (b) cylindrical coordinate system.

cylindrical system the diffusion takes place in form of an inwards and an outwards moving field front. The two fronts are associated, following the approach developed in chapter 3, to an equal number of fictitious surfaces located at an infinitesimal distance from the source. For convenience, the point source is located at the zero of the tangential axes, that is at $(0, 0, z')$ and $(\rho', 0, 0)$, with $z'$ and $\rho'$ indicating the source position in the normal direction at each case. The respective expressions at any other point of the Huygens surfaces can be trivially obtained using the properties of the Fourier transform.

### 5.6.1 Calculation in the cartesian system

We consider a dipole electric source of unit magnitude along the $y$ direction. Following the usual TREE approach, the domain is truncated at $\pm L_x/2$ and $\pm L_y/2$ in order to obtain a discrete spectrum. We are seeking expressions for the $W_a$ and $W_b$ potentials, which, as already analysed, stand for the TE$_z$ and TM$_z$ solutions, respectively (we consider $\mathbf{e}_z$ as the pivot direction). These expressions can be easily derived from the corresponding field components along the $z$ directions since the two solutions separate there. We observe thus $\overline{\mathbf{G}}_0^{ee} \cdot \mathbf{e}_y$ and $\overline{\mathbf{G}}_0^{me} \cdot \mathbf{e}_y$ along $\mathbf{e}_z$

$$\mathbf{e}_z \cdot \overline{\mathbf{G}}_0^{ee} \cdot \mathbf{e}_y = -i\omega\mu \frac{\partial_z \partial_y}{k^2} g(\mathbf{x}, \mathbf{x}') \tag{5.37}$$

$$\begin{aligned} \mathbf{e}_z \cdot \overline{\mathbf{G}}_0^{me} \cdot \mathbf{e}_y &= \mathbf{e}_z \cdot \nabla \times [g(\mathbf{x}, \mathbf{x}')\, \mathbf{e}_y] \\ &= \nabla g(\mathbf{x}, \mathbf{x}') \cdot [\mathbf{e}_y \times \mathbf{e}_z] = \partial_x g(\mathbf{x}, \mathbf{x}') \,. \end{aligned} \tag{5.38}$$

where $\mu$ stands for the permeability of the layer.

The Weyl identity (3.41) for the discrete spectrum reads

$$g(\mathbf{x},\mathbf{x}') = \frac{1}{2N^2}\sum_{l=1}^{\infty}\sum_{p=1}^{\infty}\cos(\kappa_{x;l}x)\cos(\kappa_{y;p}y)\,\frac{e^{-v_{lp}|z-z'|}}{v_{lp}} \tag{5.39}$$

with $v_{lp} = \sqrt{\kappa_{x;l}^2+\kappa_{y;p}^2+k^2}$ and $N^2 = L_xL_y/4$ the normalisation constant. The development in cosine series along the $x$ and $y$ directions reflects the even parity of the Green's function. Applying (5.39) in (5.37),(5.38) yields for the observed components

$$\mathbf{e}_z\cdot\overline{\mathbf{G}}_0^{ee}\cdot\mathbf{e}_y = \mp\frac{i\omega\mu}{2N^2k^2}\sum_{l=1}^{\infty}\sum_{p=1}^{\infty}\kappa_{y;p}\cos(\kappa_{x;l}x)\sin(\kappa_{y;p}y)\,e^{\mp v_{lp}\left(z-z'\right)} \tag{5.40}$$

$$\mathbf{e}_z\cdot\overline{\mathbf{G}}_0^{me}\cdot\mathbf{e}_y = -\frac{1}{2N^2}\sum_{l=1}^{\infty}\sum_{p=1}^{\infty}\frac{\kappa_{x;p}}{v_{lp}}\sin(\kappa_{x;l}x)\cos(\kappa_{y;p}y)\,e^{\mp v_{lp}\left(z-z'\right)}. \tag{5.41}$$

The corresponding development on the Huygens surfaces for the $W_a$ and $W_b$ potentials reads

$$W_a(x,y,z) = \frac{1}{N}\sum_{l=1}^{\infty}\sum_{p=1}^{\infty}C_{a;lp}\cos(\kappa_{x;l}x)\sin(\kappa_{y;p}y)\,e^{\mp v_{lp}\left(z-z'\right)} \tag{5.42}$$

$$W_b(x,y,z) = \frac{1}{N}\sum_{l=1}^{\infty}\sum_{p=1}^{\infty}C_{b;lp}\sin(\kappa_{x;l}x)\cos(\kappa_{y;p}y)\,e^{\mp v_{lp}\left(z-z'\right)}. \tag{5.43}$$

We now recall (2.56), which relates the electric and magnetic field with the SOVP potentials (the state vector), and take its dot product with the $\mathbf{e}_z$

$$\begin{pmatrix} B_z \\ -E_z/i\omega \end{pmatrix} = \begin{pmatrix} \partial_z^2-\nabla^2 & 0 \\ 0 & \partial_z^2-\nabla^2 \end{pmatrix}\cdot\begin{pmatrix} W_a \\ W_b \end{pmatrix} \tag{5.44}$$

and by virtue of (2.62)

$$\begin{pmatrix} B_z \\ -E_z/i\omega \end{pmatrix} = \left(\partial_z^2-k^2\right)\begin{pmatrix} W_a \\ W_b \end{pmatrix}. \tag{5.45}$$

Comparison of (5.40),(5.41) with (5.42),(5.43) taking into account (5.45) implies for $C_{a;lp}$ and $C_{b;lp}$

$$C_{a;lp} = -\frac{2\mu}{N}\frac{\kappa_{x;p}}{v_{lp}\sqrt{v_{lp}^2-k^2}} \tag{5.46}$$

$$C_{b;lp} = \pm\frac{2\mu}{N}\frac{\kappa_{y;l}}{k^2\sqrt{v_{lp}^2-k^2}}. \tag{5.47}$$

It is recalled here that $\overline{\mathbf{G}}^{me}$ stands for a magnetic field, which means that has to be multiplied with the medium permeability in the $\mathbf{B}$ calculation.

As a control of the previous calculation, and for demonstrating an alternative way of calculating the source coefficients, we shall apply directly the continuity relations across the source plane. From (2.18),(2.20) we have

$$H_x^{(1)} - H_x^{(2)} = \delta(x)\,\delta(y) \tag{5.48}$$

$$H_y^{(1)} - H_y^{(2)} = 0 \tag{5.49}$$

$$E_x^{(1)} - E_x^{(2)} = 0 \tag{5.50}$$

$$E_y^{(1)} - E_y^{(2)} = 0 \tag{5.51}$$

where the index 1 signifies the solution in the upper layer, and 2 the solution in the lower layer. Substituting the field expressions from (2.56) and using the developments in (5.42),(5.43) for $W_a$ and $W_b$ and weighting with the corresponding trigonometric functions yields

$$-\kappa_{x;l} v_{lp} \left[C_{a:lp}^{(1)} + C_{a:lp}^{(2)}\right] + k^2 \kappa_{y,p} \left[C_{b:lp}^{(1)} - C_{b:lp}^{(2)}\right] = \frac{\mu}{N} \tag{5.52}$$

$$\kappa_{y;p} v_{lp} \left[C_{a:lp}^{(1)} + C_{a:lp}^{(2)}\right] + k^2 \kappa_{x,l} \left[C_{b:lp}^{(1)} - C_{b:lp}^{(2)}\right] = 0 \tag{5.53}$$

$$-\kappa_{y;p} \left[C_{a:lp}^{(1)} - C_{a:lp}^{(2)}\right] - \kappa_{x,l} v_{lp} \left[C_{b:lp}^{(1)} + C_{b:lp}^{(2)}\right] = 0 \tag{5.54}$$

$$-\kappa_{x;l} \left[C_{a:lp}^{(1)} - C_{a:lp}^{(2)}\right] + \kappa_{y,p} v_{lp} \left[C_{b:lp}^{(1)} + C_{b:lp}^{(2)}\right] = 0 \tag{5.55}$$

where we have used the orthogonality of the sine and cosine functions. Solving the system for $C_{a:lp}^{(1)}, C_{b:lp}^{(1)}, C_{a:lp}^{(2)}, C_{b:lp}^{(2)}$ we obtain the same values with (5.46),(5.47).

The calculation for the two remaining orientations follows the same pattern and will not be presented here.

### 5.6.2 Calculation in the cylindrical system

The dipole orientation is the azimuthal direction $\phi$ as shown in (5.4). Working in an analogous way with the cartesian system, we truncate the geometry along the $z$ axis at $\pm L_z/2$, and we develop the scalar Green's function in cylindrical coordinates using identity (3.59), which for the truncated region becomes

$$g(\mathbf{x}, \mathbf{x}') = \frac{1}{2N^2} \sum_{m=-\infty}^{\infty} \sum_{n=1}^{\infty} \begin{Bmatrix} K_m(v_n\rho')\, I_m(v_n\rho) \\ I_m(v_n\rho')\, K_m(v_n\rho) \end{Bmatrix} e^{im\phi} \cos(\kappa_n z) \tag{5.56}$$

where $v_n = \sqrt{\kappa_n^2 + k^2}$, and $N^2 = \pi L_z$ stands for the normalisation constant. The bracketed colon summarises the expressions for the inward and outward evanescent solution, respectively. The $E_z$ and $H_z$ components for this source will be given by

$$\mathbf{e}_z \cdot \overline{\mathbf{G}}_0^{ee} \cdot \mathbf{e}_\phi = i\omega\mu \frac{1}{\rho'} \frac{\partial_z \partial_\phi}{k^2} g(\mathbf{x}, \mathbf{x}') \tag{5.57}$$

$$\begin{aligned} \mathbf{e}_z \cdot \overline{\mathbf{G}}_0^{me} \cdot \mathbf{e}_\phi &= \mathbf{e}_z \cdot \nabla \times [g(\mathbf{x}, \mathbf{x}')\, \mathbf{e}_\phi] \\ &= \nabla g(\mathbf{x}, \mathbf{x}') \cdot [\mathbf{e}_\phi \times \mathbf{e}_z] = \partial_\rho g(\mathbf{x}, \mathbf{x}')\,. \end{aligned} \tag{5.58}$$

which upon substitution of (5.56) yields

$$\mathbf{e}_z \cdot \overline{\mathbf{G}}_0^{ee} \cdot \mathbf{e}_y = \frac{i\omega\mu}{2N^2k^2} \sum_{m=-\infty}^{m} \sum_{n=1}^{\infty} \frac{im}{\rho'} \kappa_n I_m(v_n\rho')\, K_m(v_n\rho)\, e^{im\phi} \sin(\kappa_n z) \tag{5.59}$$

$$\mathbf{e}_z \cdot \overline{\mathbf{G}}_0^{me} \cdot \mathbf{e}_y = \frac{1}{2N^2} \sum_{m=-\infty}^{m} \sum_{n=1}^{\infty} v_n I_m(v_n\rho')\, K'_m(v_n\rho)\, e^{im\phi} \cos(\kappa_n z) \tag{5.60}$$

for the outwards evanescent term, the corresponding expression for the inward term being obtained after exchanging $I_m$ with $K_m$.

The spectral representation for $W_a$ and $W_b$ in the cylindrical coordinate system admits the form

$$W_a(x, y, z) = \frac{1}{N} \sum_{m=-\infty}^{m} \sum_{n=1}^{\infty} C_{a;mn} \left\{ \begin{array}{c} I_m(v_n\rho) \\ K_m(v_n\rho) \end{array} \right\} e^{im\phi} \cos(\kappa_n z) \tag{5.61}$$

$$W_b(x, y, z) = \frac{1}{N} \sum_{m=-\infty}^{m} \sum_{n=1}^{\infty} C_{b;mn} \left\{ \begin{array}{c} I_m(v_n\rho) \\ K_m(v_n\rho) \end{array} \right\} e^{im\phi} \sin(\kappa_n z)\,. \tag{5.62}$$

Taking again (5.45) and comparing the resulting expressions with (5.59),(5.60), we finally obtain for the series coefficients $C_{a;l}$ and $C_{b;l}$

$$C_{a;mn} = -\frac{\mu}{2N} \frac{v_n}{\kappa_n^2} \left\{ \begin{array}{c} K'_m(v_n\rho) \\ I'_m(v_n\rho) \end{array} \right\} \tag{5.63}$$

$$C_{b;mn} = \frac{\mu}{2Nk^2} \frac{im}{\kappa_n\rho'} \left\{ \begin{array}{c} K_m(v_n\rho) \\ I_m(v_n\rho) \end{array} \right\}. \tag{5.64}$$

## 5.7 Calculation of the impedance variation: the reciprocity theorem

The mutual impedance variation due to the flaw is calculated using the above solution in an elegant way by application of the reciprocity theorem (2.69) after substitution of the equivalent sources expressing the material anomaly

$$\Delta Z(\mathbf{r}_s) = -\frac{1}{I_{Tx}I_{Rx}} \int\limits_{V_f} [\delta\sigma(\mathbf{r}')\, \mathbf{E}_{Rx;p}(\mathbf{r}';\mathbf{r}_s) \cdot \mathbf{E}_{Tx}(\mathbf{r}') \\ - i\omega\delta\mu(\mathbf{r}')\, \mathbf{H}_{Rx;p}(\mathbf{r}') \cdot \mathbf{H}_{Tx}(\mathbf{r}';\mathbf{r}_s)]\, dV' \tag{5.65}$$

where $\mathbf{E}_{Rx;p}$ and $\mathbf{H}_{Rx;p}$ stand for the primary electric and magnetic field that would be produced in the flawless medium if the receiver coil Rx would be fed with current $I_{Rx}$. $\mathbf{E}_{Tx}, \mathbf{H}_{Tx}$ is the field solution obtained by (5.13) and (5.14) with the transmitting coil being active and fed with current $I_{Tx}$. Note that the functional dependence of the latter to the probe position $\mathbf{r}_s$ is implicit stemming from the corresponding dependence of the transmitter field, and has not been given in (5.65) for simplicity. The functional dependence upon the angular frequency of all variables is also implied.

In case of direct magnetic field observations, (5.65) should be replaced by a calculation of the magnetic field at the probe position, namely the (5.14) with the suitable expressions for the Green's dyads $\overline{\mathbf{G}}^{em}$ and $\overline{\mathbf{G}}^{mm}$[3].

The reciprocity relation is also simplified accordingly

$$\Delta Z_{TR}^{(d)}(\mathbf{r}_s) = -\frac{1}{I_{Tx} I_{Rx}} \int\limits_{S_f} \mathbf{n} \cdot \mathbf{E}_{Rx;p}(\mathbf{r}'; \mathbf{r}_s)\, p_{Tx}(\mathbf{r}')\, dS'. \tag{5.66}$$

The interpretation of the Tx, Rx indices remain the same with above.

## 5.8 Case studies

The application of the integral method approach for the calculation of the defect response will be illustrated through two selected examples representative for the two considered problem classes: detection of volumetric defects and thin cracks.

### 5.8.1 Volumetric flaws in ferromagnetic tubes

In the first example we are dealing with volumetric flaws (usually produced by generalised corrosion or pitting) in ferromagnetic (steel) pipes. The early detection of such defects is a crucial problem for pipe inspection and maintenance since critical wall-thinning may lead to structure failure with obvious consequences for the safety of the installation and non-negligible financial impact. Typical applications include pipeline and casing inspection in the oil and gas industry as well as NDT of heat-exchangers and condensers in power plants.

The main challenge with steel tubes stems for the weak penetration of the eddy currents due to the very small skin depth in ferromagnetic materials, a rough estimation of which is given by the approximate formula

$$\delta = \sqrt{\frac{2}{\omega\sigma\mu}}. \tag{5.67}$$

With a typical relative permeability value between 100 and 1000 for common industrial steel grades, it is obvious that the achieved skin depth is of the order of 10% compared with that obtained in non-magnetic metals. Given that the inspection is usually carried out from the interior of the tube, for obvious practical reasons, the previous numbers signify an important difficulty in locating external corrosion before it surpasses the alert limits.

An intuitive way out to this problem is to decrease the frequency, which comes however at the expense of the probe sensitivity (recall that coil impedance

---

[3] For a multilayer medium, like the ones considered in this class of problems, the Green's dyads expressions are different when source $\mathbf{r}'$ and $\mathbf{r}$ are located in different layers. This is the case for the observation equation, where the source (defect) lies in the medium whereas the observation is carried out in the air.

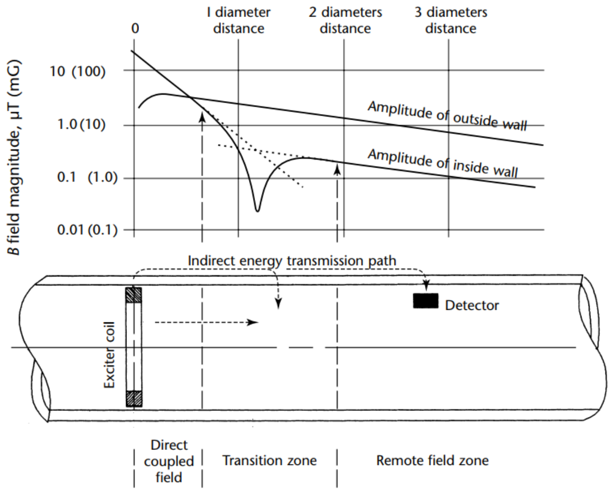

Figure 5.5: Eddy-current inspection of a ferromagnetic tube using a REFC probe. We distinguish three different zones: (a) near-field zone ($z_{obs} \leq 1$ ID), (b) transition zone (1 ID $< z_{obs} <$ 2 ID), and (c) far-field zone (2 OD $\leq z_{obs}$). Plot reproduced from [60]

is proportional to the frequency) and the resolution. A more intelligent way to increase sensitivity to external defects is to design the probe in such way that the ratio of the indirect transmitter-receiver coupling (coupling via the interaction with the tube walls) to the direct coupling is maximised. This is the main idea of the so-called remote field eddy-current (RFEC) testing technique [60–66].

The working principle is schematically explained in 5.5. The direct coupling is linked to the field propagation inside the tube, along which the field is attenuated rapidly by the circumferential eddy currents induced in the tube's wall. This part is dominant up to a distance that roughly equals the inner diameter (ID) of the tube, and is referred to as the direct field zone ($z_{obs} \leq 1$ ID). The indirect coupling mechanism consists in field radial diffusion outwards through the wall subjected to attenuation and phase-shift along the axial direction. Being diffused through the wall, it is easily understood that it carries information about the tube wall. This term decreases less rapidly that the direct part, and hence it becomes dominant at a distance greater than twice the tube ID ($z_{obs} \geq 2$ ID). This latter is the so-called remote field zone, and is the zone where we aim for placing the receiver coil. The intermediate zone (1 ID $< z_{obs} <$ 2 ID) is called the transition zone. A detailed account of the method can be found in [60, 64].

For this study, we shall use reference data acquired in CEA Saclay using a heat exchanger prototype of a fast neutron reactor. The specimen is a steel pipe with inner and outer diameters of 14 mm and 18 mm, respectively. The conductivity and relative permeability have been measured as 6.25 MS/m and 210, respectively, at 250 Hz operating frequency. The measured values correspond to the planar skin depth of 0.88 mm, which is less than half of the tube wall.

Two kinds of defects have been considered, a series of 3 mm wide external grooves, with depths of 20%, 40% and 70% of the tube thickness, and several circular cylindrical through-holes (100% deep) with a diameter of 5 mm each. The grooves have been realized by mechanical thinning, and the holes either by mechanical drilling or by electrical discharge machine (EDM). All the defects have been manufactured sufficiently afar to each other in order to avoid any mutual interaction.

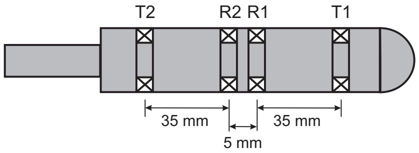

Figure 5.6: Double driving coil RFEC probe.

The layout of the RFEC probe used in the experiment is displayed in Fig. 5.6. It consists of two driving coils (T1, T2) connected in additive mode (for achieving field amplification in the inspected regions) and of two receiving coils (R1, R2) operating in differential mode. The receiving coils are placed in the remote field region (their distance from the driving coils is larger than twice the inner diameter of the tube). All the coils have the same dimensions. Their inner and outer diameter are 6.8 mm and 12.8 mm respectively, and their length is 3 mm. The number of turns is not relevant since all results are calibrated for comparison.

The probe is displaced in the axial direction past the defect positions, and the voltage difference at the terminal of the receiver coils is recorded, which represents a typical inspection scenario. The VIM has been employed for the solution of the flaw response, and the output voltage has been calculated using (5.65).

To achieve a convergent numerical solution, a number of 200 unknowns (per field component) has been used for the grooves (axisymmetric defects) and 1089 for the holes (3D-bounded defects), 161 scanning positions of the probe along the tube axis being chosen each time, with a scanning step of 1 mm.

The thus computed signals are compared against the measurements in Fig. 5.7. The flaw signals are represented in the complex plane, that is the imaginary vs. the real part for each point of the scan, which is the standard way of representing ECT signals. The down left boxes indicate two typical measures commonly used for the defect characterisation: the distance between the two curve extremes (magnitude of the signal) and the angle of the peak-to-peak axis from the abscissa (referred as phase). Both experimental and synthetic results have been calibrated using the corresponding responses for a 40% deep groove.

A second comparison is provided in Fig. 5.8 for the hole signal. The agreement here is clearly less satisfactory, yet the discrepancies remain acceptable

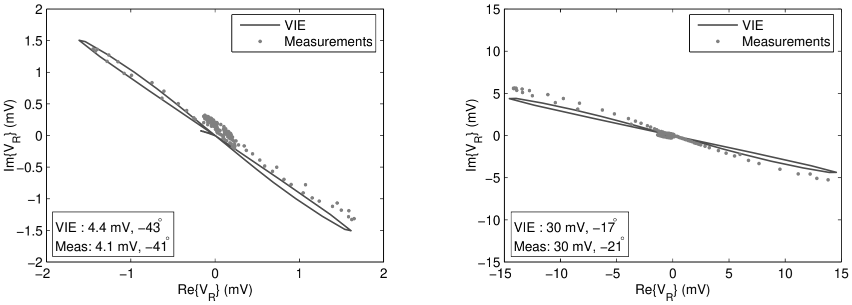

(a) (b)

Figure 5.7: Simulation vs. measured data for the receiver voltage variation in the complex plane. Results for the (a) 20% deep outer groove (a) 70% deep outer groove.

given the significant incertitude in the knowledge of the nominal permeability value. It is well known that the magnetic permeability depends on a number of factors. Notably the piece history (remanence, mechanical stresses, fabrication process) is never known exactly. Besides, the same fabrication of the flaw in the examined specimen can have an effect on its value, in the vicinity of the affected area. As a demonstration to that, one has compared in Tab. 5.1 the amplitude and phase of the measured signals obtained using two holes which have been fabricated using a different technique, i.e., mechanical drill, EDM. From the comparison of the signals, it is concluded that the fabrication technique appears to have an important impact on the results. In an explanation attempt, one may assume that the presence of residual stresses, local warming, or even change of the metallurgical properties (when EDM is applied) of the tube in the vicinity of the defect result in a local uncharted change of the value of the magnetic permeability in that area, whose exact value cannot be supplied to the numerical model.

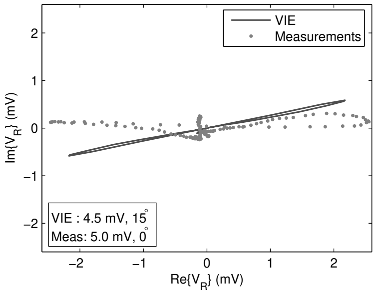

Figure 5.8: Simulation vs. measured data for the through-hole.

| | Ampl. (mV) | Phase (°) |
|---|---|---|
| EDM | 5.0 | 0 |
| Drilling | 4.2 | 6 |
| Simul. | 4.5 | 15 |

Table 5.1: Simulation vs. measured data for the through-hole.

### 5.8.2 Crack response in the vicinity of a rivet hole

An important ECT application in the aerospace industry is the structural integrity assessment of riveted structures in the aircraft fuselage. Rivets serve as fixation points attaching the aluminium multilayer structures of the fuselage together. Due to mechanical stress concentration at these regions, the rivet holes are prone to the appearance and propagation of fatigue cracks. The role of NDT here is to provide an early indication of crack generation, which is a challenging task given that the crack signature needs to be distinguished from the fastener signal itself. The use of simulation becomes thus very important for the processing and the interpretation of the acquisition signals.

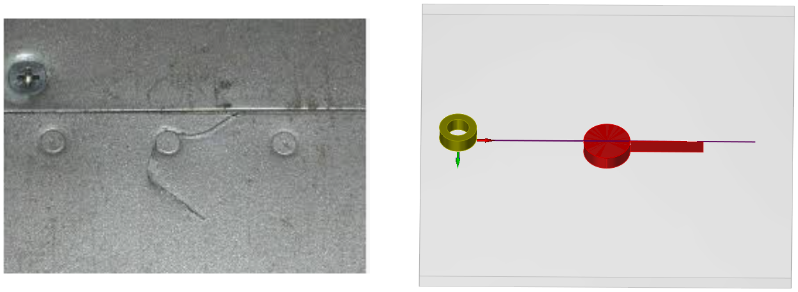

(a) (b)

Figure 5.9: (a) Fastener affected by a double fatigue crack. (b) Fastener inspection using an air-cored coil. The scan is performed from above. A straight narrow crack is assumed attached to the fastener hole.

An illustration of a real-world situation is provided in Fig. 5.9a, where an aircraft fastener is affected by a double crack. There are in general two inspection modes for this kind of applications. The first consists in removing the bolt from the rivet hole and performing the control from the interior of the hole using a specially designed probe [67, 68, 68]. The second mode is less laborious since it does not necessarily require the removal of the bolt and consists in passing the probe above the piece [69–73], but it produces more complicated signals.

The second configuration, which is schematically depicted in Fig. 5.9b, will be the object of this particular study. The inspection probe consists of a single air-cored coil, which scans the surface at a constant lift-off. The host material is non-magnetic. Although the model is valid for multilayer media, we shall restrict ourselves in this study to a single-layer riveted aluminium plate with a cylindrical hole. The hole will be considered without bolt, which again is a simplification made for convenience and not due to model limitations. A linear crack is initiated by the hole extending radially at a certain length.

The greatest challenge of this specific geometry stems from the presence of the hole, whose effect can be taken into account using two alternative strategies. The more straight-forward approach is to treat the hole as a volumetric defect and solve a coupled VIM-SIM problem. This approach has been explored by

Miorelli et al. in [57, 74]. Its main drawback is that the relative large volume of the hole (with respect to the crack) leads to a computationally demanding formulation. The second strategy consists in accounting for the hole discontinuity during the calculation of the primary field and Green's operator; and proceed to a simple SIM formulation limited to the crack surface. In the latter case, (5.18) is used for the calculation of the equivalent dipole distribution throughout the crack surface for each probe position, and the result is then substituted in (5.66) to evaluate the probe signal. Although theoretically more elaborate, the second approach offers much shorter computation times, as it will become clear by the numerical comparisons below.

For the calculation of the primary field and the construction of Green's function the adopted solution strategy is the one presented in chapter 4, where the problem is treated in two steps. In particular, the field is calculated first in an infinite multilayer medium, and this solution is then propagated to the cylindrical interface defined by the hole radius, where it is matched with the field solution for the air-column of the hole. The schematic illustration of this approach is provided in Fig. 5.10.

The calculations have been carried out for two geometries, whose parameters are given in Tab. 5.2 and Tab. 5.4.

| Coil | | Piece | |
|---|---|---|---|
| Inner diameter | 6 mm | Conductivity | 10 MS/m |
| Outer diameter | 9.3 mm | Thickness | 2 mm |
| Length | 4 mm | Hole diameter | 6.25 mm |
| Turns | 336 | Crack | |
| Lift-off | 0.5 mm | Length | 9.8 mm |
| | | Depth | 2 mm |
| | | Opening | 0.1 mm |

Table 5.2: Configuration of the first problem.

The computational results for the first problem obtained using the SIM approach with dedicated Green's kernel are compared against the simulation results of the VIM-SIM approach [74]. The comparison for the impedance variation signal (real and imaginary part) throughout the scan line is given in Fig. 5.11.

The computation time for the SIM method is reduced to 420 s compared with the VIM-SIM method for which the simulation time reaches 660 s for a computer with an Intel Core i7 at 2.93 GHz CPU and 8 Gb RAM. However, the difference in terms of computation time between the two models depends on several parameters. It is reminded that there is no need for SIM to discretize the borehole as VIM-SIM does. Hence, the performance difference between the two approaches increases with the size of the borehole. Similar effect have the size of the coil and the operation frequency, whose impact upon the flaw discretisation results in an unequal increase/decrease the computational burden for the two

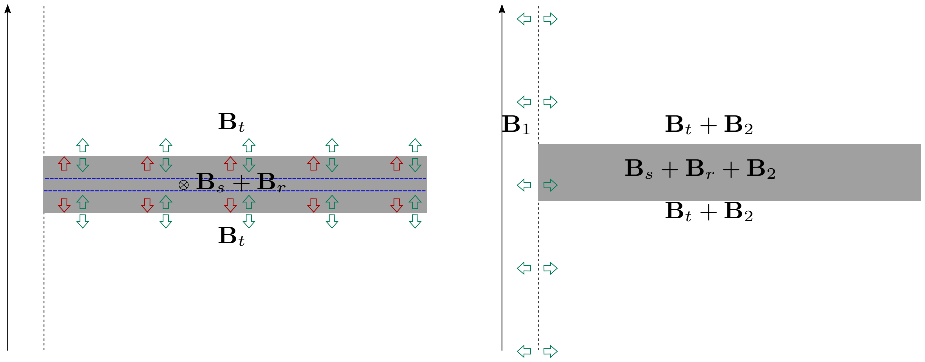

(a) (b)

Figure 5.10: Solution strategy for the construction of Green's function in the riveted hole. (a) Point source in an infinite layered medium. (b) Accounting for the perturbation from the hole surface.

approaches [40].

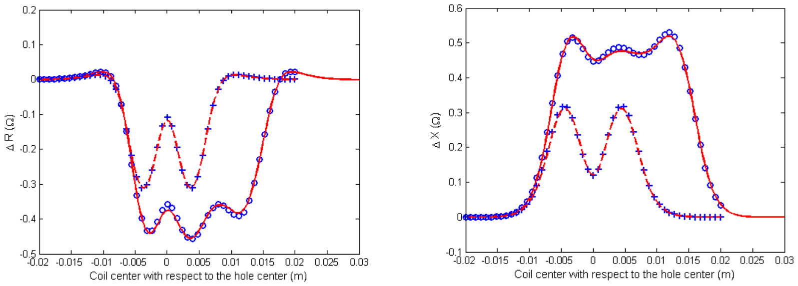

(a) (b)

Figure 5.11: Impedance variation versus coil position along a scan line passing above the borehole and the crack (configuration of Table I). The impedance change is given with respect to the value above an infinite plate. The coil is excited at 4 kHz. The total signal simulated with VIM-SIM (circles) and SIM (solid line) and the hole signal as calculated with VIM-SIM (crosses) and SIM (dashed line) are illustrated. (a) Real part. (b) Imaginary part.

The second configuration is the world federation of NDE centers (WFNDEC) benchmark problem [47]. The problem parameters are given in Tab. 5.4.

The SIM simulation results have been compared with measured data for the coil impedance and the comparison for the real and imaginary part is provided in Fig. 5.12.

It is clear from both Fig. 5.11 and Fig. 5.12 that the total signal (due to both crack and rivet hole) cannot be interpreted as a mere superposition of the two signatures; the presence of the defect changes significantly the hole signal

| Coil | | Piece | |
|---|---|---|---|
| Inner diameter | 12 mm | Conductivity | 17.34 MS/m |
| Outer diameter | 24 mm | Thickness | 2 mm |
| Length | 4 mm | Hole diameter | 10 mm |
| Turns | 1650 | Crack | |
| Lift-off | 1.08 mm | Length | 9.8 mm |
| | | Depth | 2 mm |
| | | Opening | 0.234 mm |

Table 5.3

Table 5.4: WFNDEC benchmark problem parameters.

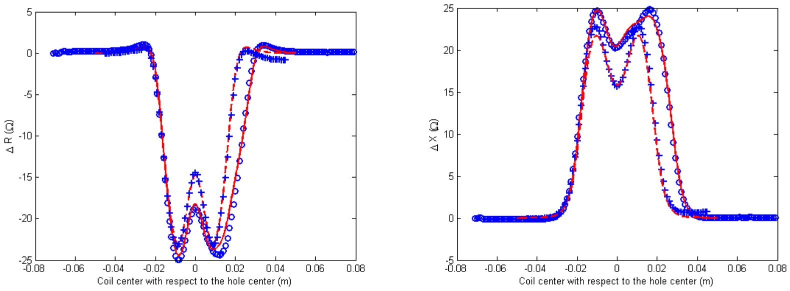

(a) (b)

Figure 5.12: Theoretical and measured data for the impedance variation versus coil position for the configuration of Tab. 5.4. The coil is operated at 1 kHz. The total measured signal (circles) and the one simulated with SIM (solid line) as well as the hole signal given by measurements (crosses) and by SIM (dashed line) are shown. (a) Real part. (b) Imaginary part.

even at the antipodal side. Indeed, the presence of the two perturbation results in a compound eddy-current path which is not easy to anticipate in an intuitive manner. It is the role of simulation to shed light to the effect, and support in this way the interpretation of the results.

## 5.9 Calculation of the defect response using global bases

We now shift to the case where the material anomaly is not localised in a small region but it is spread in a wide part of the piece. In this case, the integral equation approach can fastly become inefficient, since the number of degrees of freedom (DOF) increase rapidly with the defect volume. This increase in conjunction with the full-matrix feature of the integral equation approach can lead to prohibitive computation times.

In these cases, a more efficient approach could be devised based on augmented spectral bases, which are eigensolutions of the Helmholtz operator. The use of such bases not only reduces the number of unknowns, but additionally diagonalises the system of equations, making its inversion almost instantaneous. To the downsides of the method, one should count the difficulties with the abrupt discontinuities of the material constants (Gibbs effect), which is exactly the case we encounter when dealing with cracks of localised corrosion defects (e.g. pitting). The two approaches (the integral equation and the spectral method) can thus be considered as complementary.

It has been demonstrated in 5.2 that the effect of the material anomaly can be modelled via an equivalent electric $\mathbf{J}_e$ and an equivalent magnetic $\mathbf{J}_m$ source current density distribution as defined in (5.7),(5.8).

For the following derivations, we shall restrict the analysis to the 2D case only. According to the discussion of chapter 2, our first concern is to scalarise the problem with the use of an appropriate potential, and the most suitable candidate in this case is the magnetic vector potential $\mathbf{A}$. Nonetheless, the presence of magnetic currents complicates the analysis. To clarify this point, let us write the first two Maxwell equations with an electric and a magnetic current density

$$\nabla \times \mathbf{E} = -i\omega \mathbf{B} - \mathbf{J}_m \tag{5.68}$$

$$\nabla \times \mathbf{H} = \sigma \mathbf{E} - \mathbf{J}_e \tag{5.69}$$

With the standard definition of $\mathbf{A}$ given by (2.41) it is not possible to establish a simple relation between $\mathbf{E}$ and $\mathbf{A}$ as we did in 2.4.2. Observing from (5.68) that $\mathbf{J}_m$ must be necessarily divergence-free, we can modify the $\mathbf{A}$ definition as follows

$$\mathbf{B} = \nabla \times \mathbf{A} - \frac{1}{i\omega}\mathbf{J}_m \tag{5.70}$$

which is in accordance with the Gauss equation $\nabla \cdot \mathbf{B} = 0$. Using the new definition for $\mathbf{A}$, it turns out that $\mathbf{E} = -i\omega\mathbf{A}$ as in the source-free case, and upon substitution to (5.68),(5.69) we arrive at the following state equation

$$\nabla \times \nu \nabla \times \mathbf{A} + i\omega\sigma\mathbf{A} = \mathbf{J}_e + \frac{1}{i\omega}\nabla \times \nu \mathbf{J}_m. \tag{5.71}$$

To verify the compatibility of the above definition with the equivalent sources definition, let us substitute the equivalent currents $\mathbf{J}_e$ and $\mathbf{J}_m$ by their definition relations for the perturbed medium (5.7),(5.8). We can thus write successively

$$\begin{aligned}\nabla \times \nu_b \nabla \times \mathbf{A} + i\omega\sigma_b\mathbf{A} &= \mathbf{J}_s - i\omega\delta\sigma\mathbf{A} + \frac{1}{i\omega}\nabla \times \nu_b\left(i\omega\delta\mu\mathbf{H}\right) \\ &= \mathbf{J}_s - i\omega\delta\sigma\mathbf{A} + \nabla \times \nu_b\frac{\delta\mu}{\mu}\nabla \times \mathbf{A}\end{aligned} \tag{5.72}$$

with $\mathbf{J}_s$ the real current density of the coil, $\nu_b$ the reluctivity of the flawless medium, $\mu$ the total permeability, and $\delta\sigma, \delta\mu$ the conductivity and permeability variation owing to the anomaly. Notice that (5.72) assumes a medium **without magnetic sources** since the equivalent sources have now been replaced by field quantities, i.e. we have returned to the original problem, and hence $\mathbf{B} = \nabla \times \mathbf{A}$. Bring all terms involving $\mathbf{A}$ to the left-hand side, we obtain

$$\nabla \times \nu_b \left(1 - \frac{\delta\mu}{\mu}\right) \nabla \times \mathbf{A} + i\omega\left(\sigma_b + \delta\sigma\right)\mathbf{A} = \mathbf{J}_s \tag{5.73}$$

and consequently

$$\nabla \times \frac{1}{\mu} \nabla \times \mathbf{A} + i\omega\sigma\mathbf{A} = \mathbf{J}_s \tag{5.74}$$

which is the relation we wanted to show.

Assuming now that the sources $\mathbf{J}_e$ and $\mathbf{J}_m$ are known, we need to develop a method for the calculation of the potential $\mathbf{A}$. This solution will be useful not only for addressing the problem of a piece with a flaw but also for the calculation of the transient response as well as the treatment of non-linear magnetic materials. Both problems will be studied in the following chapters, where this link will become more clear.

If the base material is piecewise homogeneous, (5.71) can be converted to the inhomogeneous Helmholtz equation using standard manipulations

$$\left(\nabla^2 - k^2\right)\mathbf{A} = -\mu_b \mathbf{J}_e - \frac{1}{i\omega} \nabla \times \mathbf{J}_m. \tag{5.75}$$

The problem now reduces to solving (5.75) with a non-zero right-hand side. The solution of (5.75) using global (spectral) bases will be demonstrated via a problem of great practical importance: the eddy-current inspection of a planar specimen by a cylindrical coil.

## 5.10 Solution of the inhomogeneous Helmholtz equation for the 2D planar problem

We are interested in solving (5.75) for situations like the one depicted in Fig. 5.13. As long as the volumetric sources inside the plate do not break the rotational symmetry of the configuration, the problem can be treated as a 2D axisymmetric one. This is the case for defects like generalised corrosion or pitting with crater-like shape. Further, this condition is also fulfilled when treating the transient problem and non-linear isotropic materials with axisymmetric excitation, as will be discussed in the next chapters.

Introducing the standard ansatz for the magnetic vector potential $\mathbf{A} = A\mathbf{e}_\phi$ (cf. chapter 2) the inhomogeneous Helmholtz equation admits the following scalar form

$$\left(\nabla^2 - \frac{1}{\rho^2} - k^2\right) A(\rho, z) = -\mu_b J_e(\rho, z) - \frac{1}{i\omega} \mathbf{e}_\phi \cdot \nabla \times \mathbf{J}_m(\rho, z) \tag{5.76}$$

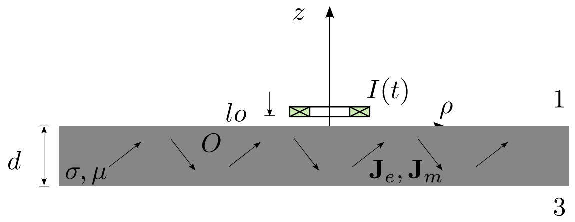

Figure 5.13: Conducting plate inspected via a cylindrical coil on its top. The plate contains an electric current source distribution, which satisfies the same symmetry condition as the excitation field.

where we have assumed for the sources

$$\begin{aligned}\mathbf{e}_\phi \times \mathbf{J}_e &= 0\\ \mathbf{e}_\phi \cdot \mathbf{J}_m &= 0.\end{aligned}$$

For the solution of (5.76), we shall adopt the same strategy used in [75, 76]. The solution to the inhomogeneous equation is decomposed into a partial solution, which eliminates the right-hand side term, and the solution of the homogeneous equation, which takes care of the current excitation and assures the fulfilment of the continuity relations across the geometry interfaces.

Following the TREE approach, the solution domain is truncated at an adequate radial distance $\rho_L$, and a perfect electric conductor (PEC) condition (or equivalently a Dirichlet condition for the $A$ potential. The general expression for the magnetic potential in the two air regions, above and beneath the plane, reads[4]

$$A^{(1)}(\rho, z) = \frac{\sqrt{2}}{\rho_L J_0(\kappa_n \rho_L)} \sum_{n=1}^{\infty} J_1(\kappa_n \rho) \left[ C_n^{(1)} e^{\kappa_n z} + D_n^{(s)} e^{-\kappa_n z} \right] \tag{5.77}$$

and

$$A^{(3)}(\rho, z) = \frac{\sqrt{2}}{\rho_L J_0(\kappa_n \rho_L)} \sum_{n=1}^{\infty} C_n^{(3)} J_1(\kappa_n \rho)\, e^{\kappa_n v_n (z-d)} \tag{5.78}$$

respectively. $D_n^{(s)}$ stands for the development coefficients for the coil field in the unbounded medium, and it is hence known. The $\kappa_n$ eigenvalues are determined by the zero tangential potential condition imposed by the PEC boundary at $\rho_L$, and are obtained by the roots of the Bessel functions

$$J_1(\kappa_n \rho_L) = 0, \qquad n = 1, 2, \ldots, \infty. \tag{5.79}$$

Inside the plate, we must address the inhomogeneous Helmholtz equation. The general solution can be expressed as the superposition of the homogeneous

---

[4] For this section as well as for the following derivations in the TD and the non-linear problem we shall prefer the explicit modal expressions to the more abstract propagator formalism presented in the previous chapters to avoid unnecessarily charged notation.

solution and a special solution, which satisfies the right-hand side term [39, 76]

$$A^{(2)}(\rho, z) = A^{(h)}(\rho, z) + A^{(s)}(\rho, z) \tag{5.80}$$

The homogeneous solution can be developed in an eigenfunction basis of the Laplace operator spanning the $(\rho, \phi)$ subspace, as it has been excessively discussed in the present text yielding

$$A^{(h)}(\rho, z) = \frac{\sqrt{2}}{\rho_L J_0(\kappa_n \rho_L)} \sum_{n=1}^{\infty} J_1(\kappa_n \rho) \left[ C_n^{(2)} e^{v_n z} + D_n^{(2)} e^{-v_n (z-d)} \right] \tag{5.81}$$

with $v_n^2 = \kappa_n^2 + k^2$ and the exponential functions standing for the propagator in the $z$ direction.

Since the modal basis used for the development of the homogeneous solution belongs to the kernel of the Helmholtz operator (ker $\left[\nabla^2 - k^2\right]$), it must be complemented with a $z$-dependent term to express the special solution, whose image is orthogonal to the kernel subspace [76, 77]. A suitable eigenbasis for this development is the two-dimension Fourier basis in the $(\rho, \phi)$ subspace

$$w_{nl}(\rho, z) := \frac{2}{\rho_L J_0(\kappa_n \rho_L) \sqrt{d}} J_1(\kappa_n \rho) \sin(q_l z) \tag{5.82}$$

with the $q_l$ eigenvalues being obtained by the zero field condition at the plate interfaces, namely

$$q_l = \frac{l\pi}{d}, \qquad l = 1, 2, \ldots, \infty. \tag{5.83}$$

It can be easily verified that $w_{nl}$ is an eigenfunction of the Laplacian, namely

$$\nabla^2 w_{nl} = -\left(\kappa_n^2 + q_l^2\right) w_{nl} \tag{5.84}$$

to which we associate the inner product

$$\langle w(\rho, z)\,, f(\rho, z)\rangle := \int_0^{\rho_L} \int_{-d}^{0} \rho J_1(\kappa_n \rho) \sin(q_n z)\, f(\rho, z)\, d\rho dz. \tag{5.85}$$

Since the solution does not satisfy any symmetry property along $z$, the full Fourier basis must be used with period slightly larger than $d$ (given that a Fourier series describes a periodic function). Such choice, however, would suffer from the Gibbs effect at the plate boundaries. Another possible choice would be to replace the sine series in (5.82) with a sine-cosine series. This option, however, would unnecessarily double the number of DOF whereas only two additional DOF are needed.

The general idea here is to split the special solution into two terms: one satisfying zero boundary conditions at the plate interfaces, and a second term accounting for the, in general nonzero, field value at those interfaces. This representation is schematically explained in Fig. 5.14.

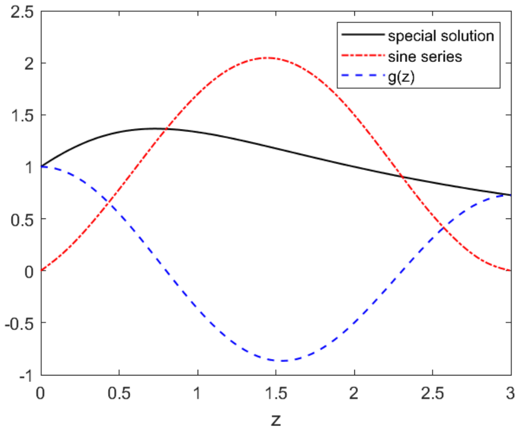

Figure 5.14: Representation of an arbitrary function as a sum of a sine series and a residual term.

The $w_{nl}$ basis must be thus complemented by a set of terms allowing to account for the nonzero value at the plate interfaces. Let $w_{nl}^{(0)}$ be this term

$$w_{nl}^{(0)}(\rho, z) \coloneqq \frac{2}{\rho_L J_0(\kappa_n \rho_L)} J_1(\kappa_n \rho)\, g_n(z) \tag{5.86}$$

We are free to choose the form of the $g_{nl}(z)$ with the condition that it contains a sufficient number of DOF in order to account for the field values at $z = 0$ and $z = -d$. These conditions are easily met by any polynomial of degree greater than 0. Another possible choice is

$$g_{nl}(z) = \begin{cases} \cos(q_l z)\,, & n = 1, 2 \\ 0, & n > 2 \end{cases} \tag{5.87}$$

with $q_l$ being given by (5.83). The latter choice is adopted here since it leads to slightly simpler equations.

By the way that it has been constructed, $w_{nl}^{(0)}$ also satisfies (5.84) (a polynomial term for the $z$ direction would correspond to zero $q_l$). Since it has been introduced to account for the potential value at the boundary, it will be associated with an inner product at the surfaces $z = 0, -d$

$$\langle w^{(0)}(\rho, z)\,, f(\rho, z)\rangle_S \coloneqq \cos(q_n z_S) \int\limits_0^{\rho_L} \rho J_1(\kappa_n \rho)\, f(\rho, z_S)\, d\rho. \tag{5.88}$$

with $z_S$ the $z$ coordinate of the surface. From (5.88) it turns out that $w^{(0)}$ are orthogonal with respect to the given inner product. The special solution is thus developed as

$$A^{(s)}(\rho, z) = \sum_{n=1}^{\infty}\sum_{l=1}^{\infty}\left[c_{nl}w_{nl}(\rho, z) + d_{nl}w_{nl}^{(0)}(\rho, z)\right]. \tag{5.89}$$

### 5.10.1 Application of the update equation: special solution calculation

Substituting (5.80) into (5.76), $A^{(h)}$ vanish by construction leaving

$$\begin{aligned}&\sum_{n=1}^{\infty}\sum_{l=1}^{\infty}\left(v_n^2 + q_l^2\right)\left[c_{nl}w_{nl}(\kappa_n\rho) + d_{nl}w_{nl}^{(0)}(\kappa_n\rho)\right] \\ &= \mu_b J_e(\rho, z) + \frac{1}{i\omega}\mathbf{e}_\phi \cdot \nabla \times \mathbf{J}_m(\rho, z).\end{aligned} \tag{5.90}$$

The $d_{nl}$ coefficients are easily obtained by observing (5.90) at the two plate interfaces (thus the first term vanishes) and weighting the two sides of the equation by $w_{nl}^{(0)}$ taking the orthogonality property into account

$$d_{nl} = \frac{\langle w_{nl}^{(0)}, f_{src}\rangle_{z=0} + (-1)^l\langle w_{nl}^{(0)}, f_{src}\rangle_{z=-d}}{2\left(v_n^2 + q_l^2\right)}, \left\{\begin{matrix} n = 1, \dots, \infty \\ l = 1, 2\end{matrix}\right\}. \tag{5.91}$$

$f_{src}(\rho, x)$ packs the two current terms together, i.e.

$$f_{src}(\rho, x) = \mu_b J_e(\rho, z) + \frac{1}{i\omega}\mathbf{e}_\phi \cdot \nabla \times \mathbf{J}_m(\rho, z).$$

Having evaluated $d_{nl}$, we can move this term to the right-hand side of (5.90) and weight both terms with the Laplace operator's eigenfunctions $J_1(\kappa_m\rho)\sin(q_n z)$ thus obtaining

$$c_{nl} = \frac{1}{v_n^2 + q_n^2}\left[\mu_b\langle w_{nl}, J_e\rangle + \frac{1}{i\omega}\langle w_{nl}, \mathbf{e}_\phi \cdot \nabla \times \mathbf{J}_m\rangle\right],\ n = 1, \dots, \infty. \tag{5.92}$$

Recalling that $\mathbf{e}_\phi \cdot \nabla\times$ is hermitian ($w_{nl}$ satisfies a Dirichlet BC at the plate interfaces and the truncation boundary), the last relation can also be written

$$\begin{aligned} c_{nl} &= \frac{\mu_b}{v_n^2 + q_n^2}\left[\langle (w_{nl}\mathbf{e}_\phi), \mathbf{J}_e\rangle + \frac{1}{i\omega\mu_b}\langle \nabla \times (w_{nl}\mathbf{e}_\phi), \mathbf{J}_m\rangle\right] \\ &= \frac{\mu_b}{v_n^2 + q_n^2}\left[\langle \mathbf{E}_{nl}^*, \mathbf{J}_e\rangle + \frac{1}{i\omega\mu_b}\langle \mathbf{B}_{nl}^*, \mathbf{J}_m\rangle\right]. \end{aligned} \tag{5.93}$$

$\mathbf{E}_{nl}^*$ and $\mathbf{B}_{nl}^*$ can be seen as adjoint electric and magnetic fields associated to the testing basis. This last form of (5.93) permits a physical interpretation of the special solution as the mixing (cross-diagonal) terms occurred by the perturbation of the medium properties. Indeed, recalling definitions (5.7) and (5.8), (5.93) becomes

$$c_{nl} = \frac{\mu_b}{v_n^2 + q_n^2}\left[\langle \mathbf{E}_{nl}^*, \delta\sigma\mathbf{E}\rangle + \langle \mathbf{H}_{nl}^*, \delta\mu\mathbf{B}\rangle\right] \tag{5.94}$$

with $\mathbf{H}_{nl}^* = \nu_b\mathbf{B}_{nl}^*$.

### 5.10.2 Application of the continuity relations: homogeneous solution calculation

The development coefficients of the homogeneous solution $C_n^{(1)}, C_n^{(2)}, D_n^{(2)}$ and $D_n^{(3)}$ are determined by the application of the continuity relations at the interfaces of the geometry. We have two conditions which the solution must satisfy: the continuity of the magnetic potential and its normal derivative. Hence, at the $z = 0$ interface we have

$$A^{(1)}\Big|_{\rho_1} = A^{(2)}\Big|_{\rho_1} \tag{5.95}$$

$$\frac{\partial A^{(1)}}{\partial z}\Big|_{\rho_1} = \frac{1}{\mu_r}\frac{\partial A^{(2)}}{\partial z}\Big|_{\rho_1} \tag{5.96}$$

and similarly for $z = -d$.

Substituting the expressions (5.77)-(5.80) and weighting with $J_1(\kappa_n \rho)$, we obtain for $z = 0$

$$C_n^{(1)} + D_n^{(s)} = C_n^{(2)} + D_n^{(2)} + \sum_{l=1}^{2} d_{nl} \tag{5.97}$$

$$\mu_r \kappa_n \left[C_n^{(1)} - D_n^{(s)}\right] = v_n \left[C_n^{(2)} - D_n^{(2)}\right] + \sum_{l=1}^{\infty} q_l c_{nl}. \tag{5.98}$$

In the same fashion the continuity relations at $z = -d$ yield

$$C_n^{(3)} = C_n^{(2)} + D_n^{(2)} + \sum_{n=1}^{2} (-1)^l d_{nl}. \tag{5.99}$$

$$\mu_r \kappa_n C_n^{(3)} = v_n \left[C_n^{(2)} - D_n^{(2)}\right] + \sum_{l=1}^{\infty} (-1)^l q_l c_{nl}. \tag{5.100}$$

It is tempting to associate the homogeneous part of the solution described by (5.77)-(5.80) to the reflection part of the (integrated) dyads in (5.33),(5.34) etc. whereas the special solution calculated by (5.94) corresponds to the direct part of the dyads.

The solution to the problem is obtained by solving (5.97)-(5.100) satisfying in parallel the special solution coefficients relations (5.91) and (5.92). The two sets of equations (for the homogeneous and the special solution) can be compiled in a system of equations and solved simultaneously, or they can be computed in an iterative scheme. This latter option will be explored in chapter 6 and chapter 8.

### 5.10.3 Source field

In the previous development, the field of the source coil in the air, represented in the modal solution via the coefficients $D_n^{(s)}$ has been considered as known. These coefficients are determined using the standard approach described in section 5.6 yielding

$$D_n^{(s)} = -\frac{2\mu_0 N}{(r_2 - r_1)\, h} \sinh\!\left(\frac{\kappa_n h}{2}\right) \frac{\chi(\kappa_n r_1, \kappa_n r_2)}{\kappa_n^5 \rho_L J_1(\kappa_n \rho_L)} e^{-\kappa_n z_c} \tag{5.101}$$

$r_i$ and $r_o$ stand for the coil inner and outer radius, respectively, $h$ its length and $N_c$ the number of turns. The coil lift-off is equal to $lo$, which implies for the axial coordinate of its centre $z_c = lo + h/2$ (cf. Fig. 5.13).

## 5.11 Publications related with the chapter content

The development of the volume integral equation for the calculation of the flaw response in a ferromagnetic tube has been the subject of two publications [49,78]. The VIM has been combined with the FEM for the treatment of defects in steam generator tubes, where the influence of structural elements like support plates is non-negligible (a problem of considerable importance for nuclear safety). The results of the approach have been presented in [79,80]. This work was a result of a common action with the French institute for radiological protection (institut de radioprotection et de sûreté nucléaire, IRSN).

The development of the Green's function in multilayered structures with boreholes, and its application for the calculation of crack signatures in the vicinity of the hole walls was the subject of the Ph.D. work of Dr. K. Pipis. The results of this work have been communicated in a number of publications [40, 81, 82]. The developed formalism has also been applied for the simulation of defects in finite tubes [59].

Finally, the spectral approach for the modelling of extended sources has been motivated by the work originally oriented to the treatment of the nonlinear problem. The same ideas were also explored in the context of the time integration of the spectral approach. The detailed presentation of these development as well as the according research results production is thus postponed to the next chapters.

# Chapter 6

# Transient solutions

In this chapter, we will be interested in constructing transient solutions for the eddy-current and the heat propagation problem. Although the harmonic excitation (mono as well as multi-frequency) remains the most commonly used kind of excitation for eddy-current applications, pulsed eddy-current testing (PECT) techniques have gained considerable interest recently. The reason lies in the intrinsic broad-frequency character of the pulsed response, which means that, at least theoretically, the information carried by a single signal is quite rich (despite, admittedly, a certain controversy in the community about the practically exploitable part of this information). The laboratory equipment for the excitation of PECT is simpler than the one for multi-frequency inspection, and the recent advances in the electronics with the development of high-resolution data acquisition cards has facilitated a lot the recording and the processing part of the acquisition chain.

Apart from the practical aspect, however, there remains a theoretical/mathematical interest per-se for the development of transient solutions motivated by the alternative physical picture that they provide and alimented by the numerical challenges that need to be addressed. Last but not least, the construction of time domain (TD) solutions may be seem as a building stone for the treatment of the non-linear problem, whose detailed study will be the subject of a later chapter.

When infrared testing (IR) comes to play, TD solutions are naturally imposed by the physics of the problem. Although harmonic excitation techniques, known in the literature as lock-in thermography exist, the pulsed excitation is by far the most usual operating mode for this technique. IR signals have also the peculiarity that the most important information is contained either in the very short time window of the signal (where lateral diffusion has not yet blurred the thermographic image) or the late time, which delivers information from the opposite to the excitation interface. Multi-resolution algorithms are hence required making the analysis in the Laplace domain the most suitable theoretical tool.

In this chapter, two families of methods will be studied. Analysis in the

Laplace domain and direct integration in the TD through time-stepping. Both methods have their own advantages and drawbacks and can be seen as complementary.

## 6.1 The Laplace transform approach

### 6.1.1 The diffusion equation in the Laplace domain

The Laplace transform (LT) of an arbitrary time function $f(0)$ with a zero initial condition $(f(0))$ is defined as follows [26]

$$F(s) := \int\limits_{0}^{\infty} f(t)\, e^{-st} dt \tag{6.1}$$

with the corresponding inverse operator given by the integral

$$f(t) = \frac{1}{2\pi i} \int\limits_{\gamma - i\infty}^{\gamma + i\infty} F(s)\, e^{st} ds. \tag{6.2}$$

The integration is performed along the Bromwich path $(\gamma - i\infty, \gamma + i\infty)$ in the complex $s$-plane, with $\gamma$ chosen so that all singularities of $f(s)$ are located on the left half-plane.

Both state equation and solutions can be deduced by the corresponding ones in the frequency domain by performing the variable change $i\omega \rightarrow s$. The state equation is thus given by the Helmholtz equation, which for the $A$ potential reads

$$\left(\nabla^2 - k^2\right) A = 0 \tag{6.3}$$

with $k^2 = s\mu\sigma$, and similarly for the SOVP potentials $W_a, W_b$ or the temperature variable $T$.

### 6.1.2 Pole extraction

In contrast with the Fourier Transform (FT), there does not exist a really universal algorithm for the numerical inversion of the LT. Most general tools are based in the numerical calculation of contour integrals in the complex plane, but their disadvantage is that they lead to heavy computational schemata and their robustness is not always guaranteed. Computationally efficient and robust specialised methods have been proposed in the literature, which are based in different principles with the specific approach chosen for the calculation of a particular inverse Laplace transform (ILT) being problem dependent. An excellent review on the different available methods for the numerical calculation of the ILT can be found in [83].

A standard approach consists in approximating the Laplace transformed expression as a rational function, which is then decomposed in simple poles, amenable to analytical inversion. The poles, which are the roots of the denominator can be computed numerically. This approach is very well suited for the semi-analytical methods considered herein and has been successfully applied to address the PECT problem in layered media [84, 85].

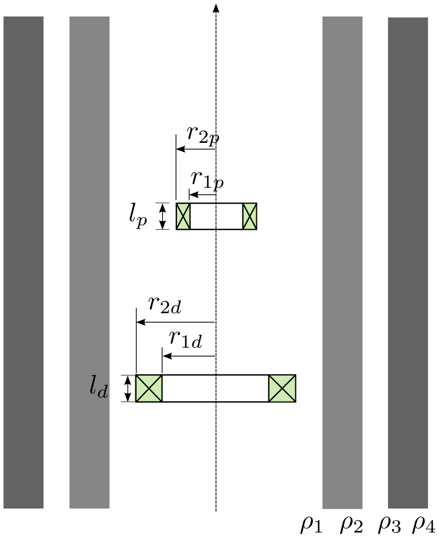

Figure 6.1: Nested tube inspection in driver-pickup mode.

The principle of the approach will be demonstrated for the calculation of the electromotive force (EMF) of the pickup coil in a nested cylindrical tube. The problem configuration is depicted in Fig. 6.1. The same ideas apply also for the computation of field quantities. It can be shown that the EMF value in the Laplace domain as it is calculated by the reciprocity theorem admits the following general form [85, 86]

$$\Delta V(s) = \sum_{n=1}^{\infty} \frac{a_n}{\kappa_n^6} I_d(s)\, R(\kappa_n, s)\, Y_d(\kappa_n)\, Y_p(\kappa_n) \tag{6.4}$$

where $Y_d$, $Y_p$ are form functions for the driver and the pickup coil, which depend on the coil geometry, $a_n$ is a scaling coefficient, and $R(\kappa_n, s)$ stands for the reflection coefficient containing the information of the piece. $I_d$ is the feed current. Following the standard TREE approach the domain is truncated at $z = 0$ and $z = L$ using a PEC and PMC condition respectively. The $a_n$, $Y_d$ and $Y_p$ coefficients read

$$a_n(s) = \frac{4\pi\mu_0}{L} \tag{6.5}$$

$$Y = \frac{iN}{(r_2 - r_1)l} \left[\cos(\kappa_i(z_c + l/2)) - \cos(\kappa_i(z_c - l/2))\right] \chi(\kappa r_1, \kappa r_2) \tag{6.6}$$

where $r_1, r_2$ are the inner and outer radii of the coil, $l$ its length, $N$ the number of turns and $z_c$ the position of its center in the $z$ axis (all parameters being understood applying once for the transmitting and once for the receiving coil). The function $\chi$ is given by the relation

$$\chi(x_1, x_2) = \int_{x_1}^{x_2} x I_1(x)\, dx. \tag{6.7}$$

It remains to determine $R(\kappa_n, s)$ which contains the projected propagators introduced in chapter 3. The procedure has been described in that chapter and will not be repeated here. For a step current excitation, $I_d(t) = I_0 H(t)$ with $H(t)$ being the Heaviside function, $I_d(s) = I_0/s$. We define thus the transfer function

$$\Gamma_n(s) \coloneqq sR(\kappa_n, s) \tag{6.8}$$

which is writen as rational function of the propagators, and we factorise it using one of the available numerical techniques for zero-finding or using Padé approximation.

The EMF can be thus brought in the form

$$\Delta V(s) = \sum_{n=1}^{\infty} \sum_{p=1}^{N_s} \frac{A_{np}}{s - s_{np}} \tag{6.9}$$

whose ILT is known in closed-form

$$\Delta V(s) = \sum_{n=1}^{\infty} \sum_{p=1}^{N_s} A_{np} e^{s_{np} t}. \tag{6.10}$$

Once the step response of the system is known, one can easily obtain the response to any arbitrary current waveform $I(t)$ by applying the Duhamel's integral [84]

$$\Delta V_I(t) = \frac{d}{dt} \int_0^t \Delta V_H(\tau)\, I(t - \tau)\, d\tau \tag{6.11}$$

with the $\Delta V_I$ and $\Delta V_H$ denoting the signals for the arbitrary and step excitation, respectively.

### 6.1.3 Numerical calculation of the ILT: the Zakian and Gaver-Stehfest methods

A class of algorithms can be derived by computing samples in the time domain (TD) and exploiting the properties of generalised functions. This class proposed by Zakian [87] consists by computing a weighted sum of Laplace samples

$$f(t) \approx \frac{2}{t} \sum_{n=1}^{N} K_n F(a_n/t) \tag{6.12}$$

where $F(.)$ is the Laplace transform of the function. The $K_n, a_n$ coefficients are determined following Zakian via two different approoches [87]: through Padé approximation of the delta function or least-square approximation. The numerical values computed by either of these approaches can be tabulated and used independently of the input signal. In Tab. 6.1 are provided the numerical values determined via the first approach

| $K_n$ | $a_n$ |
|---|---|
| $-36902 + 196990\ i$ | $12.8377 + 1.66606\ i$ |
| $61277 - 95408.6\ i$ | $12.2261 + 5.01272\ i$ |
| $-28916.6 + 18169.2\ i$ | $10.9343 + 8.40967\ i$ |
| $4655.36 - 1.90177\ i$ | $8.77643 + 11.9219\ i$ |
| $-118.741 - 141.304\ i$ | $5.22545 + 15.7295\ i$ |

Table 6.1: Tabulated values for the $K_n, a_n$ coefficients.

A variant of the Zakian method, which is commonly used for the calculation of impulse or step response is the so-called Gaver-Stehfest method, which proposes the evaluation sum

$$f(t) \approx \frac{\ln 2}{t} \sum_{n=1}^{N} V_n F\left(\frac{\ln 2}{t} n\right) \tag{6.13}$$

where $V_n$ are calculated by the formula

$$V_n = (-1)^{\frac{N}{2}+1} \sum_{k=\frac{n+1}{2}}^{\min(n,N/2)} \frac{k^{N/2}(2k)!}{(N/2-k)!k!(k-1)!(n-k)!(2k-n)!} \tag{6.14}$$

Both Zakian (6.12) and (6.13) are more or less equivalent from the computational point of view.

It should be noted here that the Zakian and the Gaver-Stehfest method apply for monotonical input and are best suited for the computation of the short-time response (whence their popularity in thermographic applications).

### 6.1.4 Comparison of the pole extraction method with the numerical calculation of the ILT

The two approaches for the calculation of the ILT, namely the pole extraction approach and the numerical inversion using the Gaver-Stefest method are compared here for a specific realisation of the nested tube configuration of Fig. 6.1. The tubes are assumed to be of the same material and are either carbon steel (ferromagnetic) or stainless steel (non-ferromagnetic) with electrical conductivity $\sigma = 3$ MS/m in both cases and relative magnetic permeability $\mu_r$ equal to 100 and 1 respectively. The inner radii of the two layers $\rho_1 = 40$ mm and

$\rho_3 = 60$ mm and both have thickness equal to 10 mm. The dimensions of the coils are summarised in Tab. 6.2. The axial distance of the driver from the pickup coil is 10 mm.

| | Driver | Pickup |
|---|---|---|
| $r_1$ (mm) | 20 | 20 |
| $r_1$ (mm) | 30 | 30 |
| $l$ (mm) | 40 | 10 |
| $N$ | 1600 | 10000 |

Table 6.2: Coils and layers dimensions and materials.

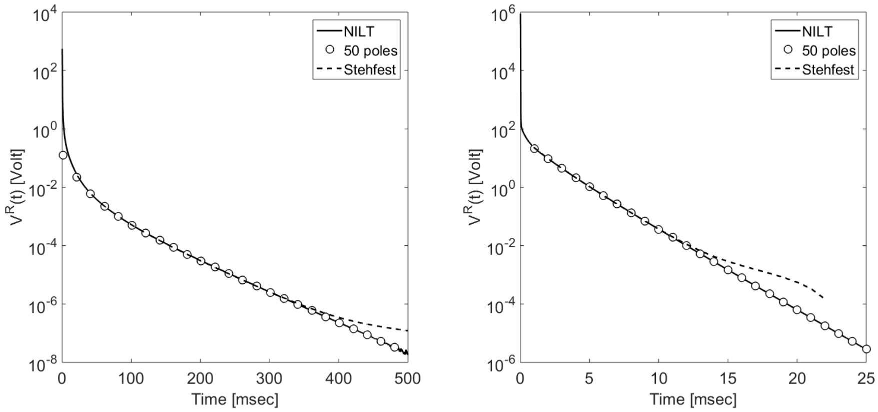

(a) (b)

Figure 6.2: Long-time comparison of Stehfest and pole extraction methods to NILT for (a) Carbon and (b) Stainless steel. Only the first pole is used for each $q_n$ eigenvalue.

The transient responses are shown in Fig. 6.2 for the two inversion methods, and they are compared against direct numerical inversion of the Laplace transform (NILT), which is taken as reference [88]. The logarithmic scale in the voltage axis better depicts the long-time behaviour of the transient signal. Adopting as reference the NILT method, we can easily observe that the pole extraction behaves very well in the long-time domains while the Stehfest method behaves well for the short-time domain and starts to deviate from a certain point in time. It seems then that these two methods, Stehfest and pole extraction, are complementary and can be used in the short- and long-time domains, respectively. The point of transition that we have established empirically, after many simulations, for a system of tubes of the same material is the time defined by $t_m = \mu_0 \mu_r \sigma b^2$, where $b$ stands for the total thickness of the tubes. From Fig. 6.2, it is evident that the logarithmic signal curve is steep in the case of the stainless steel due to its smaller relative magnetic permeability and hence to the weaker eddy-currents induced in the tube wall. This is exactly the expected behaviour [89–91].

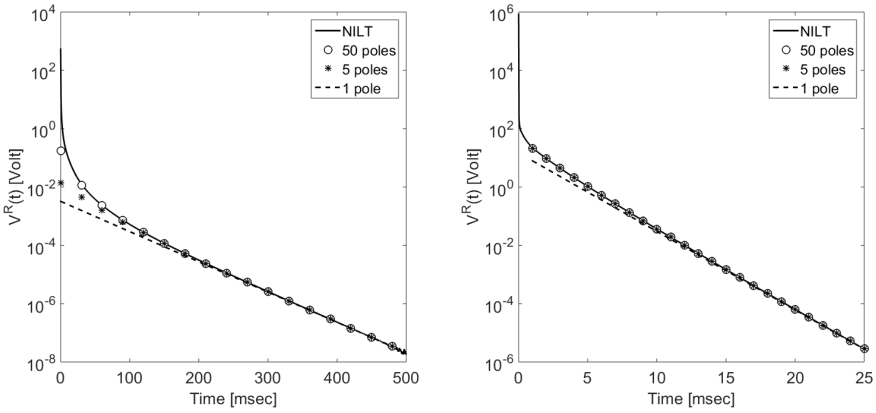

(a) (b)

Figure 6.3: Long-time comparison of NILT to pole extraction method with different number of poles for (a) Carbon and (b) Stainless steel.

In the summation of (6.9), we have used 50 terms, and for the Laplace inversion, we have only used 1 pole per eigenvalue (hence 50 poles). The boundary of the truncated domain is set to $L = 100\rho_4$ for carbon and $L = 20\rho_4$ for stainless steel. The fact that we use only 1 pole for each eigenvalue is a crude computation that nevertheless gives good results for the long time. For the long-time domain, the number of eigenvalues and thus the number of poles can be decreased further. We have run a parametric study regarding the number of poles that can be used to reliably compute the induced voltage. Fig. 6.3 shows results that compare pole extraction method (with decreasing number of poles) to the exact NILT solution. It is clear that the limiting case of using just 1 pole can also be used for a reliable representation in the long-time region.

## 6.2 Thermographic inspection of planar multilayer pieces with delamination defects

The thermal transient response of a material under impulse excitation is a typical scenario of thermographic inspection. As mentioned in the introduction of the chapter, we are interested in both early and late time IR surface images, called in IR jargon as thermograms. The former carry spatial information about the location and the size of material anomalies (it is understood that at intermediate of late times, lateral diffusion will blur the image lowering the resolution). The latter images deliver information about the depth of the discontinuities, via the diffusion time. In principle, we seek to solve the problem in a logarithmic timescale, which may lead to prohibitive computational times when classical temporal discretisation schemes are applied unless specially designed algorithms involving highly inhomogeneous time sampling are employed. The LT approach, on the other side, is very well adapted for this type of applications since the solution can be evaluated at arbitrary time instances, which makes it the preferred tool when calculating thermograms.

In this section, we will calculate the transient response of a multilayer plate affected by delamination effects between the plate layers. Due to their particular orientation, delaminations interact only weakly with eddy-currents. IR inspection, on the contrary, is very well adapted for the detection of this kind of defects since they tend to hinder the heat propagation across the specimen. In addition, thermal imaging methods can give direct information about the delamination size and geometry [92, 93]. In composite materials, eddy-current inspection is inapplicable due to the weak conductivity of the composite plies, which in the majority of applications consist of carbon fibres embedded in epoxy matrices. IR inspection is thus a well adapted tool for such materials. The modelling of composites, however, has to cope with the inherent anisotropy of the plies due to their structure, and hence we shall restrict the present discussion to isotropic multilayer structures (primarily metallic).

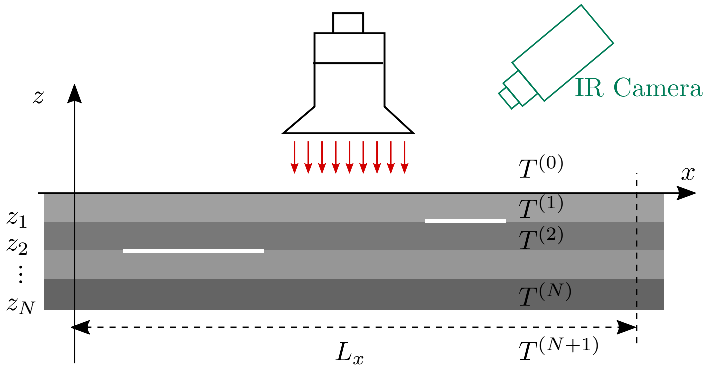

Figure 6.4: Problem configuration: a planar multilayer medium affected by a number of delamination flaws is thermally excited by an impinging photon flux. The temperature distribution is then monitored by means of an infrared camera located in the front of the rear side.

The heat can be deposited using different techniques, the flash-lamp and induction heating (primarily reserved for metallic components) being the most used ones. According to the first heat is transmitted in the material via an impinging short-duration photon flux emitted from a dedicated high-intensity flash lamp. The common experimental setup is schematically depicted in Fig. 6.4. Two main inspection modes can be realised: at the excitation surface (referred to as reflection thermography) or the rear side (in which case we are speaking about transmission thermography).

### 6.2.1 Calculation of the temperature distribution

Let us consider a planar piece composed of $N$ stacked sheets perfectly joined with another similar to the one depicted in Fig. 6.4. The medium above and underneath the considered piece is air. The piece is thermally excited from its upper interface by means of an impinging heat flux (flash lamp, laser source, air flow). The exact form of the excitation is irrelevant for the hereafter developed mathematical analysis. Solely its geometrical features, i.e. the shape and the dimensions of the flux spot as well as its intensity, that is, the heat power per unit of surface, are of interest here. We also assume that the considered medium is affected by a delamination flaw located between the $i$th and the $(i+1)$th layer. As such, it is understood a local loss of contact between the two layers, which physically takes the form of a very thin cavity between the two layers, filled with air as shown in Fig. 6.5.

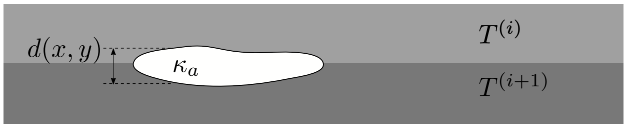

Figure 6.5: Delamination defect between two adjacent layers. $\kappa_a$ is the thermal conductivity of the air.

Each layer $i$ is characterised by its mass density $\rho_i$, its heat capacity at constant (atmospheric) pressure $c_{p_i}$ and its thermal conductivity $\kappa_i$, which in the context of this work is assumed to be isotropic.

We seek to calculate the temperature at every point of the medium throughout an observation time window comprising the excitation and a relaxation time interval after the source switch-off. In particular, we are interested in the temperature distribution at the upper and lower piece-air interface corresponding to the two aforementioned IR inspection modes. These two distributions can be extracted by the solution of the associated heat propagation problem, as developed below.

Following the formalism developed in chapter 3, the solution is represented via the temperature distributions at the specimen interfaces, which are subjected to the subsidiary conditions

$$\sum_i c_{m;i}\left[\langle m_j|\,\hat{\boldsymbol{\kappa}}_{j+}\hat{\boldsymbol{C}}_{j+}\hat{\boldsymbol{P}}_i\,|m_i\rangle - \langle m_j|\,\hat{\boldsymbol{\kappa}}_{j-}\hat{\boldsymbol{C}}_{j-}\hat{\boldsymbol{P}}_i\,|m_i\rangle\right] = \mathbf{0}, \qquad \forall j. \qquad (6.15)$$

with $i, j$ running all interfaces of the medium. $\hat{\boldsymbol{\kappa}}_j$ is the trace operator at the $j$ interface, which in its local frame is described by the matrix of (3.12), and $\hat{\boldsymbol{P}}_i$ stands for the associated propagator given by (3.51).

To evaluate (6.15) we need to determine a suitable representation for each surface $|m_i\rangle$. To construct the representation, we truncate the domain at $x = 0, L_x$ and $y = 0, L_y$ by imposing a Dirichlet condition[1] according to the TREE

---

[1] In this particular example we have assumed a source of finite support, which makes the

approach

$$T^{(i)}\Big|_{x=0} = T^{(i)}\Big|_{x=L_x} = 0, \tag{6.16}$$

$$T^{(i)}\Big|_{y=0} = T^{(i)}\Big|_{y=L_y} = 0. \tag{6.17}$$

which implies for the eigenvalues of the modal representation in the $x$ and $y$ directions

$$\sin(\kappa_m L_x) = 0, \quad \kappa_m = \frac{m\pi}{L_x}, \quad m = 1\ldots,\infty, \tag{6.18}$$

$$\sin(\lambda_n L_y) = 0, \quad \lambda_n = \frac{n\pi}{L_y}, \quad n = 1\ldots,\infty \tag{6.19}$$

and the propagator admits the following form

$$\langle m_j| \hat{\boldsymbol{P}}_i |m_i\rangle = e^{-v^{(\ell)}_{mn}|z_j - z_i|} \tag{6.20}$$

where $\ell = [j-1, j]$ stand for the layer index (cf. Fig. 6.4), and $v^{(\ell)}_{mn}$ is calculated using the dispersion equation

$$\eta^{(\ell)}_{mn} = \sqrt{\kappa_m^2 + \lambda_n^2 + \frac{s}{a_\ell}}. \tag{6.21}$$

$\alpha_\ell = \kappa_\ell / c_{p_\ell}\rho_\ell$ stands for the layer diffusivity.

Substitution to (6.15) for the interfaces without delamination, provides us with the following explicit relations

$$D^{(j-1)}_{mn} e^{-v^{(j-1)}_{mn} d_{j-1}} + C^{(j)}_{mn} - D^{(j)}_{mn} - D^{(j+1)}_{mn} e^{-v^{(j)}_{mn} d_j} = 0 \tag{6.22}$$

$$\begin{aligned} &v^{(j-1)}_{mn}\kappa_{j-1}\left[D^{(j-1)}_{mn} e^{-v^{(j-1)}_{mn} d_{j-1}} - C^{(j)}_{mn}\right] + v^{(j)}_{mn}\kappa_j\left[D^{(j)}_{mn} - C^{(j+1)}_{mn} e^{-v^{(j)}_{mn} d_j}\right] \\ &= D^{(e)}_{mn}\delta_{i,0}, \end{aligned} \tag{6.23}$$

where $d_i = z_{i-1} - z_i$, $c^{(e)}_{mn}$ and $\delta_{i,0}$ is the Kronecker delta. For convenience with the term recognition, all the coefficients corresponding to upwards diffusing terms are denoted with capital $C$ and the downwards diffusing terms with capital $D$. $D^{(e)}_{mn}$ stands for the development coefficients of the source which for the flash-lamp considered here are given by

$$D^{(e)}_{mn} = \frac{2}{\sqrt{L_x L_y}} \int\limits_{x=0}^{L_x} \int\limits_{y=0}^{L_y} S(x,y)\sin(\kappa_m x)\sin(\lambda_n y)\,dxdy. \tag{6.24}$$

where $S(x,y)$ is a shape function, and takes the value 1 $\forall x, y$ falling inside the source support and 0 outside it.

---

Dirichlet approximation at the truncation boundaries. For extended sources a Neumann type (zero-flux) condition would be more reasonable.

At the interface, where the delamination resides, the continuity relations, must be locally modified to account for the conductivity change due to the defect. Let $\mathscr{D}$ be the void domain and $d(x, y)$ be its thickness as shown in Fig. 6.5. In the general case, the latter is a function of the $x, y$ position. By applying Fourier's law across the void volume, one has

$$J_z = -\kappa_a \nabla T \tag{6.25}$$

which for relatively small values of $d(x, z)$ can be approximated by a finite difference quotient

$$J_z(x, y) \approx -\kappa_a \frac{T^{(i+)}(x, y) - T^{(i-)}(x, y)}{d(x, y)}. \tag{6.26}$$

By introducing the local thermal resistance as [94]

$$R(x, y) = \frac{d(x, y)}{\kappa_a} \tag{6.27}$$

the previous relation can be written as follows

$$T^{(i-)} - T^{(i+)} = -R(x, y)\, J_z \tag{6.28}$$

and integrating Fourier's law for the thermal currents (2.71), we arrive at

$$T^{(i-)} - T^{(i+)} = -R(x, y)\, \partial_z T^{(i-)}. \tag{6.29}$$

A few words should be spoken on the physical interpretation of (6.29). In contrast with the heat flux, which remains continuous across the interface (otherwise we would have energy accumulation), there is a temperature discontinuity which arises as the limiting case of the temperature gradient across the void, when its thickness tends to zero. This difference is linear with the heat flux, from which we have interpreted $R$ as a kind of thermal resistance.

For the purposes of this analysis, it is sufficient to consider the defect as an idealised slab of constant thickness $d(x, y) = d_a$, which implies that the thermal resistance will also be constant throughout the flaw support.

With the introduction of (6.29) into (6.22), the temperature continuity across the affected interface is modified to

$$\begin{aligned} &\sum_{m'} \sum_{n'} \left( \delta_{nm,n'm'} + R_{m'n'} \kappa_{j-1} v^{(j-1)}_{m'n'} \right) D^{(j-1)}_{m'n'} e^{-v^{(j-1)}_{m'n'} d_{j-1}} \\ &+ \sum_{m'} \sum_{n'} \left( \delta_{nm,n'm'} - R_{m'n'} \kappa_j v^{(j)}_{m'n'} \right) C^{(j)}_{m'n'} \\ &- D^{(j)}_{mn} - C^{(j+1)}_{mn} e^{-v^{(j+1)}_{mn} d_{j+1}} = 0, \end{aligned} \tag{6.30}$$

where $R_{mn}$ stands for the weighted thermal resistance function

$$R_{mn} = \int_0^{L_x} \int_0^{L_y} R(x, y)\, w(x, y)\, dx dy. \tag{6.31}$$

### 6.2.2 Characteristic results

The above developed solution will be applied in the specific case of a two-layer medium consisting of a steel and an aluminium plate in imperfect thermal contact to each other. The thermal properties of the piece materials as well as those of the air are summarised in Tab. 6.3. The two layers have the same thickness equal to 2.5 mm. Their lateral dimensions are assumed to be large enough for the edge effects to be safely ignored. They will be thus considered for the purpose of the analysis as infinite.

| Material | Thermal conductivity $k$ $(W/mK)$ | Heat capacity $C_p$ $(J/kgK)$ | Density $\rho$ $(kg/m^3)$ |
|---|---|---|---|
| Aluminium | 237 | 897 | 2707 |
| Steel | 44.5 | 475 | 7850 |
| Air | 0.02454 | 1005 | 1.1843 |

Table 6.3: Thermophysical properties of materials.

Two different contact defects are considered: a single square shaped delamination and a couple of two delamination defects, a square and a rectangular one, located a few centimeters apart at a distance such that they can interact to each other. The two configurations are depicted in Fig. 6.6

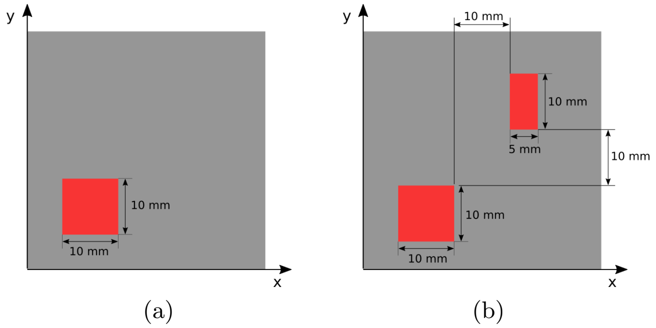

(a) (b)

Figure 6.6: Dimensions and locations of the delaminations: (a) single delamination, (b) two interacting defects.

Fig. 6.7 shows the temperature transient for the geometry described in Fig. 6.6a at a sampling point on the front and rear surface. The sampling point corresponds to the centre of the defect. Two different temperature solutions are compared: the solution obtained using the approach of 6.2.1 and a FEM solver [32]. For the former, the transient signal has been evaluated by applying the Gaver-Stehfest method described in 6.1.3 to the spectral (TREE) expression obtained for the Laplace frequencies determined by (6.13), namely $s_n = \ln 2n/T,\ n = 1, \ldots, 10$. The FEM solution is evaluated via a classic implicit time-stepping scheme. Attention must be given to the very short times of the front surface response, where the time-stepping scheme struggles to reproduce the sharp peak just after the switch off of the impinging flash beam. It is the response at these time window which makes the use of the Laplace approach interesting here.

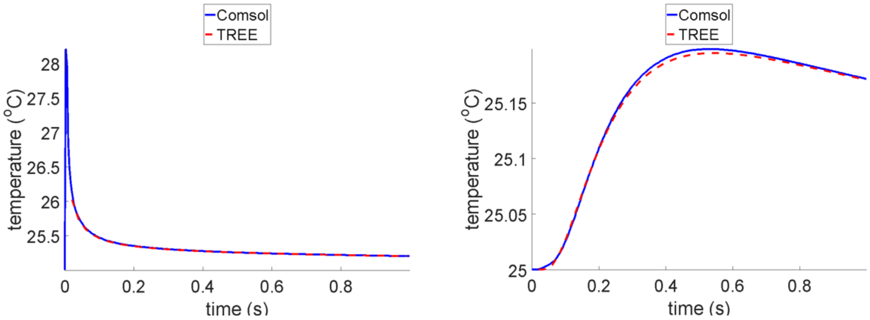

(a) (b)

Figure 6.7: Temperature variation in time for the geometry of Fig. 6.6a calculated by the spectral method and a reference commercial FEM code. (a) Temperature at the top surface above the centre of the defect (reflection mode), (b) Temperature at the rear surface below the centre of the defect (transmission mode).

The temperature profiles occurred by the interaction of the heat front with the defect are demonstrated in Fig. 6.8 and Fig. 6.9 for the front and the rear surface, respectively. The three coloured curves show the temperature transient above/below the centre of the tree defects with point 1 standing for the centre of the lower-left defect alone (Fig. 6.7a), point 2 for the same location in the presence of both defects (Fig. 6.7b) and point 3 giving the temperature transient above/below the centre of the upper-right defect.

The interaction between the two flaws becomes evident by considering the blue and the orange curves standing for the temperature variation at the same point with one and two defects. The two curves begin to deviate after the temperature change has reached its absolute maximum, i.e. as long as the direct heat front from the source has dissipated permitting to the secondary front stemming from the other defect to become visible.

## 6.3 Solution in the TD using spectral methods

An alternative to the ILT approach is the direct integration of the diffusion equation in the time domain using one of the established time-stepping schemes [95–98].

We shall consider hereafter the 2D problem by adopting the $\mathbf{A} - \Phi$ formulation according to the standard framework developed in the previous chapters. The TD analogue of the extended magnetic vector potential definition of (5.70)

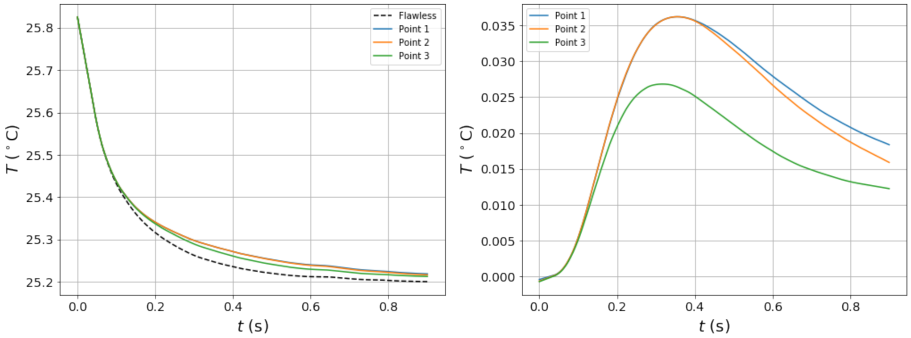

(a) (b)

Figure 6.8: Temperature variation at the top surface of the piece above the centre of the defects. (a) Absolute temperature change. (b) Temperature difference with respect to the flawless piece. The different curves correspond to the recorded transients above the defect centre, as explained in the text.

reads

$$\mathbf{B} = \nabla \times \mathbf{A} + \int_0^t \mathbf{J}_m(\tau)\, d\tau \tag{6.32}$$

with the corresponding relation for the electric field given by

$$\mathbf{E} = -\frac{d\mathbf{A}}{dt} - \nabla \Phi \tag{6.33}$$

Upon substitution to the Maxwell equations and ignoring the scalar potential $\Phi$, as is common practice in eddy-current problems, one obtains the diffusion equation for the magnetic potential

$$\nabla \times \nu \nabla \times \mathbf{A} + \sigma \frac{d\mathbf{A}}{dt} = \mathbf{J}_e + \int_0^t \nabla \times \mathbf{J}_m(\tau)\, d\tau. \tag{6.34}$$

We are especially interested in problems with rotational symmetry, like the one depicted in Fig. 5.13, and it has already been analysed that a single-component ansatz for the magnetic potential $\mathbf{A} = A\mathbf{e}_\phi$ is sufficient for producing the corresponding three-elements field solution. The curl-curl equation reduces in this case to the following scalar equation

$$\left(\nabla^2 - \frac{1}{\rho^2} - \mu\sigma \frac{d}{dt}\right) A = -\mu J_e - \mu \int_0^t \mathbf{e}_\phi \cdot \nabla \times \mathbf{J}_m(\tau)\, d\tau \tag{6.35}$$

where we have taken into account the azimuthal orientation of the magnetic potential and the excitation current ($\mathbf{J} = J\mathbf{e}_\phi$).

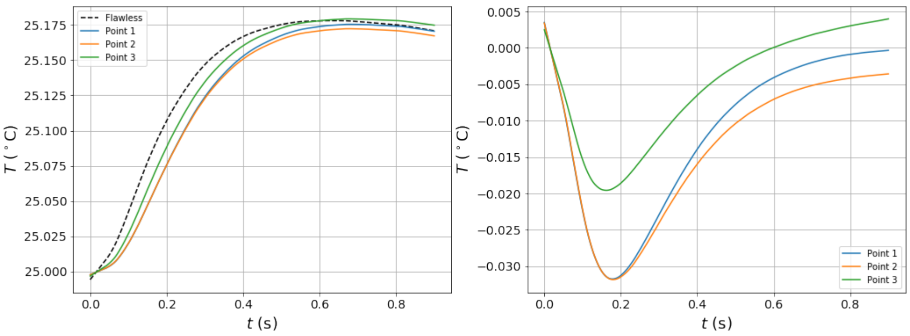

(a) (b)

Figure 6.9: Same curves Fig. 6.8 for the bottom surface.

Equation (6.35) describes an initial value problem, whose integration will yield the magnetic potential in the TD, $\mathbf{A}(\mathbf{x}, t)$. This integration is carried out in the general case numerically by introducing a temporal discretisation for the fields $t_j = j\Delta t$, $j = 1, 2, \ldots$, where $\Delta t$ is a constant time-step. Although the use of inhomogeneous time discretisation with variable time-steps is straightforward but it will not be considered herein for the sake of simplicity and to keep the discussion short. Nevertheless, variable time-step and temporal multi-grid approaches can be of interest when short and long time responses are sought, as already discussed.

With the temporal discretisation fixed, one has to discretise the temporal derivatives using a suitable finite difference quotient according to the established scheme. Keeping in mind that the eddy-current problem described by (6.35) is a parabolic problem, the Courant-Friedrichs-Levy (CFL) stability criterion imposes a very restrictive upper limit for the time-step (with respect to the characteristic time-scale of the problem), when explicit schemata are to be used. For such problems, unconditional stable backward differentiation schemata make more judicious choice. Here, we shall restrict ourselves to the simple implicit Euler scheme, which turns out to be sufficient for the type of applications we are interested in. More elaborate schemata will be discussed in the next chapter when dealing with the numerical solutions in TD using the finite integration technique (FIT) method.

According to the Euler scheme, the temporal derivative at the $j$th time-step is approximated by the quotient

$$\left.\frac{\partial A}{\partial t}\right|_{t=t_j} \approx \frac{A_j - A_{j-1}}{\Delta t} \tag{6.36}$$

which upon substitution in (6.35) results the following update equation, where the solution at $t_j$ is given by means of the solution at the previous time step

$t_{j-1}$

$$\left(\nabla^2 - \frac{1}{\rho^2} - \frac{\mu\sigma}{\Delta t}\right) A_j = -\frac{\mu\sigma}{\Delta t} A_{j-1} - \mu J_{e;j} - \mu \int\limits_0^{t_j} \mathbf{e}_\phi \cdot \nabla \times \mathbf{J}_m(\tau)\, d\tau. \tag{6.37}$$

Comparison with (5.76) reveals that (6.37) is isomorphic with the inhomogeneous Helmholtz equation with the effective (imaginary) angular frequency

$$\omega = -\sqrt{-1}/\Delta t \tag{6.38}$$

and right-hand side (excitation) $f_j$ equal to

$$f_j = \mu\left(\frac{\sigma}{\Delta t} A_{j-1} + J_{e;j}\right) + \mu\Delta t \sum_{\ell=0}^{j} \mathbf{e}_\phi \cdot \nabla \times \mathbf{J}_{m;j}. \tag{6.39}$$

which states that the potential solution at the previous time step acts as an equivalent electric current. Since the electric current source (for a medium without defects) is entirely embedded in the air region (with $\sigma = 0$) and the magnetic sources are zero, we can set $J_{e;j} = (\sigma/\Delta t)A_{j-1}$ and apply the solution developed for the defected medium in harmonic regime in section 5.10. These expressions, however, should now be evaluated at every time step $j$, i.e. the development coefficients will be functions of time. Note that the zero conductivity in the air causes that the coefficient values given by (5.77),(5.78) and (5.81) depend from the previous time steps only indirectly via the fulfilment of the boundary conditions, which have to be verified at every time step after the re-evaluation of the special solution.

The inner products (5.91) and (5.92) in case of a flawless medium take a relatively simple form since there is no mixing between $w_{nl}$ elements owing to the homogeneity of the medium. As a demonstration, we provide the explicit relations derived for the geometry of Fig. 5.13 as far as the special solution coefficients are concerned. More precisely, the zero order term coefficients $d_{j;nl}$ are calculated by the relations

$$d_{j;nl} = \frac{k^2}{v_n^2 + q_l^2}\left[d_{j-1;nl} + \frac{1}{2}\left(1 \mp e^{-v_n d}\right) C^{(2)}_{j-1;n} + \frac{1}{2}\left(1 \mp e^{v_n d}\right) D^{(2)}_{j-1;n}\right] \tag{6.40}$$

for $l = 1, 2$, and the corresponding expressions for the non-zero term coefficients $c_{j,nl}$ read

$$c_{j,mn} = \frac{k^2}{v_n^2 + q_l^2}\left[c_{j-1;nl} + C^{(2)}_{j-1;n} M_{nl} + D^{(2)}_{j-1;n} N_{nl}\right],\ l = 1, \ldots, \infty \tag{6.41}$$

with the integrals

$$\begin{aligned}\begin{Bmatrix} M_{mn} \\ N_{mn} \end{Bmatrix} &= \frac{2}{d} \int\limits_{-d}^{0} \sin(q_n z)\, e^{\pm v_m z} dz \\ &= -\frac{2}{d} \frac{q_n}{v_m^2 + q_n^2}\left[1 - e^{\mp v_m d}(-1)^n\right].\end{aligned} \tag{6.42}$$

$C_{j-1;n}, D^{(2)}_{j-1;n}$ and $d_{j-1;nl}$ are known since they have been calculated in the previous step.

## 6.4 Reciprocity theorem in TD

The most important experimental observable in PECT inspection is the electromotive force (EMF) at the pick-up coil, which makes the analogue of the mutual impedance of the classical ECT in the harmonic regime. We need thus to derive efficient and accurate ways of calculating this quantity, as we did with the impedance in the frequency domain (FD).

It has been shown in the previous chapters that the impedance variation is calculated in an elegant way using Auld's reciprocity theorem [20, 21]. For transient measurements, this theorem can be readily extended using convolution integrals. The TD case has been treated principally in the antennas' community for the calculation of receiver response to arbitrary signals [99–105]. Since, however, this problem has been scarcely explored for low-frequency problems, it will be considered herein in some detail.

The general form of the reciprocity theorem for the 2D problem with rotational symmetry reads

$$\Delta V(t) * I(t) = \frac{1}{\mu_0} \oint\limits_{\partial V} \left( A_{ec} * \nabla \frac{dA_s}{dt} - \frac{dA_s}{dt} * \nabla A_{ec} \right) \cdot d\mathbf{S} \tag{6.43}$$

where $A_s$ stands for the magnetic potential solution of the coil (source) in the free-space and $A_{ec}$ is the corresponding term in the presence of the piece. It is obtained following the standard procedure found in almost all the classical textbooks.

Interestingly, the convolution integral of right-hand-side in (6.43) can be dropped by observing that the source field, being solution of the magnetostatic problem, instantly follows the time variations of the input current. Note that this is an approximation which holds only in the context of the low-frequency quasi-static formulation, which the eddy-current problem satisfies. By virtue of this property, the time derivatives of the source field will provide Dirac functions in case that the current excitation is a Heaviside function $H(t)$. Equation (6.43) becomes

$$\Delta s(t) = \frac{1}{\mu_0} \oint\limits_{\partial V} \left[ A_{ec}(t)\, \nabla A_s^* - A_s^* \nabla A_{ec}(t) \right] \cdot d\mathbf{S} \tag{6.44}$$

where $A_s^*$ is the source field for a unit constant current and $\Delta s$ is the EMF integral

$$s(t) = \int\limits_0^t \Delta V(\tau)\, d\tau. \tag{6.45}$$

The EMF expression for an arbitrary current profile $I(t)$ can be easily obtained from the step response $\Delta s(t)$ by applying Duhamel's integral (6.11). Noting that $\Delta V_H$ is the time derivative of $s(t)$ and carrying out integration by parts (6.11) becomes

$$\Delta V_I(t) = -\frac{d}{dt}\int_0^t s(\tau)\,\dot{I}(t-\tau)\,d\tau. \tag{6.46}$$

For a discrete signal, the time integral reduces to a simple trapezoidal rule. Furthermore, the derivative can be approximated by a finite difference scheme yielding the following relation

$$\begin{aligned}\Delta V_{Ij} &= -\sum_{k=0}^{j} s_k \dot{I}_{j-k} + \sum_{k=0}^{j-1} s_k \dot{I}_{j-k-1}\\ &= \sum_{k=0}^{j-1} s_k\left(\dot{I}_{j-k-1} - \dot{I}_{j-k}\right) - s_j \dot{I}_0.\end{aligned} \tag{6.47}$$

A case of special interest consists in the excitation with a rectangular pulse since this is the most usual excitation signal used in PECT applications. In this case, the EMF calculation can be readily derived noting that

$$\Delta V_I(t) = \frac{d}{dt}\left[s(t) - s(t-T)\right] \tag{6.48}$$

where $T$ stands for the pulse duration. Assuming that $T = K\Delta t$, the discrete form of (6.48) admits the particularly simple expression

$$\Delta V_{Ij} = \left(s_j - s_{j-1} - s_{j-K} + s_{j-K-1}\right)/\Delta t. \tag{6.49}$$

We need now to calculate the surface integral in terms of the development coefficients $C^{(1)}_{i;m}$ and $D^{(s)}_{i;m}$. The analysis is strictly identical with the harmonic case, and the result reads for the $j$th time-step

$$s_j = -\frac{2\pi\rho_L^2}{\mu_0}\sum_{m=0}^{\infty} \kappa_m J_1(\kappa_m\rho_L)\, C^{(1)}_{j;m} D^{(s)}_m. \tag{6.50}$$

where the time-step index $j$ for the source coefficient $D^{(s)}_m$ has been intentionally suppressed since the source field is constant for $t > 0$.

The absolute signal at the pickup coil can be easily obtained by recalling that for two coils in air

$$V_0(t) = -M\frac{dI}{dt} \tag{6.51}$$

where $M$ is the mutual impedance between driver and pickup coil. The total signal will be the superposition of $\Delta V$ and the signal in air, i.e. $V(t) = \Delta V(t) - M\dot{I}(t)$.

## 6.5 Case of study: calculation of a coil EMF above a planar specimen

The proposed approach has been applied for the calculation of the PECT response in the inspection scenario described by Fig. 6.10.

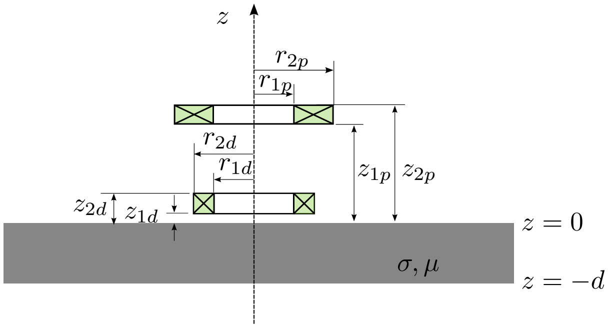

Figure 6.10: Infinite conducting plate inspected via a pair of coaxial cylindrical coils connected in driver(d) - pickup (p) mode.

The plate conductivity and relative magnetic permeability are $\sigma = 5$ MS/m and $\mu_r = 150$, respectively, which correspond more or less to the parameters of a typical construction steel. The plate thickness is 1 mm. The inner and outer radius of the driver coil is $r_{1d} = 1$ mm and $r_{2d} = 2.65$ mm, respectively, its length is $z_{2d} - z_{1d} = 2$ mm and its number of turns is $N_d = 336$. The corresponding dimensions for the pickup coil are $r_{1p} = 2$ mm and $r_{2d} = 5$ mm and $z_{2p} - z_{1p} = 2$ mm, and it is wound with $N_p = 700$ turns.

The first computation concerns the magnetic field calculation at a representative point underneath the plate ($\rho_o = r_{1d}/2$ mm, $z_o = -3d/2$). Two waveforms for the input current have been considered: a rectangular pulse and a pulse with exponential relaxation. The latter case is representative for a realistic current signal provided by a square voltage generator. The pulse duration is taken with 1 ms duration and a 40% duty cycle (dc) for both waveforms. The pulse amplitude reaches 1 A. The time constant for the exponential pulse is 0.05 ms. The signal waveform is depicted in Fig. 6.11

The field transients for both inputs are shown in Fig. 6.13. Numerical simulations obtained using the FIT method are taken as reference solution. The FIT solution is also calculated in TD using a time-stepping scheme and the difference with the herein presented approach consists in the discretisation of the spatial part using a computational grid [77, 95].

An illustration of the pulse repetition frequency effect to the solution is demonstrated in Fig. 6.12, where the field transient is calculated for a rectangular waveform at two repetition frequencies: 100 Hz and 1 kHz.

The field transients for the two considered exciting waveforms of Fig. 6.11 are shown in Fig. 6.13. Both solutions are compared against the FIT reference results all showing an excellent agreement.

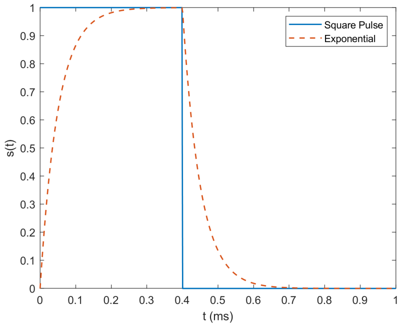

Figure 6.11: Excitation signals used for the solution validation: 40% dc square pulse and pulse with exponential relaxation (charge-discharge mode).

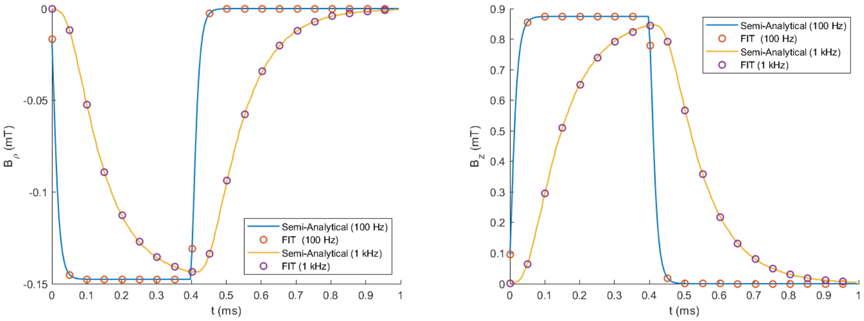

(a) (b)

Figure 6.12: Semi-analytical vs. numerical (FIT) solution at (a) 100 Hz and (b) 1 kHz pulse repetition frequency.

The induced EMF signals computed with the semi-analytical approach for the two fed current waveforms of Fig. 6.11 are compared against the corresponding FIT results in Fig. 6.14. Since the rectangular pulse is a highly idealised situation, it is rather the exponential curve described by the second signal that should be considered as the representative current profile when dealing with measurements [106]. The exact current waveform is obtained by solving the coupled field-circuit problem by considering an RL circuit fed by a standard 50 Ω signal generator. Such calculation is, however, out of the scope of the present text. Note that the EMF response is calculated with FIT via direct integration of the magnetic vector potential

$$V = -2\pi \frac{N_p}{S_p} \frac{d}{dt} \int_{pickup} A(\mathbf{r})\, dV \tag{6.52}$$

where the integration is carried out on the cross-section of the pickup coil, with

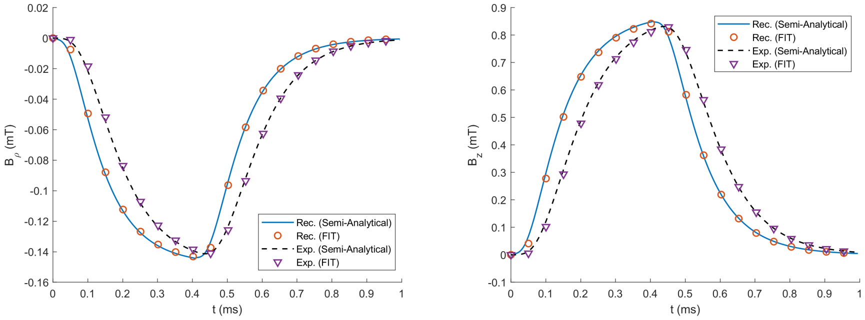

(a) (b)

Figure 6.13: Semi-analytical vs. numerical (FIT) solution for (a) $B_\rho$ and (b) $B_z$ field components as a function of time at the selected observation point under the specimen. The transient signals are shown for both current excitations of Fig. 6.11.

$S_p = (z_{2p} - z_{1p})(r_{2p} - r_{1p})$ and $N_p/S_p$ standing for the windings' density.

A final comparison is realised between the semi-analytical results for the EMF at the pickup coil calculated using the time-stepping approach and the TD reciprocity theorem and the corresponding results obtained using the Laplace approach described in [85], where the Gaver-Stehfest algorithm is used for the calculation of the inverse Laplace transform. The calculations have been carried out for a step excitation since the Gaver-Stehfest algorithm does not work for non-monotonous excitations. The comparison is shown in Fig. 6.15

## 6.6 Publications related with the chapter content

The developments in this chapter follow two lines. The solution of the thermal problem for the simulation and processing of delamination thermograms in multilayer medium was the subject of the Ph.D. research work of Dr. A. Ratsakou. The main results concerning the simulation of the direct problem have been published in [93, 107, 107]. Model based inversion techniques for the retrieval of the delamination characteristics have been studied in [92]. A shape reconstruction method of the defect indications in thermograms using the TSR and the Canny approach has been proposed in [93].

The PECT problem has been treated using the pole extraction method and the Laplace approach in [85]. A TD version of the spectral approach is proposed in [108]. The PECT response has been studied for defect characterisation in steam generator tubes near support plates (a problematic that has been also studied using harmonic signals) using dimensionality reduction and non-iterative inversion approaches. The results of the study have been presented in [109].

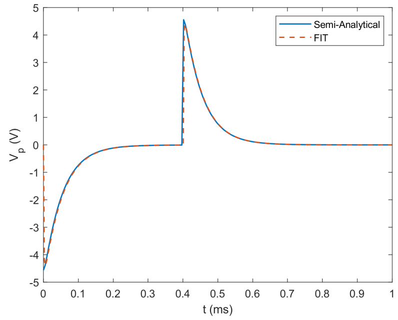

Figure 6.14: EMF at the pick-up coil for the exponential pulse. The semi-analytical results calculated via the TD reciprocity relation are compared against the FIT results calculated by direct integration of the induced voltage (6.52).

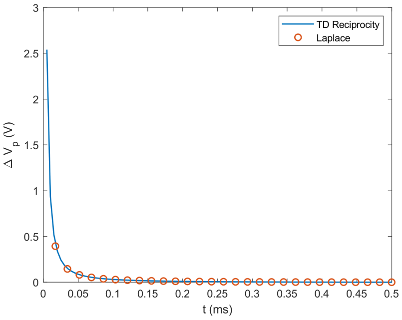

Figure 6.15: Comparison of the semi-analytical calculation of the pickup EMF using the TD and the Laplace domain approach (Stehfest) for a step excitation.

# Chapter 7

# Mixed spectral-spatial representations

In chapter 3 we considered pieces whose interfaces are symmetric in two directions (more precisely along the direction of their principal axes). This property has been relaxed in chapter 4, where a specific heterogeneity has been allowed in one of the two principal axes (in form of a finite number of discontinuities, or at the limit as a continuous material gradient), where the spectral representation had to be mixed with an 1D spatial discretisation approach in order to construct the suitable eigenspace. The piece geometry was canonical in both cases.

In the present chapter, we will take a further step towards generality by removing the restriction of canonical geometries, yet maintaining the assumption of invariance along a given direction. Therefore, all involved pieces will share the same axis of symmetry with their cross-section being arbitrary. Even not fully 3D, the considered class of problems proves to be general enough to be of interest for the vast majority of practical inspection problems. In fact, the parabolic nature of the field equations, which implies a rapid decrease of the field intensity away from the illuminating source, makes this assumption a very good approximation for many 3D pieces, provided that the source physical dimensions are not large with respect to the piece irregularities. Under these circumstances, the piece can be considered as approximately invariant at least along one direction. Since no assumptions are made concerning the geometry of the source, we shall refer to this class of problems conventionally as problems of 2.5 dimension (2.5D).

The adopted strategy for tackling these geometries is to mix a fully numerical scheme, in this case the finite integration technique (FIT), with a spectral representation along the direction of invariance. It turns out that this approach provides us with certain advantages in terms of computational efficiency and numerical precision (mesh noise, small lift-off etc.) with respect to full 3D numerical formulations. In addition, following the same line of reasoning with chapter 5, once base solutions have been constructed for the flawless piece, 3D defects can be addressed by applying the perturbation approach.

The proposed strategy can be further extended in order to include geometries comprising pieces with different symmetry axis. These configurations can be seen as assemblies of coupled sub-problems, and the key tool for their treatment is the surface equivalence theorem. The coupling being tackled, via an ensemble of exchange surfaces by virtue of this theorem, the solution to the total problem is obtained by means of an iterative, Born-type, procedure.

## 7.1 The Finite integration technique

### 7.1.1 Maxwell grid equations

In the classical FIT formulation, Maxwell's equations are discretised using a pair of mutually orthogonal, staggered grids, referred to as primary grid $G$ and dual grid $\widetilde{G}$, respectively, leading to a system of matrix equations, which form the state equations of the method.

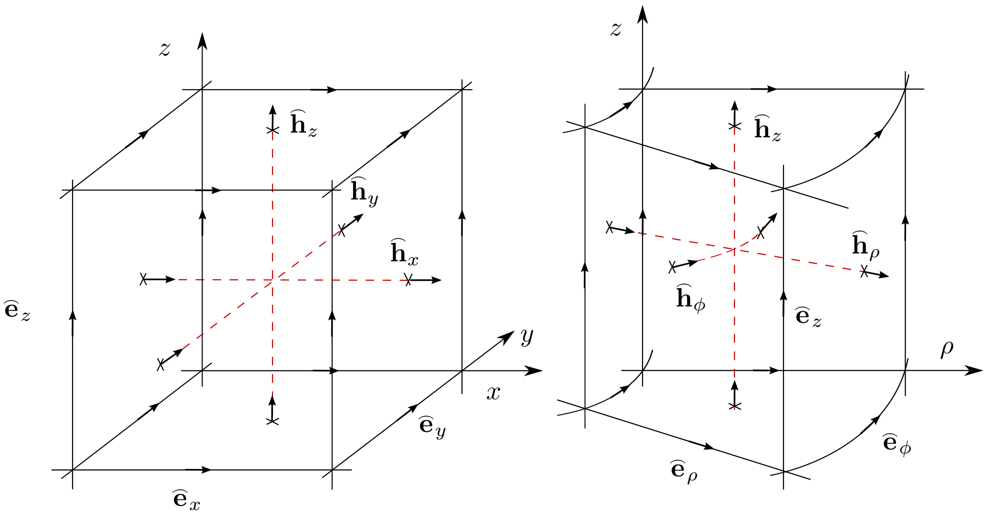

(a) (b)

Figure 7.1: FIT dual grid system for the two considered coordinate systems: (a) cartesian and (b) cylindrical.

The FIT grids $G, \widetilde{G}$ have to be structured, in contrast to the finite elements method, which poses a serious restriction for the choice of possible grid candidates. Practically, this set is limited for the vast majority of problems to grids conformal with the cartesian and the cylindrical coordinate system, although most sophisticated grid systems can be envisaged [110, 111]. For illustration, in Fig. 7.1 is shown a cell of the primary $G$ grid for the cartesian and the cylindrical reference frames and the corresponding allocation of the electric and magnetic fields at the grid primitives (edges and facets). It is recalled that according to the standard FIT conventions, the field-associated state variables are the linear integrals (potentials) of the electric and magnetic fields $\widehat{\mathbf{e}}, \widehat{\mathbf{h}}$ along the $G$ and $\widetilde{G}$ edges, and flux-associated state variables are given by the surface integrals of the corresponding variables $\widehat{\widehat{\mathbf{d}}}, \widehat{\widehat{\mathbf{b}}}$ at the $G$ and $\widetilde{G}$ facets [112–114]. This is an important characteristic of the FIT method, i.e. its state variables contain a part of the grid metric information. In analogy with the field fluxes, the corresponding electric and magnetic currents $\widehat{\widehat{\mathbf{j}}}_e, \widehat{\widehat{\mathbf{j}}}_m$ are also integrated at allocated at the primary and dual grid facets respectively. Finally, the electric and magnetic charge densities are integrated in the primary and dual grid cell volume delivering the corresponding charge vectors $\mathbf{q}_e$ and $\mathbf{q}_m$ as the corresponding state variables.

As mentioned in the beginning, the application of the above discretisation scheme to the Maxwell equations, leads to a system of metric equations for the FIT state variables, the so-called Maxwell grid equations. In their most general form, the Maxwell grid equations read

$$\mathbf{C}\widehat{\mathbf{e}} = -\frac{d}{dt}\widehat{\widehat{\mathbf{b}}} - \widehat{\widehat{\mathbf{j}}}_m \tag{7.1}$$

$$\widetilde{\mathbf{C}}\widehat{\mathbf{h}} = \frac{d}{dt}\widehat{\widehat{\mathbf{d}}} + \widehat{\widehat{\mathbf{j}}}_e \tag{7.2}$$

$$\widetilde{\mathbf{S}}\widehat{\widehat{\mathbf{d}}} = \mathbf{q}_e \tag{7.3}$$

$$\mathbf{S}\widehat{\widehat{\mathbf{b}}} = \mathbf{q}_m. \tag{7.4}$$

$\mathbf{C}, \widetilde{\mathbf{C}}$ stand for the discrete topological curl operators applying to the entities of the primary and the dual grid respectively. They are interrelated via the duality property $\widetilde{\mathbf{C}} = \mathbf{C}^T$. In the same fashion, $\mathbf{S}$ and $\widetilde{\mathbf{S}}$ matrices form the corresponding discrete div operators acting upon the two grid-related variables, and which retain the topological structure of their continuous counterparts, namely

$$\mathbf{SC} = \mathbf{0}. \tag{7.5}$$

The analogous relation exists also for the dual-grid operators.

It proves useful to introduce also the discrete grad operator $\mathbf{G}$, which satisfies the corresponding vector identity

$$\mathbf{CG} = \mathbf{0}. \tag{7.6}$$

Notice that $\mathbf{S}$ and $\mathbf{G}$ are related via $\mathbf{G} = -\widetilde{\mathbf{S}}^T$. The identity expressed by (7.5) guaranties a divergence free electric and magnetic current, $\widehat{\widehat{\mathbf{j}}}_e, \widehat{\widehat{\mathbf{j}}}_m$ in the absence of free charges as it can be easily shown by direct application in (7.2) and (7.1) respectively, which is nothing less that the electric and magnetic current conservation statement.

The above described numerical scheme is completed by the constitutive material relations, which in case of linear materials read

$$\widehat{\widehat{\mathbf{d}}} = \mathbf{M}_{\varepsilon}\widehat{\mathbf{e}} \tag{7.7}$$

$$\widehat{\widehat{\mathbf{b}}} = \mathbf{M}_{\mu}\widehat{\mathbf{h}} \tag{7.8}$$

$$\widehat{\widehat{\mathbf{j}}}_{ec} = \mathbf{M}_{\kappa}\widehat{\mathbf{e}} \tag{7.9}$$

where $\widehat{\widehat{\mathbf{j}}}_{ec}$ gives for the eddy-current contribution to the total electric current term $\widehat{\widehat{\mathbf{j}}}_{e}$, and the diagonal matrices $\mathbf{M}_{\varepsilon}$, $\mathbf{M}_{\mu}$[1] and $\mathbf{M}_{\kappa}$ stand for the electric permittivity, magnetic permeability and electric conductivity matrices respectively. For a detailed description of their structure and their construction the reader is referred to [113, 114].

The utility of the non-physical magnetic current $\widehat{\widehat{\mathbf{j}}}_{m}$ and magnetic charge $\mathbf{q}_m$ sources has been discussed in the previous chapters. It is recalled that these sources appear in the Maxwell equations when field discontinuities are introduced in the solution as a result of the truncating the physical domain. They are useful in the formulation of equivalent problem classes and the construction of hybrid techniques.

### 7.1.2 The magnetostatic formulation

The magnetostatic formulation is deduced by eliminating the time derivatives in the Maxwell grid equations (7.1)-(7.4). In analogy with the continuous case, we assume a special solution to the inhomogeneous Ampère equation

$$\widetilde{\mathbf{C}}\widehat{\mathbf{h}}_0 = \widehat{\widehat{\mathbf{j}}}_{s} \tag{7.10}$$

where $\widehat{\widehat{\mathbf{j}}}_{s}$ stands for the source current. $\widehat{\mathbf{h}}_0$ can be any (physical or non-physical) solution that satisfies (7.10). A convenient choice would be the magnetic field solution in the air, as it occurs by application of the Biot-Savart law.

The total magnetic field can thus be written

$$\widehat{\mathbf{h}} = \widehat{\mathbf{h}}_d + \widehat{\mathbf{h}}_0 \tag{7.11}$$

with $\widehat{\mathbf{h}}_d$ satisfying a zero-curl condition. Taking advantage of (7.6), we are allowed to introduce a scalar potential defined via

$$\widehat{\mathbf{h}}_d = -\widetilde{\mathbf{G}}\boldsymbol{\phi} \tag{7.12}$$

which upon substitution to the Gauss equation (7.4) yields the FIT magnetostatic formulation

$$-\mathbf{S}\mathbf{M}_{\mu}\widetilde{\mathbf{G}}\boldsymbol{\phi} = \mathbf{q}_m \tag{7.13}$$

with the equivalent magnetic charge distribution

$$\mathbf{q}_m = -\mathbf{S}\mathbf{M}_{\mu}\widehat{\mathbf{h}}_0. \tag{7.14}$$

---

[1] The magnetic permeability matrix is obtained by the inverse of the reluctivity matrix $\mathbf{M}_{\nu} = \mathbf{M}_{\mu}^{-1}$ since in the classical FIT formulation the material averaging is carried out for the reluctivity values.

### 7.1.3 The magneto-quasistatic formulation

As mentioned in chapter 2, the magneto-quasistatic formulation is obtained by assuming that the displacement current is negligible with respect to the ohmic current, i.e. $d\widehat{\widehat{\mathbf{d}}}/dt \ll \mathbf{M}_\kappa \widehat{\mathbf{e}}$. Eliminating this term from the Maxwell grid equations and after some manipulations, we obtain the eddy-current equation

$$\widetilde{\mathbf{C}}\mathbf{M}_\nu \mathbf{C}\widehat{\mathbf{e}} + \mathbf{M}_\kappa \frac{d}{dt}\widehat{\mathbf{e}} = -\frac{d}{dt}\widehat{\widehat{\mathbf{j}}}_e - \widetilde{\mathbf{C}}\mathbf{M}_\nu \widehat{\widehat{\mathbf{j}}}_m \tag{7.15}$$

with the reluctivity matrix $\mathbf{M}_\nu = \mathbf{M}_\mu^{-1}$. Equation (7.15) is known as the curl-curl equation for the magneto-quasistatic regime.

It is perhaps convenient to establish here the link between the electric field solution described by (7.15) and the magnetic field potential $\mathbf{A}$ used in the semi-analytical formulations discussed in the previous chapters. In case of a 6-component solution, the magnetic potential formulation does not offer a specific advantage with respect with the field formulation and hence the corresponding formulation in the context of a full numerical solution presents merely theoretical interest. We shall investigate however this formulation for the sake of completeness and to establish the analogy with the TREE solutions of the previous chapters.

Let us first assume the case with zero magnetic sources. The magnetic Gauss equation reads

$$\mathbf{S}\widehat{\widehat{\mathbf{b}}} = \mathbf{0}. \tag{7.16}$$

By virtue of the property (7.5), we can introduce the magnetic vector potential defined via the relation

$$\widehat{\widehat{\mathbf{b}}} = \mathbf{C}\widehat{\mathbf{a}}. \tag{7.17}$$

Note that the potential quantity described by the above definition is integrated along the primary grid edges as imposed by the appropriate metric considerations.

Equation (7.17) in combination with (7.1) and (7.6) result in the relation

$$\widehat{\mathbf{e}} = -\frac{d}{dt}\widehat{\mathbf{a}} - \mathbf{G}\boldsymbol{\phi}. \tag{7.18}$$

The absence of free space charges allows us to ignore the scalar potential term, as we did for the continuous case, bringing us to write the electric field as the negative time derivative of the magnetic potential.

In case that magnetic current sources are present, however, neither (7.17) nor (7.18) are valid. To circumference the problem we follow the same recipe proposed in section 5.9, i.e. integrate (7.1) in time and solve with respect to $\widehat{\widehat{\mathbf{b}}}$

$$\widehat{\widehat{\mathbf{b}}} = \mathbf{C}\left[-\int_0^t \widehat{\mathbf{e}}(\tau)\,d\tau\right] - \int_0^t \widehat{\widehat{\mathbf{j}}}_m(\tau)\,d\tau. \tag{7.19}$$

Obviously (7.19) reduces to (7.17) for vanishing magnetic current. Hence setting conventionally $\widehat{\mathbf{e}} = -d\widehat{\mathbf{a}}/dt$ (7.19) becomes

$$\widehat{\widehat{\mathbf{b}}} = \mathbf{C}\widehat{\mathbf{a}} - \int\limits_0^t \widehat{\widehat{\mathbf{j}}}_m(\tau)\,d\tau \tag{7.20}$$

which can be seen as the generalisation of the magnetic potential definition in the presence of magnetic current sources. Using the above definition the eddy-current equation for the magnetic potential becomes

$$\widetilde{\mathbf{C}}\mathbf{M}_\nu\mathbf{C}\widehat{\mathbf{a}} + \mathbf{M}_\kappa\frac{d}{dt}\widehat{\mathbf{a}} = \widehat{\widehat{\mathbf{j}}}_e + \widetilde{\mathbf{C}}\mathbf{M}_\nu\int\limits_0^t \widehat{\widehat{\mathbf{j}}}_m(\tau)\,d\tau. \tag{7.21}$$

The harmonic formulation is deduced straightforwardly by setting $f(t) = e^{i\omega t}$ and simplifying the time exponential term from both sides. The resulting expression is given for completeness

$$\widetilde{\mathbf{C}}\mathbf{M}_\nu\mathbf{C}\widehat{\mathbf{a}} + i\omega\mathbf{M}_\kappa\widehat{\mathbf{a}} = \widehat{\widehat{\mathbf{j}}}_e + \frac{1}{i\omega}\widetilde{\mathbf{C}}\mathbf{M}_\nu\widehat{\widehat{\mathbf{j}}}_m. \tag{7.22}$$

Equation (7.22) is the analogue of (5.71).

### 7.1.4 Coordinate conventions

As mentioned in the beginning of this chapter, we are interested in electromagnetic inspection problems basically with configurations consisting of a translationally or rotationally symmetric work-piece and an arbitrary current distribution. The reason is that, owing to the short-range of the induction field, only a very narrow fraction of the total piece around the exciting coil is affected. Since the great majority of the pieces in practical situations are either symmetric or at least possess a large curvature radius in one of their principal axes, they can be approximated with good accuracy as either translationally or rotationally symmetric. The two cases are conveniently addressed in the context of the FIT discretisation scheme using a cartesian and a cylindrical grid system, respectively.

Let $y$ and $\phi$ be the axis of invariance for the translationally and rotationally symmetric case, respectively. In order to better exploit the isomorphism of the transversal plane for the two grid systems, namely the $x - z$ plane for the cartesian and $\rho - z$ plane for the cylindrical one, a generic coordinate system $(u, v, w)$ is introduced, which is defined in the following way. Let $w$ be the symmetry axis in both cases. $u$ and $v$ are assigned to the remaining two axes in a way that they satisfy the right hand rule, namely $\hat{\mathbf{u}} \times \hat{\mathbf{v}} = \hat{\mathbf{w}}$ (and the thereupon cyclic permutations), where $\hat{\mathbf{u}}, \hat{\mathbf{v}}, \hat{\mathbf{w}}$ stand for the unit vectors in $u$, $v$ and $w$ direction. Hence we obtain the transformation rule, $(x, y, z) \rightarrow (u, -w, v)$ for the cartesian system and $(\rho, \phi, z) \rightarrow (u, -w, v)$ for the cylindrical one. Using the thus defined coordinate system, the same relations will apply hereafter indistinguishably for the two symmetries.

## 7.2 Equivalent source formulations

According to our basic hypothesis, the current sources are arbitrary with the only condition they must verify is that they must be solenoidal, namely

$$\nabla \cdot \mathbf{J}_s = 0 \tag{7.23}$$

or equivalently in the FIT basis

$$\widetilde{\mathbf{S}}\widehat{\widehat{\mathbf{j}}}_s = 0 \tag{7.24}$$

in order to be consistent with the magnetostatic or the magneto-quasistatic approximation.

In reality, the current sources involved in the majority of practical eddy current applications are coils of several shapes, which are allowed to change position and orientation during a scan. The straight forward approach to handle the excitation currents is to project them on the FIT grid system (or the mixed spatial-spectral basis that will be presented in the following paragraphs). Nevertheless, this approach has several drawbacks. The direct discretisation is cumbersome for complicated coil shapes and arbitrary orientations, and the accuracy of the current discretisation is dependent on the grid refinement, which in addition needs to be adapted at every scan position. Furthermore, we have to deal with the small coil lift-offs that are relevant in ECT applications.

An elegant way to bypass this problem is to formulate an equivalent problem, where the current source is taken into account indirectly in a similar way with what we have done for the construction of spectral solutions. In this way, the coil field in the air is calculated either analytically by straight-forward evaluation of Biot-Savart's integral or via a modal approach as shown in [115], and this field then is used as an equivalent source for the scattering problem. Beside the obvious advantages of alleviating the requirements for an adequate grid resolution, the fact that we are solving for the scattered, instead of the total field, (in the air) allows us to reduce the size of the computational domain, and hence the number of degrees of freedom (DOF).

There are two ways of formulating the equivalent problem. Either by using a perturbation approach, as we did in chapter 5, or by introducing surface sources according to the Huygens principle [3, 6].

### 7.2.1 Volume equivalent sources

Let us consider now the auxiliary problem of the coil source in the free-space. We assume that the computational domain and the thereupon constructed grids are identical with those of the original problem. The magnetic potential $\widehat{\mathbf{a}}_0$ will satisfy

$$\left(\widetilde{\mathbf{C}}\mathbf{M}_{\nu 0}\mathbf{C} + \mathbf{A}_g\right)\widehat{\mathbf{a}}_0(t) = \widehat{\widehat{\mathbf{j}}}_s(t)\,. \tag{7.25}$$

where $\mathbf{M}_{\nu 0}$ stands for the reluctivity matrix of the free-space and $\mathbf{A}_g$ is a gauge matrix whose role is to guarantee the system definitiveness. The gauging of the curl-curl equation will be discussed more in detail in a later section. Subtracting $\widehat{\mathbf{a}}_0$ from (7.21) and taking (7.25) into account, we can write

$$\left(\widetilde{\mathbf{C}}\mathbf{M}_\nu\mathbf{C} + \mathbf{A}_g + \mathbf{M}_\kappa\frac{d}{dt}\right)\widehat{\mathbf{a}}_s = -\left[\widetilde{\mathbf{C}}\left(\mathbf{M}_\nu - \mathbf{M}_{\nu 0}\right)\mathbf{C} + \mathbf{M}_\kappa\frac{d}{dt}\right]\widehat{\mathbf{a}}_0. \tag{7.26}$$

with $\widehat{\mathbf{a}}_s = \widehat{\mathbf{a}} - \widehat{\mathbf{a}}_0$ the difference (scattering) field.

Noting that the quantities $\left(\mathbf{M}_\nu - \mathbf{M}_{\nu 0}\right)\mathbf{C}\widehat{\mathbf{a}}_0$ and $\mathbf{M}_\kappa\dot{\widehat{\mathbf{a}}}_0$ can be viewed as equivalent magnetic and electric currents, consistent with the grid Maxwell equations, (7.26) can be written as

$$\left(\widetilde{\mathbf{C}}\mathbf{M}_\nu\mathbf{C} + \mathbf{A}_g + \mathbf{M}_\kappa\frac{d}{dt}\right)\widehat{\mathbf{a}}_s = \widehat{\widehat{\mathbf{j}}}_e + \widetilde{\mathbf{C}}\mathbf{M}_\nu\int\limits_0^t \widehat{\widehat{\mathbf{j}}}_m(\tau)\,d\tau \tag{7.27}$$

with the electric and magnetic equivalent current

$$\widehat{\widehat{\mathbf{j}}}_e = \mathbf{M}_\kappa\dot{\widehat{\mathbf{a}}}_0 \tag{7.28}$$

$$\widehat{\widehat{\mathbf{j}}}_m = \left(\mathbf{I} - \mathbf{M}_{\mu_r}\right)\dot{\widehat{\widehat{\mathbf{b}}}}_0 \tag{7.29}$$

where the definition relation of the magnetic potential (7.17) has been used. $\mathbf{M}_{\mu_r} := \mathbf{M}_\mu\mathbf{M}_{\nu 0}$ is the relative magnetic permeability matrix. Equation (7.27) has exactly the same form with (7.21). The material matrices in both (7.28),(7.29) denote the difference of the corresponding material coefficient from the air.

In problems involving stationary sources, a further simplification is also possible if we recall that the magnetostatic formulation in the air implies that the magnetic vector potential $\widehat{\mathbf{a}}_0(t)$ follows instantaneously the current source variations. Mathematically speaking, this is equivalent with stating that the spatial and temporal part of the magnetic potential in the air are separable. Hence, if $f(t)$ denotes the temporal variation of the feed current, one can write $\dot{\widehat{\mathbf{a}}}_0 = \widehat{\mathbf{a}}_0 f'(t)$ and $\dot{\widehat{\widehat{\mathbf{b}}}}_0 = \widehat{\widehat{\mathbf{b}}}_0 f'(t)$, where $\widehat{\mathbf{a}}_0, \widehat{\widehat{\mathbf{b}}}_0$ stands for the magnetic vector potential and the magnetic flux solutions for a constant current source and has to be calculated only once, outside the time-stepping iteration loop.

In the frequency domain, the respective equation for the scattering field follows the generic expression (7.22) with the equivalent currents

$$\widehat{\widehat{\mathbf{j}}}_e = i\omega\mathbf{M}_\kappa\widehat{\mathbf{a}}_0 \tag{7.30}$$

$$\widehat{\widehat{\mathbf{j}}}_m = i\omega\left(\mathbf{I} - \mathbf{M}_{\mu_r}\right)\widehat{\widehat{\mathbf{b}}}_0. \tag{7.31}$$

### 7.2.2 Surface equivalent sources: the Huygens principle

An alternative approach for replacing the physical sources is based on the equivalence principle, in particular, the formulation known as the induction equivalent and has been discussed in section 2.3. The quintessence of the theorem consists in the introduction of a fictitious closed boundary $\partial V$, which entirely encloses the conducting piece, and the subsequent replacement of the initial volumetric

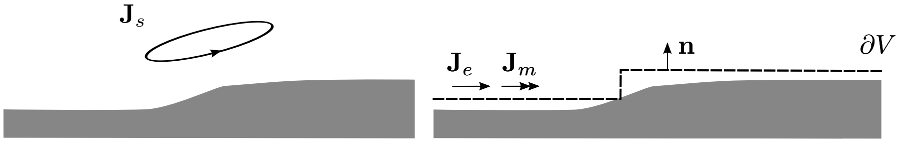

(a) (b)

Figure 7.2: Construction of the equivalent problem: (a) original configuration, (b) equivalent problem with electric and magnetic surface currents. The boundary surface is indicated by the dotted line, and is assumed to be closing in the infinity.

electric current source by surface electric and a surface magnetic sources on $\partial V$. The new problem is equivalent to the original one in the interior of the boundary $\partial V$, which will be called henceforth as the Huygens surface for brevity. A schematic representation of the equivalence principle is shown in Fig. 7.2.

Let $\mathbf{E}_0$ and $\mathbf{H}_0$ be, the electric and magnetic field induced by the current source in the absence of the work-piece. The equivalent sources are then defined via the relations

$$\mathbf{J}_e = \mathbf{n} \times \mathbf{H}_0 \tag{7.32}$$

$$\mathbf{J}_m = -\mathbf{n} \times \mathbf{E}_0 \tag{7.33}$$

$\mathbf{n}$ being the outwards pointing unit normal to $\partial V$. For the sake of simplicity, we shall consider only the first equation for a Huygens surface normal to the $v$ axis, at $v = v_s$. The analysis for the $u$ axis and the magnetic current density is analogous. The equivalent electric current density obtained by the application of the definition relation (7.32) reads

$$\begin{pmatrix} J_{e,u}(u,v) \\ J_{e,v}(u,v) \\ J_{e,w}(u,v) \end{pmatrix} = \begin{pmatrix} H_w(u,v_s) \\ 0 \\ -H_u(u,v_s) \end{pmatrix} \delta(v - v_S)\,. \tag{7.34}$$

The delta function on the right-hand side of the equation stems from the fact that the equivalent current distribution has by definition zero thickness. In order to obtain from (7.34) the respective FIT state variables, one needs to integrate both sides over the corresponding dual grid facets crossed by the equivalent current

$$\begin{pmatrix} \widehat{\widehat{\mathbf{j}}}_{e,u} \\ \widehat{\widehat{\mathbf{j}}}_{e,v} \\ \widehat{\widehat{\mathbf{j}}}_{e,w} \end{pmatrix} = \begin{pmatrix} \widehat{\mathbf{h}}_w \\ \mathbf{0} \\ -\widehat{\mathbf{h}}_u \end{pmatrix}. \tag{7.35}$$

It should be noticed that in the derivation of the above relation the delta function removes the integration along $v$, whereas the remaining integral along the tangential direction yields the FIT magnetic voltage variables $\widehat{\mathbf{h}}$. Repeating the

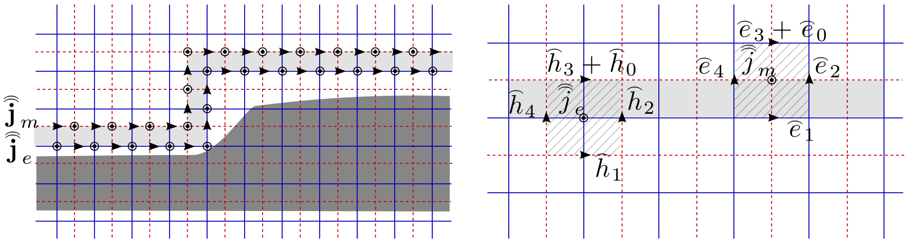

(a) (b)

Figure 7.3: Realisation of the equivalent sources formulation in the FIT grid: (a) electric and magnetic current distributions on the surfaces associated with the primary and dual grid respectively, (b) application of the Faraday and Ampère laws in a primary and a dual grid cell intersected by the corresponding boundary surfaces.

same procedure for the other components and for both different orientations of the Huygens surface, (7.32),(7.33) can be written in a matrix form

$$\widehat{\widehat{\mathbf{j}}}_e = \mathbf{N}\widehat{\mathbf{h}}_0 \tag{7.36}$$

$$\widehat{\widehat{\mathbf{j}}}_m = -\mathbf{N}\widehat{\mathbf{e}}_0, \tag{7.37}$$

with the matrix operator $\mathbf{N}$ being defined as

$$\mathbf{N} = \begin{pmatrix} \mathbf{0} & \mathbf{0} & \mathbf{s}_v \\ \mathbf{0} & \mathbf{0} & -\mathbf{s}_u \\ -\mathbf{s}_v & \mathbf{s}_u & \mathbf{0} \end{pmatrix} \tag{7.38}$$

with $\mathbf{s}_u = \mathrm{diag}\left[\mathrm{sgn}(\mathbf{n}_i \cdot \hat{u})\right]$ and $\mathbf{n}_i$ being the normal to the Huygens surface vector at the $i$th grid point.

The above definition of the equivalent currents has been based on the classical theory of the induction equivalent for the continuous case [3]. The same relation can be also derived by considering the Maxwell grid equations locally, at a cell level. Let us consider for example the shaded primary cell in Fig. 7.3. Application of Faraday's law in this cell yields

$$\widehat{e}_1 + \widehat{e}_2 - (\widehat{e}_3 + \widehat{e}_0) - \widehat{e}_4 = -\widehat{\widehat{j}}_m \tag{7.39}$$

where we have split the total electric field at the upper part of the cell to the source field contribution in the free space $\widehat{e}_0$ and the scattered field contribution $\widehat{e}_3$. Bringing the source field term in the right-hand side and taking into account the Huygens' surface orientation $s_v = 1$, we obtain

$$\widehat{e}_1 + \widehat{e}_2 - \widehat{e}_3 - \widehat{e}_4 = -\widehat{\widehat{j}}_m + s_v \widehat{e}_0. \tag{7.40}$$

Repeating the same procedure for all the cells crossing the Huygens surface and taking into account both possible orientations of the latter we arrive at the following relation

$$\mathbf{C}\widehat{\mathbf{e}} = -\widehat{\widehat{\mathbf{j}}}_m + \mathbf{N}\widehat{\mathbf{e}}_0. \tag{7.41}$$

In the same fashion we obtain for Ampère's law

$$\widetilde{\mathbf{C}}\widehat{\mathbf{h}} = \widehat{\widehat{\mathbf{j}}}_e - \mathbf{N}\widehat{\mathbf{h}}_0. \tag{7.42}$$

Comparison of (7.41),(7.42) with (7.1),(7.2) yields the equivalent currents definition of (7.36),(7.37).

## 7.3 Modal expansion in the direction of symmetry

The expressions presented in the previous paragraphs apply to any 3D problem without any particular assumptions in terms of neither the piece geometry nor the shape of the current source (provided that they describe a closed circuit). Nonetheless, as mentioned in the introduction of this chapter, the pieces involved in a large number of practical inspection configurations are, or can be approximated as, symmetric along one direction. This fact can be exploited in a non-negligible extent in order to obtain efficient numerical solutions. The adopted approach follows the same path with the solutions developed in the previous chapters, that is, a modal projection basis is introduced along the axis of invariance (which will be assumed being the $w$-axis henceforth), thus forming a mixed spatial-spectral formulation.

Adopting again the TREE working assumption, i.e. considering the eddy-current field negligible at sufficient distances from the source, we truncate the computational domain at $\pm L$ in case of the cartesian system, using a perfectly electric conductor (PEC) or perfectly magnetic conductor (PMC) condition. The use of either PEC of PMC termination implies periodicity of the solution along the truncation direction, which, given a sufficiently large $L$, does not introduce significant aliasing in the region of interest, as indicated above.

Making use of the above periodicity and taking into account the invariance of the geometry along $w$, we can expand all state variables in terms of an exponential Fourier series along that direction as follows:

$$\mathbf{x}(u, v, w) = \sum_{n=-\infty}^{\infty} \mathbf{x}_n(u, v)\, e^{i\kappa_n w} \tag{7.43}$$

with $\kappa_n = n\pi/L$ for translational and $\kappa_n = n$ for rotational symmetry, respectively. Practically, the above sum is limited to a finite number of modes $N$, which depends upon the details of the configuration. In most cases, (7.43) converges rapidly, thus a number of modes of a few tens delivers a very satisfactory precision [29, 34, 36, 39–41].

### 7.3.1 Discretisation on the transversal plane

For simplicity reasons, we shall focus on the harmonic case for the development of the basic formulation. Transient solutions can then be constructed upon by generalising the harmonic formulation.

We apply the (7.43) expansion to the FIT state variables $\widehat{\mathbf{e}}, \widehat{\mathbf{h}}, \widehat{\widehat{\mathbf{b}}}, \widehat{\widehat{\mathbf{j}}}_e$ and $\widehat{\widehat{\mathbf{j}}}_m$, and we derive the Maxwell grid equations on a FIT grid doublet $\{G, \widetilde{G}\}$ consisting of a single cell along the $w$ direction, centred at $w = 0$ (cf. Fig. 7.4). Note here that the variation along the $w$ direction is taken into account by means of (7.43), the finite cell size $\Delta w$ along the $w$ direction, is merely used for mathematical convenience and numerical stability.

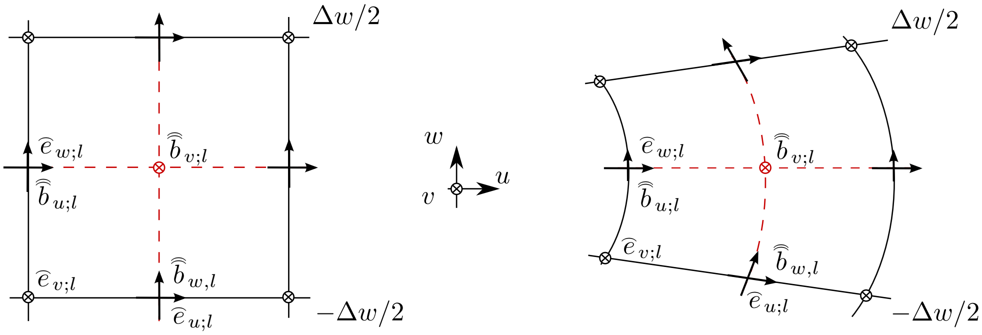

Figure 7.4: Grid section on the $u-w$ plane for the two coordinate systems. The $\widehat{\mathbf{e}}_u$, $\widehat{\mathbf{e}}_v$ and $\widehat{\widehat{\mathbf{b}}}_w$ elements are calculated at the $\pm\Delta w/2$ positions whereas $\widehat{\mathbf{e}}_w$, $\widehat{\widehat{\mathbf{b}}}_u$ and $\widehat{\widehat{\mathbf{b}}}_v$ need to be integrated in the $[-\Delta w/2, \Delta w/2]$ interval. $l$ stands for the cell index.

Let us consider the calculation of the state variables at an arbitrary cell $i$, whose $u-w$ plane section is shown in Fig. 7.1. For the sake of brevity, we shall restrict the analysis to the $\widehat{\mathbf{e}}$, $\widehat{\widehat{\mathbf{b}}}$ variables only. The same calculations apply for the remaining variables $\widehat{\mathbf{h}}$, $\widehat{\widehat{\mathbf{j}}}_e$ and $\widehat{\widehat{\mathbf{j}}}_m$.

From the geometry of the grids and the FIT allocation system it is clear that the $\widehat{e}_{u,i}$, $\widehat{e}_{v,i}$ and $\widehat{\widehat{b}}_{w,i}$ elements need to be calculated at $w = -\Delta w/2$, which yields for these variables

$$\begin{Bmatrix} \widehat{e}_{u,v;l}(-\Delta w/2) \\ \widehat{\widehat{b}}_{w;l}(-\Delta w/2) \end{Bmatrix} = \sum_{n=-\infty}^{\infty} \begin{Bmatrix} \widehat{\mathbf{e}}_{u,v;ln} \\ \widehat{\widehat{\mathbf{b}}}_{w;ln} \end{Bmatrix} \exp(-i\kappa_n \Delta w/2)\,. \tag{7.44}$$

The $e_{w;l}$ element is integrated along the $[-\Delta w/2, \Delta w/2]$ integral, which signifies

$$\begin{aligned} \widehat{e}_{w;l}(0) &= \sum_{n=-\infty}^{\infty} e_{w;ln} \int\limits_{-\Delta w/2}^{\Delta w/2} e^{i\kappa_n w} dw \\ &= \sum_{n=-\infty}^{\infty} e_{w;ln} \Delta w \operatorname{sinc}(\kappa_n w) \end{aligned} \tag{7.45}$$

In the same fashion we obtain for the $\widehat{\widehat{b}}_{u;ln}$, $\widehat{\widehat{b}}_{v;ln}$ fluxes

$$\left\{ \begin{array}{l} \widehat{\widehat{b}}_{u;l}(0) \\ \widehat{\widehat{b}}_{v;l}(0) \end{array} \right\} = \sum_{n=-\infty}^{\infty} \left\{ \begin{array}{l} \int\limits_{\Delta v_l} b_{u;n}(v)\, dv \\ \int\limits_{\Delta v_l} b_{v;n}(u)\, du \end{array} \right\} \Delta w \operatorname{sinc}(\kappa_n w) \tag{7.46}$$

with $\Delta_{v;l}\Delta w$, $\Delta_{u;l}\Delta w$ standing for the respective facets areas. Note that the metric of the grid is implicitly taken into account via the integration along the corresponding grid elements. Hence, in the case of a cylindrical grid, the $u$ integrals are carried out along the corresponding arcs $u_i \Delta w$ (recall that the $w$ coordinate in the cylindrical coordinate system is the azimuthal angle $\phi$).

In order to comply with the ordinary FIT conventions, we define

$$\widehat{e}_{w;ln} \coloneqq x_{w;ln} \Delta w \tag{7.47}$$

and

$$\widehat{\widehat{b}}_{t;ln} \coloneqq \left\{ \begin{array}{l} \int\limits_{\Delta v_l} b_{u;n}(v)\, dv \\ \int\limits_{\Delta v_l} b_{v;n}(u)\, du \end{array} \right\} \Delta w. \tag{7.48}$$

Notice that the thus defined integrated state variables differ from their exact values, which are obtained after multiplication with the $\operatorname{sinc}(\kappa \Delta w/2)$ term. The reason for this definition (which has however no impact to the accuracy of the method) is the elimination of the sinc(.) terms from the discrete equations. Once the values of the integrated variables are known, we can obtain at any moment the exact value by restoring the $\operatorname{sinc}(\kappa \Delta w/2)$ term.

Using the above conventions, the Maxwell grid equations take the following form in the spatial-spectral domain

$$(\mathbf{C}_t + i\alpha_n \mathbf{J})\, \widehat{\mathbf{e}} = -i\omega \widehat{\widehat{\mathbf{b}}} - \widehat{\widehat{\mathbf{j}}}_m \tag{7.49}$$

$$\left(\widetilde{\mathbf{C}}_t + i\alpha_n \mathbf{J}\right) \widehat{\mathbf{h}} = \widehat{\widehat{\mathbf{j}}}_e \tag{7.50}$$

$$\left(\widetilde{\mathbf{S}}_t + i\alpha_n \mathbf{E}\right) \widehat{\widehat{\mathbf{d}}} = \mathbf{q}_e \tag{7.51}$$

$$(\mathbf{S}_t + i\alpha_n \mathbf{E})\, \widehat{\widehat{\mathbf{b}}} = \mathbf{0} \tag{7.52}$$

with $\alpha_n = \kappa_n \Delta_w$. $\mathbf{C}_t$ and $\mathbf{S}_t$ stand for the transversal curl and div primary gird operators, given by

$$\mathbf{C}_t = \begin{pmatrix} \mathbf{0} & \mathbf{0} & \mathbf{P}_v \\ \mathbf{0} & \mathbf{0} & -\mathbf{P}_u \\ -\mathbf{P}_v & \mathbf{P}_u & \mathbf{0} \end{pmatrix} \tag{7.53}$$

and

$$\mathbf{S}_t = \begin{pmatrix} \mathbf{P}_u & \mathbf{P}_v & \mathbf{0} \end{pmatrix} \tag{7.54}$$

whereas $\mathbf{J}$ and $\mathbf{E}$ are unit matrices

$$\mathbf{J} = \begin{pmatrix} \mathbf{0} & -\mathbf{I} & \mathbf{0} \\ \mathbf{I} & \mathbf{0} & \mathbf{0} \\ \mathbf{0} & \mathbf{0} & \mathbf{0} \end{pmatrix} \tag{7.55}$$

and

$$\mathbf{E} = \begin{pmatrix}\mathbf{0}\,\mathbf{0}\,\mathbf{I}\end{pmatrix} \tag{7.56}$$

and $\mathbf{P}_{u,v}$ submatrices stand for the discrete differentiation operators along the two coordinate axes of the $u - v$ plane. Their detailed expressions are given in [113]. The corresponding relations for the dual-grid matrices are obtained by applying the duality principle given above. Since the spatial dependence along the normal $w$ axis has been absorbed by the modal expansion terms, there is no need to refer to the initial single $w$-cell 3D grid, the planar grid system depicted in Fig. 7.5 being more appropriate for the analysis.

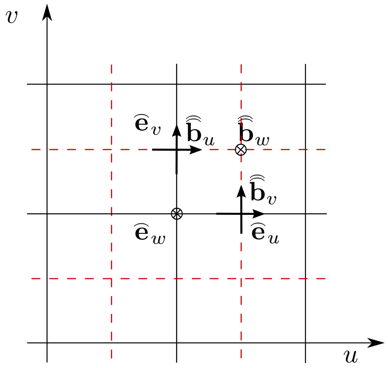

Figure 7.5: Two dimensional grid on the $u - v$ plane after application of the modal expressions.

Eliminating $\widehat{\mathbf{h}}$, $\widehat{\widehat{\mathbf{b}}}$ from the Maxwell grid equations (7.49),(7.50) taking into account the constitutive relations (7.8),(7.9) yields the following discrete curl-curl equation for the mode $n$

$$\left(\mathbf{A}_n + i\omega\mathbf{M}_\kappa\right)\widehat{\mathbf{e}}_n = -i\omega\widehat{\widehat{\mathbf{j}}}_{e,n} - \left(\widetilde{\mathbf{C}}_t + i\alpha_n\mathbf{J}\right)\mathbf{M}_\nu\widehat{\widehat{\mathbf{j}}}_{m,n}. \tag{7.57}$$

with

$$\mathbf{A}_n = \widetilde{\mathbf{C}}_t\mathbf{M}_\nu\mathbf{C}_t + i\alpha_n\left(\widetilde{\mathbf{C}}_t\mathbf{M}_\nu\mathbf{J} + \mathbf{J}\mathbf{M}_\nu\mathbf{C}_t\right) - \alpha_n^2\mathbf{J}\mathbf{M}_\nu\mathbf{J}. \tag{7.58}$$

Recall that no matter which equivalent source definition we use (volume or surface equivalent currents), their modal projection is algorithmically very easy since no geometrical considerations due to the current support along the modal axis $w$ are needed (the projection integral is a simple integral that spans the entire computational domain $[-L, L]$ or $[0, 2\pi]$).

It is interesting to derive the explicit formulations of the different matrix terms in the curl-curl equation (7.57) in order to get insight to the physical interpretation of the different terms. Hence, one can show

$$\widetilde{\mathbf{C}}_t\mathbf{M}_\nu\mathbf{C}_t = \begin{pmatrix} \mathbf{P}_v^T\mathbf{M}_w\mathbf{P}_v & -\mathbf{P}_v^T\mathbf{M}_w\mathbf{P}_u & \mathbf{0} \\ -\mathbf{P}_u^T\mathbf{M}_w\mathbf{P}_v & \mathbf{P}_u^T\mathbf{M}_w\mathbf{P}_u & \mathbf{0} \\ \mathbf{0} & \mathbf{0} & \mathbf{P}_v^T\mathbf{M}_u\mathbf{P}_v + \mathbf{P}_u^T\mathbf{M}_v\mathbf{P}_u \end{pmatrix} \tag{7.59}$$

$$\widetilde{\mathbf{C}}_t\mathbf{M}_\nu\mathbf{J}+\mathbf{J}\mathbf{M}_\nu\mathbf{C}_t=\begin{pmatrix}\mathbf{0} & \mathbf{0} & \mathbf{M}_v\mathbf{P}_u\\ \mathbf{0} & \mathbf{0} & \mathbf{M}_u\mathbf{P}_v\\ \mathbf{P}_u^T\mathbf{M}_v & \mathbf{P}_v^T\mathbf{M}_u & \mathbf{0}\end{pmatrix} \tag{7.60}$$

and

$$\mathbf{J}\mathbf{M}_\nu\mathbf{J}=-\begin{pmatrix}\mathbf{M}_v & \mathbf{0} & \mathbf{0}\\ \mathbf{0} & \mathbf{M}_u & \mathbf{0}\\ \mathbf{0} & \mathbf{0} & \mathbf{0}\end{pmatrix}. \tag{7.61}$$

where $\mathbf{M}_u, \mathbf{M}_v$ and $\mathbf{M}_w$ are the submatrices of the inverse magnetic permeability (reluctivity) matrix along the $u, v$ and $w$ directions, respectively. The two non-zero clusters lumped around the main matrix diagonal in (7.59) and (7.61) stand for the TE$_w$ and TM$_w$ parts of the curl-curl operator. The TE$_w$ and TM$_w$ solutions are coupled via the (7.60) matrix. Clearly for $a_n = 0$, the two solutions are independent, which reproduces the theoretical result of the TE$_w$ and TM$_w$ uncoupling in the 2D case.

### 7.3.2 Gauging

When applied to non-conducting regions, (7.57) leads to non-unique solutions since any term of the form $-\mathbf{G}\psi$, with $\psi$ an arbitrary scalar potential, belongs to the null-space of the curl-curl operator, as it can be easily verified using the identity (7.6). This is a well-known issue in low-frequency electromagnetic problems, and a number of different gauging strategies have been proposed in the literature to address it, the tree-cotree formulation being a well established techniques [116,117]. Yet, the matrix structure of the FIT discretisation scheme offers a simple way of gauging, based on the subtraction of a rotational-free operator, which offers the additional advantage of a direct physical interpretation [118]. A more elaborated scheme, better suited for the quasistatic regime, has been proposed by Clemens et al. [119,120] for the FIT formulation, where a similar approach with the one proposed by Bossavit for the FEM method [121] is adopted. It is interesting to note the that in the air regions, the previous approach reduces to a regularisation term similar to the one proposed by Biro and Preis [122].

In this work, a simplified version of the regularisation matrix of [119,120] has been used, in the sense that the gauging matrix is restricted in the air-regions (which makes it also equivalent with that of [122]) and by the substitution of the therein defined scaling matrix $\mathbf{M_2}$ by a scalar coefficient equal to its minimum value, namely

$$g=\frac{r}{\mu_0\varepsilon_0^2\max D_{\tilde{V}}}\mathbf{M}_\varepsilon\mathbf{G}\widetilde{\mathbf{S}}\mathbf{M}_\varepsilon \tag{7.62}$$

with $D_{\tilde{V}}$ standing for the diagonal matrix of the dual cells volumes and $r$ being an optional relaxation factor (in this work we set $r = 1$). Note that the $1/\mu_0\varepsilon_0^2$ factor scales the matrix values to the free-space reluctivity (in accordance with [122] and [119, 120]), the $\mathbf{M}_\varepsilon$ term on the left realises the mapping of electric voltages to the electric flux density and hence assures the metric consistency, and the $\mathbf{M}_\varepsilon$ factor on the left restores the symmetry of the matrix. Finally, the cell volume factor balances the gauge term metric with that of the curl-curl matrix.

Substituting (7.54) and taking into account the definition of $\mathbf{G}$, the grad-div operator $\mathbf{G}\widetilde{\mathbf{S}}$ can be decomposed in three terms in the same fashion with curl-curl operator

$$\mathbf{G}\widetilde{\mathbf{S}} = -\widetilde{\mathbf{S}}_t^T\widetilde{\mathbf{S}}_t - i\alpha_n\left(\widetilde{\mathbf{S}}_t^T\mathbf{E} + \mathbf{E}^T\widetilde{\mathbf{S}}_t\right) - \alpha_n^2\mathbf{E}^T\mathbf{E} \tag{7.63}$$

with the submatrices $\mathbf{G}_t\widetilde{\mathbf{S}}_t$, $\mathbf{G}_t\mathbf{E} + \mathbf{E}^T\widetilde{\mathbf{S}}_t$ and $\mathbf{E}^T\mathbf{E}$ given by

$$\widetilde{\mathbf{S}}_t^T\widetilde{\mathbf{S}}_t = \begin{pmatrix} \mathbf{P}_u\mathbf{P}_u^T & \mathbf{P}_u\mathbf{P}_v^T & \mathbf{0} \\ \mathbf{P}_v\mathbf{P}_u^T & \mathbf{P}_v\mathbf{P}_v^T & \mathbf{0} \\ \mathbf{0} & \mathbf{0} & \mathbf{0} \end{pmatrix} \tag{7.64}$$

$$\widetilde{\mathbf{S}}_t^T\mathbf{E} - \mathbf{E}^T\widetilde{\mathbf{S}}_t = \begin{pmatrix} \mathbf{0} & \mathbf{0} & \mathbf{P}_u \\ \mathbf{0} & \mathbf{0} & \mathbf{P}_v \\ \mathbf{P}_u^T & \mathbf{P}_v^T & \mathbf{0} \end{pmatrix} \tag{7.65}$$

and

$$\mathbf{E}^T\mathbf{E} = \begin{pmatrix} \mathbf{0} & \mathbf{0} & \mathbf{0} \\ \mathbf{0} & \mathbf{0} & \mathbf{0} \\ \mathbf{0} & \mathbf{0} & -\mathbf{I} \end{pmatrix}. \tag{7.66}$$

### 7.3.3 Parity decomposition

Up to now, the properties of the solution along the symmetry axis $w$ were not discussed. In fact, the geometry being invariant along this direction by hypothesis, the solution profile can have (or does not have) a specific parity, something that will be determined by the parity of the excitation itself.

The parity of a given state variable is determined upon application of the space inversion operator $\hat{\boldsymbol{P}}_{\boldsymbol{w}}$, namely

$$\hat{\boldsymbol{P}}_{\boldsymbol{w}}\mathbf{x}^{(e/o)}(w) = \pm\mathbf{x}^{(e/o)}(-w)\,. \tag{7.67}$$

The parity operator should not be confused with the propagator operator defined in chapter 3. Solutions with given parity (odd or even) are eigensolutions of the parity operator, and the sign in (7.67) is the corresponding eigenvalue. It is easily understood that the presence of parity is equivalent to a Dirichlet/Neumann boundary condition at the $w = 0$ plane. In fact, this is the way that one would produce solutions of a given parity if one worked directly in the spatial domain.

It is well known that any arbitrary function can be written as the sum of an even and an odd function, or more formally stated, decomposed in the two parity states

$$\mathbf{x}(w) = \frac{1}{2}\left[\mathbf{x}(w) + \mathbf{x}(-w)\right] + \frac{1}{2}\left[\mathbf{x}(w) - \mathbf{x}(-w)\right]. \tag{7.68}$$

This signifies that we can focus on the study of the two parity states, the results being directly applicable to any arbitrary solution.

Since the parity is assigned to a given component (tangential and normal to the $w$ plane components admit opposite parities), the term is ambiguous unless we adopt a clear convention for naming the parity of the solutions. Hence, **we associate the parity of a given solution to the one of the $\widehat{\mathbf{a}}_w$ component**. For example, even parities solutions will dispose even $\widehat{\mathbf{a}}_w$ and odd $\widehat{\mathbf{a}}_{u,v}$ fields.

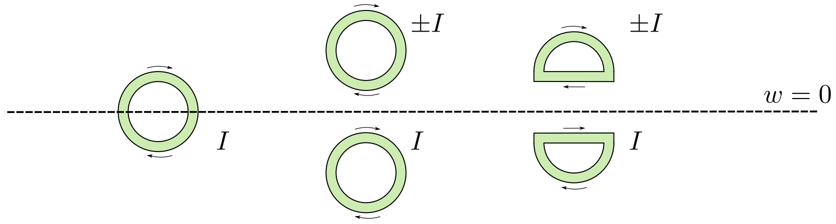

Figure 7.6: Typical coil arrangements producing even/odd parity solutions. In-phase currents produce even parity fields, whereas opposite currents are responsible for odd parity solutions.

From the practical point of view, even parity solutions follow naturally by symmetric coil configurations, such as the cylindrical coils, D-coils, etc. without tilt around the $u$ or $w$ axis and equal and in-phase feed current, as depicted in Fig. 7.6. Odd parity solutions are obtained by symmetric configurations with 180° phase difference between the elements across the $w$-plane (differential connection). Unbalanced current feeds or the presence of tilt produce in general solutions without specific parity.

From the properties of Fourier series, it turns out that the parity transformation is equivalent to inverting the sign of $n$, namely

$$\mathbf{x}(u, v, -w) = \sum_{n=-\infty}^{\infty} \mathbf{x}_n(u, v)\, e^{-i\kappa_n w} = \sum_{n=-\infty}^{\infty} \mathbf{x}_{-n}(u, v)\, e^{i\kappa_{-n} w}. \tag{7.69}$$

To examine the behaviour of the solutions to $n$ inversion, we write the state equation in the following form

$$\begin{pmatrix} \mathbf{A}^{TE} - \alpha_n^2 \mathbf{D} & i\alpha_n \mathbf{C}^T \\ i\alpha_n \mathbf{C} & \mathbf{A}^{TM} + \alpha_n^2 g \mathbf{I} \end{pmatrix} \begin{pmatrix} \widehat{\mathbf{a}}_n^{TE} \\ \widehat{\mathbf{a}}_n^{TM} \end{pmatrix} = \begin{pmatrix} \mathbf{q}_n^{TE} \\ \mathbf{q}_n^{TM} \end{pmatrix} \tag{7.70}$$

where

$$\mathbf{A}^{TE} = \begin{pmatrix} \mathbf{P}_v^T \mathbf{M}_w \mathbf{P}_v - g \mathbf{P}_u \mathbf{P}_u^T & -\mathbf{P}_v^T \mathbf{M}_w \mathbf{P}_u - g \mathbf{P}_u \mathbf{P}_v^T \\ -\mathbf{P}_u^T \mathbf{M}_w \mathbf{P}_v - g \mathbf{P}_v \mathbf{P}_u^T & \mathbf{P}_u^T \mathbf{M}_w \mathbf{P}_u - g \mathbf{P}_v \mathbf{P}_v^T \end{pmatrix} + i\omega \left[\mathbf{M}_\kappa\right]_{uv} \tag{7.71}$$

$$\mathbf{A}^{TM} = \mathbf{P}_v^T \mathbf{M}_u \mathbf{P}_v + \mathbf{P}_u^T \mathbf{M}_v \mathbf{P}_u + i\omega \left[\mathbf{M}_\kappa\right]_w \tag{7.72}$$

$$\mathbf{C} = \begin{pmatrix} \mathbf{P}_u^T \mathbf{M}_v - g \mathbf{P}_u^T & \mathbf{P}_v^T \mathbf{M}_u - g \mathbf{P}_v^T \end{pmatrix} \tag{7.73}$$

$$\mathbf{D} = \begin{pmatrix} \mathbf{M}_v & \mathbf{0} \\ \mathbf{0} & \mathbf{M}_u \end{pmatrix} \tag{7.74}$$

and

$$\mathbf{q}_n = -i\omega\widehat{\widehat{\mathbf{j}}}_{e,n} - \left(\widetilde{\mathbf{C}}_t + i\alpha_n\mathbf{J}\right)\mathbf{M}_\nu\widehat{\widehat{\mathbf{j}}}_{m,n} \tag{7.75}$$

with TE/TM signifying the first $2N$ and the last $N$ elements of the vector.

Removing the $i\alpha_n$ from the off-diagonal terms (7.70) can be also written

$$\begin{pmatrix} \mathbf{A}^{TE} - \alpha_n^2\mathbf{D} & \mathbf{C}^T \\ \mathbf{C} & \alpha_n^{-2}\mathbf{A}^{TM} + g\mathbf{I} \end{pmatrix} \begin{pmatrix} \widehat{\mathbf{a}}_n^{TE} \\ -i\alpha_n\widehat{\mathbf{a}}_n^{TM} \end{pmatrix} = \begin{pmatrix} \mathbf{q}_n^{TE} \\ \mathbf{q}_n^{TM}/i\alpha_n \end{pmatrix}. \tag{7.76}$$

The system matrix is invariant under the transformation $\alpha_n \to -\alpha_n$ (or equivalently $n \to -n$), which implies that the system can be solved once. Now assume an excitation of a given parity $p = \pm 1$

$$\begin{aligned} \hat{\boldsymbol{P}}\begin{pmatrix} \mathbf{q}_n^{TE} \\ \mathbf{q}_n^{TM}/i\alpha_n \end{pmatrix} &= \begin{pmatrix} \mathbf{q}_{-n}^{TE} \\ -\mathbf{q}_{-n}^{TM}/i\alpha_n \end{pmatrix} = \begin{pmatrix} p\mathbf{q}_n^{TE} \\ -(-p)\mathbf{q}_n^{TM}/i\alpha_n \end{pmatrix} \\ &= p\begin{pmatrix} \mathbf{q}_n^{TE} \\ \mathbf{q}_n^{TM}/i\alpha_n \end{pmatrix} \end{aligned} \tag{7.77}$$

where we have used the fact that the tangential and the normal components have opposite parities. Since the system matrix is invariant under the same transformation, we can easily deduce that

$$\hat{\boldsymbol{P}}\begin{pmatrix} \widehat{\mathbf{a}}_n^{TE} \\ \widehat{\mathbf{a}}_n^{TM}/i\alpha_n \end{pmatrix} = p\begin{pmatrix} \widehat{\mathbf{a}}_n^{TE} \\ \widehat{\mathbf{a}}_n^{TM}/i\alpha_n \end{pmatrix} \tag{7.78}$$

which means that we can spare the computation for negative $n$. Again, this economy in computational effort corresponds the respective reduction of the DOF achieved in spatial domain by truncating the domain at $w = 0$ and applying the suitable boundary condition.

Things are less evident in case of the absence of a specific parity. The solution can still be expressed as the sum of an even and an odd parity solution, as stated above, hence since the computation has to be carried out twice, this operation seems to cancel the gain by dropping the negative $n$ evaluations. Yet, one has to recall here that due to the reduction of the problem (spatial) dimensions (and correspondingly the spatial mesh) from 3 to 2, LU factorisation is in the grasp of the computational resources of any average workstation. Combined with the system invariance under parity transformations, this signifies that the computational burden is less than solving the problem for $2n$ right-hand-sides.

## 7.4 Calculation of the impedance variation

The self and/or mutual impedance calculation is by far the most important scalar observable in NDT applications, and as such one needs to address its calculation as it was the case in the development of spectral solutions. Clearly, being principally an integral of the electric field along the coil windings, it admits a straight-forward deduction from the field solution. With the use of the reciprocity theorem, one can derive a much more elegant and computationally efficient way of evaluation, also in the context of the mixed spatial-spectral formulation developed herein.

In section 7.2 two alternative ways of accounting for the primary field (the field of the driving coil in the air), based on the surface and volume equivalence theorem, have been presented. As the reciprocity theorem involves integration of the primary field, it is understood that one should switch between the surface-integral-based version of the reciprocity theorem examined in chapter 3 and chapter 4 and the volume-integral-based calculation presented in chapter 5.

We shall begin the analysis by considering the first case, that is by assuming that the primary field is accounted via the introduction of equivalent sources on a suitable exchange surface. We shall consider for simplicity a two coil probe in driver-pickup configuration. The mutual impedance of the two coils is given by (2.68)

$$\Delta Z(\mathbf{r}_s) = \frac{1}{I_{Tx} I_{Rx}} \oint\limits_{S_{exc}} \left[\mathbf{E}_{Rx;p} \times \mathbf{H}_{Tx} - \mathbf{E}_{Tx} \times \mathbf{H}_{Rx;p}\right] \cdot \mathbf{n} dS \tag{7.79}$$

where it is recalled that $\mathbf{E}_{Rx;p}$ and $\mathbf{B}_{Rx;p}$ stand for the primary electric and magnetic field produced by the receiver coil Rx which is fed with current $I_{Rx}$ ($I_{Tx} = 0$) and $\mathbf{E}_{Tx}, \mathbf{B}_{Tx}$ is the field solution obtained when the transmitting coil is fed with current $I_{Tx}$ ($I_{Rx} = 0$). The integration exceeds the exchange (Huygens) surface $S_{exc}$ illustrated in (7.3). The unit vector $\mathbf{n}$ stands for the outward normal to the surface $S_{exc}$. In fact, in order to avoid numerical issues it is safer to shift the integration surface one grid cell apart from the Huygens' surface. Applying the circular shift rule of the scalar triple product, (7.79) can be written as

$$\Delta Z(\mathbf{r}_s) = \frac{1}{I_{Tx} I_{Rx}} \oint\limits_{S_{exc}} \left[(\mathbf{n} \times \mathbf{E}_{Rx;p}) \cdot \mathbf{H}_{Tx} + (\mathbf{n} \times \mathbf{H}_{Rx;p}) \cdot \mathbf{E}_{Tx}\right] dS, \tag{7.80}$$

which taking into account the equivalent current definition relations (7.32),(7.33) becomes

$$\Delta Z(\mathbf{r}_s) = \frac{1}{I_{Tx} I_{Rx}} \oint\limits_{S_{exc}} \left(\mathbf{J}_m \cdot \mathbf{H}_{Tx} - \mathbf{J}_e \cdot \mathbf{E}_{Tx}\right) dS. \tag{7.81}$$

Application of (7.81) into FIT grid space and taking into account the decomposition along the $w$ direction (7.43) yields

$$\Delta Z(\mathbf{r}_s) = \frac{1}{I_{Tx} I_{Rx}} \sum_{n=-N}^{N} \left(\widehat{\widehat{\mathbf{j}}}^{T}_{m,-n} \widehat{\mathbf{h}}_n - \widehat{\widehat{\mathbf{j}}}^{T}_{e,-n} \widehat{\mathbf{e}}_n\right), \tag{7.82}$$

where $\widehat{\mathbf{e}}_n, \widehat{\mathbf{h}}_n$ are the electric and magnetic grid voltages obtained for the mode $n$, respectively, and $\widehat{\widehat{\mathbf{j}}}_{e,-n}, \widehat{\widehat{\mathbf{j}}}_{m,-n}$ stand for the equivalent electric and magnetic currents at the Huygens surface for the mode $-n$. The above equation is nothing more than Parserval's theorem in the discrete FIT solution space.

In case of volumetric equivalent sources, the integration over the Huygens surface has to be replaced by the volume integral throughout the sources support leading in the same relation with (5.65) in section 5.7

$$\Delta Z(\mathbf{r}_s) = \frac{1}{I_{Tx} I_{Rx}} \int\limits_{V_{src}} \left[\mathbf{J}_m \cdot \mathbf{H}_{Tx} - \mathbf{J}_e \cdot \mathbf{E}_{Tx}\right] dV' \tag{7.83}$$

which projected onto the FIT grid space will result in the same relation with the Huygens sources approach (7.82), where $\widehat{\widehat{\mathbf{j}}}_{m,-}$, $\widehat{\mathbf{h}}_n$ are obtained by (7.28),(7.29).

## 7.5 Numerical results

### 7.5.1 Comparison with reference results and performance studies

The numerical performance of the proposed formulation is tested by solving the problem of the eddy current inspection of a conducting piece near a discontinuity. Two different configurations are considered, which correspond to the two symmetries of interest: an infinitely long plate edge (with translational symmetry) and a cylindrical borehole (rotationally symmetric).

The first inspection scenario is depicted in Fig. 7.7. The considered configuration is the same with the one examined in [41], whose results were taken as a reference. The piece is considered infinite along the parallel to the edge direction, and its thickness is assumed several times greater than the skin depth at the operating frequency such that the interaction of the induced currents with the lower interface is negligible.

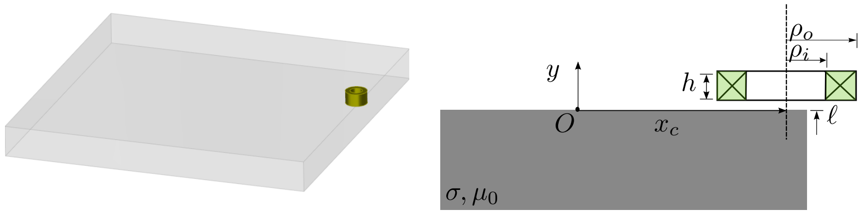

(a) (b)

Figure 7.7: Plate edge inspection with a cylindrical coil: (a) 3D view (b) cross-section.

The piece has a conductivity equal to $\sigma = 35.4$ MS/m and is assumed to be non-magnetic. The coil inner and outer radius is $\rho_i = 5$ mm and $\rho_o = 10$ mm, respectively, its length is $h = 5$ mm and is wound with $N = 2500$ turns. The coil is moving parallel to the piece's surface at a constant lift-off equal to 2 mm. The inspection is carried out at a frequency equal to $f = 1$ kHz, which upon application of the relation (5.67) for the skin depth in a half-space yields a skin depth of the order of $\delta = 2.675$ mm. The piece thickness is taken equal to 10 mm, which makes approximately 4 times the skin depth value, hence it satisfies the half-space approximation.

The results for the probe impedance variation $\Delta Z = Z - iX_0$, where $Z$ is the coil impedance and $X_0$ stands for the free-space reactance, are compared with the semi-analytical calculations presented in [41] and with 3D FEM simulations carried out using the COMSOL platform [123]. The comparison for the real and imaginary part of $\Delta Z$ as a function of the coil displacement $x_c$ are shown in Fig. 7.8. For the sake of numerical convenience, both results have been normalised with $X_0$, which for the given coil geometry and inspection frequency is equal to $X_0 = 500.51\ \Omega$.

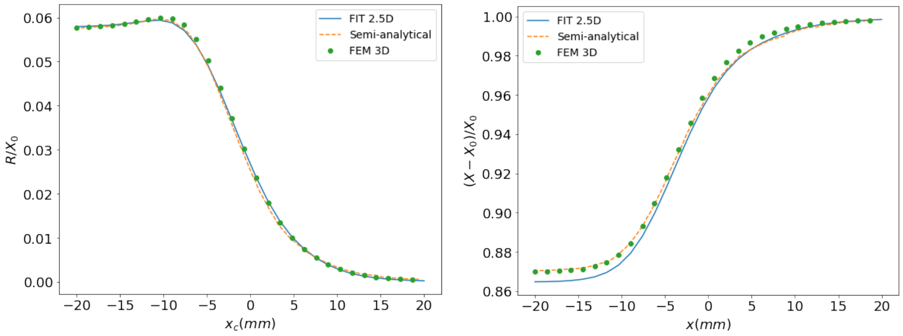

Figure 7.8: Real $\Delta R$ and imaginary part $\Delta X$ of the coil impedance variation as a function of its $x_c$ position (scan displacement). The solid line stands for the results obtained using the presented mixed spatial-spectral approach (referred to as FIT 2.5D), whereas the dotted line represents the semi-analytical (reference) solution. Both results are normalised with respect to the coil free space reactance $X_0$.

For the specific example, a discretisation with 178705 grid nodes and 10 modes along the symmetry axis has been applied. The total calculation for a number of 30 scanning positions reached 351 s, which makes coarsely 12 s per scan point in an average PC with an Intel(R) Core(TM) i7-8850H processor at 2.6 GHz and 32 GB of RAM. For comparison, the corresponding computation time for the 3D FEM solution reached 3925 s in total, which yields 131 s per position. The FEM mesh comprised 516353 DOF.

It should be noticed at this point that the reduced size of the FIT system of (7.57), consequence of restricting the spatial discretisation in the transversal $u - v$ plane, allows us to apply the LU decomposition for the matrix inversion. The benefit of using a direct solver is that one can treat more than one scan point simultaneously. It is recalled here that each scan point requires the solution of a new numerical problem since the source term at the right-hand side is different. This is a particularly important feature for applications involving moving sources as is the case for eddy-current nondestructive simulations. A second advantage of this decomposition, in combination with the indirect modelling approach of the sources via the application of the Huygens principle, is that there is no need to re-mesh the problem for each coil position. The source is always represented by the equivalent current distribution on the Huygens surface, which itself does not move. Practically, there is an upper limit concerning the number of scan points that can be treated simultaneously, which is dictated by the available memory.

The second problem deals with the eddy-current testing of a cylindrical hole in a conducting, non-magnetic half-space, as shown in Fig. 7.9. The geometry of the piece is this time rotationally symmetric. The considered configuration is the one proposed in [124]. The piece conductivity is taken equal to $\sigma = 24.36$ MS/m. The coil dimensions in this case are $\rho_i = 6.95$ mm, $\rho_o = 9.35$ mm and $h = 6.7$ mm and its number of turns is $N = 335$. The coil scans the tube at a constant radial position equal to $\rho_c = 5.63$ mm with its axis being normal to the tube walls. The inspection frequency is $f = 10$ kHz, which implies a skin depth equal to $\delta = 0.32$ mm. As underlined in the previous example, the thickness of the conducting part along the radial direction should be taken several times greater than $\delta$ in order to satisfy the assumption of an infinitely thick piece. For the present calculation, the piece thickness was taken equal to 80 mm, which largely satisfies the above constraint.

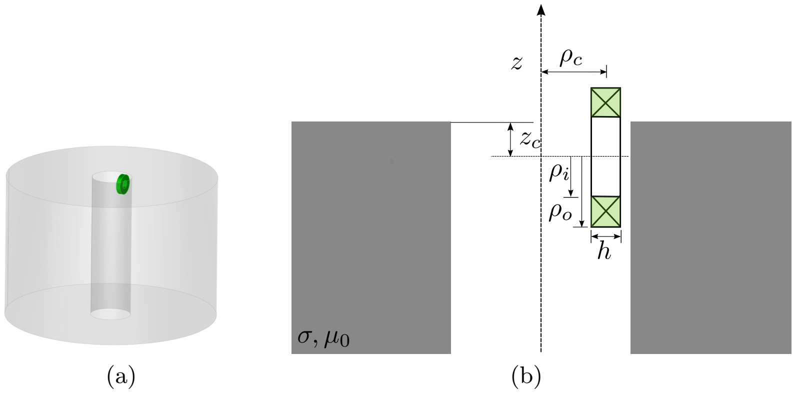

(a) (b)

Figure 7.9: Plate edge inspection with a cylindrical coil: (a) 3D view (b) cross-section.

The comparison of the calculated probe impedance variation $\Delta Z$ with the experimental results provided in [124] is given in Fig. 7.10. Both results are normalised with respect to the free space reactance, which for the given inspection frequency reads $X_0 = 110.08\ \Omega$.

The numerical results of Fig. 7.10 were obtained using the same computer as for the previous example. The spatial mesh consisted of 2.8 $10^5$ nodes and 15 modes were considered for the spectral representation in the azimuthal direction. The total calculation time for 15 scanning positions was 832 s.

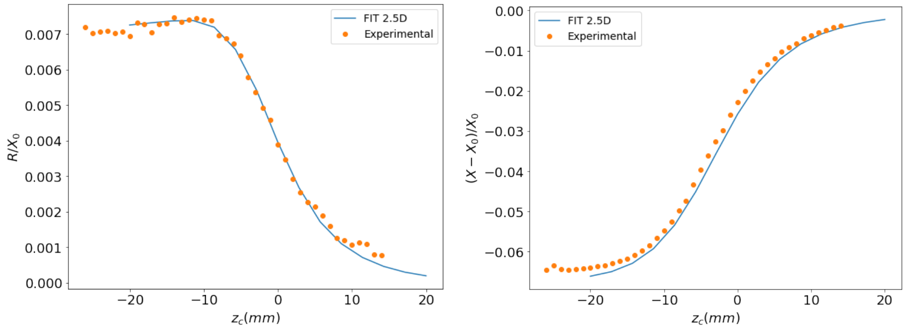

Figure 7.10: Calculated results for the real and imaginary part of the coil impedance variation along the scan line vs. measurements. The solid line represents the numerical results obtained with the spatial-spectral approach (FIT 2.5) whereas then circular marks stand for the measurements.

### 7.5.2 Performance considerations

The overall computational burden of the solution (if we neglect the time needed for the computation of the material matrices and the system assembly) is mainly determined by the number of nodes in the discretisation $u-v$ plane, $3N_d$, the number of modes along the symmetry axis, $N_m$, and the number of right-hand-side vectors (i.e. the number of independent sources and/or the positions in the case of a moving source), $N_s$.

Since the solution for each mode is independent from another, the computation time scales linearly with the number of considered modes, $N_m$, if the system is inverted using a single-core machine. Passing the system to a CPU/GPU parallel architecture, a speed-up equal to the number of parallel processes, with a theoretical maximum the number of modes, $N_m$, can be achieved.

The scaling with respect to the other two parameters, namely the nodes of the 2D grid, $N_d$, and the number of sources, $N_s$, is determined by the corresponding scaling factors for the LU decomposition for sparse systems, and it is less trivial to determine theoretically since it depends on a number of factors, among them on implementation details. We can use the known formulas for a full systems in order to set an upper limit of the computation time of the method and use this formula as a guideline for the derivation of a heuristic approximation based on numerical experiments.

Assuming thus that the system was fully populated, the computational time per mode would be given by the following formula

$$T_{sim}/T_f = 2/3N_d^3 + 2N_d^2N_s \tag{7.84}$$

where the first term gives the number of operations for the system factorisation, the second term is the respective number for the forward and backward substitution and $T_f$ stands for the CPU time per flop, which is machine dependent. Based on this relation, we may anticipate that the real computational cost for the system at hand should admit an exponential dependence of the general form

$$T_{sim}/T_f = aN_d^{\alpha} + bN_d^{\beta} N_s \tag{7.85}$$

with $a, b$ constants and $\alpha, \beta$ exponents that need to be determined, and which we expect to lie in the intervals $1 \leq \alpha < 3$ and $1 \leq \alpha < 2$. In order to come to an estimation of their specific values, the first problem of the previous section, i.e. the scanning coil over the half-space edge, has been solved for a different number of grid nodes and the computation time needed for the system inversion has been measured (the CPU time needed for the construction of the system and the post-processing is not taken into account here). The corresponding plots for different grid sizes and different numbers of coil positions is shown in Fig. 7.11. The computation time is a linear function of $N_s$, as expected. All computations have been carried out for a constant number of modes $N_m = 10$.

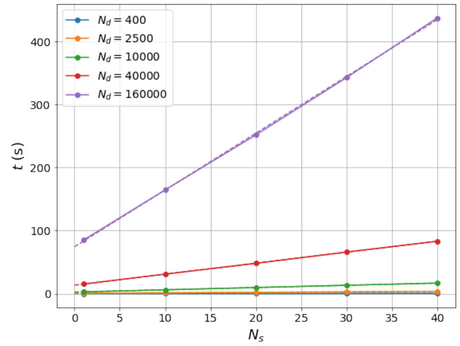

Figure 7.11: Computation time as function of the number of scan positions for a number of different grid resolutions. The computation time scales almost linearly with the size of the problem as the linear fit results confirm (dashed lines). The considered number of modes is $N_m$=10.

Calculating the best linear fit to the different datasets, and assuming the dependence of (7.85), we can associate the constant term of the fitted polynomials to $aN_d^{\alpha}$, whereas the linear term coefficients are associated to the $bN_d^{\beta}$. The variation of the two coefficients versus $N_d$ in logarithmic scale is shown in Fig. 7.12.

The slope of the two lines in the logarithmic scale will yield the sought approximation of the $\alpha$ and $\beta$ exponents. We thus finally obtain for the computational cost the following approximation

$$T_{sim}/T_f = \left(aN_d^{1.14} + bN_d^{1.16} N_s\right) N_m. \tag{7.86}$$

It must be underlined that the above procedure has been entirely based on a particular example, and it can by no means claim being a rigorous and general method for the derivation of the scaling of the computational time with the solution parameters. It can rather serve as an indicator of the true behaviour.

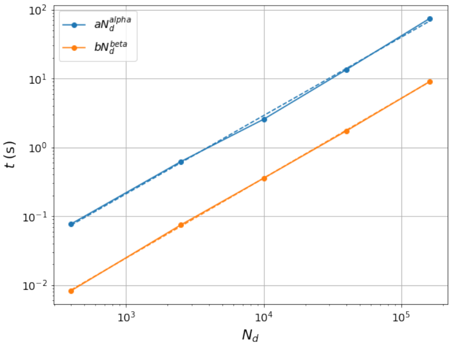

Figure 7.12: Coefficients of the fitted polynomial for the curves of Fig. **??** as function of the grid size $N_d$. The dotted line stands for the best polynomial fit in the logarithmic space.

It should be however noticed that a similar trend has been observed for other cases as well. The main conclusion of this study is that the dependence of the computation time is almost linear to the size of the 2D mesh $N_d$ and proportional to $N_s$ and $N_m$.

## 7.6 The time-domain formulation

The extension of the previous formalism in the time domain for the calculation of the transient response is quite straight-forward. Starting point will be the diffusion equation in its general form (7.21) with the electric and magnetic sources defined by (7.28),(7.29) or (7.36),(7.37). Note that although the Laplace transform (LT) approach is also applicable here, we shall continue with direct time-integration using time-stepping schemes as in section 6.3, for the same reasons presented there.

Following the established approach, we sample the time axis using a uniform temporal grid $t_j = j\Delta t$, $j = 0, 1, \ldots$ with $\Delta t$ being the discretisation step and discretise the temporal derivatives using a suitable differentiation scheme. The choice of uniform temporal discretisation is not solely driven by the sake of simplicity considerations but also from performance consideration for reasons that will be explained below. There exists a plethora of different methods (recall that we are interested here solely in implicit schemata due to the parabolic nature of the eddy-current problem) such as backward differentiation formulae (BDF), implicit Runge-Kutta of various orders [77, 95–98], but we shall restrict ourselves hereafter with the BDF schemes of first and second order, referred to as BDF1 and BDF2, respectively, since they are largely sufficient for our purposes. The following discussion, however, can be easily extended to include other schemes as well.

The discretisation of an ordinary differential equation of first oder given by the generic formula

$$y' = f(t, y) \tag{7.87}$$

using the BDF1 and BDF2 under a uniform temporal grid leads to the following iterative schemata

$$y_j - y_{j-1} = \Delta t(t_j, y_j) \tag{7.88}$$

and

$$y_j - \frac{4}{3}y_{j-1} + \frac{1}{3}y_{j-2} = \Delta t(t_j, y_j) \tag{7.89}$$

respectively.

Application of (7.88) into the diffusion equation (7.27) yields for the BDF1

$$\left(\widetilde{\mathbf{C}}\mathbf{M}_\nu\mathbf{C} + \frac{1}{\Delta t}\mathbf{M}_\kappa\right)\widehat{\mathbf{a}}_j = \frac{1}{\Delta t}\mathbf{M}_\kappa\widehat{\mathbf{a}}_{j-1} + \widehat{\widehat{\mathbf{j}}}_{e;j} + \widetilde{\mathbf{C}}\mathbf{M}_\nu\int\limits_0^{t_j}\widehat{\widehat{\mathbf{j}}}_m(\tau)\,d\tau. \tag{7.90}$$

The corresponding expression for the BDF2 reads

$$\left(\widetilde{\mathbf{C}}\mathbf{M}_\nu\mathbf{C} + \frac{3}{2\Delta t}\mathbf{M}_\kappa\right)\widehat{\mathbf{a}}_j = \frac{2}{\Delta t}\mathbf{M}_\kappa\widehat{\mathbf{a}}_{j-1} - \frac{1}{2\Delta t}\mathbf{M}_\kappa\widehat{\mathbf{a}}_{j-2} + \widehat{\widehat{\mathbf{j}}}_{e;j} + \widetilde{\mathbf{C}}\mathbf{M}_\nu\int\limits_0^{t_j}\widehat{\widehat{\mathbf{j}}}_m(\tau)\,d\tau. \tag{7.91}$$

Projection (7.90) onto the spectral basis in the symmetry direction $w$ yields

$$\left(\mathbf{A}_n + \frac{1}{\Delta t}\mathbf{M}_\kappa\right)\widehat{\mathbf{a}}_{nj} = \frac{1}{\Delta t}\mathbf{M}_\kappa\widehat{\mathbf{a}}_{n(j-1)} + \widehat{\widehat{\mathbf{j}}}_{e;nj} + \left(\widetilde{\mathbf{C}}_t + i\alpha_n\mathbf{J}\right)\mathbf{M}_\nu\int\limits_0^{t_j}\widehat{\widehat{\mathbf{j}}}_m(\tau)\,d\tau. \tag{7.92}$$

where $\mathbf{A}_n$ is the sum of the the projected curl-curl matrix given by (7.58) and the gauge matrix (7.63). The expression for the BDF2 scheme follows respectively.

Equation (7.92) describes a double loop over the mode number in $w$ and the time-step. A closer look at the system matrix reveals that the system matrix we have to invert is independent from the time step. Taking into account the orthogonality of the $w$ modes, we can interchange the order of the loops, namely, we can integrate each mode separately, which gives us a huge advantage in terms of computational efficiency. Indeed, as already mentioned for the FD case, the projected matrices $\mathbf{A}_n$ are two-dimensional, which implies that their size for standard grid resolutions allows to factorise them using an LU method, and use this factorisation for the entire integration time.

The source terms $\widehat{\widehat{\mathbf{j}}}_e, \widehat{\widehat{\mathbf{j}}}_m$ have been deliberately left unspecified up to now. Since in general the source displacement is performed at speeds of several mm/s in typical inspection scenarios, $\widehat{\widehat{\mathbf{j}}}_e, \widehat{\widehat{\mathbf{j}}}_m$ can be considered as approximately stationary even for vary low-frequency excitations. Should this be the case, the field solution in the air can be approximated by the tensor product of the magnetostatic field with the current waveform. Since the free-space solution serves then as basis for the definition of the equivalent sources, this approximation result in significant optimisation of the $\widehat{\widehat{\mathbf{j}}}_e, \widehat{\widehat{\mathbf{j}}}_m$ evaluation.

Let $\widehat{\mathbf{a}}_0, \widehat{\widehat{\mathbf{b}}}_0$ be the magnetostatic solution for the integrated magnetic vector potential and the magnetic flux and $I(t)$ the waveform of the feed current in the excitation coil. Recalling the volume equivalent sources definition (the same arguments apply also for the surface equivalence), one can write

$$\widehat{\widehat{\mathbf{j}}}_e(t) = \mathbf{M}_\kappa \widehat{\mathbf{a}}_0 \dot{I}(t) = \widehat{\widehat{\mathbf{j}}}_e \dot{I}(t) \tag{7.93}$$

$$\widehat{\widehat{\mathbf{j}}}_m(t) = (\mathbf{I} - \mathbf{M}_{\mu_r}) \widehat{\widehat{\mathbf{b}}}_0 \dot{I}(t) = \widehat{\widehat{\mathbf{j}}}_m \dot{I}(t) \tag{7.94}$$

where under $\widehat{\widehat{\mathbf{j}}}_e, \widehat{\widehat{\mathbf{j}}}_m$ is understood the spatial profile of the (stationary) currents. Substituting (7.93),(7.94), (7.92) becomes

$$\left(\mathbf{A}_n + \frac{1}{\Delta t}\mathbf{M}_\kappa\right) \widehat{\mathbf{a}}_{nj} = \frac{1}{\Delta t}\mathbf{M}_\kappa \widehat{\mathbf{a}}_{n(j-1)} + \widehat{\widehat{\mathbf{j}}}_{e;n0} \dot{I}_n + \left(\widetilde{\mathbf{C}}_t + i\alpha_n \mathbf{J}\right) \mathbf{M}_\nu \widehat{\widehat{\mathbf{j}}}_m I_n. \tag{7.95}$$

For the derivation of the last relation a zero-initial-value for the field solution has been assumed. Note that the current derivative sample $\dot{I}_n$ can be calculated analytically. This latter form of (7.92) is very convenient since it requires a single solution of the magnetostatic problem of the field in the air (which in addition can be carried out analytically by Biot-Savart integration) in the beginning of the time loop, which is then multiplied by the time sample of the current signal and its time derivative.

To calculate the EMF we need to evaluate the convolution integral (6.43). This is translated to storing the field solution for every time step and every mode and then proceed to the numerical integration, which is resource consuming. A more elegant approach would be to calculate the solution for a step excitation and retrieve the EMF for the required input waveform by evaluating Duhamel's integral as we did in section 6.4 for the spectral method.

The FIT analogue of (6.44) for the EMF variation reads

$$\Delta V_j = \sum_{n=-N}^{N} \left( \widehat{\widehat{\mathbf{j}}}^T_{m,-n} \widehat{\mathbf{h}}_{nj} - \widehat{\widehat{\mathbf{j}}}^T_{e,-n} \widehat{\mathbf{e}}_{nj} \right). \tag{7.96}$$

The integrated EMF value is obtained by evaluating the sum

$$s_j = \sum_{k=0}^{j} \Delta V_j \Delta t. \tag{7.97}$$

The sought EMF variation will be obtained by applying (7.97) into (6.47) as we did for the spectral solution.

The overall solution algorithm is explained in form of a pseudo-code in Alg. 1.

**Algorithm 1** Time integration algorithm for the FIT 2.5D scheme

```
for $n \leftarrow 0$ to $N_n$ do                                              ▷ Coil in air
    Evaluate $\widehat{\widehat{\mathbf{j}}}_{e;n}, \widehat{\widehat{\mathbf{j}}}_{m;n}$
end for
for $n \leftarrow 0$ to $N_n$ do                                              ▷ Field calculation
    $\widehat{\mathbf{a}}_{n0} \leftarrow 0$
    $\mathbf{A}_n \leftarrow \mathbf{LU}$
    for $j \leftarrow 1$ to $N_j$ do
        Solve $\mathbf{Ux} = \widehat{\mathbf{a}}_{n(j-1)} + \widehat{\widehat{\mathbf{j}}}_{e;n}\dot{I}_j + \widetilde{\mathbf{C}}\mathbf{M}_\nu \widehat{\widehat{\mathbf{j}}}_{m;n} I_j$
        Solve $\mathbf{V}\widehat{\mathbf{a}}_{nj} = \mathbf{x}$
        $\Delta V_j \leftarrow \Delta V_j + \widehat{\widehat{\mathbf{j}}}^T_{m,-n}\widehat{\mathbf{h}}_{nj} - \widehat{\widehat{\mathbf{j}}}^T_{e,-n}\widehat{\mathbf{e}}_{nj}$
    end for
end for
$s_0 \leftarrow 0$
for $j \leftarrow 1$ to $N_j$ do                                              ▷ Convolution
    $s_j \leftarrow s_{j-1} + \Delta V_j$
    $\Delta V_j \leftarrow \sum_{k=0}^{j-1} s_k \left(\dot{I}_{j-k-1} - \dot{I}_{j-k}\right) - s_j \dot{I}_0$
end for
```

## 7.7 The FIT formulation for the heat equation

### 7.7.1 Discrete heat equation

For the derivation of the discrete heat equation we consider first the energy conservation law (2.70) integrated in an arbitrary volume $V$

$$\int_V \rho c_P \frac{\partial T}{\partial t} dV = \int_V \frac{\partial Q_s}{\partial t} dV - \oint_{\partial V} \mathbf{J} \cdot d\mathbf{S} \tag{7.98}$$

where $\rho$ is the mass density of the material (in $kg\,m^{-3}$), $c_P$ is the specific heat capacity (in $J\,kg^{-1}K^{-1}$), $T$ the absolute temperature (in $K$), $Q_s$ the volume density of the heat source (in $J\,kg^{-1}$), and $\mathbf{J}$ is heat flux density vector (in $W\,m^{-2}$). The latter is related to the temperature field by Fourier's law

$$\mathbf{J} = -\overline{\kappa} \cdot \nabla T \tag{2.71}$$

with $\overline{\kappa}$ being the thermal conductivity tensor of the material (in $W\,m^{-1}K^{-1}$). For the sake of simplicity we shall restrict the analysis to materials with a diagonal tensor (otherwise stated, we assume that the principal axes of the anisotropy ellipsoid coincide with the axes of the working reference frame $(u, v, w)$, an hypothesis that can be satisfied in a number of cases with a judicious choice of the FIT frame).

Let us now apply a FIT dual grid system in the solution domain as shown

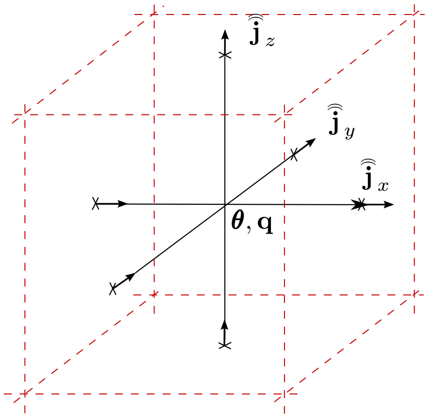

Figure 7.13: Allocation of the state variables on the FIT dual grid system.

in Fig. 7.13. Application of (7.98) in a cell volume of the dual grid yields

$$\frac{\partial}{\partial t}\int\limits_{\tilde{V}_i} \rho c_P T dV = \int\limits_{\tilde{V}_i} \dot{Q}_s dV - \oint\limits_{\partial\tilde{V}_i} \mathbf{J}\cdot d\mathbf{S}. \tag{7.99}$$

Furthermore, we integrate (2.71) over the oriented flux tube connecting the $i$ with the $j$ node ($i < j$)

$$\int\limits_{L_i} \kappa^{-1} dl \int\limits_{\tilde{A}_i} \mathbf{J}\cdot d\mathbf{S} = \int\limits_{\tilde{A}_i} T(\mathbf{x})\, dS - \int\limits_{\tilde{A}_j} T(\mathbf{x})\, dS. \tag{7.100}$$

$L_i$ is the primary grid edge element binding the $i$ with the $j$ node, and $\tilde{A}_i$ is the dual grid facet element, which contains the $i$ node and points towards the $\mathbf{x}_j - \mathbf{x}_i$ direction (parallel to $L_i$).

We develop $T$ and $\mathbf{J}$ in Taylor series around the centre of the primary grid cell $\mathbf{x}_i$

$$T(\mathbf{x}) = T(\mathbf{x}_i) + \nabla T|_{\mathbf{x}_i}\cdot\Delta\mathbf{x} + \mathscr{O}\big(\Delta\mathbf{x}^2\big) \tag{7.101}$$

$$\mathbf{J}(\mathbf{x}) = \mathbf{J}(\mathbf{x}_i) + \nabla\mathbf{J}|_{\mathbf{x}_i}\cdot\Delta\mathbf{x} + \mathscr{O}\big(\Delta\mathbf{x}^2\big) \tag{7.102}$$

which upon substitution in (7.99),(7.100) and keeping only the leading term yields

$$\frac{\partial T_i}{\partial t}\int\limits_{\tilde{V}_i} \rho c_P dV \approx \int\limits_{\tilde{V}_i} \dot{Q}_s dV - \oint\limits_{\partial\tilde{V}_i} \mathbf{J}\cdot d\mathbf{S}. \tag{7.103}$$

$$\int\limits_{\tilde{A}_i} \mathbf{J}_i\cdot d\mathbf{s} \int\limits_{L_i} \kappa^{-1} dl \approx (T_i - T_j)\,\Delta\tilde{A}_i \tag{7.104}$$

where $T_i = T(\mathbf{r}_i)$ and $\mathbf{J}_{i'} = \mathbf{J}(\mathbf{r}_{i'})$, and $\Delta A_{i'}$ stands for the oriented surface element. Note that in case that the material inside the dual cell and along the edge is homogeneous, the order of the approximation is 2 (the first order term vanishes after the integration since it is antisymmetric with respect to the development point).

Let us now define the discrete state variables

$$\theta_i := T_i \tag{7.105}$$

$$\widehat{\widehat{j}}_i := \int\limits_{\tilde{A}_i} \mathbf{J} \cdot d\mathbf{S} \tag{7.106}$$

$$q_i := \int\limits_{\tilde{V}_i} Q \cdot dV \tag{7.107}$$

as well as the material matrices

$$\mathbf{M}_C := \operatorname{diag}\left[\int\limits_{\tilde{V}_i} \rho c_P dV\right],\ i = 1, 2, \ldots \tag{7.108}$$

$$\mathbf{M}_\kappa^{-1} := \operatorname{diag}\left[\Delta\tilde{A}_i^{-1}\int\limits_{L_i} \kappa^{-1} dl\right],\ i = 1, 2, \ldots \tag{7.109}$$

Applying (7.103),(7.104) at all dual cells and primary edges and making use of the FIT topological matrices for the description of the grad and div discrete operators, we arrive at the following set of grid equations

$$\mathbf{M}_C\dot{\boldsymbol{\theta}} = \dot{\mathbf{q}} - \widetilde{\mathbf{S}}\widehat{\widehat{\mathbf{j}}} \tag{7.110}$$

$$\mathbf{M}_\kappa^{-1}\widehat{\widehat{\mathbf{j}}} = -\mathbf{G}\boldsymbol{\theta}. \tag{7.111}$$

Elimination of the heat flux leads us to the discrete heat conduction equation

$$\widetilde{\mathbf{S}}\mathbf{M}_\kappa\mathbf{G}\boldsymbol{\theta} - \mathbf{M}_C\dot{\boldsymbol{\theta}} = -\dot{\mathbf{q}}. \tag{7.112}$$

Equation (7.112) expresses the heat equation in a standard 3D FIT grid system. Note the formal similarity with the magnetostatic equation (7.13) apart from the temporal derivative term. The reformulation of the spatial 3D form in the mixed 2.5D scheme is straight forward. Introducing the (7.43) expansion for the temperature $\boldsymbol{\theta}$ and the source variables $\underset{\sim}{\mathbf{q}}$ and taking into account the expression (7.54) as well as the property $\mathbf{G} = -\widetilde{\mathbf{S}}^T$, (7.112) becomes

$$\left[\widetilde{\mathbf{S}}_t\mathbf{M}_\kappa^T\mathbf{G}_t - \alpha_n^2\mathbf{M}_\kappa^N - \mathbf{M}_C\frac{d}{dt}\right]\boldsymbol{\theta}_n = -\dot{\mathbf{q}}_n \tag{7.113}$$

where $\mathbf{M}_\kappa^T$ and $\mathbf{M}_\kappa^N$ are the coplanar and and normal thermal conductivity component submatrices and $\widetilde{\mathbf{S}}_t, \mathbf{G}_t$ stand for the topological operators projection in the discretisation plane defined in section 7.3.

The time integration of (7.113) follows the same pattern as for the eddy-current problem given in section 7.6.

### 7.7.2 Convection and radiation terms

In the derivation of the heat equation in (2.73) and (7.112), only the conduction mechanism expressed by the Fourier law (2.71) has been taken into account. The two remaining mechanisms of heat propagation, namely radiation and convection have been ignored. Although the former is practically taken into account a-posteriori for the translation of the IR image to the temperature of the emitting surface (usually this translation is carried out via a suitable calibration), it does not contribute to the heat evacuation from the piece during the solution of the heat equation. The second mechanism, however, can be non-negligible at the piece-air interface since air flow from the somewhat warmer piece surface is responsible for a part of the piece cooling.

The precise modelling of the convection mechanism requires the simultaneous solution of the heat diffusion equation with the fluid dynamics equation for the air flow, leading to a very complicated problem. Fortunately, for the inspection applications considered here, where the air column above the piece can be considered as nearly stationary, the convection term can be approximated by Newton's law of cooling [125]

$$J_{cv} = h_{cv} \left(T_s - T_f\right) \tag{7.114}$$

where $T_s, T_f$ are the surface and fluid temperature (K), and $h_c$ is the convection heat transfer coefficient ($\mathrm{Wm}^{-2}\mathrm{K}^{-1}$) $J_{cv}$ is assumed as isotropic thermal flow per solid angle integrated over the semi-sphere above the surface.

The radiation losses are calculated by the Stefan-Boltzmann law

$$J_{rd} = \sigma \varepsilon G \left(T_s^4 - T_a^4\right) \tag{7.115}$$

where $\sigma$ is Stefan-Boltzmann's constant ($\sigma = 5.67\,10^{-8}\ \mathrm{Wm}^{-2}\mathrm{K}^{-4}$), $\varepsilon$ stands for the surface emissivity, and $T_s, T_a$ are surface and air temperature, respectively. $G$ is a dimensionless geometric factor dependent of the shape and orientation of the two bodies. For two large size parallel surfaces $G = 1$. Hence for a relative lage plate-air interface we can approximate the two terms to a good extent using the relation

$$J_{tot} \approx h_{cv} \left(T_s - T_a\right) + \sigma \varepsilon \left(T_s^4 - T_a^4\right). \tag{7.116}$$

$J_{tot}$ is non-linear with the temperature, which will lead to a non-linear heat equation when integrated into the energy conservation law. Thankfully, a further approximation can be made by recalling that in thermal inspection applications the piece temperature is very close to the ambient temperature of the air, i.e. $T_s \sim T_a$. Hence we can successively write

$$\begin{aligned} J_{tot} &\approx \left[h_{cv} + \sigma \varepsilon \left(T_s^3 + T_s^2 T_a + T_s T_a^2 + T_a^3\right)\right] \left(T_s - T_a\right) \\ &\approx \left(h_{cv} + 4 \sigma \varepsilon T_a^3\right) \left(T_s - T_a\right) \\ &= h_{eff} \left(T_s - T_a\right) \end{aligned} \tag{7.117}$$

with the effective convection heat transfer coefficient $h_{eff} = h_{cv} + 4\sigma\varepsilon T_a^3$. A quantitative image of the approximation (7.117) is provided in Tab. 7.1, where the results of the radiated flow calculated with the approximate formula are compared with the exact evaluation of the Stefan-Boltzmann law for different values of piece temperature. The relative error for a temperature difference of 5 °C (which is an exaggerated value) remains below 3 %, which verifies the validity of the approximation for IR inspection applications.

| $T_s$ (°C) | $\Delta T$ (°C) | **Approximate** | **Exact** | **Error (%)** |
|---|---|---|---|---|
| 11.8 | 0.1 | 0.5242 | 0.5245 | 0.0526 % |
| 12.7 | 1.0 | 5.2419 | 5.2696 | 0.5251 % |
| 17.7 | 5.0 | 26.2097 | 26.9079 | 2.5948 % |

Table 7.1: Comparison of the results obtained with the approximative form of the Stefan-Boltzmann law with the exact evaluation for different piece temperatures. The temperature of the air is assumed to be 11.7 °C (283.85 K), which is the annual mean temperature in Paris.

The energy conservation relation expressed by (7.98) must thus be complemented at the piece-air interfaces by (7.117) to account for the convection and radiation losses

$$\int\limits_V \rho c_P \frac{\partial T}{\partial t} dV = \int\limits_V \frac{\partial Q_s}{\partial t} dV - \oint\limits_{\partial V} \mathbf{J} \cdot d\mathbf{s} - \delta_a \int\limits_{S_a} h_{eff} \left(T_s - T_a\right) ds \tag{7.118}$$

where $S_a$ signifies the air-piece interface and $\delta_a$ is a selection coefficient, which takes the value 1 when the $S_a$ intersects the integration volume and 0 elsewhere. Mathematically speaking, the convection and radiation losses act as an additional heat sink at the air-piece boundary. Notice that (7.117) is also invariant to temperature gauge transformations, which means that we can return to the °C scale used in this text ($T_a$ must however be expressed in K for the $h_{eff}$ calculation!).

Let us now return to the FIT grid equation for the energy conservation (7.110). It easily follows

$$\mathbf{M}_C \dot{\boldsymbol{\theta}} = \dot{\mathbf{q}} - \widetilde{\mathbf{S}} \widehat{\widehat{\mathbf{j}}} - \mathbf{M}_h (\boldsymbol{\theta} - \boldsymbol{\theta}_a) \tag{7.119}$$

where $\mathbf{M}_h$ stands for the effective convection coefficient matrix, defined as

$$\mathbf{M}_h = \operatorname{diag} \left[ \delta_i \int\limits_{\tilde{A}_i} h_{eff} dS \right] , \; i = 1, 2, \ldots \tag{7.120}$$

$\delta_i$ has here the same meaning as the selection flag $\delta_a$ in the continuous counterpart of the energy conservation relation. Substitution of the discrete Fourier law yields the extended heat equation

$$\left( \widetilde{\mathbf{S}} \mathbf{M}_\kappa \mathbf{G} + \mathbf{M}_h \right) \boldsymbol{\theta} - \mathbf{M}_C \dot{\boldsymbol{\theta}} = -\dot{\mathbf{q}} + \mathbf{M}_h \boldsymbol{\theta}_0. \tag{7.121}$$

### 7.7.3 An example of a multi-physics problem: induction heating in a multilayer piece

The theoretical formulation for the thermal problem presented above will be applied in the framework of a specific inspection problem, namely the induction heating in a planar multilayer piece with a hole. For simplicity, we shall restrict the study to the 2D case, which means that the induction coil is coaxial with the hole. We do also not take the convection and radiation losses into account to simplify the physics as much as possible. The problem configuration is depicted in Fig. 7.14.

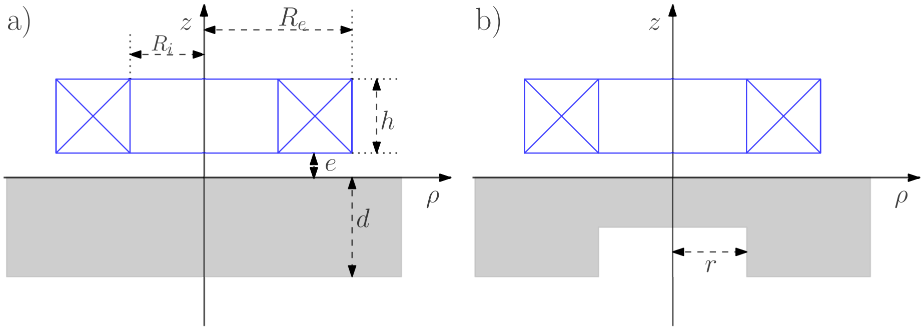

Figure 7.14: Induction heating in a planar piece with a cylindrical hole. (a) Piece without defect. (b) Defected piece.

The coil-induced eddy-currents in the conducting piece are responsible for the local heating via the Joule mechanism. The thus introduced heat distribution is then diffused in the remaining part of the geometry piece until thermal equilibrium is reached (the latter can be achieved at very long times with respect of our observation time window and hence is is not always apparent in the simulation results). Assuming that the electromagnetic problem has been solved and the eddy-current density is known throughout the piece, the Joule losses are calculated via the relation

$$\dot{q} = \frac{1}{\sigma} |\mathbf{J_s}|^2 \tag{7.122}$$

For the solution of the thermal equation it remains to discretise (7.122) and solve (7.112) (recall we have neglected the convection and radiation terms) in time using a BDF time-stepping scheme.

The coil inner and outer radius read $R_i = 11$ mm and $R_e = 84$ mm, respectively, its height is $h = 41$ mm, and its number of wire-turns is $N = 408$. The coil lift-off is taken equal to $e = 1$ mm. Two different workpieces have been considered: (i) a non-magnetic aluminum plate and (ii) a ferromagnetic steel plate. Their respective physical parameters being given in Tab. 7.2. The plate thickness in both cases is $d = 10$ mm.

The specimen heating is assumed to be carried out in a narrow time window of 50 ms, using an harmonic excitation current of frequency $f = 200$ Hz, which

| | $\mu_r$ | $\sigma$ (MS/m) | $\kappa$ (W/m/K) | $\rho$ (kg/m$^3$) | $C_p$ (J/kg/K) |
|---|---|---|---|---|---|
| Aluminum | 1 | 35 | 237 | 2707 | 897 |
| Steel | 700 | 3.21 | 44.5 | 7850 | 475 |

Table 7.2: Electromagnetic and thermal parameters of the materials.

makes an excitation of 10 cycles for the eddy-currents. Given the different characteristic scales of the electromagnetic and the thermal problem, this type of excitation acts as a pulsed heat source, with the Joule heating power described by (7.122) being equally distributed during the pulse duration.

The heat distribution in the two plates (without defect) is illustrated at different time instances in Fig. 7.15. The evolution of the heat distribution is a combination of two effects: the different penetration of the heat from the eddy-currents, which becomes striking in case of the ferromagnetic specimen, and the different diffusion speed associated with the thermal conductivity of the materials.

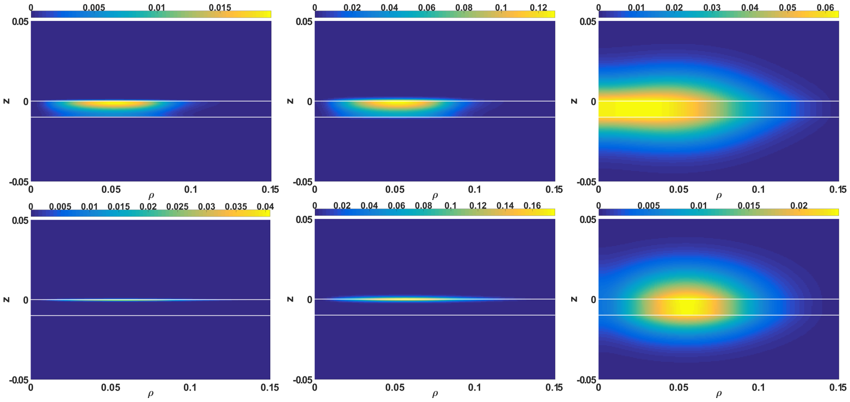

Figure 7.15: Temperature distribution images in the region of interest for different time in the flawless specimens. *Top:* Aluminum. *Bottom:* Steel. The snapshots correspond the time instances $t = t_0$, $t = t_0 + 50$ ms, $t = t_0 + 5$ s.

To study the effect of the defect to the temperature distribution, a cylindrical hole is introduced at the bottom surface of the aluminium plate, as shown in Fig. 7.14b, which emulates corrosion pitting. The hole radius is $r = 50$ mm and its thickness is taken equal to $d_h = 0.5$ mm. In order to make the geometry more realistic in terms of practical occurrence, the plate thickness is reduced to 1 mm (instead of the 10 mm plate considered for the flawless case). The temperature profile at the top and bottom surfaces for a number of different time instances is shown in Fig. 7.16. The observations have been sorted in two groups: short time observation, where the details of the defect are clearly visible, and long time observation (over a 1 s), where the detains of the defect discontinuity begin to smear out due to diffusion.

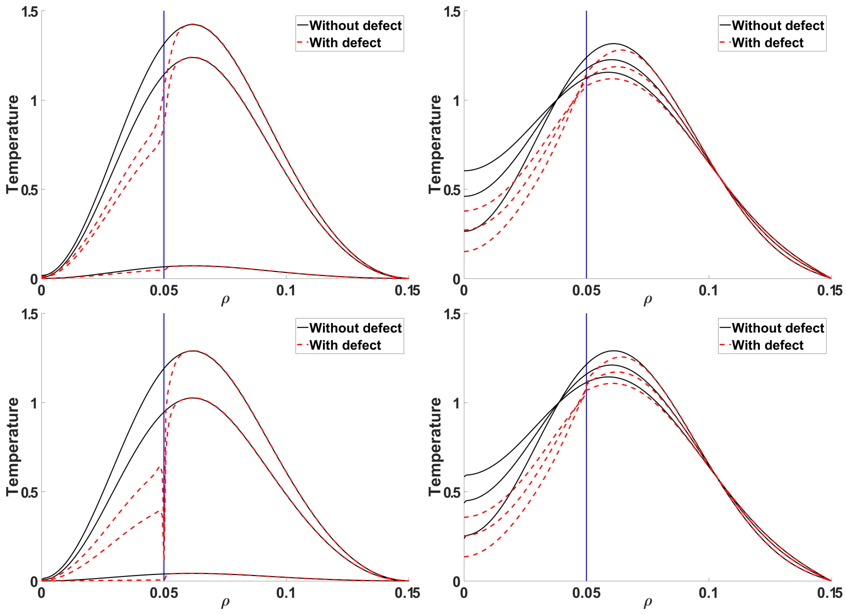

Figure 7.16: Comparison of the distribution of the temperature at the surfaces of the plates with and without defect for different observation times. *Top:* Upper surface, *Bottom:* Bottom surface. Observation time: *Left:* 10, 50, 70 ms *Right:* 1, 2, 3 s.

## 7.8 Multi-domain solutions. Hybridisation

All the problems considered so far shared the common property that the piece geometry is characterised by a symmetry axis. This assumption concerns both the pure spectral and the hybrid numerical-spectral approach developed in the previous chapters. The integral equation formalism, either VIM or SIM, discussed in chapter 5 provides a way of treating deviations from the aforementioned symmetry, for practical reasons though, linked to the computational burden, this approach is interesting for treating small anomalies, primarily material defects.

The developed tools can be extended to tackle geometries combining pieces, that verify some sort of symmetry themselves, but the ensemble is entirely 3D. This can be the case of a tilted cylindrical ferrite, for example, above a planar piece, the combination of a cylindrical piece with a rectangular edge, a case met practically during tube inspection near supporting bars, etc. The surface equivalence theorem provides us here a powerful tool, which allows the separation of the initial problem into a number of coupled subproblems, which are treated in their native coordinate system, and communicate to each other via an exchange surface, also referred to as the Huygens surface [6, 7].

The main ideas of this coupling will be made clear by working on a specific problem, which also presents practical interest: the response of a ferrite-cored induction coil above a planar specimen as shown in Fig. 7.17.

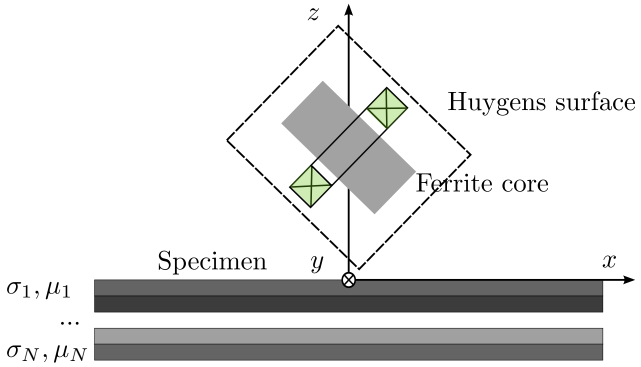

Figure 7.17: Tilted ferrite-cored coil above a ferromagnetic planar multilayer piece.

### 7.8.1 Hybrid FIT-spectral formulation

We consider an arbitrary fictitious closed surface that entirely encloses the probe ensemble. The problem can be decomposed in an interior subproblem comprising the coil and the ferrite core and an external one, which includes the remaining part of the geometry (the piece). Recall that due to the negligible electrical conductivity of the ferrite core, the electromagnetic problem in both air and ferrite domains can be formulated using a magnetostatic scalar potential $\boldsymbol{\phi}$.

As discussed in section 3.3 when developing the propagator theory, the solution of the interior problem is formally equivalent with the original one, provided that the scalar potential and/or its normal derivative on the boundary is the same for both formulations. Using the same arguments, we can set an equivalent problem in the external to the surface domain, based on the (assumedly known) magnetic potential/normal magnetic induction distribution on the boundary. The choice of the distribution that we shall take into account depends on the boundary condition we shall impose at the boundary, i.e. if it will be Dirichlet or Neumann BC. The former will result in an imposed potential distribution, whereas the latter is bound with an equivalent magnetic charge on the boundary [3].

We start the analysis by treating first the interior problem. We define a cylindrical box embedding the coil-ferrite ensemble. The cylindrical box is coaxial with the coil-ferrite ensemble. We require a non-homogeneous Neumann condition for the magnetostatic potential there (cf. Fig. 7.17). The magnetostatic formulation in the FIT basis is expressed by (7.13) with an additional source term accounting for the normal magnetic field at the domain boundary, which acts as an equivalent magnetic charge source. The rotational symmetry of the geometry entails the use of the cylindrical coordinate system. Notice that the boundary term $\widehat{\widehat{\mathbf{b}}}^{(b)}$ is subjected in general to no symmetry since it will be fixed through the interaction with the rest of the geometry, and will be thus expressed using a series of higher-order modes. Introducing the modal expansion of (7.43), (7.13) can be written

$$\left[\widetilde{\mathbf{S}}_t \mathbf{M}_\mu^T \mathbf{G}_t - \alpha_n^2 \mathbf{M}_\mu^N\right] \boldsymbol{\phi}_n = \widetilde{\mathbf{S}}_t \mathbf{M}_\mu^T \widehat{\mathbf{h}}_i \delta_{n,0} + \widehat{\widehat{\mathbf{b}}}_n^{(b)}, \quad \text{for} \quad n = -N_n \ldots N_n, \tag{7.123}$$

with $\alpha_n = n\Delta\varphi$, $\Delta\varphi$ being the angular opening of a FIT cell and $\delta_{n,0}$ the Kronecker delta. $\mathbf{M}_\mu^T$ and $\mathbf{M}_\mu^N$ are permeability submatrices at the discretisation plane $(u, v)$ and the normal direction $w$, and $\widetilde{\mathbf{S}}_t, \mathbf{G}_t$ stand for the tangential topological div and grad operators.

Assume for the moment that $\widehat{\widehat{\mathbf{b}}}^{(b)}$ is known. Solving (7.123) we obtain the magnetostatic potential $\boldsymbol{\phi}_n$ throughout the FIT box. For the treatment of the exterior problem, the solution has to be propagated in the external region and projected onto the representation basis of the outer problem following the approach of chapter 3.

For the solution in the external domain, we shall work in the local cylindrical coordinate system defined by the planar piece with the $z$-axis being normal to the piece interfaces. The origin $z = 0$ is set at the intersection point of the axis with the uppermost interface of the piece as shown in Fig. 7.17. The corresponding Darboux frame of the interface is $(t, g, n) = (\rho, \phi, z)$ (second row in Tab. 3.1). Following the TREE practice, the domain is truncated at radial distance equal to $\rho_L$ using a PMC. The solution for the external domain in the propagator language is expressed by (cf. section 3.4)

$$\begin{aligned}\sum_a \left[\langle m'\ell'|\, \hat{\boldsymbol{\nu}}_{b^+} \hat{\boldsymbol{C}}_{b^+} \hat{\boldsymbol{P}}_{a\to b^+} - \hat{\boldsymbol{\nu}}_{b^-} \hat{\boldsymbol{C}}_{b^-} \hat{\boldsymbol{P}}_{a\to b^-} \,|m\ell\rangle\right] c_{m\ell}^{(a)} \\ = \delta_{b0} \,\langle m\ell|\, \hat{\boldsymbol{\nu}}_{b^+} \hat{\boldsymbol{C}}_{b^+} \,|m\ell\rangle \, c_{m\ell}^{(0^+)}, \qquad \forall j\end{aligned} \tag{7.124}$$

where $c_{m\ell}^{(0^+)}$ are the development coefficients obtained by the projection of the FIT solution propagation onto the piece upper surface ($a = 0^+$).

Summing up, the total solution is expressed by the state variables $\boldsymbol{\phi}_n$ and $c_{m\ell}^{(a)}$, which have to satisfy (7.123) and (7.124), respectively. The two equations are coupled via the variables $\widehat{\widehat{\mathbf{b}}}_n^{(b)}$ and $c_{m_0}^{(F)}$, which in their turn are the projections of the external and internal problem field onto the FIT and TREE development basis respectively. Thus the $\widehat{\widehat{b}}_{nl}^{(b)}$ values are computed by the integrals

$$\begin{aligned}\widehat{\widehat{b}}_{nl}^{(b)} &= \frac{\Delta w}{2\pi} \operatorname{sinc}(\kappa_n w) \int_0^{2\pi} e^{inw'} dw' \begin{cases} \int_{\Delta v_l} \Phi_{0^+}(\mathbf{x})\, dv' \\ \int_{\Delta u_l} \Phi_{0^+}(\mathbf{x})\, du' \end{cases} \\ &= \langle nl | \Phi_{0^+} \rangle\end{aligned} \tag{7.125}$$

depending if the facet element $l$ lies on the side surface ($\rho = \rho_{\max}$) or the top and bottom lids ($z = z_{\min}, z_{\max}$). $\Phi_{0^+}$ stands for the outer solution for the magnetic potential ($0^+$ signifies upwards scattered field) calculated in the FIT local coordinate frame. With the standard Bessel functions basis for the $\rho_L$ truncated domain it takes the explicit form (in the piece local coordinate system)

$$\Phi_{0^+}(\rho, \phi, z) = \sum_m c_{m\ell}^{(0^+)} J_m(\lambda_{m\ell}\rho)\, e^{im\phi - \lambda_{m\ell} z} \tag{7.126}$$

where $\lambda_{m\ell}\rho_L$ is the $\ell$th root of the Bessel function of $m$ order

$$J_m(\lambda_{m\ell}\rho_L) = 0. \tag{7.127}$$

$c_{m\ell}^{(0-)}$ are evaluated by propagating the FIT solution $\boldsymbol{\phi}$ to the $z = 0$ interface. Vehicle again to this operation will be Green's second identity (3.26). The evaluation can be carried out in a straight-forward manner by numerical computation of the integral in the spatial domain. Nevertheless, this approach is confronted with two issues: the treatment of the singular kernel at points of closest proximity (in ECT problems the minimisation of the probe lift-off is of crucial importance) and the (expensive) evaluation of the four-fold integrals of the coupling matrices. Both issues are avoided by addressing the problem (once again) in the spectral domain.

There are two different expansions that can be applied, associated with the different Darboux frames defined for $\rho =$ const and $z =$ const of the side surface and the lids, each involving a branch change in different coordinate axes ($\rho$ and $z$ respectively). It is thus more convenient to split the integral into the integration surfaces depicted in Fig. 7.18, each one involving only one branch change (at the intersection of the surface with the $z = 0$ interface).

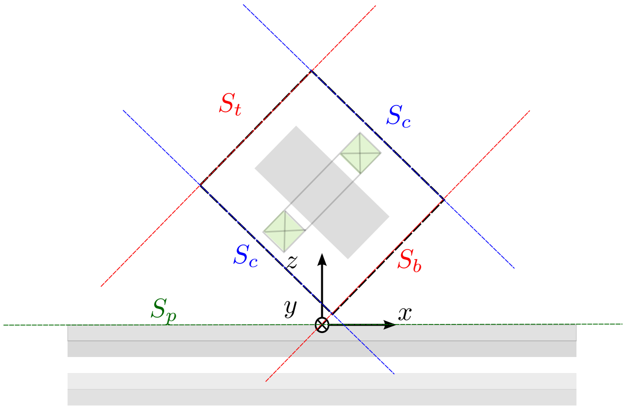

Figure 7.18: Reference surfaces for the propagation of the inner and outer solution.

The sought $\Phi_0^{(F)}$ potential term can thus be written as the sum of three separate contributions

$$\Phi_{0^+}(u,v,w) = \Phi_{0^+}^{(c)}(u,v,w) + \Phi_{0^+}^{(t)}(u,v,w) + \Phi_{0^+}^{(b)}(u,v,w) \tag{7.128}$$

where $\Phi_{0-}^{(s)}$ is the contribution from the side cylindrical surface given by (in FIT reference frame)

$$\Phi_{0^+}^{(c)}(u,v,w) = \sum_n e^{inw} \sum_{l\in S_c} \widehat{\widehat{b}}_{nl}^{(b)} e^{iq_\ell v} \begin{cases} I_n(q_\ell u)\, K_n(q_\ell u_c)\,, & u < w_c \\ K_n(q_\ell u)\, I_n(q_\ell u_c)\,, & u > w_c \end{cases} \tag{7.129}$$

$\Phi_{0^+}^{(t)}$ stands for the contribution of the top surface with

$$\Phi_{0^+}^{(t)}(u,v,w) = \sum_n e^{inw} \sum_{l\in S_t} \widehat{\widehat{b}}_{nl}^{(b)} J_n(\lambda_{n\ell} u_l)\, e^{-\lambda_{nl}|v-v_t|} \tag{7.130}$$

and $\Phi_{0^+}^{(b)}$ the respective term for the bottom lid. It is obtained using the same relation with that for the top lid setting $v_b$ instead of $v_t$. The eigenvalues used for the above expansions are determined by choosing a set of suitable truncation boundaries $u_L$ and $v_L$ for the two branches and imposing PMC and periodic BC respectively, which results for $\lambda_{nl}$ and $q_\ell$

$$J_n(\lambda_{n\ell} u_L) = 0 \tag{7.131}$$

and

$$q_\ell = \frac{\ell\pi}{v_L}. \tag{7.132}$$

Equations (7.123),(7.124) together with the coupling relations (7.125) and (7.128)-(7.130) constitute a system of linear equations whose solution yield the field in the entire domain. However, due to the high dimensionality of the coupling integrals, their simultaneous treatment will encounter memory problems. It is more easy to treat the two state equations iteratively in a two-step procedure [6]. The overall algorithm is described in Alg. 2.

### 7.8.2 Results

The proposed coupled approach is applied for the calculation of a cylindrical, ferrite-cored coil interacting with a planar conducting and non-magnetic half-space. The considered ferrite is rod-shaped and had negligible losses. The coil and core characteristics are given in Tab. 7.3. The half-space conductivity is taken 18 MS/m.

Fig. 7.19 illustrates the normal component of the induced magnetic flux density on the half-space interface calculated using two coupled approaches (i.e. the FIT-spectral one and similar coupling between a boundary elements method, BEM, implementation and the spectral approach) versus the fully numerical solution obtained by a commercial FEM package COMSOL Multiphysics ® [123] at 1 kHz. The probe axis is tilted in respect to the normal of the plane by

**Algorithm 2** Hybrid FIT 2.5D - TREE solution

```
Initialise $\widehat{\widehat{\mathbf{b}}}^{(b)} \leftarrow \mathbf{0}$, $\boldsymbol{\phi}^{i-1} \leftarrow \mathbf{0}$, $\epsilon \leftarrow 10^{20}$
while $\epsilon < tol$ do
    Solve $\left[\widetilde{\mathbf{S}}_t \mathbf{M}_\mu^T \mathbf{G}_t - \alpha_n^2 \mathbf{M}_\mu^N\right] \boldsymbol{\phi}_n^i = \widetilde{\mathbf{S}}_t \mathbf{M}_\mu^T \widehat{\mathbf{h}}_i \delta_{n,0} + \widehat{\widehat{\mathbf{b}}}_n^{(b)}$
    Evaluate $\Phi_{0-}(\boldsymbol{\phi})$: (7.128)-(7.130)
    $c_{ml}^{(0-)} \leftarrow \langle m\ell | \Phi_{0-} \rangle$
    Solve $\sum_a \langle m'\ell' | \ldots | m\ell \rangle \, c_{m\ell}^{(a)} = \delta_{b0} \, \langle m\ell | \ldots | m\ell \rangle \, c_{m\ell}^{(0-)}$
    Evaluate $\Phi_{0+}\left(c_{ml}^{(0+)}\right)$: (7.126)
    $\widehat{\widehat{b}}_{nl}^{(b)} \leftarrow \langle nl | \Phi_{0+} \rangle$: (7.125)
    $\epsilon \leftarrow ||\boldsymbol{\phi}^i - \boldsymbol{\phi}^{i-1}||$
    $i \leftarrow i + 1$
end while
```

Table 7.3: Coil and core parameters

| Coil parameters | |
|---|---|
| Inner radius $r_{in}$ | 3 mm |
| Outer radius $r_{out}$ | 6 mm |
| Length $l$ | 2 mm |
| Number of turns $N$ | 2000 |

| Core parameters | |
|---|---|
| Radius $r$ | 2 mm |
| Length $l$ | 5 mm |
| Relative permeability | 10 |

an angle of 20 degrees. The convergence of the iterative solution has been reached after 5 iterations for the hybrid FIT and 3 iterations for the hybrid BEM approach. The calculation time was ca. 5 min for both approaches on a standard PC whereas FEM simulation time was 10 minutes on a 24 GB, Xeon PC with 8 cores.

A second comparison between the results of the coupled approach and the full numerical FEM simulation has been carried out for the calculation of the probe impedance as a function of the tilt angle. The results are shown in Fig. 7.20

## 7.9 Publications related with the chapter content

The mixed spatial-spectral formulation using FIT discretisation scheme has been presented in a couple of communications in NDT conferences [126, 127] with a detailed study been published in [128]. A first presentation of the TD version has been presented at [129]. A full article is in preparation.

The coupling between FIT and the spectral approach for the treatment of the tilted ferrite has been the subject of the master thesis of Dr. Audrey Vigneron. The results of her work have been presented in [130] and in [7]. In the last

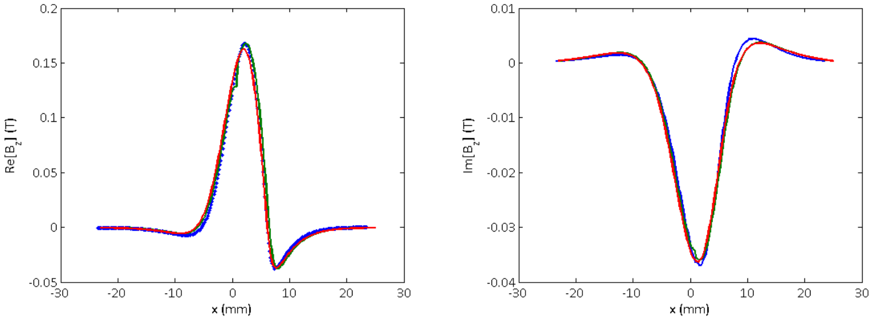

Figure 7.19: $B_z$ field component on the half-space interface calculated using the two coupled approaches versus FEM results obtained with COMSOL.

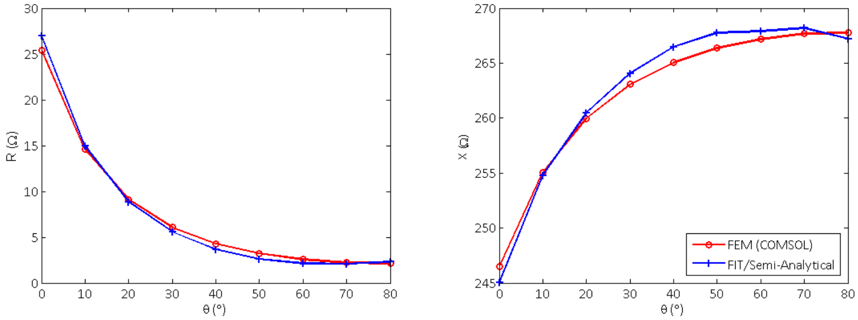

Figure 7.20: Real and imaginary part of the probe impedance variation as a function of the tilt angle.

article, the coupled approach has been generalised in order to include also the BEM approach.

# Chapter 8

# The non-linear problem

In standard ECT applications, we are confronted to the detection and characterisation of anomalies in a more or less known material, which is equivalent with stating that we are seeking to retrieve changes in the piece geometry. The problem thus belongs to the broad category of scattering problems with the peculiarity that the sensing is carried out in the near-field region.

In the so-called material characterisation family of methods, the focus is shifted from the geometry to the material itself. We are not interested in the geometry of the particular specimen, which is considered as known or irrelevant, but we are trying to characterise features of the material itself. It is well understood that for a given inspection method the material is characterised via the physical parameters to which the method is sensitive. As far as electromagnetic methods are concerned these parameters are the electrical conductivity and the magnetic properties expressed via the $\mathbf{B}(\mathbf{H})$ material curve.

The characterisation of the magnetic properties in ferromagnetic materials present particular interest, which is explained by the strong dependence of the magnetic behaviour from the material microstructure. This feature makes magnetic measurements an excellent probe for more fundamental properties of the material, such as its grain structure, the density of impurities (precipitates), lattice imperfections (dislocations) and so on. Since the microstructural parameters are also determinant of other material properties, as for example certain mechanical properties, which in addition are not easy to be measured in a non-destructive way, it becomes evident the importance of magnetic methods for the assessment of the material state.

The rich information carried by the magnetic properties comes however at a cost. The direct link of the $\mathbf{B}(\mathbf{H})$ curve and the thereupon derived variables such as the differential or the incremental permeability is extremely complicated. In addition, the solution of the macroscopic electromagnetic problem (the Maxwell equations), which is an indispensable step when the sensor response needs to be evaluated for a given material law, is by itself a difficult task due to the non-linear and hysteretic nature of the $\mathbf{B}(\mathbf{H})$ constitutive relation.

The objective of this chapter will be this last task: the analysis and the development of efficient numerical tools for addressing the solution of the electromagnetic problem with a known non-linear and hysteretic $\mathbf{B}(\mathbf{H})$ material law. It is understood that the ultimate goal for this kind of applications is the development of multi-scale approaches permitting to cross the full path spanning from the metallurgical description of the piece to the sensor response. This is however a huge task, which can be naturally viewed as a long-time perspective of this work. A roadmap towards contributions to multi-scale simulation of material evaluation applications is given with the outlook of the present work at the end of this text.

## 8.1 Description of the problem

We consider the case of a (flawless) ferromagnetic material excited by means of an air-cored inductor (coil) or an inductor equipped with a magnetic circuit (yoke) as shown in Fig. 8.1. In both cases the exciting coil is fed with a time-varying current $I(t)$. We are interested in planar sheet geometries for simplicity reasons and also because this is the usual form of semi-finalised products used in material evaluation applications (having in mind in particular hot and cold-rolled strips in steel manufacturing).

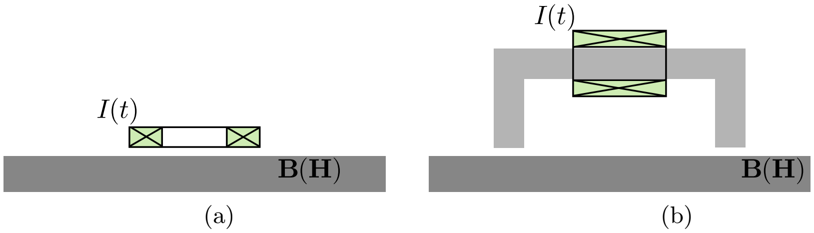

(a) (b)

Figure 8.1: Typical excitation set-ups for the electromagnetic characterisation of ferromagnetic pieces: (a) via an induction coil, (b) using a magnetic circuit.

The field in the air above or/and beneath the inspected piece is sensed by means of an induction coil (which can be the same with the exciting coil) and/or magnetic sensors such as Hall-effect probes or giant magnetoresistance sensors (GRM). The particular physics of the probe being irrelevant for our analysis, all field sensors will be considered as ideal.

The material is characterised by its electrical conductivity $\sigma$ and the magnetic constitutive relation $\mathbf{B}(\mathbf{H})$, which is non-linear and it may possess a multi-branch hysteresis behaviour. We are interested in constructing solutions for the field distribution inside the inspected piece and the probe signal for given material parameters $\sigma$ and $\mathbf{B}(\mathbf{H})$. The development of these solutions will be carried out in two steps. We shall first consider single-branch non-linear laws, which will be linearised using one of the established techniques and the electromagnetic problem will be solved via an iterative scheme. The complications of multi-branch hysteresis will be tackled thereafter by addressing the branch-switch during the signal evolution.

## 8.2 Linearisation schemes

The general form of the magnetic constitutive equation accounting for anisotropic non-linear materials was given in (2.6). It is rewritten here for convenience

$$\mathbf{B} = \mu_0 \left[\mathbf{H} + \mathbf{M}(\mathbf{H})\right] \tag{2.6}$$

where $\mathbf{M}$ the magnetisation of the medium, which is a function of the applied magnetic field. In non-magnetic materials (diamagnetic and paramagnetic) $\mathbf{M}$ is a linear function of the magnetic field, and the proportionality constant is called the **magnetic susceptibility** $\chi_m$ of the medium. Since we are talking for diamagnetic and paramagnetic materials, there is no preference direction, and hence $\chi_m$ is a scalar.

In ferromagnetic materials[1], however, $\mathbf{M}$ is a non-linear function of $\mathbf{H}$, which means that some kind of linearisation is required in order to be able to solve the Maxwell equations. There are in general two established schemes for linearising a material relation: the fixed-point method (also known as Picard-Banach or polarisarion method) and the Newton-Raphson method.

### 8.2.1 The fixed-point iteration method

Substitution of (2.6) in the Maxwell equations will result in the following relation for the magnetic vector potential

$$\nabla \times \nu_0 \nabla \times \mathbf{A} + \sigma \frac{d\mathbf{A}}{dt} = \mathbf{J} + \nabla \times \mathbf{M}(\mathbf{A}) \tag{8.1}$$

which is recognised as the diffusion equation, studied in the previous chapters, with the unknown magnetisation acting as an equivalent magnetic source. Since the free-space reluctivity is constant, it can be brought to the right-hand-side and upon application of the Coulomb gauge, (8.1) reduces to the following form

$$\left(\nabla^2 - \mu_0 \sigma \frac{d}{dt}\right) \mathbf{A} = -\mu_0 \mathbf{J} - \nabla \times \mathbf{I}(\mathbf{A})\,. \tag{8.2}$$

Both expressions will be utilised depending on the numerical scheme that will be applied for the inversion of the diffusion operator.

Since $\mathbf{M}$ (or $\mathbf{I}$) is not apriori-known, it can be approximated by an initial guess, which will be successively improved by repeated solution of (8.1) or (8.2). This can be perhaps better understood by restating the problem in operator form (we shall consider the first expression (8.1) for the demonstration).

---

[1] We distinguish three different types of magnetic materials (i.e. materials which in atomic scale present an exchange interaction): ferromagnetic, ferrimagnetic and antiferromagnetic. Only the first category will be considered herein since it contains all materials of technical importance in NDT applications, notably steels.

Defining the operators

$$\mathscr{D}_{PB} := \nabla \times \nu_0 \cdot \nabla \times + \sigma \frac{\partial}{\partial t} \tag{8.3}$$

$$\mathscr{F} := \mathbf{I}(.) \tag{8.4}$$

$$\mathrm{curl} := \nabla \times \tag{8.5}$$

(8.1) can be readily written

$$\left(\mathscr{D}_{PB} + \mathrm{curl} \circ \nu_0 \mathscr{F} \circ \mathrm{curl}\right) \mathbf{A} = -\mu_0 \mathbf{J} \tag{8.6}$$

which can be formally inverted as

$$\mathbf{A} = -\left(\mathscr{I} + \mathscr{D}_{PB}^{1} \circ \mathrm{curl} \circ \nu_0 \mathscr{F} \circ \mathrm{curl}\right) \mathscr{D}_{PB}^{1} \mu_0 \mathbf{J} \tag{8.7}$$

with $\mathscr{I}$ the unit operator. Developing the inverse operator in Neumann series yields

$$\mathbf{A} = \mathbf{A}^{(0)} + \left(\mathscr{D}_{PB}^{-1} \circ \mathrm{curl} \circ \nu_0 \mathscr{F} \circ \mathrm{curl}\right) \mathbf{A}^{(0)} + \left(\mathscr{D}_{PB}^{-1} \circ \mathrm{curl} \circ \nu_0 \mathscr{F} \circ \mathrm{curl}\right)^2 \mathbf{A}^{(0)} + \ldots \tag{8.8}$$

with $\mathbf{A}^{(0)} = -\mathscr{D}^1 \mu_0 \mathbf{J}$. This is equivalent with the iteration scheme

$$\mathbf{A}^{(l+1)} = \mathbf{A}^{(l)} + \left(\mathscr{D}_{PB}^{-1} \circ \mathrm{curl} \circ \nu_0 \mathscr{F} \circ \mathrm{curl}\right) \mathbf{A}^{(l)}, \quad l = 0, 1, \ldots \tag{8.9}$$

Should the scheme be applied for the Laplacian form (8.2), (8.9) simplifies a little yielding the iterative scheme

$$\mathbf{A}^{(l+1)} = \mathbf{A}^{(l)} + \left(\mathscr{D}_{PB}^{-1} \circ \mathrm{curl} \circ \mathscr{F} \circ \mathrm{curl}\right) \mathbf{A}^{(l)}, \quad l = 0, 1, \ldots \tag{8.10}$$

with the according field operator

$$\mathscr{D}_{PB} := \nabla^2 - \sigma \frac{d}{dt}. \tag{8.11}$$

It must be underlined at this point that the above linearisation and the corresponding material operator definition based on (2.6) is not the only option. In fact, improved convergence behaviour can be achieved by using a virtual "calculation" permeability/reluctivity, which can also be anisotropic

$$\mathbf{B} = \mu_0 \left(\mathbf{H} + \mathbf{M}\right) = \overline{\mu} \mathbf{H} + \left[\mu_0 \mathbf{M} + \left(\mu_0 - \overline{\mu}\right) \mathbf{H}\right] \tag{8.12}$$

which implies a magnetic polarisation

$$\mathbf{I} = \mu_0 \mathbf{M} + \left(\mu_0 - \overline{\mu}\right) \mathbf{H} \tag{8.13}$$

and $\nu$ in (8.9) must be replaced by $\overline{\nu} = \overline{\mu}^{-1}$. Later in this chapter criteria for fixing the calculation permeability in order to achieve improvements in the convergence speed will be given.

The iterative scheme described by (8.9),(8.10) is known as **fixed-point (FP)**, or **Picard-Banach (PB)**, or polarisation method [131–140].

### 8.2.2 The Newton-Raphson method

Let us assume again that the sought solution is described by the operation point $(\mathbf{H}_0, \mathbf{B}_0)$ on the material curve, all vectors being understood as function of the position. For probing points in the vicinity of the solution we can develop the material law $\mathbf{B}(\mathbf{H})$ in a Taylor series

$$\mathbf{B}(\mathbf{H}) \approx \mathbf{B}_0 + \left.\frac{\partial \mathbf{B}}{\partial \mathbf{H}}\right|_{\mathbf{H}_0} \cdot (\mathbf{H} - \mathbf{H}_0) + \mathscr{O}\big(\mathbf{H}^2\big) \tag{8.14}$$

and ignoring the higher order terms

$$\Delta \mathbf{B} \approx \overline{\mu}_d \cdot \Delta \mathbf{H} \tag{8.15}$$

with $\Delta \mathbf{B} = \mathbf{B} - \mathbf{B}_0$, $\Delta \mathbf{H} = \mathbf{H} - \mathbf{H}_0$ and $\overline{\mu}_d$ the differential permeability tensor defined as

$$\overline{\mu}_d \coloneqq \left.\frac{\partial \mathbf{B}}{\partial \mathbf{H}}\right|_{\mathbf{H}_0}. \tag{8.16}$$

Subtracting $\nabla \times \mathbf{H}_0$ from both sides of the Ampère equation and using (8.15) yields

$$\nabla \times \overline{\nu}_d \cdot \Delta \mathbf{B} = \sigma \mathbf{E} + \mathbf{J} - \nabla \times \mathbf{H}_0. \tag{8.17}$$

where we have called $\overline{\mu}_d^{-1} = \overline{\nu}_d$ as the differential tensor reluctivity. With the introduction of the magnetic vector potential and a slight term rearrangement, the last relation becomes

$$\nabla \times \overline{\nu}_d \cdot \nabla \times \mathbf{A} + \sigma \frac{\partial \mathbf{A}}{\partial t} = \mathbf{J} + \nabla \times \mathbf{M}_0. \tag{8.18}$$

The resulting equation (8.18) has exactly the same form with (8.1), with the only difference being the reluctivity entering the curl-curl operator. One can thus expect same treatment with the fixed-point method via an iterative procedure, i.e.

$$\mathbf{A}^{(l+1)} = \mathbf{A}^{(l)} + \big(\mathscr{D}_{NR}^{-1} \circ \mathrm{curl} \circ \overline{\nu}_d \mathscr{F} \circ \mathrm{curl}\big)\, \mathbf{A}^{(l)}, \qquad l = 0, 1, \ldots \tag{8.19}$$

with the diffusion operator

$$\mathscr{D}_{NR} \coloneqq \nabla \times \overline{\nu}_d \cdot \nabla \times + \sigma \frac{\partial}{\partial t} \tag{8.20}$$

and $A^{(0)} = \mathscr{D}_{NR}^{-1} \mathbf{J}$.

The scheme described by (8.19) is known as the **Newton-Raphson (NR) method**, and is the second established scheme for the solution of the non-linear problem [137, 138, 141–147].

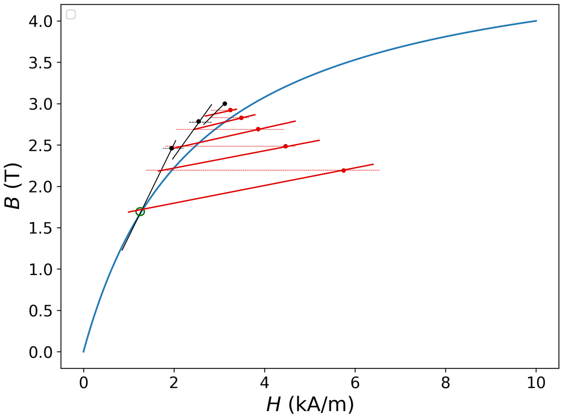

Figure 8.2: Graphical representation of the convergence for the PB (red) and NR (black) schemata. The points on the line segments stand for the solution of the linearised diffusion operator, which are back-projected to the material curve after each iteration for constant B. Following the local slope of the material curve NR arrive to convergence in less steps.

### 8.2.3 Comparison

From a direct comparison of (8.1) with (8.18), it is evident that the main difference between the two methods resides in the definition of the reluctivity (permeablility) for the linearised problem, which in the case of the fixed point method is fixed, whereas for the NR method is derived by the differential permeability of the material at the considered point, a fact that makes them formally the same method. This fact has already been realised and thoroughly discussed in the literature, and has been the base for constructing hybrid formulations combining the two approaches [137]. A graphical representation of convergence procedure for the two schemata is given in Fig. 8.2.

There are however important differences stemming from this different definition of the “working” permeability. The first one is practical and is related with the position dependence of the differential permeability, which makes the linearised material in case of the NR method highly inhomogeneous, and hence only applicable in combination with mesh-based methods, like the FEM [141, 142, 148, 149] or FIT [120, 137, 143, 144]. This issue does not arise with the PB, where the constant permeability results in piece-wise homogeneous geometries, which consequently makes it well adapted for the spectral methods presented in the previous chapters. The construction of such solutions will be demonstrated in a latter section.

A second difference lies in the convergence speed, which in case of NR is quadratic, whereas for the PB method is much slower (as one might guess by regarding the qualitative tendencies in Fig. 8.2), and depending on the selected error threshold, can arrive at a long plateau. A clear demonstration of the convergence behaviour of the two methods will be made in a later paragraph via an example.

The significantly faster convergence of the NR method, comes, however at a cost. The stability of the method is not guaranteed, and it is therefore mandatory to introduce some relaxation factor in order to assure a convergent scheme, in contrast with the PB approach, which with a suitable choice of the permeability/reluctivity value is strictly convergent. Note that the speed of convergence of the iteration sequence can be increased by using a convergence acceleration method such as Aitken's delta-squared process. The application of Aitken's method to fixed-point iteration is known as Steffensen's method, and it can be shown that Steffensen's method yields a rate of convergence that is at least quadratic [150].

## 8.3 Solution using FIT

The general iterative schemata described by (8.1) and (8.18) need to be combined with a suitable numerical scheme which evaluates the $\mathscr{D}^{-1}$ operator. The standard choice is to apply one of the established a spatial/temporal discretisation schemes based on the FEM or the FIT methods. Since in this work we have already used the FIT method, the latter will be the numerical method of choice in this context as well. As already stated, the additional benefit of using the FIT formulation is the direct analogy of the discrete operators with the continuous case, which enhances the readability of the expressions.

### 8.3.1 Time integration

The linearised curl-curl equation in the discrete FIT-grid basis reads

$$\widetilde{\mathbf{C}}\mathbf{M}_\nu\mathbf{C}\widehat{\mathbf{a}} + \mathbf{M}_\kappa \frac{d}{dt}\widehat{\mathbf{a}} = \widehat{\widehat{\mathbf{j}}} + \widetilde{\mathbf{C}}\widehat{\mathbf{m}} \tag{8.21}$$

in close analogy with (8.1) and (8.18). Notice that $\widehat{\widehat{\mathbf{j}}}$ stands here for the physical electric current density at the excitation coil. The definition of the reluctivity matrix $\mathbf{M}_\nu$ depends on the linearisation scheme, and is based on the same relations used for the continuous case, namely $\nu = \nu_0$ and (8.15) for the PB and the NR scheme, respectively. With the reluctivity matrix given, the magnetisation vector is obtained by simple application of the constitutive relation, namely

$$\widehat{\mathbf{m}} = \mathbf{M}_\nu \widehat{\widehat{\mathbf{b}}} - \widehat{\mathbf{h}}. \tag{8.22}$$

Given the algorithmic equivalence of the two schemes, the exact definition will be intentionally left unspecified to keep the discussion valid for both schemes.

Introducing the BDF1 scheme (7.90) for the discretisation of the temporal derivatives (8.21) becomes

$$\left(\widetilde{\mathbf{C}}\mathbf{M}_\nu\mathbf{C} + \frac{1}{\Delta t}\mathbf{M}_\kappa\right)\widehat{\mathbf{a}}_j = \frac{1}{\Delta t}\mathbf{M}_\kappa\widehat{\mathbf{a}}_{j-1} + \widehat{\widehat{\mathbf{j}}}_j + \widetilde{\mathbf{C}}\widehat{\mathbf{m}}_j. \tag{8.23}$$

Equation (8.23) must be solved iteratively to determine $\widehat{\mathbf{a}}_j, \widehat{\mathbf{m}}_j$ and $\mathbf{M}_\nu$ following one of the PB or the NR schemes, whence we arrive at the following generic iteration scheme

$$\left(\widetilde{\mathbf{C}}\mathbf{M}_\nu^{(l)}\mathbf{C} + \frac{1}{\Delta t}\mathbf{M}_\kappa\right)\widehat{\mathbf{a}}_j^{(l)} = \frac{1}{\Delta t}\mathbf{M}_\kappa\widehat{\mathbf{a}}_{j-1} + \widehat{\widehat{\mathbf{j}}}_j + \widetilde{\mathbf{C}}\widehat{\mathbf{m}}_j^{(l-1)} \tag{8.24}$$

where $l$ stands for iteration index of the non-linear solution scheme. Notice that $\widehat{\mathbf{a}}_{j-1}$ does not depend on $l$ since the solution at the previous time-steps is assumed having converged.

### 8.3.2 Performance and characteristic results

It has been explained in section 8.2 that the PB and the NR linearisation schemes can be utilised interchangeably in a generic iterative scheme like the one described by (8.24). To get a better image of the numerical performance of both schemes, (8.24) is applied for the solution of the prototypical problem of the electromagnetic inspection of a ferromagnetic plate, using the first set-up of Fig. 8.1. A more detailed image of the considered set-up is given in Fig. 8.3. The specimen is excited at a very low frequency by a pair of air-cored cylindrical coils, which are fed by opposite currents. The purpose of this particular type of excitation is to create a strong magnetic field parallel to the plate surfaces component in a similar way as we would do using a magnetic circuit such as in Fig. 8.1b. Variations of this configuration are used in industrial probes such as the HACOM and the IMPOC for in-line monitoring of the steel-strip properties in steel production sites [151,152]. The air-cored coils are preferred here for this type of applications in place of the yoke set-up in order to avoid the geometrical complexity and the uncertainties of the yoke material as well as the very strong sensitivity from the lift-off.

We consider the case of harmonic excitation at 60 Hz. A simple scalar material law following the Fröhlich-Kennelly relation is assumed [5]

$$B(H) = \frac{H}{\alpha + \beta\,|H|}. \tag{8.25}$$

This simple relation, derived by the high-field asymptote of the material hysteric relation, provides a fairly good approximation of the anhysteretic curve. The $\alpha, \beta$ parameters are obtained by identifying the curve with an experimental anhysteretic curve of the material of interest. In this example we use the low-carbon steel 1010 as model material, whose anhysteretic $B(H)$ curve is shown in Fig. 8.4. In the same figure is also drawn the curve obtained by Fröhlich-Kennelly relation after identification of the parameters $\alpha, \beta$. The parameters

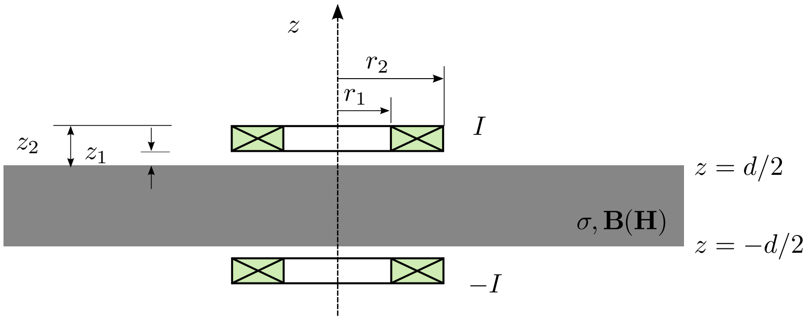

Figure 8.3: Inspection of a ferromagnetic plate using a set of 180 ° out of phase cylindrical coils.

identification has been carried out by minimisation of the $L^2$ distance yielding the values $\alpha = 206.42, \beta = 0.59148$. A very good description of the experimental curve is achieved at the high-field region, as expected, whereas the model fail to follow the real curve below the knee point. Overall, the level of approximation is acceptable to consider the model curve as close to a realistic material law.

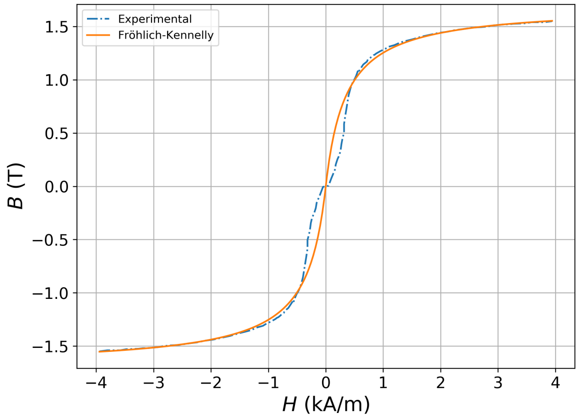

Figure 8.4: $B(H)$ curve of the 1010 steel. Experimental data and identified Fröhlich-Kennelly model.

Equation (8.24) has been solved for both PB and NR schemes, the latter using an appropriate relaxation factor. The convergence of the two schemes at a specific time step close to the maximum of the excitation is shown in Fig. 8.5a. The convergence rate is expressed in terms of the energy residual between iterations. Both schemes initiate with a comparable slope up to a residual of $10^{-4}$, where PB enters at a long plateau with a relative flat slope. NR iterations, on the contrary, converge with more-or-less constant speed reaching the stop-tolerance much faster. A third option, which combines the PB stability with the NR convergence speed, is to switch from the PB to the NR scheme at the beginning of the plateau, when the solution is already close to its exact value, and there is little risk for the NR method to get trapped away from it. This idea has been explored in different ways the literature. In [137] for example the two solutions stemming from the application of the two schemes are linearly combined through a minimisation procedure.

Interesting information is also obtained by considering the residual as function of the computational time. The fact that LU factorisation can be applied in the context of the PB scheme, makes the iterations much cheaper from those of the NR method, where the differential permeability matrix must be computed and the system must be inverted at each iteration. This extra time per iteration partly cancels out the advantage of the smaller iteration number. Again, the interest of the combined (switching) scheme becomes evident, since the important decrease of the NR iterations leads to reduced total computational times.

The objection that can rise here, deals with the generality of the approach since the LU factorisation cannot be applied for the full 3D case (at least with the contemporary computer resources). Besides the interest of the 2D problem by itself for material evaluation applications, one can refer here to the mixed spatial-spectral approach presented in chapter 7, where the problem treatment per mode makes the system factorisation feasible.

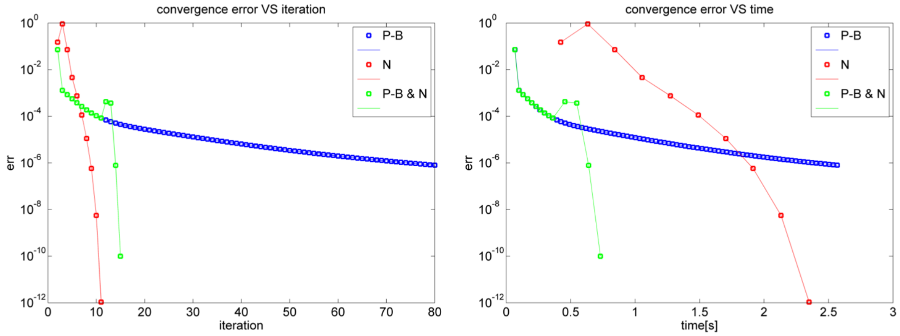
convergence error VS iteration

convergence error VS time

Figure 8.5: Convergence of the non-linear iterations during a given time-step for three different schemes: (i) pure PB, (ii) NR with relaxation (iii) combined PB-NR scheme with switching. (a) Convergence as function of the iteration index. (b) Convergence as function of solver time.

The field signals for the tangential and the normal component at different excitation levels, namely $I = 3$ A and $I = 10$ A are given in Fig. 8.6 and Fig. 8.7, respectively. The field signals are observed at three characteristic sample points inside the specimen located at $(r_1/2, d/4)$ (point 1), $((r_1 + r_2)/2, d/4)$ (point 2) and $(r_1/2 + r_2, d/4)$ (point 3). The numerical results obtained by the mixed PB/NR scheme are compared against reference results obtained using a commercial FEM code (COMSOL Multiphysics ® ), which implements a relaxed

NR approach.

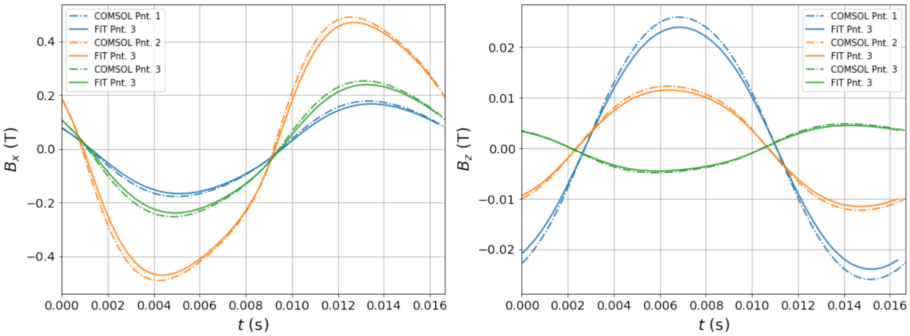

Figure 8.6: Transient signals for the $B_x$ and $B_z$ components at a number of different sample points. The coil excitation is 3 A. The FIT results are compared against reference results obtained using a commercial FEM code (COMSOL).

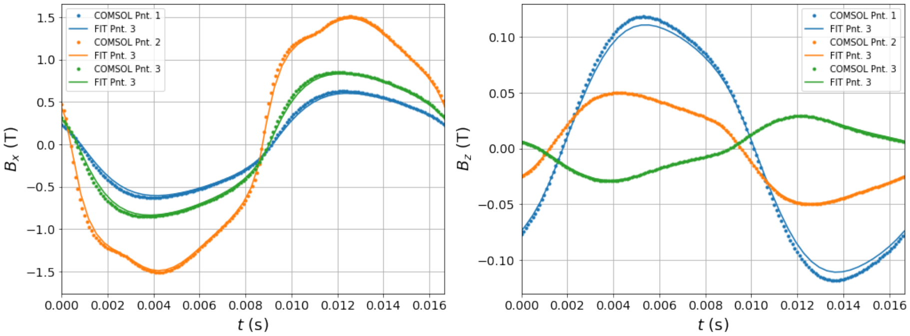

Figure 8.7: Transient signals for the $B_x$ and $B_z$ components at a number of different sample points. The coil excitation is 3 A. The FIT results are compared against reference results obtained using a comercial FEM code (COMSOL).

A closer look at (8.6) and (8.7) reveals the different deviation from the linear behaviour depending on the field component ($B_z$ being weaker in amplitude remains closer to the harmonic waveform than than $B_\rho$) and location. This location-dependence underlines the need for a careful design of the non-linear measurement in order to achieve the sought effect.

A more illustrative view of the non-linear behaviour can be readily obtained by examining the Fourier spectrum of the signals. The latter is plotted in (8.8) for the 10 A case. It is interesting to note the absence of even harmonics. This is a well known effect, and it can be proven that this is a direct consequence of the point symmetry of the $B(H)$ law.

In praxis, a commonly used figure-of-merit for the non-linear behaviour of a specific signal is its so-called harmonic distortion, defined as the ratio of the

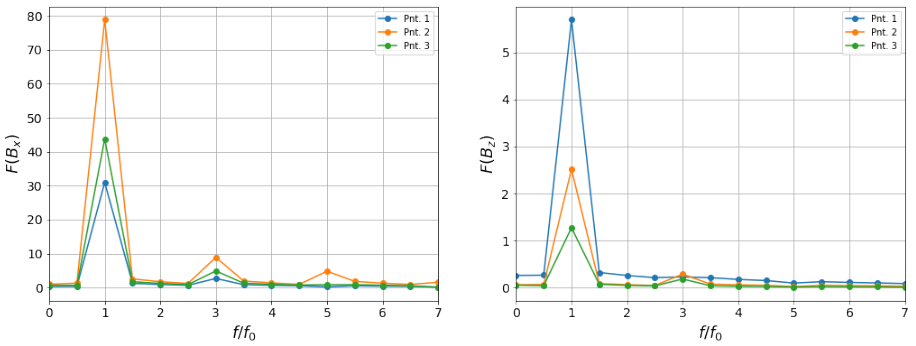

Figure 8.8: Signal spectrum for the $B_x$ and $B_z$ components at the considered sample points for a 10 A excitation current. The frequency axis is normalised with the excitation frequency $f_0 = 60$ Hz (basic harmonic). Notice the absence of even harmonics.

| | $B_\rho$ | | $B_z$ | |
|---|---|---|---|---|
| | $I = 3$ A | $I = 10$ A | $I = 3$ A | $I = 10$ A |
| Point 1 $(r_1/2, d/4)$ | 0.025 | 0.087 | 0.056 | 0.0486 |
| Point 2 $((r_1 + r_2)/2, d/4)$ | 0.067 | 0.130 | 0.044 | 0.114 |
| Point 3 $(r_1/2 + r_2, d/4)$ | 0.032 | 0.113 | 0.045 | 0.143 |

Table 8.1: Comparison of the harmonic distortion content for the $B_\rho$ and $B_z$ components under different excitation currents.

sum of the higher-harmonics to the basic one [153]

$$K = \sqrt{\frac{\sum_{p=1}^{\infty} A_{2p+1}^2}{A_1^2}}. \tag{8.26}$$

Numerical evaluation (8.26) for the signals of (8.6) and (8.7) yields the values of Tab. 8.1.

### 8.3.3 Concluding remarks

In this section we have examined the application of the two iterative schemes in the context of the FIT method. It has been demonstrated that, although slow in terms of the convergence rate, the PB approach presents some very useful features for the construction of a fast scheme. More precisely, we can state:

- The homogeneous permeability profile obtained for the linearised problem allows the system factorisation for the 2D problem making the system inversion relatively cheap.

- Spectral methods can be introduced for 2.5D configurations keeping thus the mixed spatial-spectral scheme compatible with the LU factorisation.

- The PB method is always stable which makes it the base method in combined PB-NR approaches.

The property of the homogeneous permeability can be exploited even further for geometries like Fig. 8.1a, which can be treated using spectral methods, and this idea will be our next task. Before endeavouring to this approach, however, it is meaningful to have a closer look at the PB scheme given its central importance in the developments of this work.

## 8.4 The fixed-point method revisited

The fixed-point method plays a central role in the developments of this work for a number of reasons. The simple permeability profile that it involves makes it directly applicable with spectral schemes as will be demonstrated below. Furthermore, its excellent stability behaviour makes it the tool of choice when hysteresis comes into play. In this section, we shall try to delve deeper in this method by studying its convergence properties, which in its turn will allow us to introduce quantitative criteria for the optimal choice of the linear permeability. The content of this section is strongly inspired by the pioneering work of Hantila et al. [132, 133, 154–156].

In the following, we shall focus on the (8.9) iterative scheme involving the curl-curl induction equation, which is adapted for mesh-based numerical approaches, since the majority of the results presented in this chapter have been produced using the FIT. However, the discussion is valid for (8.10) based on the Helmholtz operator as well, with the only difference that the $\langle \bullet, \bullet \rangle_\nu$ inner products need to be replaced with the non-weighted ones $\langle \bullet, \bullet \rangle$.

According to (8.9), the total scheme is an interplay of two mappings: the mapping of the magnetic induction to the magnetic polarisation $\mathbf{B} \mapsto \mathbf{I}$, performed by the material operator $\mathscr{F}$ and the calculation of the next magnetic induction approximation using the current magnetic polarisation value, namely $\mathbf{I} \mapsto \mathbf{B}$, carried out via the field operator $\mathscr{D}$ (the index PB will be dropped henceforth since there is no risk of ambiguity). For a convergent scheme, $\mathscr{F}$ should be a contraction and $\mathscr{D}$ should be non-expansive in order to assure the Lipschitzian behaviour of the combined iteration operator. Borrowing the control theory terminology, one seeks to assure a non-expansive open-loop operator.

Our task in the next paragraphs will be thus to prove the above properties and to establish some rule for estimating an optimal calculation permeability (linearisation). First, we need to proceed to a couple of definitions.

### 8.4.1 Definitions

We call a non-linear material **isotropic** when its constitutive relation admits the form

$$\mathbf{M}(\mathbf{H}) = \begin{cases} M(H)\,\frac{\mathbf{H}}{H} & \text{for} H \neq 0 \\ \mathbf{M}_r & \text{for} H = 0 \end{cases} \tag{8.27}$$

A non-linear **anisotropic** material admits a different material law per direction. In the most general case the magnetisation component is determined by a vector law employing all the magnetic field components, i.e. there is interference between components. In praxis however this case is rare. For this reason, we shall restrict ourselves to the less general case where the vector magnetisation can be described by means of three independent laws along the principal axes of the material reference frame. This kind of materials are referred to as **orthotropic**, and their constitutive relation reads

$$\mathbf{M}(\mathbf{H}) = \sum_{i=1}^{3} M_i(H_i)\,\mathbf{e}_i \tag{8.28}$$

where $\mathbf{e}_i$ runs the principal axes of the material frame. In all cases that will be examined henceforth, we shall assume that the latter are parallel to the axis of a cartesian reference frame. Materials with cylindrical anisotropy can also be of interest for the applications, though they will not be studied herein.

An important difference with the linear materials should be underlined at this point. An identical material law per direction does not signifies isotropy as is the case in linear materials. This can be easily demonstrated by considering the directional cosines for $\mathbf{M}$ and $\mathbf{H}$. For a linear material with the same susceptibility per axis it is

$$\alpha_{i,M} = \frac{M_i}{\sqrt{\sum\limits_{i=1}^{3} M_i^2}} = \frac{\chi H_i}{\sqrt{\sum\limits_{i=1}^{3} \chi^2 H_i^2}} = \frac{H_i}{\sqrt{\sum\limits_{i=1}^{3} H_i^2}} = \alpha_{i,H}. \tag{8.29}$$

It is clear that the equality does not in general hold in case of a nonlinear $M(H)$ relation.

In many control scenarios, the exciting (or biasing field) is exerted in a specific direction (using a directional set-up like a magnetic circuit or a solenoid) and the measurements are carried out in a different direction, where however the field is much weaker. This is for example the case of the incremental permeability measurement, where the biasing field is applied via a yoke and the permeability is measured in the normal direction using a small (active) pick-up coil, which is fed with a much weaker current. In these cases, the magnetic problem is to a good approximation linear to the measuring direction and hence only the non-linear material law along the excitation axis needs to be taken into account. This brings us to the situation of an orthotropic material with a constant permeability in the normal to the excitation axis.

### 8.4.2 Lipschitzian property of the material operator

**Isotropic material**

We shall consider first the case of the isotropic material as defined by (8.27). Let $\mathbf{B}_1, \mathbf{B}_2$ be two solutions of the electromagnetic problem at a given point of the computational domain $\mathbf{x} \in V$, obtained at two different iterations, and $\mathbf{I}_1, \mathbf{I}_2$ the corresponding magnetic polarisation vectors at the same points. To demonstrate the Lipschitzian character of the material operator $\mathscr{F} : \mathbf{B} \mapsto \mathbf{I}$ we need to prove the inequality

$$|\mathbf{I}(\mathbf{B}_2) - \mathbf{I}(\mathbf{B}_1)| \leq |\mathbf{B}_2 - \mathbf{B}_1|, \quad \forall \mathbf{x} \in V. \tag{8.30}$$

For the rest of the proof, we shall assume that the material has zero remanence ($\mathbf{I}_r = \mathbf{0}$). Note that a material law with non-zero $I_r$ can be always transformed to a zero-remanence law with a simple sift along the $B$-axis, i.e. by making the transformation $\mathbf{B} \to \mathbf{B} - \mathbf{I}_r$, $\mathbf{I} \to \mathbf{I} - \mathbf{I}_r$. If the transformed material operator is Lipschitzian, so will be the original operator as it can be readily deduced from (8.30).

By hypothesis the pairs $(\mathbf{B}_1, \mathbf{I}_1)$, $(\mathbf{B}_2, \mathbf{I}_2)$ as well as the corresponding magnetic field values $\mathbf{H}_1$ and $\mathbf{H}_2$ are points of the material curve. The secant defined by their amplitudes (c.f. (8.27)), has an upper and lower limit determined by the corresponding limits of the differential permeability (slope) of the BH curve

$$\mu_{min} \leq \frac{B_2 - B_1}{H_2 - H_1} \leq \mu_{max} \tag{8.31}$$

where $B_1, B_2 \ldots$ stand for amplitude values.

We consider now the ratio$\langle \Delta\mathbf{I}, \nu\Delta\mathbf{I} \rangle / \langle \Delta\mathbf{B}, \nu\Delta\mathbf{B} \rangle$ with $\Delta\mathbf{I} = \mathbf{I}_2 - \mathbf{I}_1$ and $\Delta\mathbf{B} = \mathbf{B}_2 - \mathbf{B}_1$.

$$\frac{\langle \Delta\mathbf{I}, \nu\Delta\mathbf{I} \rangle}{\langle \Delta\mathbf{B}, \nu\Delta\mathbf{B} \rangle} = \frac{\Delta\mathbf{I}^2}{\Delta\mathbf{B}^2} = \frac{|\mathbf{I}_2|^2 + |\mathbf{I}_1|^2 - 2\chi|\mathbf{I}_1||\mathbf{I}_2|}{|\mathbf{B}_2|^2 + |\mathbf{B}_1|^2 - 2\chi|\mathbf{B}_1||\mathbf{B}_2|} \tag{8.32}$$

where $\chi = \cos(\mathbf{B}_1, \mathbf{B}_2) = \cos(\mathbf{I}_1, \mathbf{I}_2)$. This expression has its extremes, as a function of $\chi$, at

$$E_{1,2} = \left( \frac{I_2 \mp I_1}{B_2 \mp B_1} \right)^2 \tag{8.33}$$

for $\chi = \pm 1$ respectively. Taking into account (8.31) and denoting

$$\mu_\Delta = \frac{B_2 - B_1}{H_2 - H_1} \tag{8.34}$$

we obtain for $E_1$

$$E_1 = \left( 1 - \frac{\mu}{\mu_\Delta} \right)^2 . \tag{8.35}$$

The last expression is upper bounded at each point of the computational domain $\mathbf{x}$ by $(1 - \mu/\mu_{\text{inf}})^2$ or $(1 - \mu/\mu_{\text{sup}})^2$, where $\mu_{\text{sup}} := \sup \mu_\Delta \leq \mu_{\text{max}}$ and

$\mu_{\inf} \coloneqq \inf \mu_\Delta \geq \mu_{\min}$ as it turns out by (8.31). There exists $k^2 < 1$ such as

$$1 - \frac{\mu}{\mu_{\sup}} \leq k \tag{8.36}$$

and

$$1 - \frac{\mu}{\mu_{\inf}} \leq -k \tag{8.37}$$

which implies

$$0 < \mu_{\sup}(1-k) \leq \mu \leq \mu_{\inf}(1+k) < 2\mu_{\inf} \tag{8.38}$$

whence we infer for $k$

$$k \geq \frac{\mu_{\sup} - \mu_{\inf}}{\mu_{\sup} + \mu_{\inf}}. \tag{8.39}$$

$k$ is the contraction factor which takes its optimal value at its minimum, which yields for the linearisation permeability

$$\mu_{opt} = \frac{2\mu_{\sup}\mu_{\inf}}{\mu_{\sup} + \mu_{\inf}}. \tag{8.40}$$

which can be also written

$$\mu_{opt} = \frac{\bar{\mu}_g^2}{\bar{\mu}_a} \tag{8.41}$$

i.e. the optimal permeability is the ratio of the squared geometrical to the arithmetic mean of the material differential permeability.

We have to test now if the second extreme $E_2$. We shall assume without loss of generality that $I_1/B_1 \leq I_2/B_2$. Recalling the identity

$$\frac{I_1}{B_1} \leq \frac{I_2 + I_1}{B_2 + B_1} \leq \frac{I_2}{B_2} \tag{8.42}$$

it turns out

$$\sup\left(\frac{I_2 + I_1}{B_2 + B_1}\right)^2 \leq \sup\left(\frac{I_2}{B_2}\right)^2 \tag{8.43}$$

At this point we shall make use of the hypothesis that the material law has zero remanence, which results

$$\sup\left(\frac{I_2}{B_2}\right)^2 = \sup\left(\frac{I_2 - 0}{B_2 - 0}\right)^2 = \sup\left(1 - \frac{\mu}{\mu_{\Delta 0}}\right)^2 \leq \sup\left(1 - \frac{\mu}{\mu_\Delta}\right)^2 = \sup E_1 \tag{8.44}$$

where $\mu_{\Delta 0}$ stands for the secant with the first point at zero, which is one of the possible values in the secant range. We conclude thus that $E_2$ has a least upper bound than $E_1$ and hence the above inequalities hold also for $E_2$.

**Anisotropic material**

We shift now to the case of the orthotropic material defined in (8.28). The analysis is restricted to orthotropic materials with principle axes parallel to the rectangular reference frame one.

We consider again the $\langle \Delta \mathbf{I}, \nu \Delta \mathbf{I} \rangle / \langle \Delta \mathbf{B}, \nu \Delta \mathbf{B} \rangle$ ratio which for a diagonal reluctivity tensor becomes

$$\frac{\langle \Delta \mathbf{I}, \overline{\nu} \Delta \mathbf{I} \rangle}{\langle \Delta \mathbf{B}, \overline{\nu} \Delta \mathbf{B} \rangle} = \frac{\nu_{xx} \left(\Delta I_x\right)^2 + \nu_{yy} \left(\Delta I_y\right)^2 + \nu_{zz} \left(\Delta I_z\right)^2}{\nu_{xx} \left(\Delta B_x\right)^2 + \nu_{yy} \left(\Delta B_y\right)^2 + \nu_{zz} \left(\Delta B_z\right)^2} \tag{8.45}$$

We recall that for an ordered set of fractions

$$\frac{\alpha}{a} \leq \frac{\beta}{b} \leq \frac{\gamma}{c} \tag{8.46}$$

the following property holds

$$\frac{\alpha}{a} \leq \frac{\alpha + \beta + \gamma}{a + b + c} \leq \frac{\gamma}{b} \tag{8.47}$$

Applying this property, we can write for the upper bound of (8.45)

$$\frac{\langle \Delta \mathbf{I}, \overline{\nu} \Delta \mathbf{I} \rangle}{\langle \Delta \mathbf{B}, \overline{\nu} \Delta \mathbf{B} \rangle} \leq \max \left[ \sup \left( \frac{\left(\Delta I_x\right)^2}{\left(\Delta B_x\right)^2} \right), \sup \left( \frac{\left(\Delta I_y\right)^2}{\left(\Delta B_y\right)^2} \right), \sup \left( \frac{\left(\Delta I_z\right)^2}{\left(\Delta B_z\right)^2} \right) \right] \tag{8.48}$$

Each of the above partial ratios has a lower bound related by the permeability bounds in the corresponding direction of the material frame $i$, namely $(1 - \mu/\mu_{i,\sup})^2$ or $(1 - \mu/\mu_{i,\inf})^2$, there exists hence a $k$ per direction that satisfies the inequality

$$0 < \mu_{i,\sup}(1 - k_i) \leq \mu \leq \mu_{i,\inf}(1 + k_i) < 2\mu_{i,\inf} \tag{8.49}$$

which take place if

$$k_i \geq k_{i,opt} = \frac{\mu_{i,\sup} - \mu_{i,\inf}}{\mu_{i,\sup} + \mu_{i,\inf}}. \tag{8.50}$$

which implies a global $k_{opt} = \max(k_{i,opt})\,, i = 1, \ldots, 3$, with a corresponding value for the permeability. As long as the magnetisation in principal axes does not interfere with another (which is the case for the orthotropic materials examined here), a tensor-type linearisation can be used with the optimal permeability value per axis as it is determined by (8.50), which signifies that no need exists for tracing a global optimum permeability. In both cases (tensor or scalar linearisation) the precontractive character of the material law is guaranteed when respecting the above derived bounds.

### 8.4.3 Non-expansive character of the magnetostatic formulation

Let two solutions of the magnetostatic problem $(\mathbf{H}_1, \mathbf{B}_1)$ and $(\mathbf{H}_2, \mathbf{B}_2)$, which share the same excitation currents and have the same boundary conditions.

Their difference $\Delta\mathbf{B} = \mathbf{B}_2 - \mathbf{B}_1$ and $\Delta\mathbf{H} = \mathbf{H}_2 - \mathbf{H}_1$ should verify the relations [155]

$$\nabla \times \Delta\mathbf{H} = \mathbf{0} \tag{8.51}$$

$$\nabla \times \Delta\mathbf{B} = \mathbf{0}. \tag{8.52}$$

We consider the integral

$$\langle \Delta\mathbf{B}, \Delta\mathbf{H} \rangle := \int\limits_V \Delta\mathbf{B} \cdot \Delta\mathbf{H} dV \tag{8.53}$$

where the integration exceeds the problem domain $V$. By virtue of (8.51) we can write

$$\Delta\mathbf{H} = -\nabla\Phi \tag{8.54}$$

which upon replacement in (8.53) and using the Gauss identity yields

$$\langle \Delta\mathbf{B}, \Delta\mathbf{H} \rangle = -\int\limits_{\partial V} \Phi \Delta\mathbf{B} \cdot d\mathbf{S} + \int\limits_V \nabla \cdot \Delta\mathbf{B} \Phi dV. \tag{8.55}$$

The first integral vanishes since by hypothesis $\Delta\mathbf{B} = 0$ on the domain boundary. The second integral is also equal to zero by the Gauss' law for the magnetic flux density. We hence conclude

$$\langle \Delta\mathbf{B}, \Delta\mathbf{H} \rangle = 0. \tag{8.56}$$

Applying the constitutive relation, we can replace $\Delta\mathbf{H}$ by $\nu(\Delta\mathbf{B} - \Delta\mathbf{I})$, whence we conclude

$$\langle \Delta\mathbf{B}, \nu\Delta\mathbf{B} \rangle = \langle \Delta\mathbf{B}, \nu\Delta\mathbf{I} \rangle \tag{8.57}$$

or equivalently

$$\|\Delta\mathbf{B}\|_\nu^2 = \langle \Delta\mathbf{B}, \Delta\mathbf{I} \rangle_\nu \tag{8.58}$$

which using the Cauchy-Schwarz inequality becomes

$$\|\Delta\mathbf{B}\|_\nu^2 \leq \|\Delta\mathbf{B}\|_\nu \|\Delta\mathbf{I}\|_\nu \tag{8.59}$$

which implies

$$\|\mathbf{B}_2 - \mathbf{B}_1\|_\nu \leq \|\mathbf{I}_2 - \mathbf{I}_1\|_\nu . \tag{8.60}$$

The last relation completes the proof of the non-expansive character of the magnetostatic formulation.

### 8.4.4 Non-expansive character of the eddy-current formulation

We keep the same hypotheses as before but this time the field variations $\Delta\mathbf{B}$, $\Delta\mathbf{H}$ and $\Delta\mathbf{E}$ must verify the source-free Maxwell equations for the quasi-static

[132].

$$\nabla \times \Delta\mathbf{E} = -\frac{d\Delta\mathbf{B}}{dt} \tag{8.61}$$

$$\nabla \times \Delta\mathbf{B} = \sigma\Delta\mathbf{E}. \tag{8.62}$$

The norm which we consider now is defined as the spatio-temporal integral

$$\langle \Delta\mathbf{B}, \nu\Delta\mathbf{B} \rangle := \int\limits_0^t \int\limits_V \Delta\mathbf{B} \cdot \Delta\mathbf{H} dV d\tau \tag{8.63}$$

Using the standard vector potential definition for the magnetic induction variation $\Delta\mathbf{B} = \nabla \times \mathbf{A}$ (8.63) becomes

$$\begin{aligned} \langle \Delta\mathbf{B}, \Delta\mathbf{H} \rangle &= \langle \nabla \times \mathbf{A}, \Delta\mathbf{H} \rangle \\ &= \langle \mathbf{A}, \nabla \times \Delta\mathbf{H} \rangle \end{aligned} \tag{8.64}$$

where use was made of the hermiticity of the curl operator under Dirichlet boundary conditions ($\Delta\mathbf{H} = 0|_{\partial V}$). Substitution of (8.62) yields

$$\begin{aligned} \langle \Delta\mathbf{B}, \Delta\mathbf{H} \rangle &= \langle \mathbf{A}, \sigma\Delta\mathbf{E} \rangle \\ &= \langle \mathbf{A}, -\sigma\frac{d\mathbf{A}}{dt} \rangle \\ &= -\left\|\mathbf{A}\right\|_\sigma^2 \leq 0 \end{aligned} \tag{8.65}$$

where $\left\|\bullet\right\|_\nu$ stands for the spatial norm of the instantaneous potential value at time $t$, namely $\mathbf{A} = \mathbf{A}(t)$. For the derivation of the last relation, we have assumed $\mathbf{A}(0) = 0$.

Following the same line of reasoning as for the magnetostatics case and making again use of the Cauchy-Schwarz inequality, we can write successively

$$\begin{aligned} \langle \Delta\mathbf{B}, \nu(\Delta\mathbf{B} - \Delta\mathbf{I}) \rangle_\sigma &\leq 0 \\ \left\|\Delta\mathbf{B}\right\|_{\nu\sigma}^2 &\leq \langle \Delta\mathbf{B}, \Delta\mathbf{I}) \rangle_{\nu\sigma} \\ \left\|\Delta\mathbf{B}\right\|_{\nu\sigma} &\leq \left\|\mathbf{I}\right\|_{\nu\sigma} \end{aligned} \tag{8.66}$$

which implies

$$\left\|\mathbf{B}_2 - \mathbf{B}_1\right\|_{\nu\sigma} \leq \left\|\mathbf{I}_2 - \mathbf{I}_1\right\|_{\nu\sigma}. \tag{8.67}$$

This last relation completes the proof of the non-expansiveness for the quasi-static (eddy-currents) formulation. Note that no hypothesis was made for the field initial conditions ($\mathbf{A}(0) = 0$ is merely a gauge condition), which means that the proof is valid independently of the initial field value.

## 8.5 Spectral approach

We return now to the problem described in Fig. 8.3. The problem has been treated in TD when FIT was used for the spatial descretisation since this is the more straight-forward approach for treating the non-linear operator in iterative schemes. When the excitation is harmonic, however, the expected spectrum of the final field signals (in permanent regime) will be an enriched spectrum including the basic frequency plus a small number of rapidly decaying higher odd-harmonics as shown in Fig. 8.8. This property can be exploited in order to significantly reduce the computation time since the time discretisation is replaced by a sweep over a very small number of contributing harmonics. This approach is known as harmonic balance and has been successfully used for the solution of non-linear electromagnetic problems in the permanent regime [136, 139, 140].

Converting (8.2) in FD and comparing it with (5.76) it turns out that the linearised problem reduces to the solution of the inhomogeneous Helmholtz equation with an equivalent magnetic current density

$$\mathbf{J}_m(\mathbf{x},t) \equiv \frac{1}{i\omega}\mathbf{I}(\mathbf{x},t) \tag{8.68}$$

in other words, the time integral of the magnetic polarisation. At a given iteration $l$ and for the $p$th harmonic (8.2) can be thus written

$$\left(\nabla^2 - \frac{1}{\rho^2} - k_p^2\right) A_p^{(l)}(\rho,z) = -\delta_{p1}\mu_0 J_e(\rho,z) - \mathbf{e}_\phi \cdot \nabla \times \mathbf{I}_p^{(l-1)}(\rho,z) \tag{8.69}$$

$J_e$ is the current density of the coil, and consequently is non-zero only for the basic harmonic $\omega_1$. $\mathbf{I}_p^{(l-1)}$ stands for the $p$th harmonic of the magnetic polarisation computed by the Fourier integral

$$\mathbf{I}_p^{(l-1)}(\rho,z) = \frac{1}{T}\int_0^T \mathbf{I}^{(l-1)}(\rho,z,t)\, e^{-i\omega_p t} dt \tag{8.70}$$

where $\mathbf{I}^{(l-1)}(\rho,z,t)$ is the magnetic polarisation obtained by application of the material law to the magnetic induction calculated in the previous iteration

$$\mathbf{I}^{(l-1)}(\rho,z,t) = \mathscr{F}\Big[\nabla \times \mathbf{A}^{(l-1)}(\rho,z,t)\Big]\,. \tag{8.71}$$

The solution of the linearised equation (8.69) follows the same lines with the one described in section 5.10 with the only difference that the developing basis must be suited for accounting the odd parity of the magnetic field distribution with respect to the $z = 0$ plane. In fact, the problem can be reduced to an equivalent problem in the upper half-space with a PEC boundary at $z = 0$. The developments in (5.81),(8.73) thus become for the odd-parity problem

$$A^{(h)}(\rho,z) = \frac{\sqrt{2}}{\rho_L J_0(\kappa_n \rho_L)} \sum_{n=1}^{\infty} J_1(\kappa_n \rho)\left[C_n^{(2)} e^{v_n(z-d/2)} + D_n^{(2)} e^{-v_n(z+d/2)}\right] \tag{8.72}$$

| | $B_\rho$ | | $B_z$ | |
|---|---|---|---|---|
| | $I = 3$ A | $I = 10$ A | $I = 3$ A | $I = 10$ A |
| FIT | 0.067 | 0.130 | 0.044 | 0.114 |
| TREE | 0.042 | 0.127 | 0.052 | 0.116 |

Table 8.2: Comparison of the harmonic distortion content for the $B_\rho$ and $B_z$ components at $((r_1+r_2)/2, d/4)$ obtained by the FIT and the spectral approach.

and

$$w_{nl}(\rho, z) := \frac{2}{\rho_L J_0(\kappa_n \rho_L)\sqrt{d}} J_1(\kappa_n \rho)\sin(q_l z) \tag{8.73}$$

respectively. The $\kappa_n$ eigenvalues for the development in the radial direction remain the same, whereas the $q_l$ eigenvalues become

$$q_l = \frac{2l\pi}{d}, \qquad l = 1, 2, \dots, \infty. \tag{8.74}$$

Finally, the zero order axial term $g_{nl}$ must accommodate a non-zero tangential field at $z = d/2$ remaining odd with respect to the $z = 0$ plane. These conditions are satisfied by setting

$$g_{nl}(z) = \begin{cases} z, n = 1 \\ 0, \text{elsewhere} \end{cases} \tag{8.75}$$

The field profile obtained for this coil arrangement at different observation points is described by the same curves illustrated in 8.3.2 and will not be repeated here. For a quantitative comparison of the results obtained using the two approaches we compute the harmonic distortion at the second observation point $((r_1 + r_2)/2, d/4)$. The computed values with the two approaches are summarised in Tab. 8.2.

## 8.6 Non-linear calculations for materials with hysteresis

### 8.6.1 Overview of the basic hysteresis properties: Mandelung's rules

In the previous sections, we focused on the development of a solution methodology for electromagnetic problems when non-linear materials are involved. Since the objective was the treatment of non-linearities, simple, single-valued $B(H)$ curves have been considered entirely neglecting hysteresis effects. The presence of hysteresis is, however, the rule and not the exception for the majority of technical materials. More than that, it is the very hysteretic properties of the material that interest us in electromagnetic material evaluation applications as owing to their link with the material microstructure and consequently its mechanical properties (which are determined in their turn by the same microstructural features).

The essential feature of hysteresis is history dependence. Hysteretic constitutive relations are thus multi-branch functions, which means that the value of the material parameter depends not only on the current value of the excitation but also its values at previous instances. In the special case of magnetic hysteresis, this dependence admits a somewhat simpler form, i.e. it is restricted to the maxima of the exciting field $\mathbf{H}$ instead of the whole field record.

A further characteristic of magnetic hysteresis, which distinguishes it by other hysteretic phenomena (e.g. during second order transitions between normal and superconducting state of type-II superconductors), is its non-scalar nature: it maps a vector to a vector and hence can be seen as a rank-2 nonlinear tensor function. The definition of isotropy and anisotropy for magnetic materials was given in 8.4.1, where material with no hysteresis were considered. The same definitions will be adopted for hysteretic materials since the existence of multiple branches does not affect the essence of the definitions.

In spite of the variety of characteristics among different magnetic materials some general features are observed in their magnetization processes. These features have been described already in 1905 [157,158] and are known as **Mandelung's rules**. Considering the hysteresis curves in Fig. 8.9, these experimentally established rules can be stated as follows:

1. The path of any transition (reversal) curve is uniquely determined by the coordinates of the reversal point, from which this curve emanates.
2. If any point 4 of the curve 3-4-1 becomes a new reversal point, then the curve 4-5-3 originating at point 4 returns to the initial point 3 (*return-point-memory*)
3. If the point 5 of the curve 4-5-3 becomes the newest reversal point and if the transition curve 5-4 extends beyond the point 4, it will pass along the part 4-1 of curve 3-4-1, as if the previous closed loop 4-5-4 did not exist at all (*wiping-out property*)

A fourth property of the hysteresis curves, perhaps the most well-known, which however does not belong to the Mandelung's rules, is the point symmetry of the major and the internal loops:

4. If $B(H)$ is describing a transition curve of a hysteretic material then $-B(-H)$ will also be a transition curve of the same material.

The properties listed above imply a static hysteresis model, that is, dynamical phenomena like dependence on the excitation frequency are ignored. This is a simplification since real hysteresis observed in the experiments does in fact demonstrate rate-dependence [159]. From the physical point of view, rate independence implies a total scale separation between microscopic mechanisms and the Maxwell equations, i.e. the response time of the irreversible changes in the

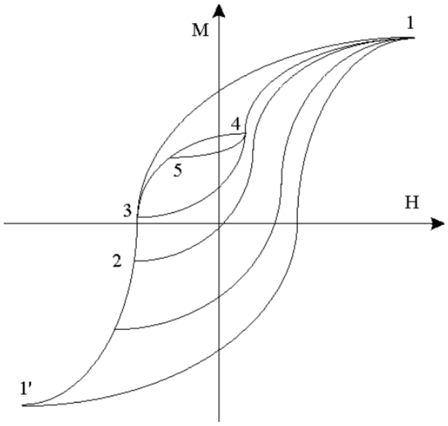

Figure 8.9: Transition curves illustrating Mandelung's rules.

material (wall movements) is order of magnitudes smaller than the characteristic time of the (macroscopic) external field, a hypothesis that is not always valid. Temperature effects do also exist though their influence is rather weak at room temperatures for Fe, Ni and Co alloys.

In the following, the above-mentioned four rules will be axiomatically accepted with both the rate-dependence and temperature effects left aside.

### 8.6.2 Determination of the state in systems with hysteresis

In accordance with the first Mandelung rule, we shall accept that the coordinates of the last reversal point $(H_r, M_r)$ together with the current value of the external magnetic field $H$ provide a full description of the material state

$$M = M(H, H_r, M_r)\,. \tag{8.76}$$

The physical interpretation of this experimentally derived rule, which is adopted here as postulate, can be linked with the thermodynamic properties of hysteresis. It is known that hysteresis characterises systems out of equilibrium, and for these systems the configuration space in equilibrium must be complemented by a number of internal variables [160]. Without entering in the very complicated discussion of searching the appropriate set of internal variables, which lies entirely outside the scope of the present text, we will be content with a pure mathematical justification of this choice in the sense that they provide the necessary additional dimensions of the augmented space in combination with the experimental evidence.

A special case of significant interest concerns symmetrical excitations, i.e. the maxima and the minima of the external field (or equivalently the excitation current) have the same absolute value. This is the case for periodic excitations, which are used in the majority of technical applications. Assuming that the system is at its demagnetised state (origin of the $M(H)$ plane) in the beginning, all reversal points are lying on the first magnetisation curve $M_{in}(H)$, which means that the system state is characterised only by the $H_r$ value. Formally, we can write

$$M = M(H, H_r, M_{in}(H_r)) = M(H, H_r)\,. \tag{8.77}$$

To the same category belong pulsed excitations without crossover whose minimum (maximum) value is zero. For the latter, only the first (third) quarter of the $M(H)$ plane is explored by the system meaning that only one reversal point occurs.

Should the system initiate from the negative (or positive) saturation state, and should the excitation accommodate a single or multiple but equal in amplitude reversal points, then $M$ admits the same representation. Recalling the definition of the first order reversal curves FORC's [161]

$$\rho(H, H_r) = -\frac{1}{2}\frac{\partial^2 M(H, H_r)}{\partial H_r \partial H} \tag{8.78}$$

it becomes evident that the $M(H, H_r)$ representation described by (8.77) is nothing more than the cumulative FORC distribution, namely

$$M(H, H_r) = -1 + 2\int\limits_{H_r}^{H} d\beta \int\limits_{0}^{H_r} \rho(\alpha, \beta)\, d\alpha. \tag{8.79}$$

The visualisation of the integration domain for the two cases, namely single and symmetric FORC initiating from the virgin and the saturation state, is shown in Fig. 8.10. This is equivalent to the integration domain of the Preisach model. In the case of a system initiation by the virgin state, one must also include the necessary integration domain for totally canceling out any remanent magnetisation via a succession of demagnetisation cycles of decreasing amplitude (light grey area in Fig. 8.10b). The triangular integration domain is therefore an idealisation of a large number of demagnetisation cycles, indicated by their step-formed shape of the upper triangular boundary. In each case the state vector is formed by the coordinates of the upper-right corner of the integration domain.

The entirety of the $M$ states is contained in the triangular domain depicted in Fig. 8.10, which means that an efficient way of evaluating $M(H, H_r)$ is via interpolation from a set of pre-evaluated samples (a kind of hysteresis metamodel [162]). An additional advantage of this approach, besides algorithmic convenience, is that the evaluation does not depend on how the samples have been obtained, which can be a combination of models or a mixture of theoretical calculations and experimental data. $M(H, H_r)$ contains all the information we need.

When coming to the interpolation, it is more convenient to work with a rectangular domain instead of the triangular one of (8.10). Introducing the

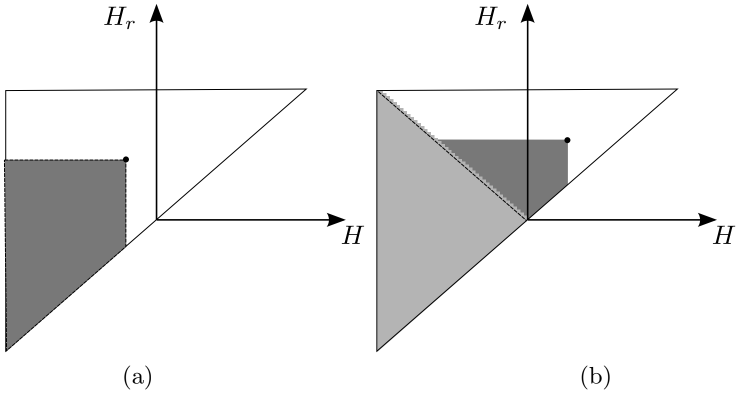

Figure 8.10: Cumulative FORC representation of the magnetisation $M$ for (a) system initiating from the negative saturation state (b) system initiating from the demagnetised state. With dark grey is denoted the integration domain of the FORC distribution, and light grey in the second plot stands for the integration area necessary for achieving the virgin state.

non-linear coordinate transformation

$$\xi = \frac{H}{H_s} \tag{8.80}$$

$$\eta = \frac{H_r}{H} \tag{8.81}$$

with $H_s$ defined as

$$H_s \coloneqq \min(\arg\max M)\,. \tag{8.82}$$

The above definition assumes that the saturation state $M = M_s$ will be reached somewhere and $H_s$ will be the lower bound of the magnetic field required to reach this state. The ideal saturation is, however, a rather theoretical state, achieved at very high fields for some materials and subjected to thermal fluctuations. It is therefore more reasonable to define a threshold $M_t$ of a "technical" saturation and reformulate the definition relation (8.82) as follows

$$H_s \coloneqq \sup_{M \leq M_t} H(M)\,. \tag{8.83}$$

In the following, the distinction between the ideal $M_s$ and the technical saturation $M_t$ will be dropped, and every time we shall be referring to the saturation value we will mean the technical saturation threshold.

With the change of variables (8.80),(8.81) we have a rectangular domain for $M$, namely

$$M = M(\xi, \eta)\,, \qquad \xi, \eta \in [0, 1] \tag{8.84}$$

and the magnetisation at each internal point of the domain can be easily obtained by interpolation.

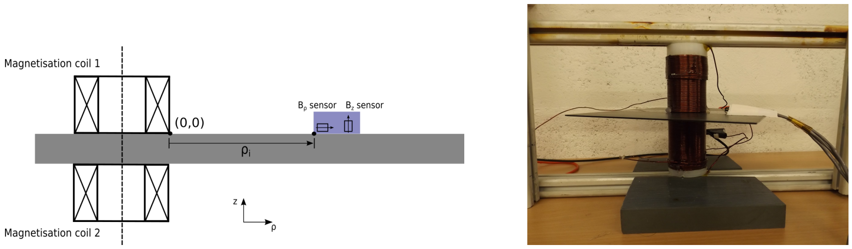

(a) (b)

Figure 8.11: Laboratory realisation of the set-up described in 8.3.2. (a) Schematic diagram. (b) Coils and specimen arrangement.

It has been shown above that the **A** formulation requires the evaluation of the inverse magnetisation function $H = H(B) = B^{-1}(B)$ instead of the direct function. It makes thus sense to change the working state variables for the expression of the magnetisation state from $(H, H_r)$ to $(B, B_r)$, and proceed to the respective change of variables (we keep the same variable names to avoid excessive symbol proliferation)

$$\xi = \frac{B}{B_s} \tag{8.85}$$

$$\eta = \frac{B_r}{B}. \tag{8.86}$$

Now the evaluation of the inverse function $H = H(\xi, \eta)$ becomes trivial by interpolating in the $\xi, \eta = [0, 1]$ rectangle, assuming that $H$ has been precalculated at a sufficient number of sampling points.

## 8.7 Comparison with experimental results

The solution of the electromagnetic problem involving the hysteretic constitutive relation and the interpolation approach in the augmented $(B, B_r)$ space has been compared to experimental results acquired using the set-up examined in 8.3.2. The laboratory realisation of the set-up is illustrated in Fig. 8.11.

The two coils are connected in series but with opposite polarity to the voltage source. The two field components (tangential $B_\rho$ and normal $B_z$) are measured by means of a pair of Hall sensors. The two sensors are placed in a common plastic housing, which holds them fixed, and which is free to move on the specimen surface at a constant lift-off. The coils characteristics are summarised in Tab. 8.3. The two coils are assumed to be identical within construction tolerances. The coils lift-off is estimated to be about 0.1 mm, though its precise value is not expected to have a significant impact to the results.

The plate material is a typical structural steel (SS), a material with moderate mechanical and magnetic hardness as its BH-loop curves indicate (cf. Fig. 8.12). The first step of the experimental procedure was the characterisation of the plate

| | |
|---|---|
| Inner radius $r_{in}$ | 9 mm |
| Outer radius $r_{out}$ | 25 mm |
| Length $l$ | 67 mm |
| Number of turns $N$ | 545 |

Table 8.3: Parameters of the induction coils.

steel. For this purpose, a narrow strip has been cut away from one of its edges. Since the particular type of steel can be considered with very good approximation as isotropic, the choice of the edge is of no importance. The electrical conductivity has been then measured by applying the four-point method in the strip sample. The same specimen has also been used for the measurement of its magnetic characteristics, namely the BH loops. The experimental approach used for the hysteresis measurement was the solenoid method.

The measured loops for a number of different excitation voltages at the solenoid are plotted in Fig. 8.12a. The theoretical hysteresis model chosen for the realisation of the numerical calculations is the Mel'gui model [163]. The choice of this particular model was driven by the stability issues during the evaluation of the inner loops. In fact the Mel'gui model turns to be more stable than the Jiles-Atherton model when coming to the calculation of the inner loops. The model has been identified using the measurements for the maximum loop (the one obtained at the highest level of excitation). The comparison of the identified model with the corresponding experimental curve is shown in Fig. 8.12b. It turns out that the Mel'gui model reproduces very well the experimental data for a number of steels, which in combination with its simplicity makes it a handy model for numerical simulations involving symmetrical loops.

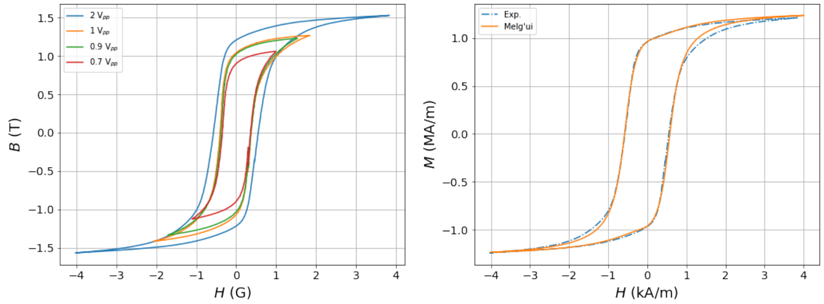

(a) (b)

Figure 8.12: (a) Measured BH loops of the plate material for various levels of the solenoid voltage. (b) Identification of the Mel'gui model using the maximum loop data.

Despite the enhanced stability of the Mel'gui model for the calculation of the inner loops, still action must be taken for loops with relatively low-field reversal points (under 10% of the maximum reversal point), where negative slopes and hence unphysical results may occur. For this reason, the Mel'gui model has been combined with the Rayleigh model, which provides a good approximation at weak fields. The Rayleigh model is parametrised by imposing the continuity of the magnetisation and its first derivative (the magnetic susceptibility) at the transition point of the first magnetisation curve.

The main experiment consists in exciting the coils with a sinusoidal current at a given frequency and measuring the tangential and normal field component using the field probe. The excitation frequency has been chosen 10 Hz and the excitation voltage was set at 0.7, 1.4, 2.8 and 5.6 V. The coil current obtained for the four voltage levels has been measured using a current clamp. The resulting voltage-current are summarised in Tab. 8.4

| Excitation voltage (V) | Coil current (A) |
|---|---|
| 0.7 | 1.886 |
| 1.4 | 3.639 |
| 2.8 | 6.880 |
| 5.6 | 13.0448 |

Table 8.4: Excitation voltage and the corresponding coil current used for the realisation of the field measurements.

The first test consists in examining the influence of the hysteresis loop on the measured signals. For this reason, we solve the non-linear problem by ignoring hysteretic effects, i.e. we consider a single-valued material law described by the virgin curve, such as it is determined by the Mel'gui model. The comparison between simulation results and experimental signals measured by the field probe with the observation point located beside the magnetising coil of the upper part of the set-up (in touch with it) for the four excitation levels are shown in Fig. 8.13.

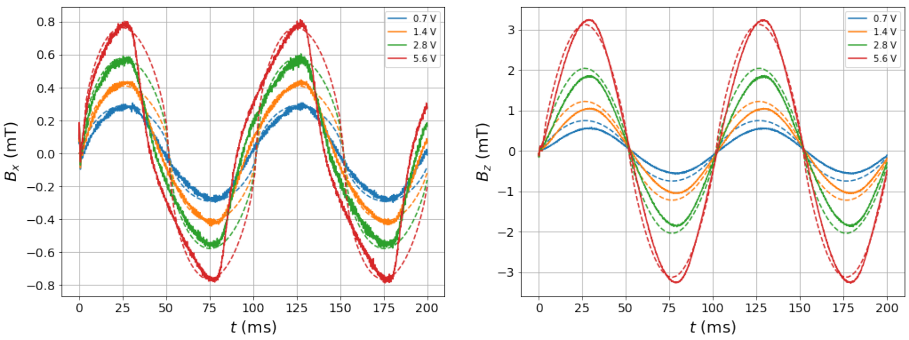

Figure 8.13: Experimental signals vs. simulation results for the $B_\rho$ and $B_z$ components when only the virgin curve is used as material law.

We can make the following observations. The tangential field signals presents a notable deviation from the sinusoidal curve, with the deformation increasing with the voltage, as expected. On the contrary, the normal component remains practically linear for all excitations. This difference is justified by the conception of the experiment, namely the different polarity of the coils results in a stronger tangential component at the vicinity of the coils, whereas the normal component is significantly weaker. This may seem being in contradiction with the signals amplitude in Fig. 8.13 ($B_z$ appears stronger than $B_\rho$) yet it must be recalled that these plots concern measurements in the air, and the continuity of the normal induction imply a much weaker value inside the plate.

The second important observation is related to the failure of the non-hysteretic material law to describe correctly the descending part of the curves. In fact, the sigle-valued curve we considered for the numerical simulations yield a symmetric signal (in terms of the ascending and descending part), which differs with what is observed in reality.

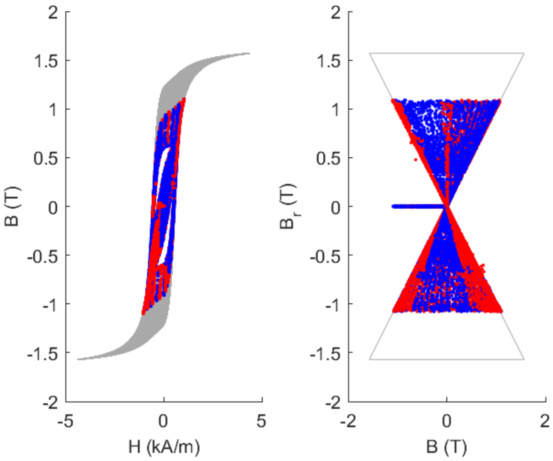

Figure 8.14: Sampling of the BH loops and corresponding path in the Preisach plane. One can distinguish the transition between the Rayleigh and the Mel'gui models.

Let us now take the actual hysteretic law of the material as it is approximated by the hybrid Mel'gui-Rayleigh model. A characteristic sampling of the magnetic loops and the corresponding points in the Preisach plane are shown in Fig. 8.14. The simulation results for the same situation with the one examined above are shown in Fig. 8.15.

There is a clear improvement in the accordance of the simulation results with the experimental curves when the hysteresis is taken into account. It must be also underlined at this point the versatility that the $(B, B_r)$ representation contributes to the solution: we were able to combine the Mel'gui model with the Rayleigh relation, thus enhancing the stability of the solver in a very straight-

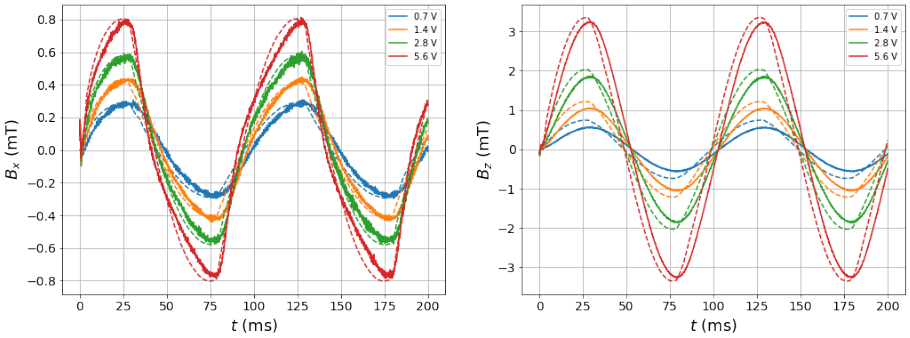

Figure 8.15: Experimental signals vs. simulation results for the $B_\rho$ and $B_z$ components when the full hysteretic model is taken into account.

forward way by just juxtaposing sample curves calculated with the two models. In the same way, we could have proceeded to any other combination of models or models and experimental curves.

## 8.8 Remanent measurements after quarter-cycle excitation: the IMPOC device

An industrial realisation of the above examined set-up represents the IMPOC system, used for the in-line quality evaluation of the steel properties during mechanical and thermal treatment in the production line of strip steel products [151, 152, 164][2].

The main characteristic of the IMPOC system is that it is based upon remanent field gradient measurements, which is carried out after the fading-out of a pulsed excitation at the magnetisation coils. This type of measurements presents certain advantages for the driving circuit since the absence of current cross-over allows the coil loading via the discharge of large capacitors. In addition, the remanent field measurement proves to be very well correlated with the tensile stress of the strip under testing. A qualitative explanation to this correlation can be given with the aid of the Fig. 8.13 and Fig. 8.15, where it has been shown that the descending part of the hysteresis loop has a major effect on the field signal. It is well known on the other side that the coercive field, whose strong correlation with the mechanical properties is well reported, is determinant for the hysteresis curve. The indirect dependence of the measurement with the coercive field and via that the mechanical properties of the specimen can thus explain the sensitivity to the tensile stress and thereupon justify the

---

[2] The results presented in this section have been produced in the context of the research project ‘Product Uniformity Control (PUC)” funded from the European Union’s Research Fund for Coal and Steel (RFCS) research programme under grant agreement no. RFSR-CT-2013-00031.

interest of the measurement.

In terms of numerical simulation, we are speaking for a quarter-cycle operation, in the sense that only the part of the BH loop that lies in the first quarter plane is explored. The excitation signal and the followed path on the BH plane are shown in Fig. 8.16. It should be noted that the numerical solution of the problem can be quite challenging since we are interested in the solution close to the remanence, where the excitation field is weak and the magnetic field source is dominated by the piece magnetisation, which is derived by the field solution at the previous instances.

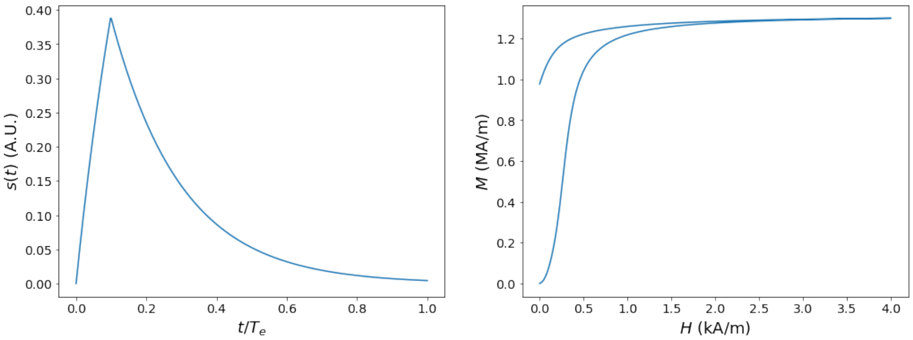

Figure 8.16: Excitation cycle and path the the BH plane. The time axis is normalised with the duration of the excitation pulse $T_e$.

The numerical simulation reproduces a number of important experimental trends observed during in-line measurements using installed IMPOC systems in production lines. Two of the most pronounced effects is the effect of the strip speed and the strip thickness.

Recalling that IMPOC output is basically a transcription of the excitation coils magnetic imprint on the measured specimen, it is well understood that the strip velocity might have an important effect to the measurement owing to the elongation of the magnetisation spot during movement. This is an annoying effect in steel production lines, where the produced product is sliding with speeds that can exceed beyond 10 m/s. Simulation can be a significant aid here by providing calibration curves. Fig. 8.17 demonstrates the effect using both experimental as well simulation results for a number of different strip grades. In both cases, the dependence of the IMPOC output from the strip speed is linear with a slope that decreases for harder grades. This decrease is consistent with the expectations since the harder the material is the more resilient becomes against magnetisation. In addition, harder grades (dual-phase, DP) demonstrate clearly lower remanences that the softer steels such as interstitial-free (IF) steels. The slope in Fig. 8.17a is -4.44% per 100 m/min which lies between the slopes obtained for the low-carbon (LC) and micro-alloyed (MA) steel. Taking into account that the measurements have been obtained using an LC steel with different characteristics than the one used for the simulation and given the fact that the experimental results have been produced with little control to conditions such as the former piece state (no demagnetisation has been carried out), the agreement can be deemed quite satisfactory.

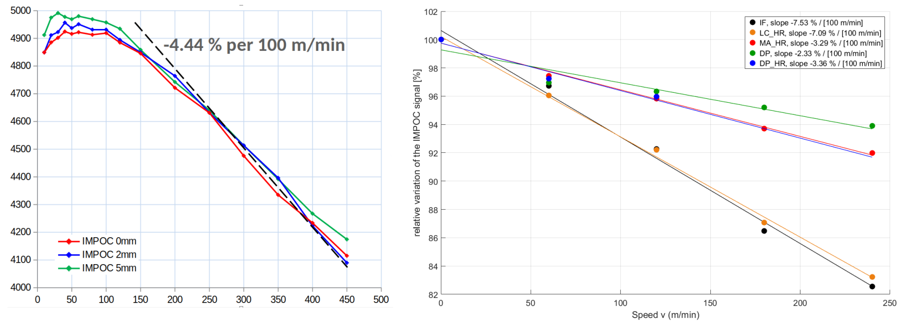

(a) (b)

Figure 8.17: IMPOC signal as function of the strip velocity. (a) Measurements for a hot-rolled low-carbon steel of different thickness. (b) Simulation results for different steel grades. The lines represent the best linear fit to the simulation values (one line per steel grade). The considered grades are: interstitial-free (IF), low-carbon (LC), micro-alloyed (MA) and dual-phase (DP). Measurements courtesy of EMG.

The influence of the strip thickness to the measurements is the second important effect that needs to be compensated. Again, the simulation results are compared against measurements carried out using stacked tin strips of different total thicknesses. The comparison of the experimental results vs. simulation for IF and DP steels is provided in Fig. 8.18. The experimental results have been kindly provided by ThyssenKrupp in the context of the PUC european project.

Layered specimens have been preferred for this measurement in order to assure a better control upon the metallurgical properties: the lamination procedure having a direct influence to the material parameters makes it extremely complicated to obtain specimens of different thicknesses with exactly the same properties.

The comparison of the curves in Fig. 8.18 reveals that the thickness effect is manifested in a different way depending on the hardness of the steel grade, namely a more pronounced effect is observed for the (harder) DP steel than the IF. This conclusion is also supported by the fair agreement between the experimental curve of the (magnetically soft) tin specimen and the IF one. Unfortunately, the details of the tin material used for the experiment were not accessible, hence a direct comparison with the simulation results obtained with the same material is not possible. Nonetheless, the observed agreement is quite acceptable even using steels of similar but not the same properties.

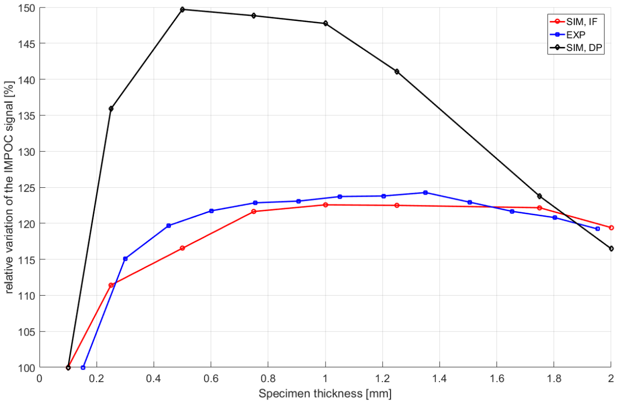

Figure 8.18: IMPOC signal as function of the strip thickness for an IF and DP steel. The blue line represents experimental results obtained using stacked tin strips. Measurements courtesy of ThyssenKrupp.

## 8.9 Publications related with the chapter content

The spectral approach for the solution of the 1D non-linear problem in planar slabs and infinite rods has been proposed in [75]. The corresponding problem of a ferromagnetic plate inspection has been treated using TREE in [76]. The numerical studies presented in 8.2.3 and the numerical results using the double-coil and the yoke configuration have been realised in the context of the post-doctoral work of Dr. T. Svatoň [165, 166].

The benchmark measurements used for the validation of the numerical results of the material with hysteresis in section 8.7 have been carried out in close collaboration with Prof. N. Poulakis from the University of Western Macedonia in Greece and are the subject of an article in preparation.

Many of the results presented in section 8.8 are the outcome of the *Product Uniformity Control (PUC)* European project funded from the Research Fund for Coal and Steel (RFCS) under the Grant Agreement Number RFSR-CT-2013-00031 [151, 152, 167]. This research topic remains active in the succession of the PUC project, the *Online Microstructure Analytics (OMA)* project also funded by RFCS under the Grant Agreement Number 847296.

# Chapter 9

# Perspectives, ongoing developments and projections

## 9.1 Towards faster and precise solutions for application in problem inversion

The finite elements method (FEM) has become nowadays the standard tool for the solution of partial differential applications, having benefited from a long time of research and fine-tuning from a very broad community grouping different domains in physics. As a result, very powerful and reliable implementations exist nowadays in form of either mature commercial products or open source codes.

The most important weaknesses of the method remain the strong dependence from the mesh resolution (which is more pronounced in specific critical regions of the geometry such as the lift-off or inside ferromagnetic materials where strong field gradients are produced) and the solution times. Both difficulties are inherent of the method. Although special formulations (e.g. using line elements) and various smart tricks have been elaborated for overcoming the precision problems linked the gradients mentioned above, the choice of the optimal mesh resolution is a point requiring always special care from the user. As far as computational time is concerned, hardware evolution and parallel architectures have made accessible problems intractable before, yet hardware acceleration is not always a practical (or sometimes affordable) approach.

It has been argued several times in this text, that spectral or mixed spatial/spatial solutions are particularly well adapted for NDT applications, since they are insensitive to lift-off problems, and they are less sensitive on the field resolution in particular regions (the values at interfaces being determinant for the solution precision). In addition, combined with the integral equation approach, where they contribute in the construction of dedicated kernels, they offer very efficient computations of the impedance (of field) variations at the observation points, which are our basic observables.

To the above arguments in favour of the further development of such approaches, one must also count the very interesting computation times. This argument stems not from a simple seek for commodity but must be seen in the light of chained or iterative calculations, such as the one needed for the solution of an optimisation problem, the conductance of sensitivity studies and problem inversion.

It is also one of the conclusions of this work that hybridisation of methods is the most promising way of addressing complex geometries without compromising neither the physics (through oversimplification) nor the computational efficiency (by getting the maximum of the spectral approaches).

Current trends in research and industry allow to assume that the major future challenges for computational methods for the modelling and simulation of physical processes will mainly move in the following axes:

- Integration in fully-fledged multi-level simulation codes of complex procedures (the so-called digital twin).
- Multi-physics and multiscale approaches addressing more complex problems.

As far as the first direction is concerned, speed and robustness become major issues. The second direction, notable the multiscale approaches will be analysed in more detail in the next paragraphs.

## 9.2 Material characterisation: interest in multi-scale approaches

One large class of problems, whose certain aspects have been studied in chapter 8, are the so-called material characterisation applications. Here, the principal objective consists in retrieving information about the state of the material based on macroscopic magnetic measurements, the most established among them being the harmonic analysis, hysteresis loops, permeability (either differential or incremental) and magnetic Barkhausen noise (MBN). The interest in using the magnetic methods lies in the thermodynamical nature of magnetism itself, which establishes a very strong link between the state of the material (in particular its metallurgical state characterised by the grain size, dislocations density, existence of different phases and texture, etc.), residual stresses (usually remnants of thermal and mechanical treatments), and the previous history in terms of mechanical and magnetic external loading. All these factors can be interrelated, with the final result to the material being sometimes extremely hard to predict. The selection the most representative observables, which are sensitive to specific physical mechanisms, is therefore an important part of the experimental protocol design.

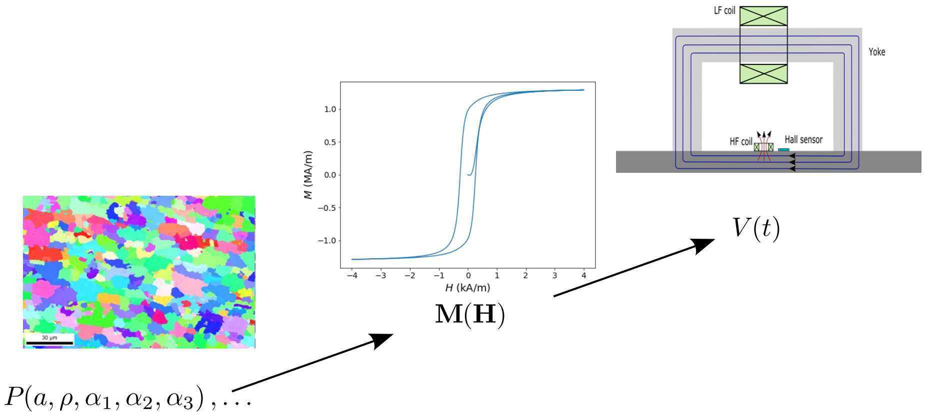

Figure 9.1: Schematic overview of the models hierarchy for the simulation of material characterisation experiments.

The schematic overview of the modelling problem illustrating the hierarchy of the different involved scales and the corresponding state variables/observables is shown in Fig. 9.1. At the smallest scale, the material is characterised by its microstructure, described via statistical distributions of the grain size $a$, the dislocation density $\rho$, the Euler angles of the easy-axis $(\alpha_1, \alpha_2, \alpha_3)$, etc. The complex mechanisms related to the interplay between magnetic domains and the details of the microstructure give rise to the macroscopic constitutive relation $\mathbf{M}(\mathbf{H})$. Measurement of the magnetisation (or one of the thereupon dependent variables like the MBN) can thus deliver information about the material state. These variables, however, are measured indirectly via a number of magnetic field probes (induction coils or semiconductor sensors), where the geometry effect and the eventual material anisotropy come into play and interfere with the measurement. It is again the model's work to separate the intrinsic magnetic material response from the field measurement (via the solution of the inverse problem).

The specific challenges and perspectives for the different scales of the chain will be discussed hereafter in a more concise manner, and a roadmap for future research will be proposed based on the state-of-the-art.

### 9.2.1 Accounting for the grain and texture effects at mesoscopic scale

Different approaches have been proposed for the calculation of the magnetic properties in ferromagnetic materials, which address the problem at different scales. Direct calculations of spin interactions form the base of the Ising model (and its extensions for two and three axes, namely the XY and Heisenberg models respectively) [168–176] or the Landau-Lifshitz-Gilbert (LLG) model [160, 177]. Although these approaches have been proven extremely successful for the prediction of phase transitions and simulations of spin-orbit coupling phenomena in 2D materials, they struggle to account for the details of the metallurgical microstructure due to the very small scale to which they apply.

An alternative approach (more pragmatical in case of industrial materials) is to treat the problem in the scale of magnetic domains (and above) by considering the mechanics of the domain wall [178, 179]. This scale will be conventionally referred to as *mesoscopic scale*, since it lies half-way between the quasi-microscopic spin models and the macroscopic Maxwell equations. The intermediate resolution of this scale allows predictions of both thermodynamical (such as the critical exponents, realm of statistical physics models [178–183]) and macroscopic laws such as hysteresis and permeability behaviour [184, 185]).

In this second family of models, one can also classify in a broad sense the so-called multiscale model, developed by L. Daniel, O. Hubert et al. for the construction of constitutive relations in ferromagnetic materials under magnetic and mechanical loading, which remains nowadays one of the most successful and elaborate existing approaches [186–194]. Texture can be taken into account using grain orientation distribution information by electron backscatter diffraction (EBSD) scans [187, 188]. The demagnetisation effect due to grain boundaries is taken into account using statistical averaging.

It is clear that for real materials, the grain information, in particular the grain size and orientation distributions, can be determinant for their magnetic behaviour. Nonetheless, this is usually the most challenging term to model because of the long-range nature of this contribution (in contrast with the short-range character of the other major mechanisms like the exchange interaction and the crystal anisotropy). A detailed accounting of the magnetostatic energy term for realistic microstructures would imply to involve numerical solutions of the field problem for a given microstructure.

A characteristic example of the use of the mesoscopic approach for accounting the effect of the demagnetisation field in initial permeability predictions is given by F. Zhou, C. Davis et al. in [195, 196]. In their approach, a synthetic microstructure constructed for the case of a dual-phase (ferrite- martensite) steel has been provided in a FEM solver, and the resulting field distribution has been integrated to derive the initial permeability as function of the phase fraction. A characteristic image of the field solution in the synthetic microstructure is given in Fig. 9.2. A scanning electron microscope (SEM) of a real dual-phase microstructure is provided in the same figure for reference. According to the authors, the model is very successful in reproducing the experimental trends for different ferrite fractions (detailed comparisons can be found in the cited articles).

Other examples, where FEM simulations have been used for reproducing Barkhausen noise data and hysteresis curves based on simple domain configurations are found in [185, 197]. In particular, it is shown in [197] that the introduction of random distributions of pinning centres in the domain configuration has allowed to control the basic statistical features the MBN events.

From the previous discussion, one may conclude that the introduction of microstructural characteristics such as the grain configuration along with the

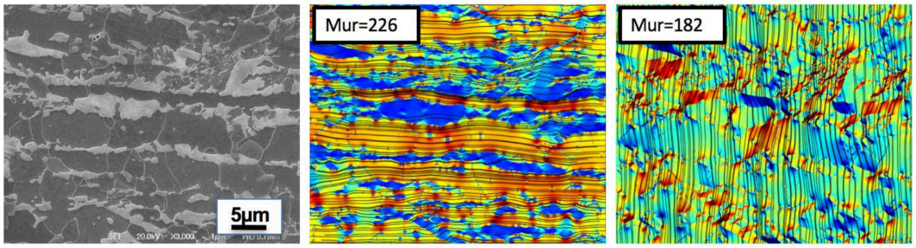

Figure 9.2: The modelled effective permeability (Mur) results and flux distribution in a DP800 steel microstructure. Left: SEM image showing phase distribution of ferrite (dark) and martensite (bright); middle: modelled magnetic flux distribution when horizontal and, right, vertical magnetic fields are applied (Image reproduced from [196]).

easy-axis orientation distribution and statistical moments of major pinning centres simulating lattice imperfections, can provide a way of establishing the link with the basic features of the microstructure, and deepening in the same time the understanding of the underlying physical mechanisms.

Further, one can understand that these simulations must be fast, since one will have to deal with large domains and recursive calculations in optimisation loops. In this context, spectral and hybrid techniques such as those presented in chapter 5 and chapter 7 can contribute accelerate field solutions for given domain, grain and second-phase combinations. In combination with already established tools like the multiscale approach it may be thus hoped enlarging the domain of applicability towards more complicated physics with accent to non-reversible approaches like the MBN. It is noted here that the combination of the multiscale approach with phenomenological models like the Jiles-Atherton model has already produced interesting results concerning the MBN envelope predictions without and under mechanical stress [198, 199]. A characteristic example of a successful MBN envelope prediction using a coupled Jiles-Atherton-multiscale model calculation is given in Fig. 9.3.

### 9.2.2 Geometry effect and inversion

As mentioned in a previous point, the intrinsic material properties are not always directly accessible, at least unless specially-designed, partially destructive setups are utilized. In the latter category, one can include the classical one-sheet tester and Epstein experiments, where a narrow ribbon (or more of them in the case of the Epstein frame) has to be cut away from the specimen, a destructive procedure which may also alter the material properties through the introduction of residual stresses for example. In non-destructive measurements, one has to cope with the set-up geometry, whose effect needs to be resolved through simulation and compensated via some kind of calibration (in the simplest case) or inversion.

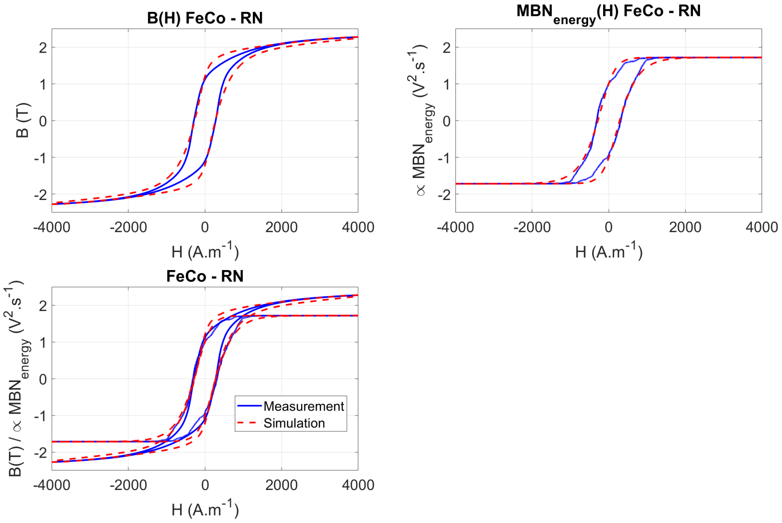

Figure 9.3: Comparisons simulations/experimental results, B(H) and MBN energy envelope for the FeCo including the simulation parameters. The RN grade identifier stands for fully recrystallised FeCo after annealing. (Results from [198]).

Geometry and other parasitic effects (such as eddy-current attenuation) are somehow always present, no matter how careful the experiment has been designed. The demagnetisation field is always present (yet at different extend depending on the set-up and the specimen), when yoke measurements are involved. A more annoying effect is the filtering through attenuation of high frequency signals (MBN events or incremental permeability signals) when passing through the medium (cf. Fig. 9.4). The fact that measurements are always carried out from the exterior of the material, makes it impossible to get rid of the effect, and the only way to compensate is again through simulation.

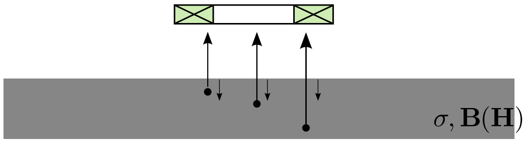

Figure 9.4: Measurements of events from different depths are subjected to different attenuation and reflections from the interface.

When simple parametric material models like the Jiles-Atherton model are used, the material information can be obtained by solving the inverse problem. In order this inversion to be theoretically feasible and practically accessible, one needs a robust, accurate and fast direct model. Although the solution of the inverse problem has gained remarkable maturity in some specific domains, very little results have been presented in the context of material characterisation, due to problem complexity and the excessive computational burden of non-linear solution. Some first encouraging results based on synthetic results obtained using a FIT-based direct solver combined with interpolation in the augmented $(B, B_r)$ space have been presented in [200] and are partially reproduced in section 8.6. The drawn points show relation between predicted and real values for the $\alpha$, $k$ and $M_s$ parameters of the Jiles-Atherton model. The considered set-up is an IMPOC-like configuration presented in detail in section 8.8.

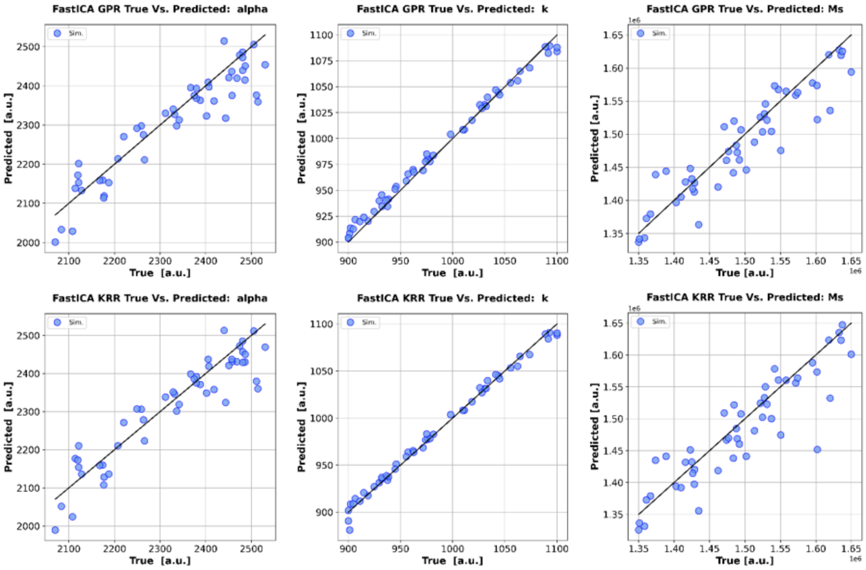

Figure 9.5: Prediction of the $\alpha$, $k$ and $M_s$ parameters of the Jiles-Atherton model for an IMPOC-like set-up using different regressors. Upper line: Gausian process regressor. Bottom line: Kernel ridge regressor.

# Appendix A

# Explicit expressions of the continuity and translation operators

In this appendix the expressions of the magnetic vector potential and magnetic field will be derived in terms of the $(W_a, W_b)$ potentials, and will be given the explicit form of the trace operator in the cartesian and cylindrical coordinate systems for the Darboux frame definitions summarised in Tab. 3.1.

## A.1 Field components

### A.1.1 Cartesian system

Due to the intrinsic isotropy of the cartesian system, the choice of the coordinate axes is arbitrary since any possible piece orientation can be obtained by applying the suitable rotation. The pivot element is taken parallel to the $z$ axis by convention.

The magnetic flux density components are given in terms of the $W_a$ and $W_b$ potentials by the relations

$$B_x = \partial_{xz} W_a + k^2 \partial_y W_b \tag{A.1}$$

$$B_y = \partial_{yz} W_a - k^2 \partial_x W_b \tag{A.2}$$

$$B_z = \left(\partial_z^2 - k^2\right) W_a. \tag{A.3}$$

The magnetic vector potential components read

$$A_x = \partial_y W_a - \partial_{xz} W_b \tag{A.4}$$

$$A_y = -\partial_x W_a - \partial_{yz} W_b \tag{A.5}$$

$$A_z = -\left(\partial_z^2 - k^2\right) W_b. \tag{A.6}$$

### A.1.2 Cylindrical system

In the cylindrical coordinate system, the only choice for the pivot axis is to set $\mathbf{c} = \mathbf{e}_c$, which signifies for the magnetic induction and magnetic vector potential components

$$B_\rho = \partial_{\rho z} W_a + k^2 \rho^{-1} \partial_\phi W_b \tag{A.7}$$

$$B_\phi = \rho^{-1} \partial_{\phi z} W_a - k^2 \partial_\rho W_b \tag{A.8}$$

$$B_z = \left(\partial_z^2 - k^2\right) W_a \tag{A.9}$$

and

$$A_\rho = \rho^{-1} \partial_\phi W_a - \partial_{\rho z} W_b \tag{A.10}$$

$$A_\phi = -\partial_\rho W_a - \rho^{-1} \partial_{\phi z} W_b \tag{A.11}$$

$$A_z = -\left(\partial_z^2 - k^2\right) W_b. \tag{A.12}$$

### A.1.3 Spherical system

In the spherical system, the pivot vector is equal to the position vector $\mathbf{c} = \mathbf{x}$. $\mathbf{B}$ and $\mathbf{A}$ are given in terms of the $(W_a, W_b)$ potentials via the relations

$$B_r = r\left(\partial_r^2 + 2r\partial_r - k^2\right) W_a \tag{A.13}$$

$$B_\theta = \left(\partial_r + \frac{1}{r}\right) \partial_\theta W_a + \frac{k^2}{\sin\theta} \partial_\phi W_b \tag{A.14}$$

$$B_\phi = \frac{1}{\sin\theta}\left(\partial_r + \frac{1}{r}\right) \partial_\phi W_a - k^2 \partial_\theta W_b \tag{A.15}$$

and

$$A_r = \frac{1}{r}\left(\frac{1}{\sin\theta} \partial_\theta \sin\theta \partial_\theta + \frac{1}{\sin^2\theta} \partial_\phi^2\right) W_b \tag{A.16}$$

$$A_\theta = \frac{1}{\sin\theta} \partial_\phi W_a - \left(\partial_r + \frac{1}{r}\right) \partial_\theta W_b \tag{A.17}$$

$$A_\phi = -\partial_\theta W_a - \frac{1}{\sin\theta}\left(\partial_r + \frac{1}{r}\right) \partial_\phi W_b. \tag{A.18}$$

## A.2 Continuity operator

### A.2.1 Cartesian system

We assign by convention the symmetry axis ($g$ coordinate of the Darboux frame) parallel to the $y$ axis, whereas the normal is taken parallel to $z$. The Darboux frame is hence defined as $(t, g, n) = (x, y, z)$. With these conventions, the continuity matrices read

- Air-conductor interface, continuity matrix in the air region

$$\mathbf{C} = \begin{pmatrix} \partial_{xz} \\ \partial_{yz} \\ \partial_z^2 \end{pmatrix} \tag{A.19}$$

- Air-conductor interface, continuity matrix in the conducting region

$$\mathbf{C} = \begin{pmatrix} \partial_{xz} & k^2\partial_y \\ \partial_{yz} & -k^2\partial_x \\ \partial_z^2 - k^2 & 0 \end{pmatrix} \tag{A.20}$$

- Conductor-conductor interface

$$\mathbf{C} = \begin{pmatrix} \partial_{xz} & k^2\partial_y \\ \partial_{yz} & -k^2\partial_x \\ -\partial_y & \partial_{xz} \\ \partial_x & \partial_{yz} \end{pmatrix}. \tag{A.21}$$

### A.2.2 Cylindrical system with rotational symmetry

The symmetry axis is the azimuth, which following the conventions of section 3.2.1 siginfies for the associated Darboux frame $(t, g, n) = (z, \phi, -\rho)$ (cf. Tab. 3.1).

The explicit expressions of the continuity matrices read in this case

- Air-conductor interface, continuity matrix in the air region

$$\mathbf{C} = \begin{pmatrix} \partial_z^2 \\ \rho^{-1}\partial_\phi \\ -\partial_\rho \end{pmatrix} \tag{A.22}$$

- Air-conductor interface, continuity matrix in the conducting region

$$\mathbf{C} = \begin{pmatrix} \partial_z^2 - k^2 & 0 \\ \rho^{-1}\partial_{\phi z} & k^2\partial_\rho \\ -\partial_{\rho z} & k^2\rho^{-1}\partial_\phi \end{pmatrix} \tag{A.23}$$

- Conductor-conductor interface

$$\mathbf{C} = \begin{pmatrix} \partial_z^2 - k^2 & 0 \\ \rho^{-1}\partial_{\phi z} & k^2\partial_\rho \\ 0 & \partial_z^2 - k^2 \\ \partial_\rho & \rho^{-1}\partial_{\phi z} \end{pmatrix}. \tag{A.24}$$

### A.2.3 Cylindrical system with translational symmetry

The symmetry axis coincides with the axis of the coordinate system, hence $(t, g, n) = (\phi, z, \rho)$. The continuity matrices are obtained by the suitable line interchange from the previous case, and change of sign for the $\rho$ direction.

- Air-conductor interface, continuity matrix in the air region

$$\mathbf{C} = \begin{pmatrix} \rho^{-1}\partial_\phi \\ \partial_z^2 \\ \partial_\rho \end{pmatrix} \tag{A.25}$$

- Air-conductor interface, continuity matrix in the conducting region

$$\mathbf{C} = \begin{pmatrix} \rho^{-1}\partial_{\phi z} & k^2\partial_\rho \\ \partial_z^2 - k^2 & 0 \\ \partial_{\rho z} & -k^2\rho^{-1}\partial_\phi \end{pmatrix} \tag{A.26}$$

- Conductor-conductor interface

$$\mathbf{C} = \begin{pmatrix} \rho^{-1}\partial_{\phi z} & k^2\partial_\rho \\ \partial_z^2 - k^2 & 0 \\ \partial_\rho & \rho^{-1}\partial_{\phi z} \\ 0 & \partial_z^2 - k^2 \end{pmatrix}. \tag{A.27}$$

# Appendix B

# Derivation of the volume integral formulation

We consider a closed domain $V$ embedding a linear, isotropic and homogeneous medium[1]. The domain comprises a number of electric and magnetic sources, which are responsible for the creation of the electromagnetic field inside it. Both sources are **entirelly embedded** in the domain sharing no common point with the domain boundary $\partial V$. We assume that the excitation frequency is sufficiently low such that the displacement currents can be ignored (quasi-static approximation). Under these assumptions, the Maxwell equations in $V$ read

$$\nabla \times \mathbf{E}(\mathbf{x}) = -i\omega\mu\mathbf{H}(\mathbf{x}) + \mathbf{J}_m(\mathbf{x}) \tag{B.1}$$

$$\nabla \times \mathbf{H}(\mathbf{x}) = \sigma\mathbf{E}(\mathbf{x}) + \mathbf{J}_e(\mathbf{x})\,. \tag{B.2}$$

We define the electric current source associated Green's dyads, as the field response to an electric point dipole source

$$\nabla \times \overline{\mathbf{G}}^{ee}(\mathbf{x},\mathbf{x}') = -i\omega\mu\overline{\mathbf{G}}^{me}(\mathbf{x},\mathbf{x}') \tag{B.3}$$

$$\nabla \times \overline{\mathbf{G}}^{me}(\mathbf{x},\mathbf{x}') = \sigma\overline{\mathbf{G}}^{ee}(\mathbf{x},\mathbf{x}') + \bar{\mathbf{I}}\delta(\mathbf{x}-\mathbf{x}')\,. \tag{B.4}$$

In an analogous way, we define the corresponding magnetic current source associated Green's dyads

$$\nabla \times \overline{\mathbf{G}}^{em}(\mathbf{x},\mathbf{x}') = -i\omega\mu\overline{\mathbf{G}}^{mm}(\mathbf{x},\mathbf{x}') + \bar{\mathbf{I}}\delta(\mathbf{x}-\mathbf{x}') \tag{B.5}$$

$$\nabla \times \overline{\mathbf{G}}^{mm}(\mathbf{x},\mathbf{x}') = \sigma\overline{\mathbf{G}}^{em}(\mathbf{x},\mathbf{x}')\,. \tag{B.6}$$

---

[1] We provide here the proof in homogeneous media in order for the text to be self-contained. The generalisation to piecewise homogeneous (stratified) media although straight-forward, is more elaborate and lies beyond the scope of this appendix. For the detailed proof in stratified media, the reader is referred to the literature

We apply the vector form of the Green's second identity in the domain $V$

$$\begin{aligned}&\int\limits_{V} \left[\mathbf{P} \cdot \left(\nabla \times \nabla \times \overline{\mathbf{Q}}\right) - \left(\nabla \times \nabla \times \mathbf{P}\right) \cdot \overline{\mathbf{Q}}\right] dV' \\ &= - \oint\limits_{\partial V} \left[\mathbf{P} \times \left(\nabla \times \overline{\mathbf{Q}}\right) - \left(\nabla \times \mathbf{P}\right) \times \overline{\mathbf{Q}}\right] \cdot \mathbf{n} dS' \end{aligned} \qquad \text{(B.7)}$$

where $\mathbf{n}$ is the outward pointing normal to the boundary vector. Application of (B.7) with $\mathbf{P} = \mathbf{E}$ and $\overline{\mathbf{Q}} = \overline{\mathbf{G}}^{ee}$ yields

$$\begin{aligned}&\int\limits_{V} \left\{\mathbf{E}(\mathbf{x}') \cdot \left[\nabla \times \nabla \times \overline{\mathbf{G}}^{ee}(\mathbf{x},\mathbf{x}')\right] - \left[\nabla \times \nabla \times \mathbf{E}(\mathbf{x}')\right] \cdot \overline{\mathbf{G}}^{ee}(\mathbf{x},\mathbf{x}')\right\} dV' \\ &= - \oint\limits_{\partial V} \left\{\mathbf{E}(\mathbf{x}') \times \left[\nabla \times \overline{\mathbf{G}}^{ee}(\mathbf{x},\mathbf{x}')\right] - \left[\nabla \times \mathbf{E}(\mathbf{x}')\right] \times \overline{\mathbf{G}}^{ee}(\mathbf{x},\mathbf{x}')\right\} \cdot \mathbf{n} dS' \end{aligned} \qquad \text{(B.8)}$$

From (B.1),(B.2) we obtain the curl-curl equation for the electric field

$$\nabla \times \nabla \times \mathbf{E}(\mathbf{x}) + k^2 \mathbf{E}(\mathbf{x}') = -i\omega\mu \mathbf{J}_e(\mathbf{x}) - \nabla \times \mathbf{J}_m(\mathbf{x}) \qquad \text{(B.9)}$$

with $k^2 = i\omega\mu\sigma$. Similarly from the combination of (B.3),(B.4), we obtain the curl-curl equation for the $\overline{\mathbf{G}}^{ee}$ dyad

$$\nabla \times \nabla \times \overline{\mathbf{G}}^{ee}(\mathbf{x},\mathbf{x}') + k^2 \overline{\mathbf{G}}^{ee}(\mathbf{x},\mathbf{x}') = -i\omega\mu \bar{\mathbf{I}} \delta(\mathbf{x} - \mathbf{x}') \,. \qquad \text{(B.10)}$$

Substitution of (B.9) and (B.10) in (B.8) taking into account (B.1) and (B.3), yields

$$\begin{aligned}&- \int\limits_{V} \left\{\mathbf{E}(\mathbf{x}') \cdot \left[k^2 \overline{\mathbf{G}}^{ee}(\mathbf{x},\mathbf{x}') + i\omega\mu \bar{\mathbf{I}} \delta(\mathbf{x} - \mathbf{x}')\right] \right. \\ &\qquad \left. - \left[k^2 \mathbf{E}(\mathbf{x}') + i\omega\mu \mathbf{J}_e(\mathbf{x}') + \nabla \times \mathbf{J}_m(\mathbf{x}')\right] \cdot \overline{\mathbf{G}}^{ee}(\mathbf{x},\mathbf{x}')\right\} dV' \\ &= i\omega\mu \oint\limits_{\partial V} \left[\mathbf{E}(\mathbf{x}') \times \overline{\mathbf{G}}^{me}(\mathbf{x},\mathbf{x}') + \mathbf{H}(\mathbf{x}') \times \overline{\mathbf{G}}^{ee}(\mathbf{x},\mathbf{x}')\right] \cdot \mathbf{n} dS'. \end{aligned} \qquad \text{(B.11)}$$

Carrying out the simplifications and solving for $\mathbf{E}$ we obtain

$$\begin{aligned}\mathbf{E}(\mathbf{x}) &= \int\limits_{V} \overline{\mathbf{G}}^{ee}(\mathbf{x},\mathbf{x}') \cdot \mathbf{J}_e(\mathbf{x}') \, dV' + \frac{1}{i\omega\mu} \int\limits_{V} \overline{\mathbf{G}}^{ee}(\mathbf{x},\mathbf{x}') \cdot \nabla \times \mathbf{J}_m(\mathbf{x}') \, dV' \\ &\quad - \oint\limits_{\partial V} \left[\mathbf{E}(\mathbf{x}') \times \overline{\mathbf{G}}^{me}(\mathbf{x},\mathbf{x}') + \mathbf{H}(\mathbf{x}') \times \overline{\mathbf{G}}^{ee}(\mathbf{x},\mathbf{x}')\right] \cdot \mathbf{n} dS'. \end{aligned} \qquad \text{(B.12)}$$

Carrying out integration by parts, the second volume integral, we can be written successively

$$\begin{aligned}\int\limits_V \overline{\mathbf{G}}^{ee}(\mathbf{x},\mathbf{x}')\cdot\nabla\times\mathbf{J}_m(\mathbf{x}')\,dV' &= \oint\limits_V \nabla\cdot\Big[\mathbf{J}_m(\mathbf{x}')\times\overline{\mathbf{G}}^{ee}(\mathbf{x},\mathbf{x}')\Big]\cdot\mathbf{n}dS'\\ &\quad+\int\limits_V \nabla\times\overline{\mathbf{G}}^{ee}(\mathbf{x},\mathbf{x}')\cdot\mathbf{J}_m(\mathbf{x}')\,dV'\\ &= -i\omega\mu\int\limits_V \overline{\mathbf{G}}^{me}(\mathbf{x},\mathbf{x}')\cdot\mathbf{J}_m(\mathbf{x}')\,dV' \qquad \text{(B.13)}\end{aligned}$$

where we have used Gauss' theorem and the fact that the magnetic source is zero on the boundary by hypothesis. Substituting (B.10) into (B.12) we arrive at the following relation

$$\begin{aligned}\mathbf{E}(\mathbf{x}) &= \int\limits_V \overline{\mathbf{G}}^{ee}(\mathbf{x},\mathbf{x}')\cdot\mathbf{J}_e(\mathbf{x}')\,dV' - \int\limits_V \overline{\mathbf{G}}^{me}(\mathbf{x},\mathbf{x}')\cdot\mathbf{J}_m(\mathbf{x}')\,dV'\\ &\quad-\oint\limits_{\partial V}\Big[\mathbf{E}(\mathbf{x}')\times\overline{\mathbf{G}}^{me}(\mathbf{x},\mathbf{x}')+\mathbf{H}(\mathbf{x}')\times\overline{\mathbf{G}}^{ee}(\mathbf{x},\mathbf{x}')\Big]\cdot\mathbf{n}dS' \qquad \text{(B.14)}\end{aligned}$$

which is (5.11) plus a surface integral term. This integral stands for the boundary values of the electric and the magnetic field. In BEM these values are part of the problem's DOF and are calculated after imposing the field continuity relations and solving the thus produced formulation. In the VIM method we are interested in, the domain exceeds up to infinity making this contribution vanish. This however implies that the Green dyads for the entire space are known, and this is the price to be paid with this family of methods, as explained in detail in chapter 5.

The derivation of the magnetic field integral equation follows the same pattern starting from (B.7) with $\mathbf{P}=\mathbf{H}$ and $\overline{\mathbf{Q}}=\overline{\mathbf{G}}^{mm}$

$$\begin{aligned}&\int\limits_V \Big\{\mathbf{H}(\mathbf{x}')\cdot\Big[\nabla\times\nabla\times\overline{\mathbf{G}}^{mm}(\mathbf{x},\mathbf{x}')\Big]-[\nabla\times\nabla\times\mathbf{H}(\mathbf{x}')]\cdot\overline{\mathbf{G}}^{mm}(\mathbf{x},\mathbf{x}')\Big\}\,dV'\\ &= -\oint\limits_{\partial V}\Big\{\mathbf{H}(\mathbf{x}')\times\Big[\nabla\times\overline{\mathbf{G}}^{mm}(\mathbf{x},\mathbf{x}')\Big]-[\nabla\times\mathbf{H}(\mathbf{x}')]\times\overline{\mathbf{G}}^{mm}(\mathbf{x},\mathbf{x}')\Big\}\cdot\mathbf{n}dS'\end{aligned} \qquad \text{(B.15)}$$

The corresponding curl-curl equations for the magnetic field and the $\overline{\mathbf{G}}^{mm}$ dyad read

$$\nabla\times\nabla\times\mathbf{H}(\mathbf{x})+k^2\mathbf{H}(\mathbf{x}')=\nabla\times\mathbf{J}_e(\mathbf{x})-\sigma\mathbf{J}_m(\mathbf{x}) \qquad \text{(B.16)}$$

and

$$\nabla\times\nabla\times\overline{\mathbf{G}}^{mm}(\mathbf{x},\mathbf{x}')+k^2\overline{\mathbf{G}}^{mm}(\mathbf{x},\mathbf{x}')=\sigma\bar{\mathbf{I}}\delta(\mathbf{x}-\mathbf{x}')\,. \qquad \text{(B.17)}$$

Substituting in (B.15) taking into account (B.2) and (B.5) we obtain

$$\begin{aligned}
-\int\limits_V \Big\{ &\mathbf{H}(\mathbf{x}') \cdot \Big[k^2 \overline{\mathbf{G}}^{mm}(\mathbf{x},\mathbf{x}') + \sigma \overline{\mathbf{I}} \delta(\mathbf{x}-\mathbf{x}')\Big] \\
&- \big[-k^2 \mathbf{H}(\mathbf{x}') + \nabla \times \mathbf{J}_e(\mathbf{x}') - \sigma \mathbf{J}_m(\mathbf{x}')\big] \cdot \overline{\mathbf{G}}^{mm}(\mathbf{x},\mathbf{x}') \Big\}\, dV' \\
= -\sigma \oint\limits_{\partial V} &\Big[\mathbf{H}(\mathbf{x}') \times \overline{\mathbf{G}}^{em}(\mathbf{x},\mathbf{x}') + \mathbf{E}(\mathbf{x}') \times \overline{\mathbf{G}}^{mm}(\mathbf{x},\mathbf{x}')\Big] \cdot \mathbf{n} dS'. \qquad \text{(B.18)}
\end{aligned}$$

whence it turns out for the magnetic field

$$\begin{aligned}
\mathbf{H}(\mathbf{x}) = \frac{1}{\sigma} &\int\limits_V \overline{\mathbf{G}}^{mm}(\mathbf{x},\mathbf{x}') \cdot \nabla \times \mathbf{J}_e(\mathbf{x}')\, dV' - \int\limits_V \overline{\mathbf{G}}^{ee}(\mathbf{x},\mathbf{x}') \cdot \mathbf{J}_m(\mathbf{x}')\, dV' \\
&+ \oint\limits_{\partial V} \Big[\mathbf{E}(\mathbf{x}') \times \overline{\mathbf{G}}^{em}(\mathbf{x},\mathbf{x}') + \mathbf{H}(\mathbf{x}') \times \overline{\mathbf{G}}^{mm}(\mathbf{x},\mathbf{x}')\Big] \cdot \mathbf{n} dS'. \qquad \text{(B.19)}
\end{aligned}$$

Integration by parts and term rearrangement reduce the previous expression to the relation

$$\begin{aligned}
\mathbf{H}(\mathbf{x}) = &\int\limits_V \overline{\mathbf{G}}^{em}(\mathbf{x},\mathbf{x}') \cdot \mathbf{J}_e(\mathbf{x}')\, dV' - \int\limits_V \overline{\mathbf{G}}^{mm}(\mathbf{x},\mathbf{x}') \cdot \mathbf{J}_m(\mathbf{x}')\, dV' \\
&- \oint\limits_{\partial V} \Big[\mathbf{E}(\mathbf{x}') \times \overline{\mathbf{G}}^{em}(\mathbf{x},\mathbf{x}') + \mathbf{H}(\mathbf{x}') \times \overline{\mathbf{G}}^{mm}(\mathbf{x},\mathbf{x}')\Big] \cdot \mathbf{n} dS' \qquad \text{(B.20)}
\end{aligned}$$

which is our final relation for the magnetic field. The resulting equation is equal with (5.11) plus a surface integral term, which can be eliminated by extending the integration volume up to the infinity.

# Notation

## Generic variables

| | |
|---|---|
| $i$ | imaginary unit $i = \sqrt{-1}$ |
| $t$ | time |
| $f, \omega$ | frequency and angular frequency |
| $s$ | Laplace variable |
| $\mathbf{x}$ | position vector |
| $\langle \bullet, \bullet \rangle$ | inner product |
| $\lvert\lvert \bullet \rvert\rvert, \lvert\lvert \bullet \rvert\rvert_w$ | $L^2$ norm and $w$-weighted $L^2$ norm |
| $\lvert \mathbf{s} \rangle, \langle \mathbf{s} \rvert$ | ket and bra representation of the state vector $\mathbf{s}$ |
| $\hat{\boldsymbol{A}}$ | operator |
| $\langle \mathbf{s} \rvert \hat{\boldsymbol{A}} \lvert \mathbf{s} \rangle$ | matrix representation of the operator $\hat{\boldsymbol{A}}$ |
| $\delta(x)$ | Dirac delta function |
| $H(x)$ | Heaviside step function |

## Classical electrodynamics

| | |
|---|---|
| $\mathbf{E}, \mathbf{H}$ | electric and magnetic field intensity |
| $\mathbf{D}, \mathbf{B}$ | electric and magnetic flux density |
| $\mathbf{J}_e, \mathbf{J}_m$ | electric and magnetic current density |
| $\mathbf{p}, \mathbf{P}$ | electric dipole moment and electric polarisation |
| $\mathbf{m}, \mathbf{M}$ | magnetic dipole moment and magnetisation |
| $\mathbf{I}$ | magnetic polarisation |
| $\varepsilon, \overline{\varepsilon}$ | scalar and tensor permittivity |
| $\mu, \overline{\mu}$ | scalar and tensor permeability |
| $\sigma, \overline{\sigma}$ | scalar and tensor electrical conductivity |
| $\chi_e, \overline{\chi}_e$ | scalar and tensor electric susceptibility |
| $\chi_m, \overline{\chi}_m$ | scalar and tensor magnetic susceptibility |

| | |
|---|---|
| $\mathbf{A}, \Phi$ | magnetic vector and scalar potential |
| $\mathbf{W}$ | second order vector potential |

| | |
|---|---|
| $W_a, W_b$ | second order scalar potentials |

## Diffraction theory and ECT

| | |
|---|---|
| $\mathbf{E}^p, \mathbf{H}^p$ | primary electric and magnetic field intensity |
| $\mathbf{E}, \mathbf{H}$ | total electric and magnetic field intensity |
| $\mathbf{p}$ | electric dipole density in the thin-crack formulation |
| $g$ | scalar Green's function |
| $\overline{\mathbf{G}}^{ee}, \overline{\mathbf{G}}^{me}$ | electric source associated electric and magnetic Green's dyads |
| $\overline{\mathbf{G}}^{em}, \overline{\mathbf{G}}^{mm}$ | magnetic source associated electric and magnetic Green's dyads |
| $\overline{\mathbf{G}}_0^{xy}$ | free-space Green's dyads ($xy = EE, ME, EM, MM$) |
| $\overline{\mathbf{G}}_{mn}^{xy}, \widetilde{\overline{\mathbf{G}}}_{mn}^{xy}$ | total and reflected part of the $xy$ dyad for observation and source point at the $m$th and $n$th layer, respectively |
| $Z_{ij}$ | mutual impedance between $i$th and $j$th coil |

## Heat conduction

| | |
|---|---|
| $T$ | temperature |
| $\mathbf{J}$ | heat current density |
| $\kappa, \overline{\kappa}$ | scalar and tensor thermal conductivity |
| $c_p, \mathscr{C}_p$ | specific and volumetric heat capacity (under constant pressure) |
| $\rho$ | mass density |
| $\alpha$ | diffusivity |

## Finite integration technique

| | |
|---|---|
| $\overset{\frown}{\mathbf{e}}, \overset{\frown}{\mathbf{h}}$ | electric and magnetic voltage vector |
| $\overset{\frown}{\overset{\frown}{\mathbf{d}}}, \overset{\frown}{\overset{\frown}{\mathbf{b}}}$ | electric and magnetic flux vector |
| $\overset{\frown}{\overset{\frown}{\mathbf{j}}}_e, \overset{\frown}{\overset{\frown}{\mathbf{j}}}_m$ | electric and magnetic current vector |
| $\mathbf{q}_e, \mathbf{q}_m$ | electric and magnetic charge vector |
| $\overset{\frown}{\mathbf{m}}$ | magnetisation-voltage vector |
| $\overset{\frown}{\overset{\frown}{\mathbf{p}}}, \overset{\frown}{\overset{\frown}{\mathbf{i}}}$ | electric and magnetic polarisation vector |
| $\boldsymbol{\theta}$ | temperature vector |
| $\mathbf{M}_\varepsilon, \mathbf{M}_\kappa$ | electric permittivity and electric (and thermal) conductivity matrix |
| $\mathbf{M}_\mu, \mathbf{M}_\nu$ | magnetic permeability and magnetic reluctivity matrix |
| $\mathbf{M}_C, \mathbf{M}_\rho$ | heat capacity (at constant pressure) and mass density matrix |
| | |
| $G, \widetilde{G}$ | primary and dual grid |
| $\mathbf{C}, \widetilde{\mathbf{C}}$ | primary and dual grid-associated curl operator |
| $\mathbf{S}, \widetilde{\mathbf{S}}$ | primary and dual grid-associated div operator |

| | |
|---|---|
| $\mathbf{G}$ | grad operator (on the primary grid) |
| $\mathbf{D}_S, \widetilde{\mathbf{D}}_S$ | primary and dual grid edge matrix |
| $\mathbf{D}_A, \widetilde{\mathbf{D}}_A$ | primary and dual grid flux matrix |

# Abbreviations

| | |
|---|---|
| ACFM | Alternating current field measurement |
| BC | Boundary condition |
| BDF | Backward differentiation formula |
| BEM | Boundary elements method |
| DOF | Degrees of freedom |
| ECT | Eddy-current testing |
| EDM | Electrical discharge machining |
| EMF | Electromotive force |
| FD | Frequency domain |
| FORC | First order reversal curve |
| FP | Fixed-point |
| FT | Fourier transform |
| FEM | Finite elements method |
| FIT | Finite integration technique |
| ILT | Inverse Laplace transform |
| LT | Laplace transform |
| MBN | Magnetic Barkhausen noise |
| NDT | Nondestructive testing |
| NR | Newton-Raphson |
| PB | Picard-Banach |
| PEC | Perfect electric conductor |
| PECT | Pulsed eddy current testing |
| PMC | Perfect magnetic conductor |
| SIM | Surface integral method |
| SOVP | Second order vector potential |
| TD | Time domain |
| TREE | Truncated region eigenfunction expansion |
| VIM | Volume integral method |
| WFNDEC | World federation of NDE centers |

# Steel grades acronyms

| | |
|---|---|
| DP | Dual-phase |
| IF | Interstitial-free |
| LC | Low-carbon |
| MA | Micro-alloyed |
| SS | Structural steel |

# Bibliography

[1] J. D. Jackson, Classical electrodynamics, 3rd Edition, John Willey & Sons, Inc., New Jersey, 1998.

[2] J. A. Stratton, Electromagnetic Theory, McGraw-Hill, New York, 1941.

[3] C. A. Balanis, Advanced Engineering Electromagnetics, John Willey & Sons, Inc., 1989.

[4] W. C. Chew, Waves and Fields in Inhomogeneous Media, Wiley-IEEE Press, New York, 1995.

[5] R. M. Bozorth, Ferromagnetism, Wiley-IEEE Press, New York, 1993.

[6] A. Skarlatos, R. Schuhmann, T. Weiland, Solution of radiation and scattering problems in complex environments using a hybrid finite integration technique - uniform theory of diffraction approach, IEEE Trans. Antennas Propag. 53 (10) (2005) 3347–3357. `doi:10.1109/TAP.2005.856358`.

[7] A. Skarlatos, E. Demaldent, A. Vigneron, C. Reboud, Modelling of specimen interaction with ferrite cored coils by coupling semi-analytical and numerical techniques, in: L. J. Klara Capova, Lalita Udpa, B. Rao (Eds.), Electromagnetic Nondestructive Evaluation (XVII), Vol. 33 of Studies in Applied Electromagnetics and Mechanics, IOS Press, 2014, pp. 128–135. `doi:10.3233/978-1-61499-407-7-128`.

[8] T. P. Theodoulidis, E. E. Kriezis, Eddy Current Canonical Problems (with applications to nondestructive evaluation), Tech Science Press, Forsyth GA, 2006.

[9] J. T. Weaver, The general theory of electromagnetic induction in a conducting half-space, Geophysical Journal of the Royal Astronomical Society 22 (1970) 83–100.

[10] S. K. Burke, Impedance of a horizontal coil above a conducting half-space, J. Phys. D: Appl. Phys. 19 (7) (1986) 1159–1173.

[11] C. Bouwkamp, H. Casimir, On multipole expansions in the theory of electromagnetic radiation, Physica 20 (1) (1954) 539–554. `doi:10.1016/S0031-8914(54)80068-1`.

[12] P. Debye, Der Lichtdruck auf Kugeln von beliebigem Material, Ann. Phys. 30 (1909) 57–136.

[13] J. R. Bowler, N. Harfield, Evaluation of probe impedance due to thin-skin eddy-current interaction with surface cracks, IEEE Trans. Magn. 34 (2) (1998) 515–523.

[14] W. R. Smythe, Static and Dynamic Electricity, McGraw-Hill, New York, 1968.

[15] K. Weigelt, Solution of complex eignevalue equations as used in the analytical solution of eddy-current problems of coupled regions, J. Mag. Mag. Mater. 83 (1990) 501–505.

[16] J. R. Bowler, Eddy current calculations using half-space green's functions, J. Appl. Phys. 61 (3) (1987) 833–839. `doi:10.1063/1.338131`.

[17] L. Hannakam, Wirbelströme im leitenden Halbraum bei beliebiger Form der erregenden Leiterschleife, Archiv für Elektrotechnik 54 (1972) 251–261.

[18] L. Hannakam, Leitender Rechteckkeil im Felde einer Doppelleitung, Archiv für Elektrotechnik 54 (1982) 363–368.

[19] A. Nethe, Einschaltstrome in Spulen mit leitendem permeablem Kern bei Berucksichtigung der induzierten Wirbelstrome, Archiv für Elektrotechnik 74 (1991) 389–401.

[20] B. A. Auld, F. Muennemann, D. K. Winslow, Eddy current probe response to open and closed surface flaws, J. Nondestr. Eval. 2 (1) (1981) 1–21.

[21] B. A. Auld, Theoretical characterization and comparison of resonant-probe microwave eddy-current testing with conventional low-frequency eddy-current methods, in: George Birnbaum and George Free, Eds., American Society for Testing and Materials (Ed.), Eddy-Current Characterization of Material and Structures, Vol. 12, 1981, pp. 332–347.

[22] B. A. Auld, F. G. Muennemann, M. Riaziat, Quantitative modelling of flaw responses in eddy current testing, Nondestructive Testing 7 (1984).

[23] E. Hameiri, I. Shimshoni, Estimating the principal curvatures and the darboux frame from real 3d range data,, in: Proceedings. First International Symposium on 3D Data Processing Visualization and Transmission, 2002, pp. 258–267. `doi:10.1109/TDPVT.2002.1024070`.

[24] M. P. do Carno, Differential Geometry of Curves and Surfaces, Prentice-Hall, Englewood Cliffs, NJ, 1976.

[25] P. Moon, D. E. Spencer, Field Theory Handbook, 2nd Edition, Springer-Verlag, Berlin, 1971.

[26] F. W. Olver, D. W. Lozier, R. F. Boisvert, C. W. Clark (Eds.), NIST Handbook of Mathematical Functions, Cambridge University Press, New York, 2010.

[27] T. P. Theodoulidis, J. R. Bowler, Eddy current coil interaction with a right-angled conductive wedge, Proc. R. Soc. London, Ser. A 461 (2062) (2005) 3123–3139. `doi:{10.1098/rspa.2005.1509}`.

[28] J. R. Bowler, T. Theodoulidis, N. Poulakis, Eddy current probe signals due to a crack at a right-angled corner, IEEE Trans. Magn. 48 (12) (2012) 4735–4746. `doi:10.1109/TMAG.2012.2203918`.

[29] A. Skarlatos, T. Theodoulidis, Solution to the eddy-current induction problem in a conducting half-space with a vertical cylindrical borehole, Proc. R. Soc. London, Ser. A 468 (2142) (2012) 1758–1777. `doi:10.1098/rspa.2011.0684`.

[30] A. Skarlatos, T. Theodoulidis, Impedance calculation of a bobbin coil in a conductive tube with eccentric walls, IEEE Trans. Magn. 46 (11) (2010) 3885–3892.

[31] T. P. Theodoulidis, Analytical modeling of wobble in eddy current tube testing with bobbin coils, Res. Nondestr. Eval. 14 (2) (2002) 111–126.

[32] Comsol multiphysics (2010).
URL `http://www.comsol.com`

[33] R. F. Harrington, Time-Harmonic Electromagnetic Fields, McGraw-Hill, New York, 1961.

[34] A. Skarlatos, T. Theodoulidis, Semi-analytical calculation of the low-frequency electromagnetic scattering from a near-surface spherical inclusion in a conducting half-space, Proc. R. Soc. London, Ser. A 470 (2170) (Jun. 2014). `doi:10.1098/rspa.2014.0269`.

[35] G. Han, Y. Han, H. Zhang, Relations between cylindrical and spherical vector wavefunctions, J. Opt. A: Pure Appl. Opt. 10 (1) (2008) 015006–1–7. `doi:10.1088/1464-4258/10/01/015006`.

[36] A. Skarlatos, T. Theodoulidis, Analytical treatment of eddy-current induction in a conducting half-space with a cylindrical hole parallel to the surface, IEEE Trans. Magn. 47 (11) (2011) 4592–4599.

[37] T. Theodoulidis, A. Skarlatos, Eddy current interaction of an arbitrarily positioned probe coil with a conductive cylinder, IEEE Trans. Magn. 48 (8) (2012) 2392–2394. `doi:{10.1109/TMAG.2012.2191300}`.

[38] P. Vafeas, A. Skarlatos, T. Theodoulidis, D. Lesselier, Semi–analytical method for the identification of inclusions by air–cored coil interaction in ferromagnetic media, Math. Method. Appl. Sci. 41 (16) (2018) 6422–6442. `doi:10.1002/mma.5168`.

[39] A. Skarlatos, T. Theodoulidis, Calculation of the eddy-current flow around a cylindrical through-hole in a finite-thickness plate, IEEE Trans. Magn. 51 (9) (2015) 6201507. `doi:10.1109/TMAG.2015.2426676`.

[40] K. Pipis, A. Skarlatos, T. Theodoros, D. Lesselier, ECT-signal calculation of cracks near fastener holes using an integral equation formalism with dedicated Green's kernel, IEEE Trans. Magn. 52 (4) (2016) 6200608. `doi:10.1109/TMAG.2015.2496189`.

[41] T. Theodoulidis, J. R. Bowler, Interaction of an eddy-current coil with a right-angled conductive wedge, IEEE Trans. Magn. 46 (4) (2010) 1034–1042. `doi:{10.1109/TMAG.2009.2036724}`.

[42] J. N. Lyness, Numerical algorithms based on the theory of complex variable, Proc. ACM (1967) 125–133.

[43] L. M. Delves, J. N. Lyness, A numerical method for locating the zeros of an analytic function, Math. Comp. 21, (100) (1967) 543–560.

[44] A. Skarlatos, T. Theodoulidis, Eddy-current interaction between a probe coil and a conducting plate with a cylindrical borehole, in: F. K. Joao M. A. Rebello, T. Chasy (Eds.), Electromagnetic Nondestructive Evaluation (XVI), Vol. 38 of Studies in Applied Electromagnetics and Mechanics, IOS Press, 2014, pp. 181–188. `doi:10.3233/978-1-61499-354-4-181`.

[45] M. Abramowitz, I. Stegun, Handbook of Mathematical Functions with Formulas, Graphs, and Mathematical Tables, Dover, New York, 1972.

[46] D. J. Harrison, L. . D. Jones, S. K. Burke, Benchmark problems for defect size and shape determination in eddy-current nondestructive evaluation, J. Nondestr. Eval. 15 (1) (1996) 21–34. `doi:{10.1007/BF00733823}`.

[47] R. Miorelli, C. Reboud, T. Theodoulidis, 2013 eddy current benchmark problem: solution via a coupled integral approach, in: D. O. T. Dale E. Chimenti, Leonard J. Bond (Ed.), 40th Annual Review of Progress in Quantitative Nondestructive Evaluation, Vol. 33B of AIP Conference Proceedings, AIP Publishing, 2014, pp. 2086–2092. `doi:10.1063/1.4865080`.

[48] T. Theodoulidis, A. Skarlatos, Computation of eigenvalues and eigenfunctions in the solution of eddy current problems with modal methods, in: 22nd International Conference on the Computation of Electromagnetic Fields, COMPUMAG, 2019.

[49] A. Skarlatos, G. Pichenot, D. Lesselier, M. Lambert, B. Duchêne, Electromagnetic modeling of a damaged ferromagnetic metal tube by a volume integral equation formulation, IEEE Trans. Magn. 44 (2008) 623–632.

[50] H. A. Sabbagh, A model of eddy-current probes with ferrite cores, IEEE Trans. Magn. 23 (1987) 1888–1904.

[51] J. R. Bowler, Eddy-current interaction with an ideal crack. I. The forward problem, J. Appl. Phys. 75 (12) (1994) 8128–8137.

[52] J. R. Bowler, Eddy-current interaction with an ideal crack. II. The inverse problem, J. Appl. Phys. 75 (12) (1994) 8138–8144.

[53] Y. Yoshida, J. R. Bowler, Thin-skin eddy-current interaction with semielliptical and epicyclic cracks, IEEE Trans. Magn. 36 (1) (2000) 281–291.

[54] J. R. Bowler, N. Harfield, Vector potential integral formulation for eddy-current probe response to cracks, IEEE Trans. Magn. 36 (2) (2000) 461–469.

[55] T. Theodoulidis, Developments in efficiently modelling eddy current testing of narrow cracks, NDT E Int. 43 (7) (2010) 591–598. `doi:10.1016/j.ndteint.2010.06.003`.

[56] T. Theodoulidis, N. Poulakis, A. Dragogias, Rapid computation of eddy current signals from narrow cracks, NDT E Int. 43 (1) (2010) 13–19. `doi:10.1016/j.ndteint.2009.08.005`.

[57] R. Miorelli, C. Reboud, T. Theodoulidis, N. Poulakis, D. Lesselier, Efficient modeling of ECT signals for realistic cracks in layered half-space, IEEE Trans. Magn. 49 (6) (2013) 2886–2892. `doi:10.1109/TMAG.2012.2236102`.

[58] J. R. Bowler, T. P. Theodoulidis, Boundary element calculation of eddy currents in cylindrical structures containing cracks, IEEE Trans. Magn. 45 (2009) 1012–1015.

[59] K. Pipis, A. Skarlatos, T. Theodoulidis, D. Lesselier, Impedance of an induction coil accounting for the end-effect in eddy-current inspection of steam generator tubes, in: H. K. Noritaka Yusa, Tetsuya Uchimoto (Ed.), Electromagnetic Nondestructive Evaluation (XIX), Vol. 41 of Studies in Applied Electromagnetics and Mechanics, IOS Press, 2016, pp. 237–244. `doi:10.3233/978-1-61499-639-2-237`.

[60] D. E. Russell, D. D. Mackintosh, A. A. Shatat, Remote field testing, in: S. Udpa, P. O. Moore (Eds.), Nondestructive testing handbook, Vol. 5. Electromagnetic testing, Americal society for nondestructive testing, Columbus OH, 2004, Ch. 8, pp. 207–226.

[61] D. L. Atherton, S. Sullivan, M. Daly, A remote field eddy current tool for inspecting nuclear reactor pressure tubes, Brit. J. Nondestruct. Test. 30 (1988) 22–28.

[62] D. L. Atherton, W. Czura, Finite element poynting vector calculations for remote field eddy current inspection of tubes with circumferential slots, IEEE Trans. Magn. 27 (5) (1991) 3920 – 3922. `doi:10.1109/20.104960`.

[63] D. L. Atherton, W. Czura, Remote field eddy current technique: phantom exciter model calculations, Res. Nondestr. Eval. 5 (1993) 123–134. `doi:10.1007/BF01606361`.

[64] D. L. Atherton, Remote field eddy current inspection, IEEE Trans. Magn. 31 (6) (1995) 4142 – 4147. `doi:10.1109/20.104960`.

[65] S. M. Hauglajd, Fundamental analysis of the remote-field eddy-current effect, IEEE Trans. Magn. 32 (1996) 3195–3211.

[66] S. Sharma, Y. Sun, L. Udpa, Finite element modeling for simulating remote field flaw detection in aircraft frame, IEEE Trans. Magn. 35 (3) (1999) 1750 – 1753. `doi:10.1109/20.767368`.

[67] J. C. Aldrin, H. A. Sabbagh, E. Sabbagh, R. K. Murphy, M. Keiser, D. S. Forsyth, E. Lindgren, Model-based inverse methods for bolt-hole eddy current (BHEC) inspections, in: AIP Conference Proceedings, Vol. 1581, 2014, pp. 1433–1440. `doi:10.1063/1.4864990`.

[68] J. C. Aldrin, M. Keiser, D. Motes, J. Flores-Lamb, D. S. Forsyth, H. A. Sabbagh, E. Sabbagh, R. K. Murphy, R. Mooers, C. Henry, E. Lindgren, Progress and challenges of inverse methods for sizing cracks in multilayer bolt-hole eddy curent inspections, in: A. Tamburrino, Y. Deng, S. Chakrapani (Eds.), Electromagnetic Nondestructive Evaluation (XXII), Vol. 44 of Studies in Applied Electromagnetics and Mechanics, IOS Press, 2019, pp. 92–97. `doi:10.3233/SAEM190010`.

[69] J. S. Knopp, J. C. Aldrin, Funamental feature extraction methods for the analysis of eddy current data, in: L. Udpa, Y. Melikhov, A. Tamburrino (Eds.), Electromagnetic Nondestructive Evaluation (XI), Vol. 31 of Studies in Applied Electromagnetics and Mechanics, IOS Press, 2008, pp. 133–140. `doi:10.3233/SAEM190010`.

[70] J. S. Knopp, J. C. Aldrin, J. Misra, Considerations in the validation and application of models for eddy current inspection of cracks around fastener holes, J. Nondestr. Eval. 25 (3) (2006) 123–137.

[71] J. S. Knopp, J. C. Aldrin, K. V. Jata, Computational methods in eddy current crack detection at fastener sites in multi-layer structures, Nondestructive Testing and Evaluation 24 (1-2) (2009) 103–120.

[72] G. Yang, A. Tamburrino, L. Udpa, S. S. Udpa, Z. Zeng, Y. Deng, P. Que, Pulsed eddy-current based giant magnetoresistive system for the inspection of aircraft structures, IEEE Trans. Magn. 46 (3) (2010) 910–917.

[73] G. Yang, G. Dib, L. Udpa, A. Tamburrino, S. S. Udpa, Rotating field ec-gmr sensor for crack detection at fastener site in layered structures, IEEE Sensors J. 15 (1) (2015) 463–470. `doi:10.1109/JSEN.2014.2341653`.

[74] R. Miorelli, C. Reboud, T. Theodoulidis, J. Martinos, N. Poulakis, D. Lesselier, Coupled approach VIM–BEM for efficient modeling of ect signal due to narrow cracks and volumetric flaws in planar layered media, NDT E Int. 62 (2014) 178–183. `doi:10.1016/j.ndteint.2013.12.013`.

[75] A. Skarlatos, T. Theodoulidis, A modal approach for the solution of the non-linear induction problem in ferromagnetic media, IEEE Trans. Magn. 55 (2) (2016) 7000211. `doi:10.1109/TMAG.2015.2480043`.

[76] A. Skarlatos, T. Theodoulidis, Study of the non-linear eddy-current response in a ferromagnetic plate: Theoretical analysis for the 2D case, NDT E Int. 93 (Supplement C) (2018) 150–156. `doi:10.1016/j.ndteint.2017.09.003`.

[77] A. Skarlatos, M. Clemens, T. Weiland, Start vector generation for implicit Newmark time integration of the wave equation, IEEE Trans. Magn. 42 (4) (2006) 631–634. `doi:10.1109/TMAG.2006.872008`.

[78] A. Skarlatos, G. Pichenot, D. Lesselier, M. Lambert, B. Duchêne, Numerical modeling of eddy current nondestructive evaluation of ferromagnetic tubes via an integral equation approach, in: A. Tamburrino, Y. Melikhov, Z. Chen, L. Udpa (Eds.), Electromagnetic Nondestructive Evaluation (XI), Vol. 31 of Studies in Applied Electromagnetics and Mechanics, IOS Press, 2008, pp. 225–230. `doi:10.3233/978-1-58603-896-0-225`.

[79] A. Skarlatos, C. Gilles-Pascaud, G. Pichenot, G. Cattiaux, T. Sollier, Modeling of steam generator tubes inspection in the proximity of support plate's area via a coupled finite element - volume integral method approach, in: Y. K. Shin, H. B. Lee, S. J. Song (Eds.), Electromagnetic Nondestructive Evaluation (XII), Vol. 32 of Studies in Applied Electromagnetics and Mechanics, IOS Press, 2009, pp. 51–58. `doi:10.3233/978-1-60750-023-0-51`.

[80] A. Skarlatos, C. Gilles-Pascaud, G. Pichenot, G. Cattiaux, T. Sollier, Eddy current inspection of steam generator tubes near support plates with trefoil and quatrefoil-shaped holes: a hybrid volume integral – finite elements approach, in: J. Knopp, M. Blodgett, B. Wincheski, N. Bowler (Eds.), Electromagnetic Nondestructive Evaluation (XIII), Vol. 33 of Studies in Applied Electromagnetics and Mechanics, IOS Press, 2010, pp. 26–33. `doi:10.3233/978-1-60750-554-9-26`.

[81] K. Pipis, A. Skarlatos, T. Theodoulidis, D. Lesselier, Eddy-current inspection modelling of a thin crack located in the vicinity of a fastener borehole, in: Proc. of the 19th ACES conference, 2014.

[82] K. Pipis, A. Skarlatos, D. Lesselier, T. Theodoulidis, A fast integral equation model with a dedicated green's kernel for eddy-current inspection of fastener holes, AIP Conference Proceedings 1650 (1) (2015) 477–483. `doi:10.1063/1.4914644`.

[83] B. Davis, B. Martin, Numerical inversion of Laplace transform: a survey and comparison of methods, J. Comput. Phys. 33 (1) (1979) 1–32. `doi:10.1016/0021-9991(79)90025-1`.

[84] T. Theodoulidis, Developments in calculating the transient eddy-current response from a conductive plate, IEEE Trans. Magn. 44 (7) (2008) 1894–1896.

[85] T. Theodoulidis, A. Skarlatos, Efficient calculation of transient eddy current response from multilayer cylindrical conductive media, Phil. Trans. R. Soc. A 378 (2020) 20190588. `doi:10.1098/rsta.2019.0588`.

[86] J. R. Bowler, T. P. Theodoulidis, Eddy currents induced in a conducting rod of finite length by a coaxial encircling coil, J. Phys. D: Appl. Phys. 38 (16) (2005) 2861–2868. `doi:{doi:10.1088/0022-3727/38/16/019}`.

[87] V. Zakian, Optimisation of numerical inversion of Laplace transforms, Electron. Lett 6 (21) (1970) 677–679.

[88] L. Brancik, Programs for fast numerical inversion of Laplace transforms in Matlab language environment, 1999.
URL `http://dsp.vscht.cz/konference_matlab/MATLAB99/`

[89] W. Cheng, Pulsed eddy current testing of carbon steel pipes' wall-thinning through insulation and cladding, J. Nondestr. Eval. 31 (2012) 215–224. `doi:10.1007/s10921-012-0137-9`.

[90] N. Ulapane, A. Alempijevic, J. V. Miro, TeresaVidal-Calleja, Review of pulsed eddy current signal feature extraction methods for conductive ferromagnetic material-thickness quantification, NDT E Int. 100 (2018) 108–114. `doi:10.1016/j.ndteint.2018.08.003`.

[91] X. Chen, Y. Lei, Excitation current waveform for eddy current testing on the thickness of ferromagnetic plates, NDT E Int. 66 (2014) 28–33. `doi:10.1016/j.ndteint.2014.04.006`.

[92] A. Ratsakou, C. Reboud, A. Skarlatos, D. Lesselier, Model based characterisation of delamination by means of thermographic inspection, J. Phys. Conf. Ser. 1476 (2020) 012005. `doi:10.1088/1742-6596/1476/1/012005`.

[93] A. Ratsakou, A. Skarlatos, C. Reboud, D. Lesselier, Shape reconstruction of delamination defects using thermographic infrared signals based on an enhanced Canny approach, Infrared Phys. Technol. 111 (2020) 103527. `doi:10.1016/j.infrared.2020.103527`.

[94] D. Maillet, S. André, J. C. Batsale, A. Degiovanni, C. Moyne, Thermal quadrupoles: soving the heat equation through integral transforms, 1st Edition, John Willey & Sons, Inc., 2000.

[95] M. Clemens, T. Weiland, Transient eddy-current calculation with the FI-method, IEEE Trans. Magn. 35 (3) (1999) 1163–1166. `doi:{10.1109/20.996104}`.

[96] M. Clemens, M. Wilke, T. Weiland, Extrapolation strategies in transient magnetic field simulations, IEEE Trans. Magn. 39 (3) (2003) 1171–1174. `doi:{10.1109/TMAG.2003.810523}`.

[97] G. Benderskaya, M. Clemens, H. D. Gersem, T. Weiland, Embedded runge-kutta methods for field-circuit coupled problems with switching elements, IEEE Trans. Magn. 41 (5) (2005) 1612–1615. `doi:10.1109/TMAG.2005.845018`.

[98] G. Benderskaya, W. Ackermann, H. D. Gersem, T. Weiland, Adaptive time stepping for electromagnetic models with sinusoidal dynamics, IEEE Trans. Magn. 44 (6) (2008) 1262–1265. `doi:10.1109/TMAG.2007.916278`.

[99] W. J. Welch, Reciprocity theorems for electromagnetic fields whose time dependence is arbitrary, IRE Trans. Antennas Propagat. 8 (1) (1960) 68–73.

[100] W. J. Welch, Comments on reciprocity theorems for electromagnetic fields whose time dependence is arbitrary, IRE Trans. Antennas Propagat. 9 (1) (1961) 114–115.

[101] B. Cheo, A reciprocity theorems for electromagnetic fields with general time dependence, IRE Trans. Antennas Propagat. 13 (2) (1965) 278–284.

[102] A. de Hoop, Time-domain reciprocity theorems for electromagnetic fields in dispersive media, Radio Sci. 22 (7) (1987) 1171–1178.

[103] A. de Hoop, I. E. Lager, V. Tomassetti, The pulsed-field multiport antenna system reciprocity relation and its applications — a time-domain approach, IEEE Trans. Antennas Propag. 57 (3) (2009) 594–605.

[104] A. Shlivinski, E. Heyman, R. Kastner, Antenna characterization in the time-domain, IEEE Trans. Antennas Propag. 45 (7) (1997) 1140–1148.

[105] A. Shlivinski, Time-domain coupled response of antennas - reciprocity theorem approach, IEEE Trans. Antennas Propag. 65 (4) (2017) 1714–1727.

[106] J. Bowler, M. Johnson, Pulsed eddy-current response to a conducting half-space, IEEE Trans. Magn. 33 (3) (1997) 2258–2264.

[107] A. Ratsakou, C. Reboud, A. Skarlatos, D. Lesselier, Fast simulation approach dedicated to infrared thermographic inspection of delaminated planar pieces, AIP Conference Proceedings 2102 (1) (2019) 120004. `doi:10.1063/1.5099846`.

[108] A. Skarlatos, T. Theodoulidis, N. Poulakis, A fast and robust semi-analytical approach for the calculation of coil transient eddy-current response above planar specimens, IEEE Trans. Magn. 58 (9) (2022) 1–9. `doi:10.1109/TMAG.2022.3183019`.

[109] R. Miorelli, A. Skarlatos, C. Reboud, Flaw characterization in conductive media based on pulsed eddy current measurements: a fast non-iterative inversion approach, IET Sci. Meas. Technol. 15 (3) (2021) 259–267. `doi:10.1049/smt2.12027`.

[110] R. Schuhmann, T. Weiland, A stable interpolation technique for fdtd on nonorthogonal grids, Int. J. Numer. Modell. 11 (1998) 299–306. `doi:{10.1002/(SICI)1099-1204(199811/12)11:6<299::AID-JNM314>3.0.CO;2-A}`.

[111] R. Schuhmann, Die nichtorthogonale Finite-Integrations-Methode zur Simulation Elektromagnetischer Felder, Ph.D. thesis, Technische Universität Darmstadt (1999).

[112] T. Weiland, Time domain electromagnetic field computation with finite difference methods, Int. J. Numer. Modell. 9 (4) (1996) 295–319. `doi:{10.1002/(SICI)1099-1204(199607)9:4<295::AID-JNM240>3.0.CO;2-8}`.

[113] R. Schuhmann, T. Weiland, Conservation of discrete energy and related laws in the finite integration technique, Progress Electromagn. Res. (PIER) 32 (2001) 301–316. `doi:{10.2528/PIER00080112}`.

[114] M. Clemens, T. Weiland, Discrete electromagnetism with the finite integration technique, Progress Electromagn. Res. (PIER) 32 (2001) 65–87. `doi:{10.2528/PIER00080102}`.

[115] C. Reboud, T. Theodoulidis, Field computations of inductive sensors with various shapes for semi-analytical ect simulation, in: B. Rao, T. Jayakumar, K. Balasubramanian, B. Raj (Eds.), Electromagnetic Nondestructive Evaluation (XV), Studies in Applied Electromagnetics and Mechanics, IOS Press BV, Nieuwe Hemweg 6B, 1013 BG Amsterdam, Netherlands, 2012, pp. 3–10.

[116] R. Albanese, G. Rubinacci, Solution of three dimensional eddy current problems by integral and differential methods, IEEE Trans. Magn. 24 (1) (1988) 98–101.

[117] J. B. Manges, Z. J. Cendes, A generalised tree-cotree gauge for magnetic field computation, IEEE Trans. Magn. 31 (3) (1995) 1342–1347.

[118] P. Hahne, T. Weiland, 3D eddy-current computation in the frequency-domain regarding the displacement current, IEEE Trans. Magn. 28 (2) (1992) 1801–1804. `doi:{10.1109/20.124056}`.

[119] M. Clemens, T. Weiland, Regularization of eddy current formulations using discrete grad-div operators, IEEE Trans. Magn. 38 (2) (2002) 569–572. `doi:10.1109/20.996149`.

[120] M. Clemens, S. Schöps, H. D. Gersem, A. Bartel, Decomposition and regularization of nonlinear anisotropic curl-curl DAEs, COMPEL 30 (6) (2011) 1701–1714. `doi:10.1108/03321641111168039`.

[121] A. Bossavit, Stiff problems in eddy-current theory and the regularization of Maxwell's equations, IEEE Trans. Magn. 37 (5) (2001) 3542–3545. `doi:10.1109/20.952657`.

[122] O. Bíró, K. Preis, Finite element analysis of 3-D eddy currents, IEEE Trans. Magn. 26 (2) (1990) 418–423. `doi:10.1137/16M1077817`.

[123] Comsol multiphysics® v. 5.2.
URL `www.comsol.com`

[124] T. P. Theodoulidis, J. R. Bowler, Impedance of an induction coil at the opening of a borehole in a conductor, J. Appl. Phys. 103 (2) (2008) 024905–1–024905–9.

[125] X. P. V. Maldague, P. O. Moore, Nondestructive Testing Handbook: Infrared and Thermal Testing, Vol. 3, The American Society for Nondestructive Testing, 2001.

[126] A. Skarlatos, C. Reboud, Numerical modelling of eddy-current testing in tubes with non-canonical wall profile using modal description of the sources, in: F. K. Joao M. A. Rebello, T. Chasy (Eds.), Electromagnetic Nondestructive Evaluation (XVI), Vol. 38 of Studies in Applied Electromagnetics and Mechanics, IOS Press, 2014, pp. 111–118. `doi:10.3233/978-1-61499-354-4-111`.

[127] A. Skarlatos, C. Reboud, Eddy-current inspection modelling of symmetrical work-pieces using three-dimensional probes based on a mixed numerical/modal formulation, AIP Conference Proceedings 1581 (1) (2014) 1413–1420. `doi:10.1063/1.4864987`.

[128] A. Skarlatos, A mixed spatial-spectral eddy-current formulation for pieces with one symmetry axis, IEEE Trans. Magn. 56 (9) (2020) 1–11. `doi:10.1109/TMAG.2020.3008092`.

[129] A. Skarlatos, C. Reboud, Transient eddy-current calculations using combined fourier/spatial bases, in: 20th International Symposium on Applied Electromagnetics and Mechanics, 2022.

[130] A. Vigneron, A. Skarlatos, C. Reboud, Numerical modelling of axissymetrical ferrite-core probes over planar specimens using a coupled FIT/semi-analytical formulation, in: 22nd International Conference on the Computation of Electromagnetic Fields, COMPUMAG, 2013.

[131] R. Albanese, F. I. Hantila, G. Rubinacci, A nonlinear eddy current integral formulation in terms of a two-component current density vector potential, IEEE Trans. Magn. 32 (3) (1996) 784–787.

[132] R. Albanese, F. I. Hantila, G. Preda, G. Rubinacci, A nonlinear eddy-current integral formulation for moving bodies, IEEE Trans. Magn. 34 (5) (1998) 2529–2534.

[133] F. I. Hănţilă, G. Preda, M. Vasiliu, Polarization method for static fields, IEEE Trans. Magn. 36 (4) (2000) 672–675.

[134] O. Bíró, K. Preis, An efficient time domain method for nonlinear periodic eddy current problems, IEEE Trans. Magn. 42 (4) (2006) 695–698.

[135] O. Bíró, G. Koczka, K. Preis, Fast time-domain finite element analysis of 3-D nonlinear time-periodic eddy current problems with $T, \Phi - \Phi$ formulation, IEEE Trans. Magn. 47 (5) (2011) 1170–1173.

[136] I. R. Circ, F. Hantila, An efficient harmonic method for solving nonlinear time-periodic eddy-current problems, IEEE Trans. Magn. 43 (4) (2007) 1185–1188.

[137] I. Munteanu, S. Drobny, T. Weiland, D. Ioan, Triangle search method for nonlinear electromagnetic field computation, COMPEL 20 (2) (2001) 417–430.

[138] J. Yuan, Numerical simulation of hysteresis effects in ferromagnetic material with the finite integration technique, Ph.D. thesis, Technische Universität Darmstadt, Cuvillier Verlag Göttingen (2005).

[139] M. d'Aquino, G. Rubinacci, A. Tamburrino, S. Ventre, Efficient numerical solution of magnetic field problems in presence of hysteretic media for non-destructive evaluation, IEEE Trans. Magn. 49 (7) (2013) 3167–3170.

[140] M. d'Aquino, G. Rubinacci, A. Tamburrino, S. Ventre, Three-dimensional computation of magnetic fields in hysteretic media with time-periodic sources, IEEE Trans. Magn. 50 (2) (2014) 53–56.

[141] R. Albanese, G. Rubinacci, Numerical procedures for the solution of non-linear electromagnetic problems, IEEE Trans. Magn. 28 (2) (1992) 1228–1231.

[142] J. O'Dwyer, T. O'Donnell, Choosing the relaxation parameter for the solution of nonlinear magnetic field problems by the Newton-Raphson method, IEEE Trans. Magn. 31 (3) (1995) 1484–1487.

[143] S. Drobny, T. Weiland, Numerical calculation of nonlinear transient field problems with the newton-raphson method, IEEE Trans. Magn. 36 (4) (2000) 809–812.

[144] H. D. Gersem, I. Munteanu, T. Weiland, Construction of differential material matrices for the orthogonal finite-integration technique with nonlinear materials, IEEE Trans. Magn. 44 (6) (2008) 710–713.

[145] J. Yuan, M. Clemens, T. Weiland, Simulation of hysteresis effects with the classical preisach model in fi/sup 2/td methods, Int. J. Appl. Electromagnet Mech 19 (1-4) (2004) 19–24.

[146] J. Yuan, M. Clemens, H. De Gersem, T. Weiland, Solution of transient hysteretic magnetic field problems with hybrid newton-polarization methods, IEEE Trans. Magn. 41 (5) (2005) 1720–1723. `doi:10.1109/TMAG.2005.846050`.

[147] J. Yuan, M. Clemens, T. Weiland, Transient magnetic field calculations in hysteretic media with fi/sup 2/td formulations, in: Sixth International Conference on Electrical Machines and Systems, 2003. ICEMS 2003., Vol. 2, 2003, pp. 769–773 vol.2.

[148] O. Bíró, K. Preis, K. R. Richter, Various FEM formulations for the calculation of transient 3d eddy currents in nonlinear media, IEEE Trans. Magn. 31 (3) (1995) 1307–1312.

[149] J. Saitz, Newton-Raphson method and fixed-point technique in finite element computation of magnetic field problems in media with hysteresis, IEEE Trans. Magn. 35 (3) (1999) 1398–1401.

[150] C. Brezinski, M. R. Zaglia, Generalizations of Aitken's process for accelerating the convergence of sequences, Comput. Appl. Math. 26 (2) (2007) 171–189. `doi:10.1590/S0101-82052007000200001`.

[151] F. Van-Den-Berg, P. Kok, H. Yang, M. Aarnts, J.-J. Vink, W. Beugeling, P. Meilland, T. Kebe, M. Stolzemberg, D. Krix, A. Peyton, W. Zhu, A. Martinez-De-Guerenu, I. Gutierrez, D. Jorge-Badiola, K. Gurruchaga, P. Lundin, A. Volker, M. Mota, J. Monster, H. Wirdelius, C. Mocci, G. Nastasi, V. Colla, C. Davis, L. Zhou, R. Schmidt, S. Labbé, C. Reboud, A. Skarlatos, T. Svatoň, V. Leconte, P. Lombard, In-line characterisation of microstructure and mechanical properties in the manufacturing of steel strip for the purpose of product uniformity control (Jun. 2016).

[152] F. D. Van Den Berg, P. Kok, H. Yang, M. Aarnts, P. Meilland, T. Kebe, M. Stolzenberg, D. Krix, W. Zhu, A. Peyton, A. Martinez-De-Guerenu, I. Gutierrez, D. Jorge-Badiola, M. Malmström, A. Volker, A. Duijster, H. Wirdelius, A. Boström, C. Mocci, M. Vannucci, V. Colla, C. Davis, L. Zhou, R. Schmidt, S. Labbé, C. Reboud, A. Skarlatos, V. Leconte, P. Lombard, Product Uniformity Control – A Research Collaboration of European Steel Industries to Non-Destructive Evaluation of Microstructure and Mechanical Properties, in: Electromagnetic Nondestructive Evaluation (XXII), Vol. 43 of Studies in Applied Electromagnetics and Mechanics, IOS Press, 2018, pp. 120–129. `doi:10.3233/978-1-61499-836-5-120`.

[153] G. Dobmann, I. Altpeter, B. Wolter, R. Kern, Industrial applications of 3MA - Micromagnetic Multiparameter Microstructure and Stress Analysis, in: A. Tamburrino, Y. Melikhov, Z. Chen, L. Udpa (Eds.), Electromagnetic Nondestructive Evaluation (XI), Vol. 31 of Studies in Applied Electromagnetics and Mechanics, IOS Press, 2008, pp. 18–25. `doi:10.3233/978-1-58603-896-0-18`.

[154] F. I. Hănţilă, Mathematical models of the relation between b and h for non-linear media, Rev. Roum. Sci. Tech.-Électrotechn. et Énerg. 19 (3) (1974) 429–448.

[155] F. I. Hănţilă, A method of solving stationary magnetic field in non-linear media, Rev. Roum. Sci. Tech.-Électrotechn. et Énerg. 20 (3) (1975) 397–407.

[156] I. F. Hănţilă, G. Grama, An overrelaxation method for the computation of the fixed point of a contractive mapping, Rev. Roum. Sci. Tech.-Électrotechn. et Énerg. 27 (4) (1982) 395–398.

[157] E. Mandelung, On the magnetization by a fast current and an operation principle of the magnetodetectors of rutherford-marconi, Ann. Phys. 17 (1905) 861–890.

[158] L. Dupré, J. Melkebeek, Electromagnetic hysteresis modelling: from material science to finite element analysis of devices, International Compumag Society Newsletter. 10(3). 10 (3) (2003) 4–15.

[159] I. Mayergoyz, Mathematical Models of Hysteresis and Their Applications, 1st Edition, Elsevier Science Inc., New York, 2003.

[160] G. Bertotti, V. Basso, M. Lobue, A. Magni, Chapter 1 - thermodynamics, hysteresis, and micromagnetics, in: G. Bertotti, I. D. Mayergoyz (Eds.), The Science of Hysteresis, Academic Press, Oxford, 2006, pp. 1–106. `doi:10.1016/B978-012480874-4/50012-9`.

[161] A. Stancu, P. Andrei, Characterization of static hysteresis models using first-order reversal curves diagram method, Physica B 372 (1) (2006) 72–75. `doi:doi.org/10.1016/j.physb.2005.10.022`.

[162] A. Skarlatos, A. Martínez-de Guerenu, R. Miorelli, A. Lasaosa, C. Reboud, Use of meta-modelling for identification and interpolation of parametric hysteresis models applied to the characterization of carbon steels, Physica B 549 (2018) 122–126. `doi:10.1016/j.physb.2017.11.053`.

[163] M. A. Mel'gui, Formulas for describing nonlinear and hysteretic properties of ferromagnets, Defektoskopiya 11 (1987) 3–10, (Translated from rusian).

[164] A. Skarlatos, C. Reboud, T. Kebe, F. van den Berg, R. Schmidt, Simulation of IMPOC ystem for online monitoring of steel mechanical properties, in: 12th European Conference on Nondestructive Testing, 2018.

[165] T. Svatoň, A. Skarlatos, Application de l'approche de l'intégration finie aux problèmes d'évaluation des matériaux à l'aide des méthodes électro-magnétiques, in: 8ème Conférence Européenne sur les Méthodes Numériques en Electromagnétisme (NUMELEC), 2015.

[166] T. Svatoň, A. Skarlatos, N. Poulakis, T. Theodoulidis, Impact of the hysteresis description model on the numerical simulation results for yoke-oriented inspection configurations, in: H. K. Noritaka Yusa, Tetsuya Uchimoto (Ed.), Electromagnetic Nondestructive Evaluation (XIX), Vol. 41 of Studies in Applied Electromagnetics and Mechanics, IOS Press, 2016, pp. 118–125. `doi:10.3233/978-1-61499-639-2-118`.

[167] A. Skarlatos, C. Reboud, T. Svatoň, A. M. de Guerenu, T. Kebe, F. van den Berg, Modelling the IMPOC response for different steel strips, in: 19th World Conference on Nondestructive Testing, 2016.

[168] J. P. Sethna, K. A. Dahmen, O. Perković, Random-field Ising models of hysteresis, in: G. Bertotti, I. D. Mayergoyz (Eds.), The Science of Hysteresis, 1st Edition, Vol. II, Academic Press, 2006, Ch. 2, pp. 105–179.

[169] J. P. Sethna, K. A. Dahmen, S. Kartha, J. A. Krumhansl, B. Roberts, J. Shore, Hysteresis and hierarchies: Dynamics of disorder-driven first-order phase transformations, Phys. Rev. Lett. 70 (21) (1993) 3347–3350. `doi:10.1103/PhysRevLett.70.3347`.

[170] O. Perković, K. A. Dahmen, J. P. Sethna, Avalanches, Barkhausen noise, and plain old criticality, Phys. Rev. Lett. 75 (24) (1995) 4528–4531. `doi:10.1103/PhysRevLett.75.4528`.

[171] K. A. Dahmen, J. P. Sethna, Hysteresis avalanches, and disorder-induced critical scaling: A renormalization-group approach, Phys. Rev. B 53 (22) (1996) 14872–14905. `doi:10.1103/PhysRevB.53.14872`.

[172] M. C. Kuntz, O. Perković, K. A. Dahmen, B. W. Roberts, J. P. Sethna, Hysteresis, avalanches, and noise, Comput. Sci. Eng. 1 (4) (1999) 73–81. `doi:10.1109/5992.774844`.

[173] M. C. Kuntz, J. P. Sethna, Noise in disorder systems: The power spectrum and dynamic exponents in avalanche models, Phys. Rev. B 62 (17) (2000) 11699–11708. `doi:10.1103/PhysRevB.62.11699`.

[174] K. A. Dahmen, J. P. Sethna, M. C. Kuntz, O. Perković, Hysteresis and avalanches: phase transitions and critical phenomena in driven disordered systems, J. Mag. Mag. Mater. 226-230 (Part 2) (2001) 1287–1292. `doi:10.1016/S0304-8853(00)00749-6`.

[175] A. P. Mehta, A. C. Mills, K. A. Dahmen, J. P. Sethna, Universal pulse shape function and exponents: Critical test for avalanche models applied to Barkhausen noise, Phys. Rev. E 65 (2002) 046139. `doi:10.1103/PhysRevE.65.046139`.

[176] A. Skarlatos, A. Martínez-de Guerenu, D. J. Badiola, I. Lelidis, Interpretation of the magnetic susceptibility behaviour of soft carbon steels based on the scaling theory of second order phase transitions for systems with supercritical disorder, J. Mag. Mag. Mater. 555 (2022) 169265. `doi:10.1016/j.jmmm.2022.169265`.

[177] T. L. Gilbert, A phenomenological theory of damping in ferromagnetic materials, IEEE Trans. Magn. 40 (6) (2004) 3443–3449. `doi:10.1109/TMAG.2004.836740`.

[178] G. Durin, S. Zapperi, The Barkhausen effect, in: G. Bertotti, I. D. Mayergoyz (Eds.), The Science of Hysteresis, 1st Edition, Vol. II, Academic Press, 2006, Ch. 3, pp. 181–267.

[179] S. Zapperi, P. Cizeau, G. Durin, H. E. Stanley, Dynamics of a ferromagnetic domain wall: Avalanches depinning transition, and the Barkhausen effect, Phys. Rev. B 58 (10) (1998) 6353–6366. `doi:10.1103/PhysRevB.58.6353`.

[180] S. Zapperi, P. Ray, H. E. Stanley, A. Vespignani, First-order transition in the breakdown of disordered media, Phys. Rev. Lett. 78 (8) (1997) 1408–1411.

[181] P. Cizeau, S. Zapperi, G. Durin, H. E. Stanley, Dynamics of a ferromagnetic domain wall and the Barkhausen effect, Phys. Rev. Lett. 79 (23) (1997) 4669–4672.

[182] G. Durin, S. Zapperi, Complex dynamics of magnetic domain walls, Physica A 314 (1-4) (2002) 230–234. `doi:10.1016/S0378-4371(02)01164-0`.

[183] F. Colaiori, S. Zapperi, G. Durin, Shape of a barkhausen pulse, J. Mag. Mag. Mater. 272-276 (2004) E533–E534. `doi:10.1016/j.jmmm.2003.12.1063`.

[184] S. Zapperi, A. Magni, G. Durin, Microscopic foundations of the Rayleigh law of hysteresis, J. Mag. Mag. Mater. 242-245 (2002) 987–992. `doi:10.1016/S0304-8853(01)01131-3`.

[185] A. van den Berg, L. Dupré, B. V. de Wiele, G. Crevecoeur, A mesoscopic hysteresis model based on the unconstrained minimization of the Gibbs free energy, IEEE Trans. Magn. 46 (2) (2010) 220–223. `doi:10.1109/TMAG.2009.2031978`.

[186] O. Hubert, L. Daniel, Effect of plastic straining on magnetostriction of ferromagnetic polycrystals - experiments and multiscale modeling, J. Mag. Mag. Mater. 304 (2006) e489–e491. `doi:{10.1016/j.jmmm.2006.02.132}`.

[187] L. Daniel, O. Hubert, N. Buiron, R. Billardon, Reversible magneto-elastic behavior: A multiscale approach, J. Mech. Phys. Solids 56 (2008) 1018–1042. `doi:{10.1016/j.jmps.2007.06.003}`.

[188] O. Hubert, L. Daniel, Multiscale modeling of the magneto-mechanical behavior of grain-oriented silicon steels, J. Mag. Mag. Mater. 320 (2008) 1412–1422. `doi:{10.1016/j.jmmm.2008.01.013}`.

[189] L. Daniel, O. Hubert, An analytical model for the $\delta$e effect in magnetic materials, EPJ AP 45 (3) (2009) 31101. `doi:{10.1051/epjap/2009012}`.

[190] L. Daniel, O. Hubert, An equivalent stress for the influence of multiaxial stress on the magnetic behavior, J. Appl. Phys. 105 (7) (2009) 07A313. `doi:10.1063/1.3068646`.

[191] O. Hubert, L. Daniel, Energetical and multiscale approaches for the definition of an equivalent stress for magneto-elastic couplings, J. Mag. Mag. Mater. 323 (2011) 1766–1781. `doi:{10.1016/j.jmmm.2011.01.041}`.

[192] S. Lazreg, O. Hubert, A multidomain modeling of the magnetoelastic behavior for nondestructive evaluation, J. Appl. Phys. 109 (2011) 07E508. `doi:{10.1063/1.3540416}`.

[193] L. Daniel, M. Rekik, O. Hubert, A multiscale model for magneto-elastic behaviour including hysteresis effects, Arch. Appl. Mech 84 (2014) 1307–1323. `doi:10.1007/s00419-014-0863-9`.

[194] L. Daniel, O. Hubert, M. Rekik, A simplified 3-D constitutive law for magnetomechanical behavior, IEEE Trans. Magn. 51 (3) (2015) 7300704. `doi:10.1109/TMAG.2014.2361643`.

[195] L. Zhou, C. Davis, P. Kok, Steel microstructure – magnetic permeability modelling: the effect of ferrite grain size and phase fraction, J. Mag. Mag. Mater. 519 (2021) 167439. `doi:10.1016/j.jmmm.2020.167439`.

[196] L. Zhou, C. Davis, P. Kok, F. van den Berg, Magnetic NDT for steel microstructure characterisation – modelling the effect of second phase distribution on magnetic relative permeabilty, 2016.

[197] T. M. T. Bui, Contribution à la modélisation du bruit Barkhausen en relation avec la microstructure des matériaux ferromagnétiques, Ph.D. thesis, Laboratoire Roberval UTC-CNRS, UMR 6253 (2010).

[198] P. Fagan, B. Ducharne, L. Daniel, A. Skarlatos, Multiscale modelling of the magnetic barkhausen noise energy cycles, J. Mag. Mag. Mater. 517 (2021) 167395. `doi:10.1016/j.jmmm.2020.167395`.

[199] P. Fagan, B. Ducharne, L. Daniel, A. Skarlatos, M. Domenjoud, C. Reboud, Effect of stress on the magnetic Barkhausen noise energy cycles: A route for stress evaluation in ferromagnetic materials, Mater. Sci. Eng. B 278 (2022) 115650. `doi:10.1016/j.mseb.2022.115650`.

[200] A. Skarlatos, R. Miorelli, C. Reboud, F. van den Berg, Magnetic characterization of steel strips using quarter-cycle field-gradient measurements, in: 20th International Symposium on Applied Electromagnetics and Mechanics, 2022.